Emergent Properties of Biomolecular Organization

Stanislav Tsitkov

Submitted in partial fulfillment of the
requirements for the degree of
Doctor of Philosophy
under the Executive Committee
of the Graduate School of Arts and Sciences

COLUMBIA UNIVERSITY

2021

ABSTRACT

Emergent Properties of Biomolecular Organization

Stanislav Tsitkov

The organization of molecules within a cell is central to cellular processes ranging from metabolism and damage repair to migration and replication. Uncovering the emergent properties of this biomolecular organization can improve our understanding of how organisms function and reveal ways to repurpose their components outside of the cell. This dissertation focuses on the role of organization in two widely studied systems: enzyme cascades and active cytoskeletal filaments.

Part I of this dissertation studies the emergent properties of the spatial organization of enzyme cascades. Enzyme cascades consist of a series of enzymes that catalyze sequential reactions: the product of one enzyme is the substrate of a subsequent enzyme. Enzyme cascades are a fundamental component of cellular reaction pathways, and spatial organization of the cascading enzymes is often essential to their function. For example, cascading enzymes assembled into multi-enzyme complexes can protect unstable cascade intermediates from the environment by forming tunnels between active sites.

We use mathematical modeling to investigate the role of spatial organization in three specific systems. First, we examine enzyme cascade reactions occurring in multi-enzyme complexes where active sites are connected by tunnels. Using stochastic simulations and theoretical results from queueing theory, we demonstrate that the fluctuations arising from the small number of molecules involved can cause non-negligible disruptions to cascade throughput. Second, we

develop a set of design principles for a compartmentalized cascade reaction with an unstable intermediate and show that there exists a critical kinetics-dependent threshold at which compartments become useful. Third, we investigate enzyme cascades immobilized on a synthetic DNA origami scaffold and show that the scaffold can create a favorable microenvironment for catalysis.

Part II of this dissertation focuses on the organization of active cytoskeletal filaments. Many mechanical processes of a cell, such as cell division, cell migration, and intracellular transport, are driven by the ATP-fueled motion of motor proteins (kinesin, dynein, or myosin) along cytoskeletal filaments (microtubules or actin filaments). Over the past two decades, researchers have been repurposing motor protein-driven propulsion outside of the cell to create systems where cytoskeletal filaments glide on surfaces coated with motor proteins. The study of these systems not only elucidates the mechanisms of force production within the cell, but also opens new avenues for applications ranging from molecular detection to computation.

We examine how microtubules gliding on surfaces coated with kinesin motor proteins can generate collective behavior in response to mutualistic interactions between the filaments and motors, thereby maximizing the utilization of system components and production. To this end, we used a microtubule-kinesin system where motors reversibly bind to the surface. In experiments, microtubules gliding on these reversibly bound motors were unable to cross each other and at high enough densities began to align and form long, dense bundles. The kinesin motors accumulated in trails surrounding the microtubule bundles and participated in microtubule transport.

In conclusion, our study of the emergent properties of the spatial organization of enzyme cascades and the mutualistic interactions within active systems of motor proteins and

cytoskeletal filaments provides insight into both how these systems function within cells and how they can be repurposed outside of them.

Table of Contents

Table of Figures

Acknowledgements

First, I would like to express my deepest gratitude to my advisor, Professor Henry Hess, for his steadfast mentorship, reliable guidance, and patience. Thank you for the freedom you gave me to explore new ideas, even though they sometimes led to a wild goose chase about swarming. Thank you for being so down-to-earth and constructive in your criticisms and for imparting me with proverbial wisdom about the elk. It is because of your positivity and encouragement that, even over 250 one-on-one meetings later, I still look forward to our discussions every week.

Next, I would like to thank my dissertation defense committee, Professor Elizabeth Olson, Professor Tal Danino, Professor Arne Gennerich, and Professor Nandan Nerurkar for their time and feedback on this dissertation.

I would like to thank all the Hess Lab members, Yifei, Neda, Megan, Altug, Gadiel, Henri and Joseph, and the visiting Professors, Professor Kakugo and Professor Shefi, for the exciting discussions and the fun times.

I would also like to thank my friends for their never-ending support, and for making life in New York so awesome.

Most of all, I would like to thank my parents and grandparents for spending so much time educating me, for raising me to succeed, for always believing in me, and for loving me. This is all possible only because of you.

Introduction

This dissertation studies the emergent properties of the organization of two biomolecular systems: enzyme cascades[1] (chapters 1-4) and active cytoskeletal filaments[2] (chapters 5-6). Enzyme cascades are collections of enzymes that catalyze sequential transformations of substrate molecules. Systems of active cytoskeletal filaments refer to dynamic systems where the components of the cellular cytoskeleton, actin filaments or microtubules, are repurposed outside of the cell to be propelled on surfaces coated with molecular motor proteins: myosin for actin filaments, and kinesin or dynein for microtubules.

Part I: Emergent properties of colocalized enzyme cascades

In cells, collections of enzymes catalyze the conversion of substrate molecules into product molecules via several intermediate molecules in multi-step reaction pathways called enzyme cascades.[3] An example of this is the glycolysis pathway of cellular respiration,[4] where a molecule of glucose, the initial substrate, is transformed into two molecules of pyruvate, the product, via nine intermediates in a ten-step enzymatic cascade, beginning with the conversion of glucose into glucose-6-phosphate catalyzed by hexokinase, and ending with the conversion of phosphoenolpyruvate into pyruvate catalyzed by pyruvate kinase.[5]

Often times, enzymes in a cascade demonstrate spatial organization.[3] The scale of this organization extends from the single molecule level, where protein-protein interactions between cascading enzymes can generate a favorable microenvironment for catalysis,[6, 7] to the cellular level, where portions of reaction pathways are compartmentalized into organelles.[8-10] For example, the subunits of the tryptophan synthase bi-enzyme complex, which is responsible for

catalyzing the conversion of indole-3-glycerol phosphate into tryptophan in certain bacteria, form a 2.5 nm-long tunnel between active sites to protect the unstable indole intermediate.[11] Alternatively, in the bacterium *Salmonella enterica*, the two-step reaction pathway responsible for the metabolism of propanediol to proponal and propionyl-phosphate is confined to the proteinaceous propanediol utilization bacterial microcompartment, which allows for the quarantine of the toxic propionaldehyde intermediate.[12, 13]

The study of enzyme cascades not only improves our understanding of biological systems, but also uncovers new approaches for molecular synthesis outside of the cell.[14] The goal is to achieve one-pot reactions which could efficiently convert substrate molecules into desired products without the need for laborious intermediate steps of filtration. [15-19] To this end, vast protein libraries are already available and they are constantly growing with the discoveries of new proteins in nature and the design of synthetic proteins via directed evolution.[20, 21] Recently, a synthetic 9-enzyme cascade was used to synthesize the HIV drug islatravir.[22] As the complexity of these one-pot reactions grows, it can be expected that they will begin to require an organization reminiscent to that of cascading enzymes within cells. For example, compartmentalization could prevent cross-reactivity between portions of synthetic enzyme cascades. [19, 23-30]

Despite the numerous experimental advances in work related to spatial organization of enzyme cascades, the development of a quantitative theory which explains the role of system parameters (i.e. enzyme kinetics, channeling properties, etc.) has only recently begun.[31-36] Developing a quantitative model of spatially organized enzymatic cascade reactions would not only improve our understanding of the functioning of the cell, but also aid in the design of bioreactors using cascading enzymes outside of the cell.

The first goal of this dissertation is to use mathematical modeling of enzyme kinetics to determine the role of spatial organization in enzyme cascades. Chapter 1 will introduce a mathematical model for an enzyme cascade reaction. The model will be used to show that assembling cascading enzymes in close proximity, so as to permit substrate channeling, can provide two benefits. First, it can decrease the lag time to reaction steady state. Second, if the cascade intermediate is unstable, it can enhance reaction throughput. Chapter 2 will extend the notion of substrate channeling to include temporary storage of intermediate substrate molecules; in this chapter, the model will be expanded to study tunneled enzyme cascade reactions, where cascading enzymes are assembled into multi-enzyme complexes and form tunnels of finite capacity between active sites to channel unstable intermediates. Using stochastic simulations and analytical results from queueing theory, it will be shown that the fluctuations arising from the small number of molecules involved in the tunneled cascade can cause significant disruptions to cascade throughput under certain conditions.[37] In Chapter 3, we will examine compartmentalized cascade reactions, where cascading enzymes are sequestered into compartments and pores in compartment boundaries create a diffusion barrier to both substrate influx and intermediate outflux. We will determine the optimal design principles for compartmentalized cascade reactions with unstable intermediates and demonstrate that there exists a critical threshold at which compartments become useful.[38] Finally, in Chapter 4, we will demonstrate how synthetic scaffolding for enzyme cascades can enhance cascade throughput by generating a favorable microenvironment for catalysis.[39]

Part II: Organization in systems of active cytoskeletal filaments

In cells, microtubules and actin filaments are organized to both provide support for cellular structure and serve as rails for force-production by the ATP-fueled motor proteins, kinesin,

dynein, and myosin.[40] The stepping of motor proteins along filaments drives cellular mechanical processes such as cellular replication, intracellular cargo transport, and cellular migration.[5] These motor-filament systems can be reconstituted outside of the cell in *in vitro* motility assays, in either a "native configuration," where motors step along surface bound filaments, or an "inverted" configuration, where filaments glide on motor-coated surfaces.[41] The study of motor-filament interactions in motility assays is of interest to researchers not only because it elucidates the force production mechanisms of cells, but also because of the potential for motor proteins to provide reliable nanoscale actuation in devices.[42] In Chapter 5, we will provide a review on the construction, components, and applications of nanoscale devices powered by motor protein-driven propulsion. In Chapter 6, we will introduce a dynamic system in the inverted configuration in which microtubules and kinesin motors exhibit mutualistic interactions and self-organize to generate collective behavior. To do this, we build off of a microtubule-kinesin system where motors are reversibly bound to the surface via an interaction between a hexahistidine (His_6) tag on the motor and a Ni(II) – nitrilotriacetic acid (Ni-NTA) moiety on the surface.[43, 44] In experiments, microtubules gliding on these reversibly bound motors were unable to cross each other and at high enough densities began to align and form long, dense bundles. In turn, the kinesin motors accumulated in trails surrounding the microtubule bundles and participated in microtubule transport. The organization of the microtubules into bundles and the kinesin motors into trails surrounding the bundles maximizes the utilization of system components and production.

Part I

Emergent Properties of Colocalized Enzyme Cascades

Chapter 1. Modeling Enzyme Cascades Reactions with Substrate Channeling

Introduction

Molecules undergoing sequential transformations catalyzed by enzymes in an enzyme cascade reaction must perform a diffusion-based search for active sites through the bulk solution between catalysis events.[45] It is reasonable to expect that the colocalization of cascading enzymes on a scaffold in close proximity will shorten this diffusive search, allowing a fraction of the molecules produced by one enzyme to be directly channeled into the active site of the subsequent enzyme in the cascade. [31, 46-48] It has been hypothesized that the result of this "substrate channeling" would be an enhanced cascade reaction throughput.[48] In experiments, enzyme cascades immobilized in close proximity on synthetic scaffolds have been reported to demonstrate enhanced cascade reaction throughput when compared to the scaffold-free case. [47, 49, 50]

In this chapter, we will introduce the methods for modeling enzyme cascade reactions with substrate channeling. These models will be used to demonstrate that, in the case of stable cascade intermediates, substrate channeling can only enhance the lag time to the steady state of a cascade reaction, and not the cascade throughput. It will also be shown that, in the case of unstable cascade intermediates, substrate channeling can enhance cascade throughput. The results of this section are similar to those of Idan and Hess,[31] although the approach is slightly different; in particular, the approach given here avoids the use of the Michaelis-Menten equation (Equation 1.9) for describing the kinetics of the downstream enzyme.

Methods

The Michaelis-Menten model for an enzyme-catalyzed reaction. The dynamics of enzyme-catalyzed reactions can be modeled using Michaelis-Menten kinetics, [51, 52] where the reaction is approximated by two steps: a reversible binding step between substrate and enzyme into an enzyme-substrate complex (with an on-rate constant, k_{on} and an off-rate constant, k_{off}) , and an irreversible conversion of enzyme-substrate complex into enzyme and product with rate constant k_{cat}:

$$E + S \underset{k_{off}}{\overset{k_{on}}{\rightleftharpoons}} ES \overset{k_{cat}}{\longrightarrow} E + P \tag{1.1}$$

The system of ordinary differential equations describing this chemical reaction can be written down as follows:

$$\frac{d[S]}{dt} = -k_{on}[E][S] + k_{off}[ES] \tag{1.2}$$

$$\frac{d[ES]}{dt} = k_{on}[E][S] - k_{off}[ES] - k_{cat}[ES] \tag{1.3}$$

$$\frac{d[E]}{dt} = -k_{on}[E][S] + k_{off}[ES] + k_{cat}[ES] \tag{1.4}$$

$$\frac{d[P]}{dt} = k_{cat}[ES] \tag{1.5}$$

The initial conditions are:

$$[S](t = 0) = [S_0] \tag{1.6}$$

$$[P](t = 0) = [ES](t = 0) = 0 \tag{1.7}$$

$$[E](t = 0) = [E_0] \tag{1.8}$$

In the above equations, [S] denotes substrate concentration, [S_0] denotes initial substrate concentration, [E] denotes unbound enzyme concentration, [ES] denotes enzyme-substrate complex concentration, [E_0] denotes total enzyme concentration, and [P] denotes product concentration. It can be shown that for sufficiently high [S_0], one can employ the quasi-steady state assumption (QSSA), $d[ES]/dt \approx 0$, and rewrite these equations as:

$$[ES] = \frac{[E_0][S]}{K_M + [S]} \tag{1.9}$$

$$\frac{d[S]}{dt} = -\frac{k_{cat}[E_0][S]}{K_M + [S]} \tag{1.10}$$

$$\frac{d[P]}{dt} = \frac{k_{cat}[E_0][S]}{K_M + [S]} \tag{1.11}$$

Where $K_M = \frac{k_{off}+k_{cat}}{k_{on}}$ is the Michaelis Menten constant, which is the substrate concentration at which the enzyme reaction velocity reaches half of its maximum, and it can be regarded as the substrate concentration at which the reaction velocity begins to saturate.

Modeling an enzyme cascade with substrate channeling. Consider an enzyme cascade consisting of two types of enzymes: enzyme 1 converts a substrate molecule, S, into an intermediate molecule, I, and enzyme 2 converts the intermediate molecule into a product molecule, P:

$$E_1 + S \rightleftharpoons E_1S \longrightarrow E_1 + I \tag{1.12}$$

$$E_2 + I \rightleftarrows E_2I \longrightarrow E_2 + P \tag{1.13}$$

The set of ordinary differential equations describing this set of reactions are written down in Appendix Section A.1. To model substrate channeling, we introduce an additional pathway by which the E_1S complex can be directly channeled into the E_2I complex:

$$E_1S \longrightarrow E_2I \tag{1.14}$$

Channeling is quantified by introducing a parameter, $f_{channel}$, which describes the fraction of intermediate molecules that are directly channeled into forming a complex with the downstream enzyme. The channeling fraction can be written down more explicitly as:

$$f_{channel} = f_{dir} \cdot p_{bind} = f_{dir} \cdot \frac{k_{on,2}}{k_{diff}} \tag{1.15}$$

where f_{dir} is the fraction of molecules that are directly positioned to bind to the downstream enzyme, k_{diff} is the diffusion-limited reaction rate, and $p_{bind} = k_{on,2}/k_{diff}$ is the binding probability.

To simplify the system analysis, we will assume that enzyme 1 produces molecules at a constant, zeroth-order rate V_S. This assumption is justified in Appendix Section A.2. Then, the system of equations can be written down as:

$$\frac{d[I]}{dt} = V_S\left(1 - \frac{\left([E_{2,0}] - [E_2I]\right)}{[E_{2,0}]} f_{channel}\right) - k_{on}\left([E_{2,0}] - [E_2I]\right)[I] + k_{off}[E_2I] \tag{1.16}$$

$$\frac{d[E_2I]}{dt} = V_S\frac{\left([E_{2,0}] - [E_2I]\right)}{[E_{2,0}]} f_{channel} + k_{on}\left([E_{2,0}] - [E_2I]\right)[I] - k_{off}[E_2I] - k_{cat}[E_2I] \tag{1.17}$$

$$\frac{d[P]}{dt} = k_{cat}[E_2I] \tag{1.18}$$

The rate constants k_{on}, k_{off}, and k_{cat} are the rate constants for enzyme 2, but the indices in their subscripts were removed for brevity of notation. $[E_{2,0}]$ denotes the total concentration of enzyme 2. There is a prefactor of $[E_2]/[E_{2,0}]$ before $f_{channel}$ to take into account the probability that the active site of enzyme 2 is occupied. From this point on, we will assume V_S to be a constant, and refer to the quasi steady-state throughput as the steady state throughput.

Results

Substrate channeling does not affect reaction throughput in steady state. Equations 1.16-17 can be solved for steady state by setting $\frac{d[I]}{dt} = \frac{d[E_2I]}{dt} = 0$. With $[E_2I]^*$ denoting the steady state concentration of $[E_2I]$, we find:

$$k_{cat}[E_2I]^* = V_S \tag{1.19}$$

$$\frac{d[P]}{dt} = k_{cat}[E_2I]^* = V_S \tag{1.20}$$

The above equation reflects the concept that, if a steady state exists for the intermediate and enzyme-intermediate complex concentrations, then the rate of intermediate production (V_S) must match the rate of intermediate consumption ($d[P]/dt$). As a result, the reaction throughput is independent of substrate channeling fraction. The key assumption to this analysis is that steady state is reached. This is not the case if $k_{cat}[E_{2,0}] < V_S$, where enzyme 2 becomes the rate-limiting enzyme.

Additionally, the steady state concentration of [I], denoted by $[I]^*$, can be written down as:

$$[I]^* = K_M \cdot \frac{V_S}{V_I - V_S} - \frac{V_S}{k_{on}[E_{2,0}]} f_{channel} \tag{1.21}$$

The parameter $V_I = k_{cat}[E_{2,0}]$ denotes the maximum reaction velocity of enzyme 2. This equation will be used in the next section.

Substrate channeling does not affect the characteristic time to reach steady state. The characteristic time scales of a fixed point of a nonlinear system of ordinary differential equations are used to determine the stability of a steady state and the relaxation time back to the steady state after small perturbations. They can also be used as a measure for the time to steady state if the initial conditions are close enough in the phase space. In this section, we will show that the characteristic time scales of the steady state found in Equations 1.16-17 are independent of the channeling fraction, $f_{channel}$.

The characteristic times of the steady state can be found by determining the eigenvalues of the Jacobian, *J*, of the nonlinear system in Equations 1.16-17 evaluated at steady state (details in Appendix Section A.3):

$$J = \begin{bmatrix} \frac{d[\dot{I}]}{d[I]} & \frac{d[\dot{I}]}{d[E_2I]} \\ \frac{d[\dot{E_2I}]}{d[I]} & \frac{d[\dot{E_2I}]}{d[E_2I]} \end{bmatrix}_{\substack{[I]=[I]^* \\ [E_2I]=[E_2I]^*}} \tag{1.22}$$

$$J\vec{v} = \lambda\vec{v} \tag{1.23}$$

where λ is the eigenvalue of the Jacobian corresponding to the characteristic time of the steady state and v is the corresponding eigenvector. Plugging in the steady state concentrations, $[I]^*$ from Equation 1.21, and $[E_2]^*$ from Equation 1.19, we find:

$$\lambda^2 + k_{on}\left(K_M\frac{V_I}{V_I - V_S} + \frac{V_I - V_S}{k_{cat}}\right)\lambda + k_{on}(V_I - V_S) = 0 \tag{1.24}$$

Without even solving for an explicit form of λ, it is clear that a change in the value of $f_{channel}$ will not affect the value of λ: Equation 1.24 is independent of the channeling fraction. This result has the interesting implication that channeling cannot contribute to the robustness of the throughput of an enzyme cascade, as fluctuations in intermediate concentrations will be relaxed at a time scale independent of the channeling fraction. The independence of the characteristic time scale is confirmed in Figure 1.1a, where we simulate Equations 1.16-18, and fit the time-dependent profile of the intermediate concentration with a rate parameter for a first order model. We find that the rate parameter is approximated well with the solution of Equation 1.24 for both the unchanneled and channeled case, and that channeling does not increase the value of the rate parameter.

This result may appear to contradict the established notion that substrate channeling lowers the time to steady state of an enzyme cascade. In the next section, we will show that channeling does indeed enhance the time to steady state; however, it does this by lowering the steady state intermediate concentration rather than by changing the rate at which it is reached.

The Michaelis-Menten equation is not valid for the downstream enzyme. A key tool in the study of enzyme kinetics is the quasi steady state assumption (QSSA). It claims that, during an enzymatic reaction, the concentration of the enzyme-substrate complex remains approximately constant relative to the substrate concentration. It will now be shown that the equation for the quasi steady state concentration of the enzyme-intermediate complex takes a different form than in the single-enzyme case given in Equation 1.9.

According to the QSSA, we assume that $\frac{d[E_2I]}{dt} \approx 0$ in Equation 1.17. Solving for [E_2I] in terms of [I], we find the following relation:

$$[E_2I]_{QSSA} = \frac{\frac{V_S}{k_{on}} f_{channel} + [E_{2,0}][I]}{\frac{V_S}{k_{on}[E_{2,0}]} f_{channel} + K_M + [I]} \tag{1.25}$$

The extra terms of $\frac{V_S}{k_{on}[E_{2,0}]} f_{channel}$ in the numerator and denominator differentiate this expression from the Michaelis-Menten equation (Equation 1.9). However, if we introduce a 'modified' intermediate concentration, $[\mathcal{I}]$ defined by:

$$[\mathcal{I}] = [I] + \frac{V_s}{k_{on}[E_{2,0}]} f_{channel} \tag{1.26}$$

Then the quasi steady state enzyme-intermediate complex concentration can be written down in a Michaelis-Menten form by substituting in the modified intermediate concentration:

$$[E_2I]_{QSSA} = \frac{[E_{2,0}]\left(\frac{V_S}{k_{on}[E_{2,0}]} f_{channel} + [I]\right)}{\frac{V_S}{k_{on}[E_{2,0}]} f_{channel} + K_M + [I]} = \frac{[E_{2,0}][\mathcal{I}]}{K_M + [\mathcal{I}]} \tag{1.27}$$

This equation may appear to imply that substrate channeling enhances the reaction velocity by raising the apparent intermediate concentration; however, this is not the case as the intermediate concentration is lowered due to the presence of channeling by a value of $\frac{V_s}{k_{on}[E_{2,0}]} f_{channel}$, as we can see from Equation 1.21.

To use Equation 1.27, it is necessary to determine how rapidly it becomes valid relative to changes in intermediate concentration. The details of this analysis are written down in Appendix

Section A.4. The main conclusion is that we can use Equation 1.27 in our analysis as long as enzyme concentrations are below the K_M of the enzyme 2, and that the intermediate-enzyme complex concentration equilibrates relative to the intermediate concentration on a time scale of $\tau_{QSSA} < k_{cat}^{-1}$.

The rapid approach to steady state for the enzyme-intermediate complex allows us to further simplify the dynamics of the channeled enzyme cascade reaction. Plugging in the QSS for the enzyme intermediate complex, we have:

$$\frac{d[I]}{dt} = V_S - k_{cat}[E_2 I]_{QSSA} = V_S - k_{cat}\frac{[E_{2,0}]\left(\frac{V_S}{k_{on}[E_{2,0}]}f_{channel} + [I]\right)}{\frac{V_S}{k_{on}[E_{2,0}]}f_{channel} + K_M + [I]} \tag{1.28}$$

$$\frac{d[P]}{dt} = k_{cat}[E_2 I]_{QSSA} \tag{1.29}$$

In the next section we will use this expression to solve for the lag time to steady state of the channeled enzyme cascade reaction.

Lag time reduction in a channeled enzyme cascade reaction. In experiments, the time to steady state of a cascade reaction is determined by calculating the metric known as the lag time.[53-57] Because steady state results in a constant rate of product throughput, the total amount of product molecules generated should eventually take a linear shape when plotted against time. If the linear regime of this plot is fit with a line, the lag time may be found by determining the time-axis intercept of the fit line. An example is shown in Figure 1.1b. The lag time can be calculated in closed form by considering:

$$[P](t) = \int_{\tau=0}^{\tau=t} k_{cat}[E_2 I]_{QSSA} d\tau = V_S t - \int_{\tau=0}^{\tau=t} [\dot{I}] d\tau = V_S \left(t - \frac{[I]^*}{V_S} \right) \tag{1.30}$$

In the above equation, we substituted in the QSS enzyme-intermediate complex concentration from Equation 1.28 and used the expression for intermediate concentration at steady state from Equation 1.21. As a result, the lag time for this system is:

$$t_{lag} = \frac{[I]^*}{V_S} = \frac{K_M}{V_I - V_S} - \frac{1}{k_{on}[E_{2,0}]} f_{channel} \tag{1.31}$$

The implication of Equation 1.31 is that the lag time is determined by the time it takes to reach the steady state intermediate concentration. This reveals how substrate channeling enhances the time to steady state: it lowers the steady state intermediate concentration in the bulk, allowing it to be reached faster.

The extent to which lag time may be reduced by channeling, Δt_{lag}, may be determined from the channeling-dependent term in Equation 1.31:

$$\Delta t_{lag} = \frac{1}{k_{on}[E_{2,0}]} f_{channel} \tag{1.32}$$

If we plug in the expression for $f_{channel}$ from Equation 1.15, we get the same result as Idan and Hess[31]:

$$\Delta t_{lag} = \frac{1}{k_{on}[E_{2,0}]} \cdot f_{dir} \cdot \frac{k_{on}}{k_{diff}} = \frac{f_{dir}}{k_{diff}[E_{2,0}]} \tag{1.33}$$

This expression is valid for artificial systems where enzymes may be tethered together. However, it returns very small values; for $f_{dir} = 1$, $[E_{2,0}] = 1$ nM, and using $k_{diff} = 4\pi DR$ [58] with a diffusion coefficient $D = 10^{-9}$ m^2 s^{-1} and enzyme radius $R = 3$ nm, we find that $\Delta t_{lag} \approx$

40 ms. However, in biology, it is conceivable that tunnels or allosteric regulation between active sites in a channeled reaction could raise the value of $f_{channel}$ by increasing the probability of binding to the second active site beyond the value of k_{on}/k_{diff}. In this case, channeling would effectively eliminate the waiting time for the build up of intermediate in the bulk solution. The extent of channeling could then be quantified by dividing Δt_{lag} by the unchanneled lag time:

$$\frac{\Delta t_{lag}}{t_{lag,no\ channeling}} = \frac{\frac{1}{k_{on}[E_{2,0}]} f_{channel}}{\frac{K_M}{V_I - V_S}} = \frac{k_{cat}}{k_{cat} + k_{off}} f_{channel} \left(1 - \frac{V_S}{V_I}\right) \tag{1.34}$$

In this case, the question of the benefits of channeling is reduced to considering the probability that an intermediate molecule, once bound to the enzyme, is more likely to be catalyzed into product or released back into the bulk.

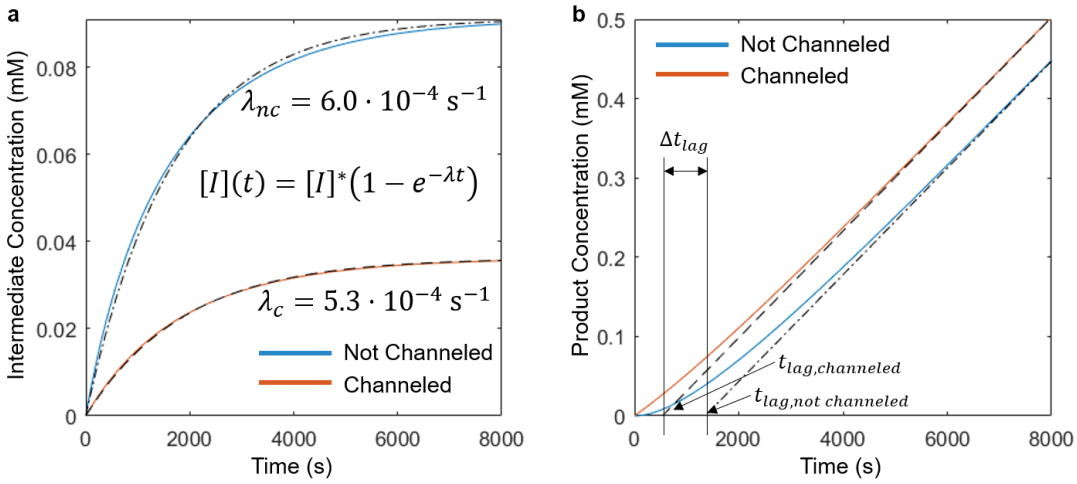

Figure 1.1: Substrate channeling changes reaction steady states, rather than characteristic time scales. (A) Bulk intermediate concentration plotted against time for a simulation of Equations 1.16-18 for a cascade reaction with (red) and without (channeling). Concentration profiles are fit with a one parameter (λ) model, $[I](t) = [I]^*(1 - e^{-\lambda t})$ (fits plotted as dashed black lines). The resulting time scales for both the channeled and unchanneled cascade are similar to the expected value of $\lambda = 4.9 \cdot 10^{-4}\ s^{-1}$ found by solving Equation 1.24. The higher channeling fraction does not increase the fit value of λ. (B) Example of lag time calculation for the same cascade reaction with substrate channeling. Parameters used mimic those of the experimentally studied glucose oxidase/horseradish peroxidase systems, with $[S_0]$=100 mM, $K_{M,1}$=4 mM, $k_{cat,1}$=70 s^{-1}, $K_{M,2}$=0.18 mM, $k_{cat,2}$=200 s^{-1}, and $[E_{1,0}]=[E_{2,0}]$=1 nM.[31] To emphasize the role of substrate channeling, we set the parameter $k_{on,2}$=1.2 $mM^{-1}s^{-1}$, and $k_{off,2}$ accordingly. The channeling fraction was set to $f_{channel}$=0 for the unchanneled case and $f_{channel}$=1 for the channeled case.

Substrate channeling enhances cascade throughput if the intermediate is unstable. Often times, in cells, cascade intermediates are unstable.[59, 60] For example, the indole intermediate produced by the tryptophan synthase bi-enzyme complex is hydrophobic; if it escapes the complex before being catalyzed into tryptophan, it can cross the cell membrane due to its hydrophobicity and escape.[61] This section will show that channeling can enhance the throughput of a cascade reaction when the intermediate is unstable.

We can model intermediate instability by adding a first-order elimination to the ODE describing intermediate concentration dynamics, as follows:

$$\frac{d[I]}{dt} = V_S\left(1 - \frac{[E_2]}{[E_{2,0}]}f_{channel}\right) - k_{on}([E_{2,0}] - [E_2I])[I] + k_{off}[E_2I] - k_e[I] \tag{1.35}$$

Where k_e is an elimination rate constant. The equations describing the dynamics of enzyme-intermediate complex and product concentrations remain unchanged. The steady state solutions are:

$$V_s = k_e[I]^* + k_{cat}[E_2I]^* \tag{1.36}$$

$$[E_2I]^* = \frac{k_e}{2k_{cat}} \cdot \left((K_M + \mathcal{A} + \mathcal{B}) - \sqrt{(K_M + \mathcal{A} + \mathcal{B})^2 - 4\mathcal{A}\mathcal{B}}\right) \tag{1.37}$$

$$\mathcal{A} = \frac{V_S}{k_{on}[E_{2,0}]}\left(f_{channel} + \frac{k_{on}[E_{2,0}]}{k_e}\right) = \frac{V_S}{k_{on}[E_{2,0}]}f_{channel} + \frac{V_S}{k_e} \tag{1.38}$$

$$\mathcal{B} = \frac{V_I}{k_e} \tag{1.39}$$

As expected, the steady state enzyme-intermediate complex concentration is a monotonic increasing function of the channeling fraction. The term denoted by $\mathcal{A}$ is the only channeling-

dependent term in Equation 1.38. Therefore, a necessary condition for $\mathcal{A}$ to be significantly affected by changes in $f_{channel}$ is:

$$1 > f_{channel} \gg \frac{k_{on}[E_{2,0}]}{k_e} \tag{1.40}$$

The on-rate of intermediate-complex formation must be much smaller than the intermediate elimination rate. Combining Equation 1.40 with Equation 1.15 returns the same result as determined by Idan and Hess.[31]

For very large values of the intermediate elimination rate constant, the product throughput approaches the following expression:

$$\frac{d[P]}{dt} = k_{cat}[E_2I]^*_{k_e\to\infty} = V_S \cdot f_{channel} \frac{1}{1 + \frac{k_{off}}{k_{cat}} + \frac{V_S}{V_I} f_{channel}} \tag{1.41}$$

This expression is similar to the one determined for the estimate of the lag time to steady state, in that it captures the role of the magnitude of the catalytic rate constant as compared to the off-rate constant. The additional term of $V_S f_{channel}/V_I$ in the denominator describes the effect of saturation of the active sites of the second enzyme. This expression is also equivalent to Equation 1.27 multiplied by a factor of k_{cat} and evaluated with $[I] = 0$.

Conclusion

In this section, we have constructed a simple model for a colocalized enzyme cascade by modeling the effects of substrate channeling. In the case of stable intermediate molecules, channeling can only provide enhancements to the lag time to steady state. It is interesting that this enhancement in lag time does not originate from a change in the characteristic time scales in

the reaction. Rather, it comes from a rapid, channeling-independent, approach to an initial quasi-steady state for the enzyme-intermediate complex where the bulk intermediate concentration is low, yet the second enzyme is producing at a channeling-dependent rate given in Equation 1.41.

In the case where cascade intermediates are unstable, channeling can benefit reaction throughput if the rate constant of intermediate instability is much greater than the on-rate for intermediate-complex formation. For very high intermediate elimination rate constants, the reaction throughput collapses to the QSS throughput found for the second enzyme in Equation 1.37.

The limiting factor which prevents substrate channeling from being effective is the low binding probability, estimated here as $p_{bind} = k_{on}/k_{diff}$. One approach to raising the binding probability is to confine intermediate molecules in an "inter-enzyme space" of small volume, which would prevent them escaping prematurely and allow for continuous attempts to form a complex with the subsequent enzyme. Examples of such spaces exist in nature. Researchers have discovered several multi-enzyme complexes where active sites participating in cascading reactions are connected by physical tunnels.[62] The tunnels connecting these active sites have the capacity to store several intermediate molecules, and often protect them from the outside cellular environment, where they would otherwise be unstable. In the next chapter, we will expand our model of an enzyme cascade with substrate channeling to study the emergent properties of tunneled enzyme cascade reactions.

Chapter 2. A Queueing Theory-Based Perspective of the Kinetics of "Channeled" Enzyme Cascade Reactions

This section follows, *"A queueing theory-based perspective of the kinetics of 'channeled' enzyme cascade reactions," by Stanislav Tsitkov, Theo Pesenti, Henri Palacci, Jose Blanchet, Henry Hess, ACS Catalysis, 8 (11), 10721-10731, 2018*.

Introduction

Cascade reactions catalyzed by enzymes are reminiscent of factory processes where parts are transformed and combined as they travel from one workstation to the next.[45, 63, 64] The promise of nanotechnology is to enable the construction of "molecular assembly lines", where a molecule produced by one enzyme is directed straight to the next enzyme, which processes it in order of arrival.[50, 65-67] Biological systems have already evolved structures enabling such sequential transformations of individual molecules.[68] Specifically, these structures enable "substrate channeling" either via tunnels connecting active sites, or via surface paths which attract intermediate substrate molecules and prevent them from leaving the enzyme complex as they travel from one active site to the next.[69]

Since the sequential transformation of substrates within an enzyme cascade is similar to the processing of parts at different work stations in a factory, it is reasonable to expect that natural and synthetic enzyme complexes with substrate channeling would exhibit complexities in the organization of the workflow reminiscent of a factory, where the description and optimization of the production processes has given rise to the engineering discipline of logistics.[70, 71] Traditionally,

chemical reactions are described by coupled differential equations, whose evolution represents the time-varying concentrations of the different molecular species. It is likely that these differential equations are only imperfect approximations of the discrete transformation processes occurring in a "molecular assembly line."[72]

Therefore, the goal of this chapter is to explore the impact of stochastic effects on an N-step reaction cascade catalyzed by N enzymes immobilized on a scaffold using a queueing model.[73] Queueing models have been recently utilized to model a variety of biological systems, including multi-site enzymes [74], gene expression and regulation [75, 76], the spread of invasive species [77], and physiological insulin levels.[78] The traditional queueing model describes the dynamics of customers being served in a waiting room.[79] In our analysis, the molecule is the customer, the enzyme is the server, and the waiting room is the inter-enzyme space of limited capacity where the molecule is held while it is waiting to be processed by the next enzyme (Figure 2.1a). Examples of this interenzyme space can be the tunnel found within the naturally occurring tryptophan synthase enzyme complex [61] (Figure 2.1b), or the DNA-origami compartment created to house the synthetic glucose-oxidase and horseradish-peroxidase cascade [80] (Figure 2.1c). Other examples of naturally occurring molecular tunnels connecting enzyme active sites include those used in the formation of carbamoyl phosphate[81], in the activation of glutamine phosphoribosylpyrophosphate amidotransferase[82], in the formation of asparagine by asparagine synthetase B[83], and more.[53, 61, 84-86]

The discrete character of the queueing model captures the stochastic effects and predicts significant deviations in throughput from the predictions of a system of differential equations under specific circumstances.

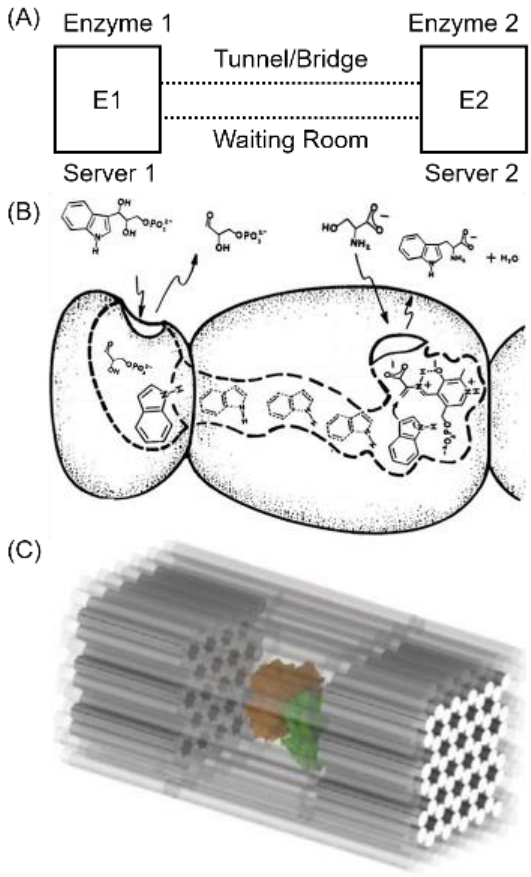

Figure 2.1. Examples of enzyme cascades exhibiting confinement of intermediate substrates. (A) Equivalence between an enzyme cascade and a queueing model. (B) Substrate channeling through a tunnel connecting two active sites in tryptophan synthase.[87] Adapted from Dunn[87]. (C) Glucose oxidase and horseradish peroxidase encased in an artificial DNA scaffold. Adapted from Zhao et al. [80]

Methods

General model for a tunneled enzyme cascade. Our goal is to construct a model for a tunneled N-enzyme cascade with partial confinement of intermediate molecules. We begin with the standard model for an enzyme-catalyzed reaction, introduced in Chapter 1:

$$S + E \underset{k_{off}}{\overset{k_{on}}{\rightleftharpoons}} ES \xrightarrow{k_{cat}} P + E \tag{2.1}$$

In the chemical reaction above, S is the substrate, E the (free) enzyme, ES the enzyme-substrate complex, P the product, k_{on} the rate constant associated with the forward reaction, k_{off} the rate constant associated with the reverse reaction and k_{cat} the enzyme catalytic rate constant.

For an N-enzyme cascade with enzymes [E_1, E_2,…, E_N], the intermediate substrates [S_1, S_2, …, S_{N-1}], are produced by the enzyme of the same index, [E_1, E_2,…, E_{N-1}], and consumed by the enzyme of the next index, [E_2, E_2,…, E_N], according to the reaction in Equation 2.1 with appropriate rate constants.

Between production and consumption reactions, the intermediate substrate molecules are confined to an accessible inter-enzyme space of small volume between active sites. From now on, we will refer to this inter-enzyme space as the "waiting room." We assume the following about its properties:

1. The waiting room has a limit on the number of intermediate substrate molecules that it can store. For example, the tunnel found in tryptophan synthase (Figure 1b), can accommodate up to four indole molecules.[61]
2. If the waiting room is full, intermediate substrate molecules produced by the preceding enzyme will be released into the bulk.
3. If the waiting room is full, intermediate substrate molecules that unbind from the enzyme-substrate complex in the reverse reaction will release the substrate to the bulk.

4. Enzymes in the cascade can only recruit substrate molecules from their waiting rooms and not from the bulk solution. This assumption will be justified in the Discussion.
5. Substrate molecules can escape from the waiting room with a first order rate constant k_{loss}; following queueing theory terminology, this loss rate constant will be referred to as the "impatience:"

$$S_i \xrightarrow{k_{loss}} \emptyset \tag{2.2}$$

6. Molecules that have escaped the waiting room into the bulk cannot return into the waiting room. This assumption will also be justified in the discussion.

Modeling the deterministic reaction kinetics. The deterministic model of the cascade reaction will employ the Michaelis-Menten (MM) equation[51, 88] introduced in Chapter 1:

$$\frac{d[P]}{dt} = \frac{k_{cat}[S]}{K_M + [S]} \cdot [E]_T \tag{2.3}$$

$$K_M = \frac{k_{off} + k_{cat}}{k_{on}} \tag{2.4}$$

where $[S]$ is the substrate concentration, $[E]_T = [E] + [ES]$ the total enzyme concentration, $[P]$ is the product concentration, and K_M the Michaelis constant.

For an N-enzyme cascades, enzyme E_i will produce intermediate substrate molecules S_i at a rate of $r_{MM,i}$, given by:

$$r_{MM,i} = \frac{k_{cat,i}[S_{i-1}]}{K_{M,i}+[S_{i-1}]} \cdot \frac{1}{N_A V} \tag{2.5}$$

Where N_A is Avogadro's number and V the volume accessible to the confined intermediate substrates.

The rate of change of the concentration of intermediate substrate S_i is given by the difference between its production rate by E_i and its consumption rate by E_{i+1}. Therefore, for each substrate S_i - except S_0 -, we would like to express the net production as:

$$\frac{d[S_i(t)]}{dt} = \begin{cases} \frac{k_{cat,i}[S_{i-1}(t)]}{K_{M,i}+[S_{i-1}(t)]}[E_i]_T - \frac{k_{cat,i+1}[S_i(t)]}{K_{M,i+1}+[S_i(t)]}[E_{i+1}]_T - k_{off}[S_i(t)], \ [S_i(t)] < \frac{n_{WR,i}}{N_A V} \\ -\frac{k_{cat,i+1}[S_i(t)]}{K_{M,i+1}+[S_i(t)]}[E_{i+1}]_T - k_{off}[S_i(t)], \ [S_i(t)] \geq \frac{n_{WR,i}}{N_A V} \end{cases} \quad (2.6)$$

where $n_{WR,i}$ is the capacity (in number of molecules) of the waiting room. However, due to the discontinuity in $[S_i]$, the solution to this differential equation does not exist. Instead, we model the discontinuity with a logistic term, $L([S_i(t)]) = \left(1 + e^{\gamma([S_i(t)]-[S_{max}])}\right)^{-1}$ with a high steepness parameter, $\gamma = 10$, and $[S_{max}] = \frac{n_{WR,i}}{N_A V}$. Then, the set of equations turns into:

$$\frac{d[S_i(t)]}{dt} = \frac{k_{cat,i}[S_{i-1}(t)]}{K_{M,i} + [S_{i-1}(t)]}[E_i]_T \cdot L([S_i(t)]) - \frac{k_{cat,i+1}[S_i(t)]}{K_{M,i+1} + [S_i(t)]}[E_{i+1}]_T - k_{loss}[S_i(t)] \quad (2.7)$$

We further assume that there is no waiting room for E_0, so it produces S_1 at a constant velocity[55, 89] v_0 until the waiting room is filled. Hence, we have the following simplification for S_1 net production:

$$\frac{d[S_1(t)]}{dt} = v_0 \cdot L([S_1(t)]) - \frac{k_{cat,2}[S_1(t)]}{K_{M,2} + [S_1(t)]}[E_2]_T - k_{loss}[S_1(t)] \quad (2.8)$$

For simplicity, v_0 will be approximated as $v_0 = k_{cat,1}/(N_A V)$.

With $[P]$ denoting the final product concentration, the output rate of the enzymatic cascade, r, is given by

$$r = \frac{d[P(t)]}{dt} = \frac{k_{cat,N}[S_{N-1}(t)]}{K_{M,N} + [S_{N-1}(t)]}[E_N]_T \tag{2.9}$$

Note that no loss rate is considered for the final product P since it is not confined. The system is solved using either the ode45 or ode23s solver of the MATLAB® software by setting all the concentrations to 0 at t=0.

Modeling the stochastic reaction kinetics. A stochastic process is defined by the transition probabilities between states. These transition probabilities can be written down in the form of the master equation, which describes the time dependent evolution of the distribution of the stochastic process. These transition probabilities also form the basis of processes examined in queueing theory.[79] The stochastic evolution of a set of chemical reactions can be described by the chemical master equation.[90, 91] We solve the chemical master equation using the stochastic simulation algorithm (SSA) also known as the Gillespie algorithm.[92] The main difference with the deterministic approach is that chemical reactions are not described by a rate constant but by their probability of occurring between time *t* and *t*+*dt*. This probability is characterized by a likelihood, or propensity function. The definition of these functions is similar to the definition of an elementary chemical reaction rate. Here, we highlight the main features of the discrete stochastic approach (see Appendix Sections B.1 and B.2 for details).

We model the enzymatic cascade as a succession of *N* servers (Figure 2.2). Waiting rooms contain integral quantities of intermediate substrate molecules. Each enzyme can be in one of two

states: (1) in complex with exactly one intermediate substrate molecule or (2) empty. The Gillespie algorithm iterates over two steps, the outcome of which is a change in the state of a single molecule. Step 1 of the algorithm determines the time until the next reaction. This is calculated by sampling an exponential random variable with rate parameter equal to the sum of all possible reaction rates in the system. This is equivalent to determining the minimum time until the next reaction when looking at all possible reactions separately. Step 2 of the algorithm chooses the reaction that occurred. This is done by sampling a uniform random variable and using it to pick a reaction with probability proportional to its rate.

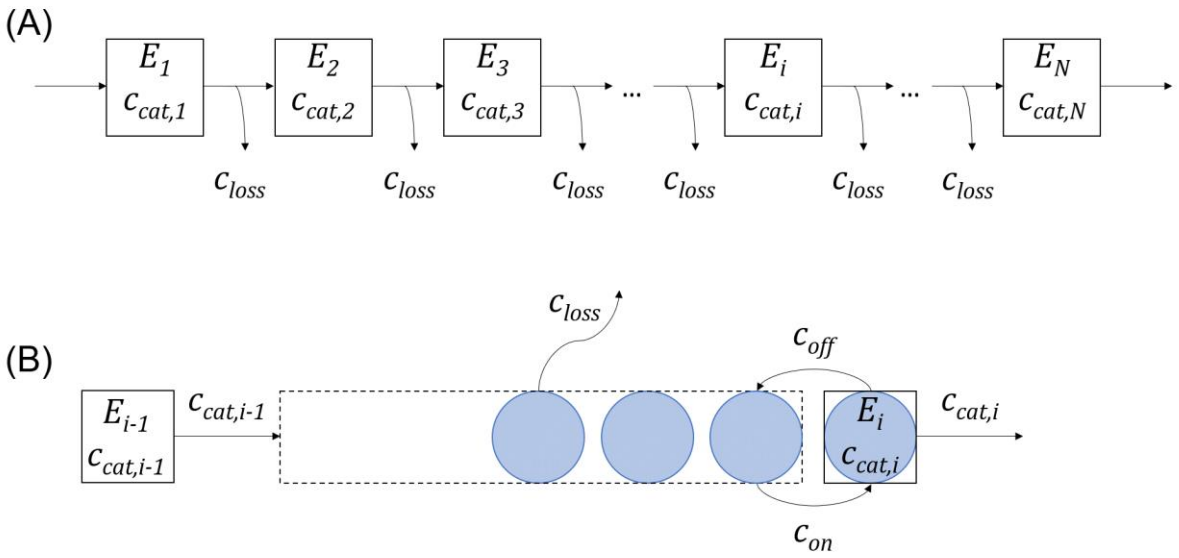

Figure 2.2. Schematic representation of the stochastic model. (A) The enzyme cascade is modeled as a series of N servers with service rates equal to the stochastic enzyme catalytic rates. In between enzymes, there is a tunnel or surface path which stores molecules; we refer to this space as the waiting room. Molecules may exit the waiting room either by forming a complex with the next enzyme, or by being lost to the environment (impatience). (B) Model of the waiting room *i* between E_{i-1} and E_i. c_{on}, c_{off}, $c_{cat,i-1}$, and c_{loss} are stochastic rate constants associated to the simulated chemical reactions (Equation (2.1)) used in the computation of the propensity function. Note that no other simplifications are assumed in the stochastic model.

Simulations. To determine the rate of product throughput for each condition, the stochastic simulation was independently run 100 times over a time scale of 100s (unless the cascade consisted of more than two enzymes, in which case runs were performed over a time period of 1000s to ensure steady state). The calculated throughputs from each run were averaged to attain the final, presented result. The standard error of the mean is provided with each data point.

The kinetic parameters in the simulation were chosen to represent the widely studied glucose oxidase-horseradish peroxidase (GOx-HRP) cascade in which hydrogen peroxide is the intermediate produced by GOx, and consumed by HRP. The rate constant at which hydrogen peroxide is produced by GOx is varied between 0 and 180 s^{-1}, and the catalytic rate constant of HRP is set to 30 s^{-1}.[39] The volume accessible to the intermediate substrate is assumed to be 10 nm^3 for all waiting rooms, based on typical tunnel dimensions in enzymes.[61] The K_M of HRP is set to 2.5 μM.[39] This K_M, as the K_M of almost every enzyme, is below the concentration created by a single intermediate substrate molecule in the waiting room (~170 mM). Since the MM model generally assumes the rapid establishment of equilibrium between the enzyme, the substrate and the enzyme substrate complex, we set the substrate unbinding rate constant k_{off} to be 100-fold higher than the k_{cat} and calculated the substrate binding rate constant k_{on} from k_{cat} and K_M using Equation (3). The computations of stochastic rate constants from deterministic rate constants are performed according to Sanft et al.[93] All parameters are listed in Table 2.1.

Table 2.1. Values of Parameters Used in Stochastic Simulations.

Parameter	Symbol	Value
Number of enzymes in the cascade	N	2-10
Waiting room capacity	n_{WR}	1-10 (or $+\infty$)
Interenzyme volume	V	10 nm^3
Michaelis constant (enzyme E_2)	$K_{M,2}$	2.5 μM or 250 mM
Deterministic catalytic rate constant (E_1)	$k_{cat,1}$	0 to 180 s^{-1}
Deterministic enzyme catalytic rate constant (E_2)	$k_{cat,2}$	30 s^{-1}
Deterministic reverse reaction rate constant	$k_{off} = 100\ k_{cat,2}$	3000 s^{-1}
Deterministic forward reaction rate constant	$k_{on} = \frac{k_{off} + k_{cat,2}}{K_{M,2}}$	12.12 to 12.12*10^5 $mM^{-1}.s^{-1}$
Stochastic catalytic rate constant (E_1)	$c_{cat,1} = k_{cat,1}$	0-180 s^{-1}
Stochastic catalytic rate constant (E_2)	$c_{cat,2} = k_{cat,2}$	30 s^{-1}
Stochastic reverse reaction rate constant	$c_{off} = k_{off}$	3000 s^{-1}
Stochastic forward reaction rate constant	$c_{on} = \frac{k_{on}}{N_A V}$	2013 to 2013*10^5 s^{-1}

Results

Cascades without impatience. The most basic system is a two-enzyme cascade with no impatience in the waiting room and a K_M of the second enzyme far below the concentration corresponding to just one intermediate molecule in the accessible volume of the waiting room (~170 mM for a volume of 10 nm^3). Under these conditions, any intermediate substrate molecule entering the waiting room is accepted by the second enzyme without delay if the second enzyme is not occupied. We computed the output rate of the cascade with both deterministic and stochastic models. In the deterministic model, the overall output rate is equal to the smaller of the production rate of the first enzyme ($k_{cat,1}$) or the catalytic rate constant of the second enzyme ($k_{cat,2}$). The stochastic model shows deviations from the deterministic model only when the two enzymes have similar catalytic rate constants and when the waiting room capacity is small (Figure 2.3). For a waiting room with infinite capacity, both models agree within the error of the stochastic simulation.

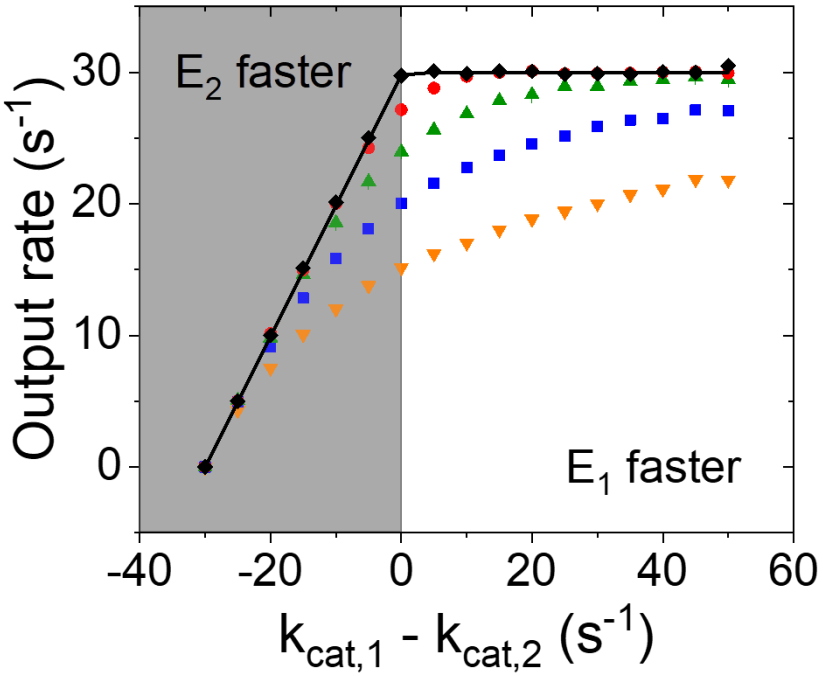

Figure 2.3. Deterministic model solutions and simulations of a two-enzyme cascade with a low K_M and a finite waiting room in between enzymes. The solid line represents the solutions of the MM ODEs system (Equation (2.7)) and a maximum concentration in the intermediate volume representing 1, 2, 4, 10 and ∞ molecules (solutions overlap). Symbols represent the results of the stochastic simulations for a waiting room capacity of 1 (orange triangles), 2 (blue squares), 4 (green triangles), 10 (red circles) and ∞ molecules (black diamonds). Error bars for standard error are smaller than the marker. K_M = 2.5 μM (c_{on} = 2013*10^5 s^{-1})

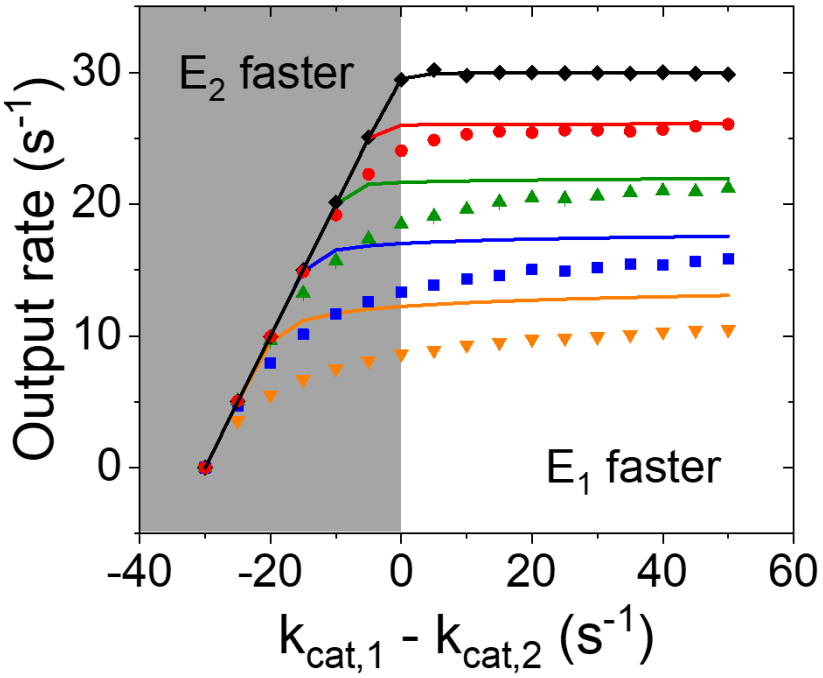

Figure 2.4. Deterministic model solutions and simulations of a two-enzyme cascade with a high K_M and a finite waiting room in between enzymes. Solid lines represent the solutions of the MM ODEs system (Equation (2.7)) and a maximum concentration in the intermediate volume representing 1 (orange), 2 (blue), 4 (green), 10 (red) and ∞ (black) molecules. Symbols represent the results of the stochastic simulations for a waiting room capacity of 1 (orange triangles), 2 (blue squares), 4 (green triangles), 10 (red circles) and ∞ molecules (black diamonds). Error bars for standard error are smaller than the marker. K_M = 250 mM (c_{on} = 2013 s^{-1})

The system slightly increases in complexity if the K_M of the second enzyme is chosen so high (e.g. 250 mM), that it requires a significant population (an average of ~1.5 molecules for 250 mM) in the waiting room (Figure 2.4). In this case, the results of the deterministic model depend on the waiting room capacity if the first enzyme is producing faster than the second enzyme, because the second enzyme cannot be saturated without filling the waiting room and triggering the overflow condition (molecules produced by the first enzyme are returned to the bulk). The maximal output rate for the downstream enzyme is achieved when the number of intermediate molecules available is equal to the waiting room capacity; then, the maximal output rate, based on the MM model, $r_{MM,2}^{max}$, for $k_{cat,2} << k_{cat,1}$ is given by:

$$r_{MM,2}^{max} = \max\left(k_{cat,2} \cdot \frac{[S]}{[S] + K_M}[E_2]_T\right) = k_{cat,2} \cdot \frac{n_{WR}}{n_{WR} + K_M V N_A}[E_2]_T \tag{2.10}$$

The critical value between the regime where the upstream enzyme sets the overall output rate and the one where the downstream enzyme depends on the waiting room capacity is found by setting the output rate of the first enzyme equal to the maximum output rate of the second enzyme. Then, we have:

$$k_{cat,1}^{crit} = k_{cat,2} \cdot \frac{n_{WR}}{n_{WR} + K_M V N_A} \tag{2.11}$$

We have therefore shown that there are significant differences in output rates for deterministic and stochastic models. However, by computing the relative error $|r_{deter} - r_{stoch}|/r_{deter}$ where r_{deter} is the output rate with the deterministic model and r_{stoch} is the output rate with the stochastic model, these differences are below 20% for capacities greater than 4 molecules (or up to 50% for a capacity of

1 molecule) which are small compared to other sources of variation in throughput, such as temperature and pH. On the other hand, these difference are amplified for longer enzyme cascades, such as the 10-enzyme cascade experimentally studied by Mukai et al.[94] Note that deviations of 20% are of the same order of magnitude as other deviations found in the study of stochastic effects on the MM model.[89]

To investigate the "worst case" scenario, we simulated a N-enzyme cascade where all the downstream enzymes have the same set of parameters (K_M = 2.5 μM and k_{cat} = 30 s^{-1}), waiting rooms of equal size, and an upstream enzyme (E_1) catalytic rate constant of 30 s^{-1} (Figure 2.5). The deterministic model exhibited, as expected, an output rate equal to $k_{cat}/(N_A V)$ regardless of cascade length. In the stochastic simulations the overall output rate decreased with increasing cascade length. In the worst case scenario i.e. a very long enzyme cascade with very small waiting rooms, the output rate computed using stochastic simulations can be more than 5-fold smaller than the one predicted by the deterministic model.

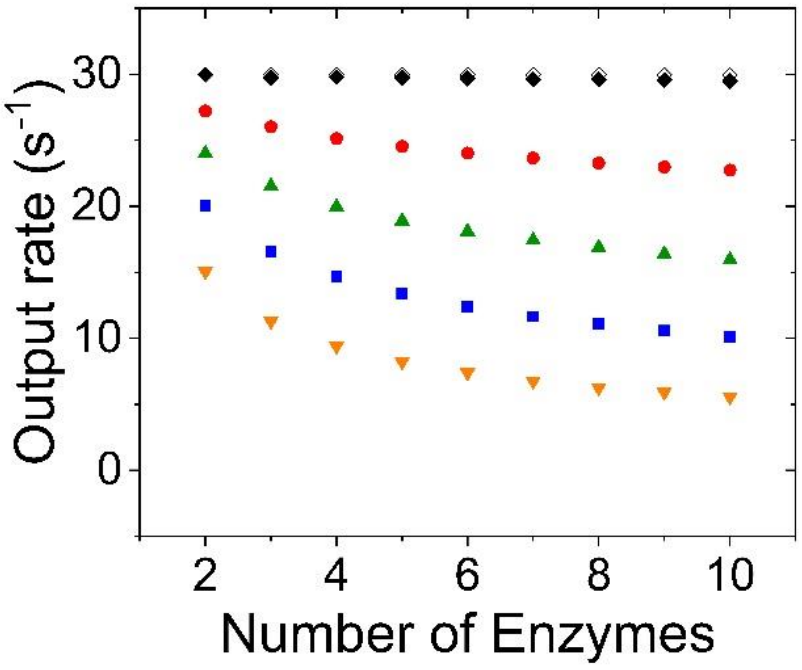

Figure 2.5. The output rate calculated with stochastic simulations and the deterministic model as a function of the number of enzymes in series. All waiting rooms have the same capacity of 1 (orange triangles), 2 (blue squares), 4 (green triangles) or 10 molecules (red circles). Black diamonds correspond to the identical results of the stochastic model (solid diamonds) with infinite waiting room size and the deterministic model (open diamonds). Error bars for standard error are smaller than the marker.

Cascades with impatience. Impatience represents the escape of substrate molecules from their confinement in the waiting room to the bulk. We model impatience as a Poisson process with a rate of 20 s^{-1}, which is of similar magnitude to the catalytic rate constants of the enzymes in order to have an appreciable impact. We considered again a low (2.5 μM, Figure 6) and a high (250 mM, Figure 2.7) K_M case. Just as before, waiting room capacity does not have any effect in the deterministic model in low K_M. However, for the stochastic simulations, the amplitude of the capacity effect is much smaller than in the absence of impatience and the result for an infinite waiting room now differs from the deterministic model.

For high K_M (250 mM, Figure 2.7), the shape of the curves is similar to those of the same system without impatience (Figure 2.4). Since the impatience reduces the rate at which substrate molecules reach the downstream enzyme, the critical value between the regime where the upstream enzyme sets the overall output rate and the one where the downstream enzyme previously described by Equation (2.10) is now given by:

$$k_{cat,1}^{crit}[E_1]_T = k_{cat,2} \cdot \frac{n_{WR}}{n_{WR} + K_M V N_A}[E_2]_T + k_{loss} \cdot \frac{n_{WR}}{V N_A} \tag{2.12}$$

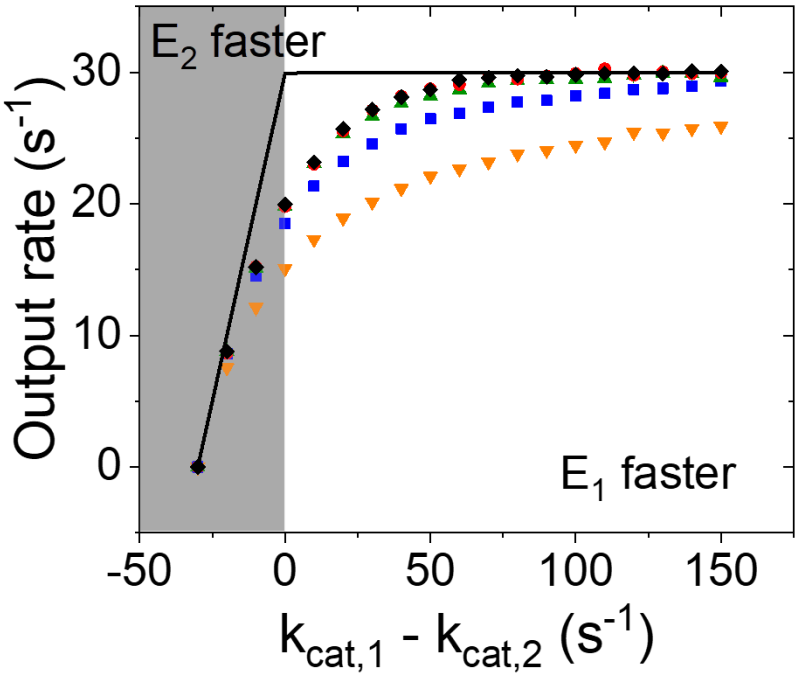

Figure 2.6. Deterministic model solutions and simulations of a two-enzyme cascade with a low K_M and a finite waiting room in between enzymes in the presence of impatience. The black solid line represents the overlapping solutions of the MM ODEs system (Equation (2.7)) for maximum concentration in the intermediate volume of 1, 2, 4, 10 and ∞ molecules. Symbols represent the results of the stochastic simulations for a waiting room capacity of 1 (orange triangles), 2 (blue squares), 4 (green triangles), 10 (red circles) and ∞ molecules (black diamonds). Error bars for standard error are smaller than the marker. K_M = 2.5 μM (c_{on} = 2013*10^5 s^{-1}). k_{loss} = 20 s^{-1}.

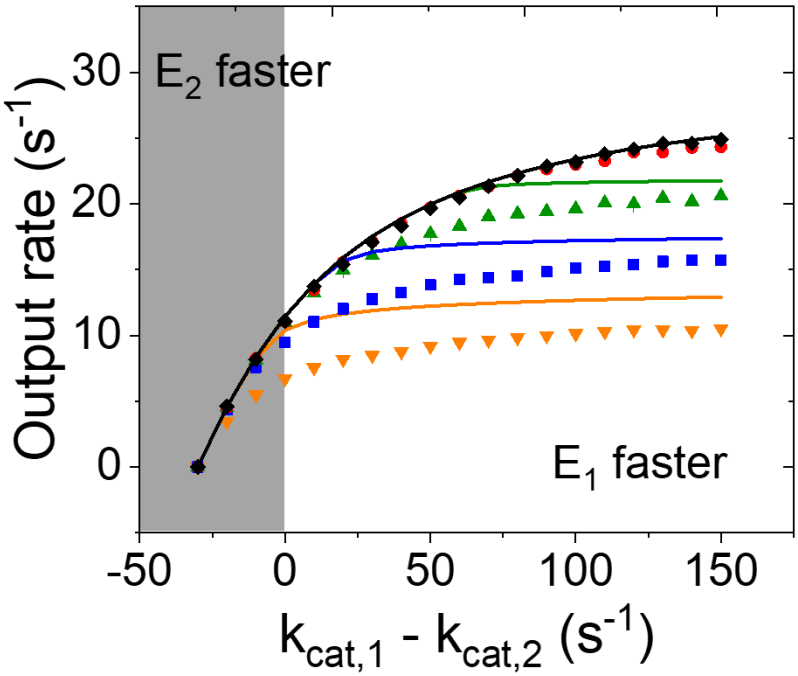

Figure 2.7. Deterministic model solutions and simulations of a two-enzyme cascade with a high K_M and a finite waiting room in between enzymes in the presence of impatience. The black solid line represents the overlapping solutions of the MM ODEs system (Equation (2.7)) for maximum concentration in the intermediate volume of 1, 2, 4, 10 and ∞ molecules. Symbols represent the results of the stochastic simulations for a waiting room capacity of 1 (orange triangles), 2 (blue squares), 4 (green triangles), 10 (red circles) and ∞ molecules (black diamonds). Error bars for standard error are smaller than the marker. K_M = 250 mM (c_{on} = 2013 s^{-1}). k_{loss} = 20 s^{-1}.

Discussion

The first important result is that the deterministic model and the stochastic simulations yield identical results for infinite waiting room size when impatience is not considered. This is in agreement with Thomas et al.[95] who highlighted the importance of a large number of substrate molecules in the MM model. Secondly, if the output rate of the first enzyme is significantly different from the catalytic rate constant of the second enzyme, the results of the deterministic model and the stochastic simulations are also identical. This agreement between the models arises because the waiting room is either mostly empty or mostly full (Figure 8), which is well approximated by the deterministic model. Our discussion will therefore focus on the particular case when the catalytic rate constants of the enzymes in the cascade are similar, first for a two-enzyme cascade and then for longer cascades. We will also discuss the validity of MM model assumptions, the validity of the assumption on bulk intermediate contributions, and methods for experimental validation of our system.

The two-enzyme cascade. Stochastic simulations give results which deviate up to 50% from the deterministic model when the waiting room is small and the enzymes have similar rate constants. The origins of this deviation are illustrated in Figure 2.8, where we plot the distribution of the number of molecules in the waiting room for stochastic simulations (K_M = 2.5 μM; no impatience: k_{loss} = 0). For $k_{cat,1}$ less than $k_{cat,2}$ (downstream enzyme faster), the probability for the waiting room to be empty is very high; the downstream enzyme is not rate-limiting and operates at rate $r_{MM,1}$ given by Equation (2.4). For $k_{cat,1}$ greater than $k_{cat,2}$ (upstream enzyme faster), the probability for the waiting room to be empty is negligible and the upstream enzyme operates at a rate close to its catalytic rate. Surprisingly, however, the waiting room is rarely maximally filled. The origin of this behavior lies in the rapid rate of substrate-enzyme complex formation (c_{on}) and dissociation

(c_{off}) (when compared to catalysis, c_{cat}). If the waiting room becomes full, it will lose a molecule almost immediately (time scale of $\frac{1}{c_{on}} \approx 10^{-8}$ s) after the enzyme-substrate complex dissociates (time scale of $\frac{1}{c_{off}} \approx 10^{-3}$s), while the substrate molecule previously in the complex will be lost to the bulk. Then, between catalysis events, the occupancy of a waiting room of capacity n_{WR} will fluctuate between n_{WR} (full waiting room, free enzyme state), and n_{WR}-1 (1 below capacity waiting room, enzyme complex state). It will spend a fraction $\frac{c_{on}}{c_{on}+c_{off}} \approx 1$ of time in the n_{WR}-1 state and $\frac{c_{on}}{c_{on}+c_{off}} \approx 10^{-5}$ in the filled waiting room state.

For $k_{cat,1}$ similar to $k_{cat,2}$, the waiting room population is evenly distributed, and the probability for the waiting room to be empty is similar to the probability of finding any other number of molecules in the waiting room. This substantial probability of an empty waiting room slows the production of the downstream enzyme. This is consistent with previous work of Hochendoner et al. who linked the probability for an enzyme to be unoccupied and its catalytic rate.[74] In contrast, the deterministic model always evolves towards an intermediate substrate concentration which is equal to the maximal allowed concentration, and thereby keeps the downstream enzyme producing at its maximum rate.

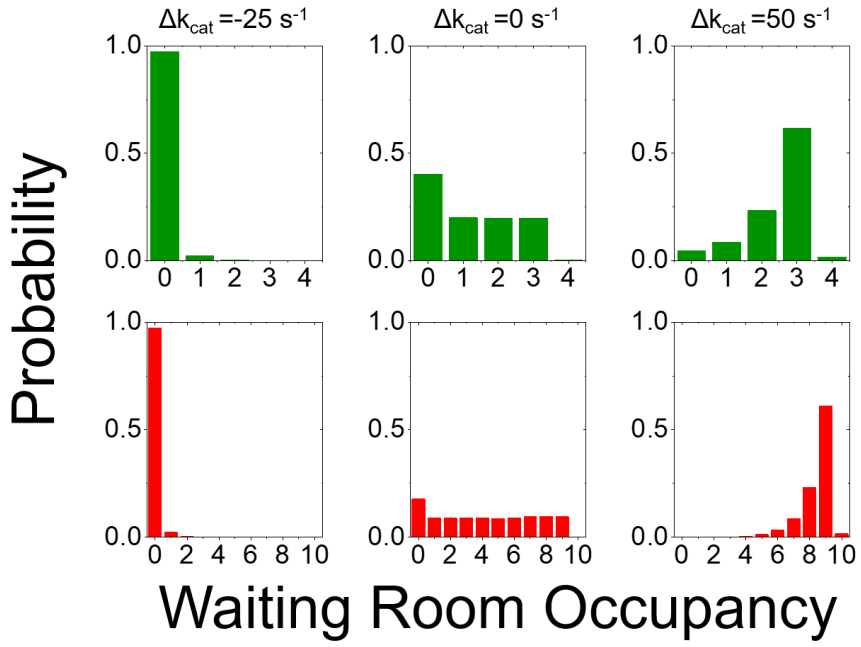

Figure 2.8. Substrate population distributions in the waiting room of a two enzyme cascade in steady state. Top (green): The waiting room capacity is 4 molecules. Bottom (red): The waiting room capacity is 10 molecules. Left: $k_{cat,1} - k_{cat,2} = -25\ s^{-1}$ (downstream enzyme faster). Middle: $k_{cat,1} - k_{cat,2} = 0$. Right: $k_{cat,1} - k_{cat,2} = 50\ s^{-1}$ (upstream enzyme faster). $K_M = 2.5\ \mu M$.

Figure 2.3 also shows that the higher the value of n_{WR}, the maximum number of molecules that can fit in the waiting room, the better the agreement between the two models for $k_{cat,1}$ close to $k_{cat,2}$. The probability of an empty waiting room decreases when n_{WR} increases. This result is well understood in queueing theory.[96] When the catalytic rates of two enzymes are equal, only the number of molecules processed in unit time on average are equal. On average, one molecule is converted each $1/k_{cat,1}$ second. But since the turnover events are assumed to be Poisson distributed, non-negligible disruptions in the production by the upstream enzyme can occur. Such disruptions would lead to a decrease in the overall output rate since the downstream enzyme would not be fed for non-negligible periods. However, if a waiting room is present in between enzymes, it can act as a reservoir and compensate for the shortages. If the waiting room is too small, long shortages will still decrease the output rate because the waiting room can be fully exhausted by the downstream enzyme (zero occupancy). These disruptions are relevant only for enzymes with comparable processing rates. If the upstream enzyme is much faster, the disruptions are relatively short and the waiting room is typically filled, so the second enzyme will not have time to empty it. If the upstream enzyme is much slower than the downstream enzyme, the upstream enzyme is rate-limiting so events occurring downstream (e.g. stochastic feeding of the downstream server) do not have any effect on the overall output rate. The waiting room effect is intrinsically a stochastic phenomenon which cannot be described with a deterministic approach. The deterministic model does not account for a correlation between the catalytic events of the two enzymes (here, a temporary upstream slowdown which leads to a downstream slowdown) since each catalytic rate is defined independently from the other one. The two approaches agree as soon as this correlation does not matter anymore e.g. when the waiting room is relatively large and essentially never emptied so that upstream process does not impact the downstream process.

Impatience, the loss of molecules from the waiting room, reduces the effect of the waiting room (Figures 6-7). Impatience can be considered as negative feedback for substrate production since the probability of an unbinding event increases with increasing substrate population in the waiting room. Thus, a steady-state is reached even if the waiting room is infinitely large. Consequently, if the loss rate constant is high enough, it will set an implicit limit for the size of the waiting room population which is much lower than the waiting room size. Thus, for high loss rates the overall output rate is unaffected by the waiting room capacity. That is why even for an infinite waiting room capacity, the actual number of substrate molecules is not large enough to make the two models agree (Figure 6).

Multi-Enzyme Cascades. The dependency of stochastic effects on cascade length is not intuitively obvious. Experimentally, cascades of up to 10 successive enzymatic reactions have been described. The deterministic model predicts that the overall output is equal to the catalytic rate $r_{MM,i}^{max}$ of the slowest enzyme regardless of cascade length. Similar results have been reported in queueing theory if the waiting room is of infinite size. For servers with the same service rate, Hunt[79] computed the maximum utilization factor ρ_{max} which corresponds to the ratio between the mean overall output rate and the maximum service rate.[97] Waiting rooms of infinite size resulted in $\rho_{max} = 1$ regardless of the number of enzymes. However, if the waiting rooms are small, the maximum utilization factor ρ_{max} decreases with increasing cascade length (see Appendix Section B.3 for details).

Our simulations demonstrate that cascade throughput decreases with increasing cascade length for small waiting rooms. At the same time, we show that cascade throughput is constant with increasing cascade length for infinite waiting rooms (Figure 2.5). This is in agreement with the analytical results of Hunt for low K_M (see Appendix Section B.3). Ultimately, the cascade

production rate predicted by the stochastic simulations can be as little as 20% of the production rate predicted by the deterministic model. Most of this discrepancy is created by the first few enzymes, because the reduced throughput of the first enzyme pair (due to the stochastic effects) feeds the third enzyme at a slower rate than its maximum catalytic rate, which creates a mismatch between the upstream and downstream catalytic rates and diminishes the stochastic effects arising from the waiting room between the second and third enzyme (Figure 2.3). The mismatch increases further down the line and thereby downstream stochastic effects contribute less and less to the overall discrepancy between the deterministic model and the stochastic simulations.

The mismatch between the output of an initial stage of the cascade and the catalytic rate of the following enzyme could be minimized if the catalytic rate of the following enzyme is reduced to match the output rate. This progressive reduction in catalytic rate along the cascade reduces throughput, but one might expect an increase in the difference of the predictions of the deterministic and the stochastic simulations. To study this case, we simulated a cascade where the catalytic rate constant of the i+1 enzyme matches the decreased output of the previous i enzymes. In this cascade ($k_{cat,1}$ = 30 s^{-1}, K_M = 2.5 μM, and n_{WR} = 1), the first two enzymes have a catalytic rate of $k_{cat,1} = k_{cat,2}$ and – as suggested by Hunts equation (Equation B.9) – the catalytic rate of each subsequent enzyme is reduced by half. For a 10-enzyme cascade, the final throughput as predicted by the simulation is 0.070 +/- 0.002 s^{-1}(95% confidence interval) compared to 0.117 s^{-1} predicted by the continuum model. The difference in predicted production rates between the stochastic and deterministic model is approximately 50%, which is actually smaller than the difference between the predictions for the cascade with constant catalytic rates. In this case, the accuracy of the continuum model actually improves because the predicted production rate (equal to the slowest

enzyme in the cascade) drops in the same ratio as the predicted production rate of the stochastic model as the length of the cascade increases.

Validity of Michaelis-Menten Model. The validity of the Michaelis Menten model assumptions has been extensively studied over the past decades.[89, 98, 99] Some authors have also reported a MM-like formula[100, 101] for a single enzyme molecule. We reaffirm the results of Grima et al.[89], that the MM equation deviates roughly 20% from stochastic simulations for single enzymes. Note that our stochastic simulations solve the most general form of the chemical master equation, foregoing the use of the K_M, Equation (2.3), and any other approximations. In this context, our results highlight the robustness of the MM equation already noticed in literature.[89] Meanwhile, we highlight the impact of a new parameter for the magnitude of the reported deviations: the difference between the catalytic rate constants of the successive enzymes.

Contributions from the bulk. In our study, we assume that intermediate molecules lost to the bulk cannot diffuse back into the waiting room. This assumption is valid because, typically, the time scale of the reaction is too small for the bulk intermediate concentration to build up significantly. In fact, Liu et al. performed studies on a synthetic cascade consisting of hexokinase and glucose-6-phosphate dehydrogenase connected via a polylysine bridge [54, 102], and found that intermediate bulk concentration never reached the steady state level, and that contributions from the bulk could be deemed negligible.[54] In addition, the intermediate molecules can be unstable in the environment outside the cascade [59, 60].

In the end, the goal of this study is to compare the results of the queueing model with the continuum model. In the worst case, contributions from the bulk counteract the effects of waiting

room impatience. Then, the system reverts to the cases considered in Figures 2.3 and 2.4, and deviations in predicted throughput between the queueing model and continuum model can still extend up to 50%.

Model validation. The predicted differences in the steady-state production rates between the stochastic and the deterministic model of up to 50% (low K_M and small waiting room) are large compared to the experimental errors in measuring catalytic rates in enzyme reactions (<5%).[39] However, the measured catalytic rates of individual enzymes may not represent the catalytic rates of the same enzymes when they are assembled to form tunnels, cages, or bridges, for example due to a changed enzyme microenvironment.[1] The tryptophan synthase bienzyme complex is one of the best studied systems with a tunnel.[103] It consists of two subunits: the upstream (α) subunit catalyzes the formation of indole from indole 3-glycerol phosphate, and the downstream (β) subunit catalyzes the formation of tryptophan from the newly formed indole molecule and also serine. Somewhat counterintuitively, the downstream subunit regulates the activity of the upstream subunit. In the absence of serine, the upstream subunit's catalytic activity (k_{cat}=0.14 s^{-1}) is about 20 times lower than that of the downstream subunit (k_{cat}=3.6 s^{-1}).[104] However, once a serine molecule begins reacting with the downstream subunit, a conformational change occurs in the upstream subunit,[11] increasing its catalytic activity by over 20 times, to the point that it nearly matches that of the downstream subunit (new upstream k_{cat}=3.0 s^{-1}).[104] Considering that the tunnel of tryptophan synthase can contain up to 4 intermediate (indole) molecules,[62] the stochastic effects would not be negligible when the upstream subunit is activated. Typically, the purpose of this regulating mechanism is considered to be keeping the outputs of both subunits in phase.[103, 105] However, from the queueing perspective, it is also conceivable that this protein has evolved this

regulatory mechanism to minimize the stochastic effects that would arise if both subunits were continuously matched. We plan to investigate this more complex system in a future study.

Another interesting enzyme complex is carbamoyl phosphate synthetase, which catalyzes a three step reaction and contains two narrow tunnels connecting three active sites.[86] However, the catalytic activities of the individual active sites are still undetermined.[106] Current DNA nanocages have large volumes (creating large waiting rooms) and therefore the difference in the predictions of the stochastic and deterministic model are again small. An interesting system may be one where the intermediate is a protein, because the large size of the protein would reduce the waiting room capacity. A swinging arm transferring substrate between two enzymes, as described by Fu et al., [107] can be considered to be a waiting room of size one if the substrate cannot reach the second enzyme without the swinging arm. This is not the case in the study by Fu et al.[107] and may be difficult to experimentally realize.

The pre-steady state is in principle also accessible to our modeling, and could conceivably enable the validation of the predicted difference between stochastic and deterministic models. The duration of the pre-steady state can be quantified by the transient/lag time.[53-57] In our simulations, we observed that lag time increased with the number of enzymes, the K_M, and the waiting room size. The lag time was calculated by performing a nonlinear fit of the production rate as described by Farrell et al.[108] The longest lag time was obtained for a cascade of 10 enzymes with identical kinetics (k_{cat} = 30 s^{-1}, K_M = 250 mM) and an infinite waiting room. In this case, the continuum model predicts a lag time of 3.95 +/- 0.06 s (95% confidence interval) and the queueing model predicts a lag time of 4.08 +/- 0.16 s (95% confidence interval). If the cascade is shortened to 2 enzymes, the continuum model predicts a lag time of 0.18 +/- 0.02 s, while the queueing model predicts a lag time of 0.22 +/- 0.04 s (95% confidence intervals). These differences in predicted

lag times are not statistically significant. Therefore, characterizing steady state throughput is the best approach for a potential validation of our model predictions.

Conclusion

We have modeled enzyme cascade reactions with deterministic and stochastic approaches to consider phenomena arising from the inherent stochasticity and discreteness of chemical reactions. We focused on enzyme cascade systems where the intermediate substrates are confined and "waiting rooms" of limited capacity are created. In this case, up to five-fold differences between the two models have been found for specific parameter values. Differences are found when enzymes have similar catalytic rates and the waiting room capacity is only one or several molecules. For most cases (unequal catalytic rates, waiting room capacities exceeding 10 molecules), the discrepancies between the deterministic model and the stochastic model are not practically relevant. However, from a theoretical point of view, an interesting analogy with queueing theory has been highlighted, based on the agreement between our simulations and analytical results taken from operations research. The challenge for an experimental validation of our results is to find an enzyme cascade where the catalytic rates are well-matched and a waiting room with a capacity of a few molecules exists naturally or can be constructed.

In the waiting room model considered here, intermediate molecules are confined to tunnels between active sites participating in sequential reactions. The tunnels store intermediate molecules awaiting catalysis, and protect them from elimination in the outside environment. In the next chapter, we will discuss cascade reaction conducted in cellular compartments: structures over 100 nm in diameter that can store molecules on a larger scale. These compartments can take the form of proteinaceous shells in cyanobacteria or membrane-bound organelles in eukaryotic cells. One of their main roles is to protect unstable cascade intermediates from

degradation in the cytosol and to quarantine volatile cascade intermediates that could exhibit cross-reactivity with other cellular processes.

Chapter 3. Design Principles for a Compartmentalized Enzyme Cascade Reaction

This section follows *"Design principles for a compartmentalized enzyme cascade reaction," by Stanislav Tsitkov and Henry Hess, ACS Catalysis 9 (3), 2432-2439, 2019.*

Introduction

Compartmentalization is vital to the functioning of cells and a topic of tremendous interest in biocatalysis and synthetic biology.[17, 23, 26-29, 32, 109, 110] Despite its intuitive usefulness in containing toxic reactants and enhancing the concentration of unstable intermediates, quantitative models have only recently been published. Proteome-scale network-based approaches,[110] such as those used by Alam et al.[32], have revealed that compartmentalization reduced the number of inhibitory enzymatic interactions in the cell. Chen et al.[33] provide closed form solutions for the reaction diffusion equation governing a second messenger reaction pathway, where a source of cyclic adenosine monophosphate (cAMP) is compartmentalized to prevent degradation by phosphodiesterases. Recent work by Hinzpeter et al.[34] examines the spatial reaction dynamics of a compartmentalized cascade reaction by evaluating its productivity, defined as the ratio of the compartment flux to the total number of enzymes within the compartment. Mangan et al.[35] provide an in-depth study of the bacterial carboxysome by solving the relevant reaction diffusion equations for a cascade involving the RuBiSCo and carbonic anhydrase enzymes. Jakobson et al.[36] perform a similar study as Mangan et al.[35] for the propanediol utilization microcompartment in bacteria. However, despite the growing variety of approaches to modeling compartments, a simple, intuitive

model which captures only the essential physics of the problem is still missing. Such a basic quantitative understanding would be of use in evaluating the numerous recent advances in experimental work geared towards compartmentalization of enzyme cascade reactions.[111, 112]

In this chapter, we aim to develop a basic model of compartmentalized cascade reactions, identify the optimal design, and determine when compartmentalization provides benefits. This basic model describes a two-enzyme cascade and makes the generally valid assumption of a well-mixed interior and exterior of the compartment. Substrate, intermediate, and product molecules can enter the compartment through openings in the compartment boundary. We assume that the total number of molecules moving through all these openings per unit of time (with units of moles per second) is proportional to the concentration difference across the opening, and call the proportionality constant the diffusive conductance (with units of $M^{-1}s^{-1}$). This diffusive conductance is a property of the compartment and accounts for the number, permeability, and size of the openings. First, we show that for given numbers of enzymes, the rate at which product leaves the compartment is maximized at an intermediate value of the conductance as one would intuitively expect. If the numbers of enzymes can be adjusted, the optimization problem is more complicated and can best be formulated as: Given a certain maximum number of enzymes (due to packing constraints) and a certain desired throughput (within the limit of the turnover rates of enzymes 1 and 2), for which numbers of enzymes and compartment diffusive conductance is the intermediate loss from the compartment minimized? The solution of this problem is presented in a second section.

The insights we gain from our analysis provide a set of simple, quantitative conclusions that can be used to engineer more efficient micro- and nanoscale bioreactors. We show that spatial considerations are usually negligible in nanoscale compartment design which greatly simplifies

the requirements for most models. In contrast to previous models,[34, 59] our analysis replaces arbitrary definitions of cascade efficiency with a concrete design objective (minimize intermediate outflux given an enzyme packing constraint and a desired product throughput). Finally, we show that compartmentalizing an enzyme cascade reaction is beneficial whenever the rate of intermediate removal in solution (due to instability) is greater than the turnover rate of the first reaction step.

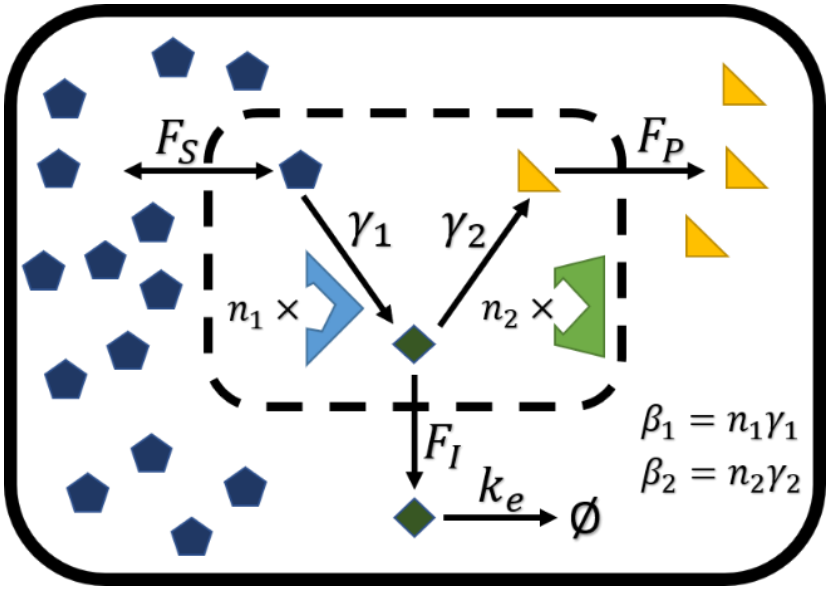

Figure 3.1: Scheme of a Compartmentalized Cascade Reaction. An outer shell represents the boundary of the cell, reaction vessel, or simply periodic boundary conditions. A defined number of Enzyme 1 molecules (light blue) utilizes substrate molecules (dark blue) to produce intermediate molecules (dark green) with catalytic efficiency γ_1. Intermediate molecules are consumed by a defined number of Enzyme 2 molecules (light green) to produce product molecules (yellow) with catalytic efficiency γ_2. A semi-permeable compartment wall with diffusive conductances F_S, F_I and F_P can restrict the exchange of molecules with the surrounding cell, where intermediate molecules are removed at rate k_e.

Methods

Modeling the reaction kinetics. We construct a model (Figure 3.1) similar to that of Hinzpeter et al.[34] The compartment contains two types of enzymes, E_1 and E_2, which can be described by Michaelis-Menten (MM) kinetics. The substrate, S, is converted into the intermediate, I, by enzyme E_1 with catalytic rate constant $k_{cat,1}$ and MM constant $K_{M,1}$. The intermediate is then converted into product, P, by enzyme E_2 with catalytic rate constant $k_{cat,2}$ and MM constant $K_{M,2}$.

Modeling the transport across the compartment boundary. A species inside the compartment is well mixed if its reaction time scale is much longer than its diffusion time scale.[34] For the substrate or product of an enzymatic reaction, this is true if:

$$\frac{DK_M}{k_{cat}} \gg r^2[E] = \frac{3n_E}{4\pi r} \tag{3.1}$$

where D is the diffusion coefficient of the substrate or product, r is the radius of the compartment, and $[E]$ and n_E are the concentration and number of the enzyme, respectively. This condition is met in all practical cellular compartments (Appendix Section C.1). As a result, we model the influx and outflux of S, I and P from the compartment at rates proportional to their concentrations, which we call diffusive conductances, F_S, F_I and F_P determined by the properties of the boundary (e.g. the number and size of openings). The diffusive conductance is equal to the product of the compartment boundary permeability, the surface area and Avogadro's Number. The inverse of this quantity, the diffusive resistance, is defined by Berg as discussed below.[58]

Modeling the environment outside the compartment. Similar to Castellana et al.,[59] we assume that the substrate concentration is maintained at a constant level. Furthermore, the intermediate, I, is assumed to be unstable, and immediately degraded if it leaves the compartment ($k_e \to \infty$ in Figure 1). A finite removal rate is discussed later in Equations (3.21-24). With *V* denoting the volume of the compartment, and N_A denoting Avogadro's Number, the following set of equations describe the reaction dynamics:

$$\frac{d[S]}{dt} = \frac{F_S([S_0] - [S])}{V\mathrm{N_A}} - \frac{k_{cat,1}[E_1][S]}{K_{M,1} + [S]} \tag{3.2}$$

$$\frac{d[I]}{dt} = \frac{k_{cat,1}[E_1][S]}{K_{M,1} + [S]} - \frac{F_I[I]}{V\mathrm{N_A}} - \frac{k_{cat,2}[E_2][I]}{K_{M,2} + [I]} \tag{3.3}$$

$$\frac{d[P]}{dt} = \frac{k_{cat,2}[E_2][I]}{K_{M,2} + [I]} - \frac{F_P[P]}{V\mathrm{N_A}} \tag{3.4}$$

Since substrate concentrations in the cell are typically much lower than the K_M of their respective enzymes, we analyze the linear regime of the kinetics.[5] In addition, we will analyze the system in steady state, because we assume that environmental substrate concentrations are homeostatically maintained at a constant level. Furthermore, typical values of compartment permeability derived for bacterial microcompartments (1-100 μm/s) ensure that the process of transport across the compartment boundary will equilibrate within the first second for a compartment on the 100 nm-size scale (the time scale being roughly equal to the quotient of compartment radius and permeability). In steady state, Equations (3.2-4) then simplify to:

$$F_s([S_0] - [S]) - \frac{k_{cat,1}n_1[S]}{K_{M,1}} = 0 \tag{3.5}$$

$$\frac{k_{cat,1}n_1[S]}{K_{M,1}} - F_I[I] - \frac{k_{cat,2}n_2[I]}{K_{M,2}} = 0 \tag{3.6}$$

$$\frac{k_{cat,2} n_2 [I]}{K_{M,2}} - F_P[P] = 0 \tag{3.7}$$

where n_1 denotes the number of molecules of enzyme E_1 and n_2 denotes the number of molecules of enzyme E_2 in the compartment.

To keep equations concise, we define the turnover rates β_i as the product of the enzymatic catalytic efficiency (γ_i) and number of molecules of the enzyme (n_i):

$$\beta_1 = \gamma_1 n_1 = \frac{k_{cat,1} n_1}{K_{M,1}} \tag{3.8}$$

$$\beta_2 = \gamma_2 n_2 = \frac{k_{cat,2} n_2}{K_{M,2}} \tag{3.9}$$

Results

Numbers of enzymes describe the system better than enzyme concentrations. Equations (3.5-7) reveal that the steady state system is affected by the volume of the compartment only indirectly, that is if changing the volume affects either the transport across the boundary (e.g. by increasing the number of pores) or the number of enzymes. Hinzpeter et al.[34] discuss the kinetics as a function of the compartment radius while assuming that an increase in the surface area of the spherical compartment leads to a proportional increase in the diffusive conductance due to a constant permeability (defined by the number and size of pores per area). Since the number of pores is defined by the number of pore proteins and the size of the compartment is dependent on the properties of the shell proteins or lipid molecules, this proportionality is not required and more suitable ratios of surface conductance to surface area can be engineered. Therefore, we optimize

compartment properties in terms of numbers of enzymes, enzyme properties, and diffusive conductances.

Maximizing product outflux for given numbers of enzymes. Our initial goal is to optimize this system by engineering a compartment with the optimum diffusive conductance, F, to maximize product outflow. According to Equation (3.5), the amount of substrate in the compartment in steady state may be expressed as:

$$[S] = \frac{F_S}{F_S + \beta_1}[S_0] \tag{3.10}$$

Based on Equation (3.6), the amount of intermediate is then:

$$[I] = \frac{1}{F_I + \beta_2} \cdot \frac{\beta_1 F_S}{F_S + \beta_1}[\mathrm{S}_0] \tag{3.11}$$

Here, the origin of the optimal diffusive conductance can be seen. When the conductance rate F_S is low, substrate cannot cross the boundary, limiting the production of intermediate. On the other hand, if the diffusive conductance F_I is high, the intermediate will be lost before it can be converted into product. To attain the optimal conductance between these regimes, we maximize $\beta_2[I] = F_P[P]$, the rate of intermediate conversion and, due to our steady state assumption, product outflux. If $F_S \approx F_I$, the value of F that returns the maximal product outflux is (see Appendix Section C.2 for derivation):

$$F_{S,I} = \sqrt{\beta_1 \beta_2} \tag{3.12}$$

The dependence of product and intermediate outflux on the diffusive conductance is shown in Figure 3.2. In Appendix Section C.3, we examine this derivation in the case of species-dependent permeabilities, when $F_S \neq F_I$.

The product outflux, R_{opt}, at optimal conductance can be found by inserting Equation (3.12) into Equation (3.11):

$$R_{opt} = F_P[P] = \beta_2[I] = \frac{\beta_1 \beta_2}{\left(\sqrt{\beta_1} + \sqrt{\beta_2}\right)^2}[S_0] \tag{3.13}$$

Equation (3.13) states that for an optimally chosen conductance (or conductances in the case of species-dependent permeabilities), product outflux can be increased by increasing the turnover rates β_1 and β_2.

Maximizing product outflux for given numbers of enzymes in the case of enzyme saturation. Since bacterial microcompartments often contain enzymes with a low K_M, it is necessary to discuss the effects of enzyme saturation in a cascade reaction, i.e. when the full, nonlinear form of Equations (3.2-4) must be taken into consideration.

As seen in Figure 3.2, product throughput initially grows with increasing diffusive conductance. If an enzyme becomes saturated before the optimal diffusive conductance is reached, there is no point in further increasing the conductance. This would only result in more intermediate outflux with little increase in intermediate conversion.

Since the optimal diffusive conductance will be reached on the boundary between the linear and nonlinear regimes of the Michaelis-Menten kinetics, the substrate turnover can be estimated by inserting Equation (3.10) into the turnover term of Equation (3.2). Assuming that the second enzyme is not yet saturated, this gives the steady state intermediate concentration of:

$$[I] = \frac{1}{F_I + \beta_2} \cdot \frac{\beta_1 F_s [\mathrm{S_0}]}{F_S + \beta_1 + F_S \frac{[\mathrm{S_0}]}{K_{M,1}}} \tag{3.14}$$

This intermediate concentration (and therefore product throughput) is maximized – setting again $F_S \approx F_I$ – when:

$$F_{sat} = \sqrt{\frac{\beta_1 \beta_2}{1 + \frac{[S_0]}{K_{M,1}}}} \approx \sqrt{\beta_1 \beta_2} \sqrt{\frac{K_{M,1}}{[S_0]}}, \tag{3.15}$$

where we have assumed that $[S_0] \gg K_{M,1}$. By comparing Equation (3.15) with Equation (3.12), we see that the saturation of the first enzyme effectively lowers the optimal diffusive conductance by a factor of $\sqrt{K_{M,1}/[S_0]}$. A similar expression can be derived for saturation of the second enzyme (Appendix Section C.4).

As with the linear regime, the product outflux in the saturated case may be further increased by increasing the number of enzymes, although with diminishing returns. The question then becomes: Given the available volume and the available enzyme catalytic efficiencies, what are the optimal numbers of enzymes and conductances which minimize the outflux of the toxic or unstable intermediate.

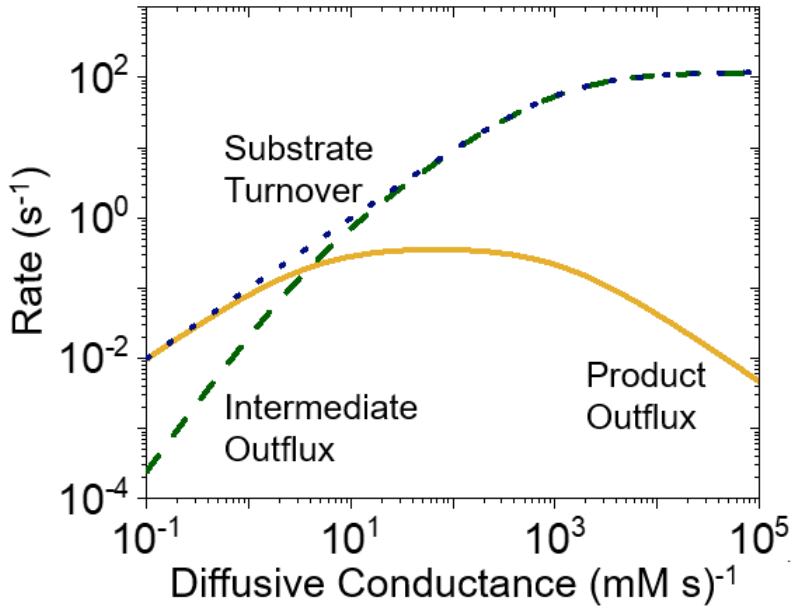

Figure 3.2: Dependence of compartment dynamics on diffusive conductance. Substrate conversion (blue, dotted line), intermediate outflux (green, dashed line), and product outflux (orange, solid line) depend on the diffusive conductance of the compartment for a given set of numbers of enzymes and catalytic efficiencies. At a low diffusive conductance, very little substrate enters the compartment. At a high diffusive conductance, most of the produced intermediate leaves the compartment before it can be converted into product. We used the kinetic parameters from the cascade consisting of the NAD^+-dependent alcohol dehydrogenase and NADH-dependent amine-dehydrogenase from the study of Zhang et al.[113] We assume $\gamma_1 = 24\ \mathrm{mM^{-1}s^{-1}}$ and $\gamma_2 = 0.080\ \mathrm{mM^{-1}s^{-1}}$, $n_1 = n_2 = 50$, and set $[S_0] = 0.1$ mM.

Minimizing intermediate loss for a given product output. Compartments often serve as a tool for containing either volatile or toxic intermediates. In this section, we consider a volatile intermediate, meaning the intermediate is rapidly removed outside the compartment. Then, the design problem becomes: Given a required product outflux, *R*, a total number of enzymes, n_0, and enzyme catalytic efficiencies, γ_1 and γ_2, how are diffusive conductances, F_S and F_I, and numbers of each enzyme, n_1 and n_2, chosen to minimize intermediate outflux, $F_I[I]$? This design problem is written in equation form as:

$$\min_{n_1, n_2, F} F_I[I] \tag{3.16}$$

$$\beta_2[I] = F_P[P] = R \tag{3.17}$$

$$n_1 + n_2 = n_0 \tag{3.18}$$

Both constraints are necessary. Without the first constraint, zero intermediate outflux can be attained by setting the number of Enzyme 1 molecules to zero, but this would also halt product outflux. Without the second constraint, the intermediate outflux rate could be lowered closer to zero by packing the compartment with more Enzyme 2.

For simplicity, we consider $F_S = F_I$, which describes a situation where the diffusive conductance of substrate and intermediate is similar. However, selectively permeable boundaries may be taken into account by setting $F_S = cF_I$ with a proportionality constant *c* (Discussed in Appendix Section C.5), since the main difference in transport rates between species in the compartment will be the changing resistance of a single pore to different molecules.

To visualize the optimization problem, it is necessary to reduce the dimensionality of the objective function by applying the constraint on product outflux (Equation 3.17). Then, the intermediate outflux surface may be plotted as a function of the number of molecules of each

enzyme, n_1 and n_2 (Figure 3.3a). The feasible set of parameters, i.e. the set of parameters that satisfy the design constraints, is found by intersecting the surface with the plane corresponding to the constraint on total number of enzymes (Figure 3.3b).

This constrained minimization problem can be analytically solved using Lagrange multipliers. As critical points, we find two sets of relations for *F*:

$$F_1 = \sqrt{\beta_1 \beta_2} \tag{3.19}$$

$$F_2 = \frac{\beta_1 n_1}{n_2} \tag{3.20}$$

We gain a better understanding of Equations (3.19-20) by plotting intermediate outflux as a function of the number of Enzyme 1 (Figure 3.3b), while satisfying both constraints, Equations (3.17-18). As we see in Figure 3.3b, the first critical point, F_1, corresponds to the boundaries of the feasible set; the solutions for the number of Enzyme 1 are the most extreme values of n_1 that can still satisfy the constraint on product outflux. The second critical point, F_2, corresponds to critical points within the interior of the feasible set, and the solutions for the number of Enzyme 1 are the extrema for the intermediate outflux while satisfying the constraints.

The expression for F_1 is the same as Equation (3.12); it corresponds to the lower and upper bounds on the number of Enzyme 1 molecules such that the constraint on product outflux, Equation (3.14), can still be satisfied. If the objective was to maximize product outflux instead of to minimize intermediate outflux, F_1 would be the optimal choice for diffusive conductance. By choosing F_2, we sacrifice product outflux to minimize intermediate outflux.

Once we set the diffusive conductance equal to F_2, we can find the values of n_1 and n_2 that minimize (or maximize) the intermediate outflux. The exact closed form solutions for the number

of molecules of each enzyme are not available, as they require solving a fourth order polynomial. However, they are easily found numerically. In addition, for sufficiently high n_0, their closed form solution may be approximated (see Appendix Section C.6).

In this section, we have considered a volatile intermediate, meaning an intermediate which is rapidly removed from the environment. This is motivated by the acetalydehyde intermediate molecule produced in the ethanolamine utilization bacterial microcompartment, which rapidly escapes the cell if it is lost from the compartment.[114] We may also consider the case of a toxic intermediate by a reformulation of Equations (3.16-18) where the objective would be to maximize product outflux while constraining intermediate outflux to limit toxicity. This problem is analyzed in Appendix Section C.7.

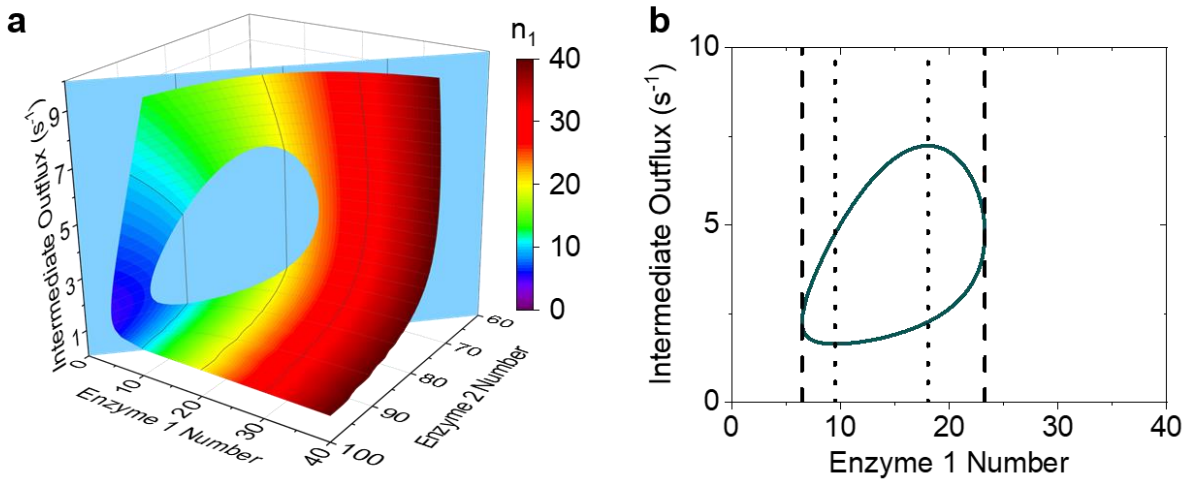

Figure 3.3: Visualization of the optimization problem for a compartmentalized cascade. (a) The multi-colored surface represents intermediate outflux (elimination rate) under the constraint of a specific product outflux, as a function of the number of both enzymes. The light-blue plane denotes the constraint on the total number of enzyme molecules. Its intersection with the surface gives the curve of the feasible set of parameters. (b) The critical points of the optimization problem correspond to the boundaries of the feasible set (black, dashed line), and its maximum and minimum (blue, dotted line). As in Figure 1, $\gamma_1 = 24$ mM^{-1}s^{-1} and $\gamma_2 = 0.080$ mM^{-1}s^{-1}, $n_0 = 100$, $[S_0]$ =0.1 mM, and the desired product outflux is R=0.5 s^{-1}.

Comparison to the non-compartmentalized reaction. Intuitively, a free solution reaction is disadvantageous when a high rate of intermediate removal prevents a sufficient rate of product formation. On the other hand, the drawback of the compartment is that it limits substrate influx. The question becomes: how high must the rate of intermediate removal be in order for a compartment to become favorable. Answering this question requires the modification of the reaction equations, which so far assumed that intermediate reaching the cytosol is immediately removed.

We model the removal of intermediate in the cytosol in terms of a removal rate, k_e (e for elimination), and the cell volume, V_{cell}. This removal rate is assumed to be an intrinsic property of the cell that cannot be tuned. Then, the model for the non-compartmentalized cascade reaction is:

$$V_{cell}\frac{d[I_c]}{dt} = \frac{k_{cat,1}n_1}{K_{m1}}[\mathrm{S}_0] - \frac{k_{cat,2}n_2}{K_{m,2}}[I_c] - k_e[I_c] \tag{3.21}$$

$$V_{cell}\frac{d[P_c]}{dt} = \frac{k_{cat,2}n_2}{K_{m,2}}[I_c] \tag{3.22}$$

At steady state, the volume of the cell cancels out, and we attain expressions in terms of turnover rates. Using the same notation as before, the rate of product formation in the non-compartmentalized reaction, R_P, becomes:

$$R_P = \frac{\beta_2}{\beta_2 + k_e}\beta_1[S_0] \tag{3.23}$$

We can compare this rate with the product outflux at optimal conductance for a compartmentalized reaction by modifying Equations (3.2-4) to account for return of intermediate to the compartment if the outside concentration of intermediate is not negligible (Figure 3.4). This comparison reveals a surprising result (Appendix Section C.8): the optimal diffusive conductance becomes infinite for a non-zero value of k_e which we name $k_{e,crit}$. It is given by:

$$k_{e,crit} = \frac{\beta_1}{2}\left(1 + \sqrt{1 + \frac{4\beta_2}{\beta_1}}\right) \tag{3.24}$$

For removal rates below this critical value, the non-compartmentalized reaction is optimal, and the product formation rate is given by Equation (3.23). If the removal rate exceeds $k_{e,crit}$, then compartmentalization is beneficial, and the maximal product formation rate approaches the result given in Equation (3.13) with increasing removal rate (Figure 3.4, green arrow). This result shows that the model forms a natural connection between the non-compartmentalized and compartmentalized cascade.

The condition, $k_e > k_{e,crit,}$ is satisfied when the removal rate is much larger than the turnover rate of the first reaction (β_1). For large values of k_e, the throughput of the non-compartmentalized reaction is inversely proportional to k_e and approaches zero, while the product outflux of the compartmentalized reaction asymptotically approaches the value given by Equation (3.13).

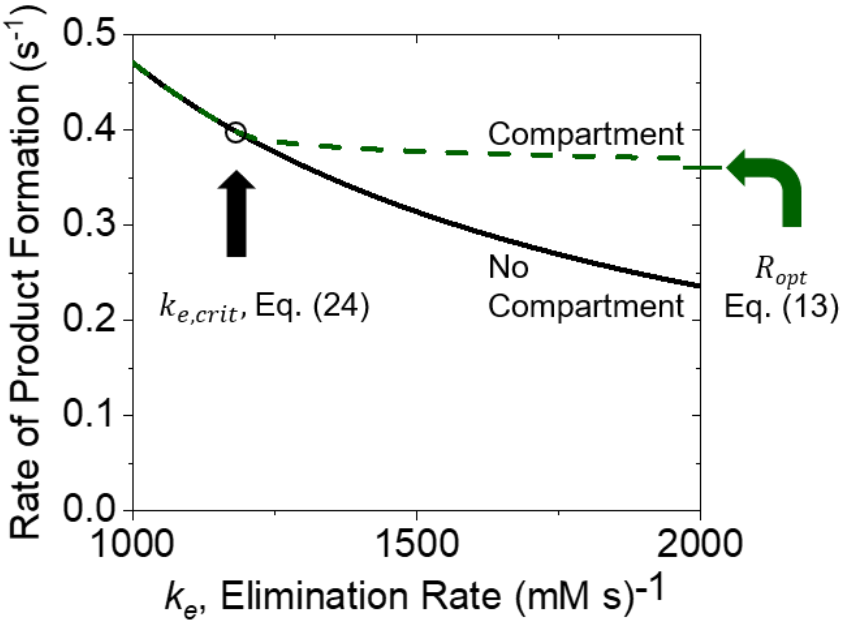

Figure 3.4: Comparison of product output between the non-compartmentalized reaction and the compartmentalized reaction as a function of the cytosol intermediate removal rate, k_e. In the non-compartmentalized reaction (black solid line), the rate of product formation is inversely proportional to k_e and approaches zero with increasing k_e. At the same time, the rate of product outflux (green dashed line) asymptotically approaches the non-zero value defined by Equation (3.13) (indicated by a green arrow on the right vertical axis). The optimal product output rates are identical up until a critical value of k_e (indicated by a circle on the graph and black arrow) after which the optimal diffusive conductance for the compartmentalized reaction becomes finite and compartmentalization provides benefits. $\gamma_1 = 24$ mM^{-1}s^{-1} and $\gamma_2 = 0.080$ mM^{-1}s^{-1}, $n_1 = n_2 = 50$, (as in Figure 2) and $[S_0] = 0.1$ mM.

Discussion

In general, the cell compartmentalizes either in space, where certain sets of enzymes are confined to specific organelles,[23, 115] or time, where enzymes only function at pre-defined points in the cell cycle.[109, 115] Recently, metabolic engineers have been investigating how compartmentalization could enhance the throughput and efficiency of biocatalysis in engineered cellular pathways. This is because the repurposing of cellular machinery provides an often appealing alternative to classic chemical synthesis.[15-19] However, non-native enzymatic cascades often have compatibility issues.[6, 17, 116, 117] For example, cascade intermediates and byproducts tend to activate inhibitory pathways and can be toxic to the cell.[23-26] Compartments are advantageous in that they can both quarantine such toxic byproducts from entering the cytosol[19, 27-29] and prevent the cellular environment from degrading unstable enzymes that participate in the desired reaction.[30] There are already several reports in the scientific literature demonstrating that the relocation of a synthetic cascade from the cytosol to the mitochondria improves reaction throughput.[10, 28, 29, 118]

As synthetic compartments for cascade reactions become more widespread, a rational and efficient design process for optimizing compartmentalized cascade properties is required. Our modeling shows that cascade reactions in the well-mixed, linear regime can be described by numbers of molecules of each enzyme, rather than concentrations, and that the compartment volume only plays an indirect role in the steady state. The model allowed us to formulate and solve the compartment optimization problem for the cases when the intermediate is volatile or toxic. Finally, we determined that a compartmentalized reaction provides significant benefits over a non-compartmentalized reaction when the rate of intermediate elimination in the non-compartmentalized reaction exceeds the maximum turnover rate of the cascade. These results can be viewed in the larger context of reactor design.

Metrics on compartment quality. In general, the design of chemical reactors is quantified by measuring the reactor conversion, yield, and selectivity.[119-121] Previous approaches to studying compartments have been based on optimizing other metrics that aim to describe compartment performance. These include the reaction efficiency,[34, 59] which is similar to the reactor conversion, and reaction productivity.[34] In the analysis of compartment performance, the best metric would reward product outflux but penalize intermediate outflux.

Reaction conversion, or reaction efficiency as defined by Castellana et al., η, is a metric of a cascade reaction which is defined as the ratio of product outflux to substrate influx [59]:

$$\eta = \frac{F_P[P]}{F_S[S_0]} \tag{3.25}$$

The reaction efficiency reaches 100% when every substrate molecule entering the compartment is converted into product. However, optimizing this metric is not desirable because substrate molecules which enter the compartment and leave again as unreacted substrate do not negatively affect product formation or intermediate toxicity.

Reaction productivity, *p*, as defined by Hinzpeter et al. [34], is the ratio of product outflux to the number of enzymes in the compartment:

$$p = \frac{F_P[P]}{n_1 + n_2} \tag{3.26}$$

Maximizing productivity is equivalent to maximizing product outflux while maintaining a constraint on the total number of enzymes. While this metric rewards a high product outflux, it does not penalize loss of intermediate.

The reaction yield and reaction selectivity are two metrics that are often used to quantify chemical reactor performance; however, they have not been used to quantify compartment performance. The reaction yield, Y,[53] of a cascade reaction is defined as the ratio of product outflux to the rate of substrate turnover:

$$Y = \frac{\mathrm{F_P}[P]}{\beta_1[S]} = \frac{F_P[P]}{F_P[P] + F_I[I]} \tag{3.27}$$

This metric penalizes intermediate outflux: it is high when the outflux of intermediate is low. However, this metric is also imperfect; Y approaches its maximum when the number of Enzyme 1 molecules approaches zero.

The reaction selectivity, *Se*, is defined as the ratio of the outfluxes of desired to undesired species; in this case, this is the ratio of product outflux to intermediate outflux:

$$Se = \frac{\mathrm{F_P}[P]}{\mathrm{F_I}[I]} \tag{3.28}$$

This metric rewards product outflux and penalizes intermediate outflux. However, it suffers from the same problem as the yield: it attains its maximal value when the number of Enzyme 1 is zero.

Each of these metrics is imperfect. Here, we avoid the use of these metrics and replace them with concrete design specifications. This gives a clear understanding of how the final compartment parameters depend on the initial specifications.

Defining Diffusive Conductance. Different researchers have adopted different interpretations for the value of the diffusive conductance or its inverse the diffusive resistance. On one hand, Berg[58] defines the diffusive resistance by considering the case of a sphere with perfectly adsorbing patches spread out along the surface. The diffusive resistance becomes related to the extent by which the substrate becomes depleted around the sphere. On the other hand, Hinzpeter et al.[34] considers diffusive resistance in terms of permeability, where the diffusive current into the membrane is dependent on the thickness of the membrane. Deciding which approach is suitable for specific situations would require complex molecular simulations which take into account pore size, pore density, molecule size, and molecular interactions.[122] As first approximation, the larger of the two resistances can be used. The resistance due to substrate depletion, R_D, is according to Berg (written in units of Ms):

$$R_D = \frac{1}{4\pi \mathrm{N_A} D r} \cdot \frac{1}{1 + \frac{\pi r}{N s}} \tag{3.29}$$

The resistance due to membrane permeability, R_P, is according to Hinzpeter et al. (written in units of Ms):

$$R_P = \frac{1}{N \mathrm{N}_A \pi s^2 \frac{D}{\delta}} \tag{3.30}$$

Where N is the number of pores, $\mathrm{N_A}$ is Avogadro's number, s is the apparent pore radius (which takes into account the molecule size, the pore size, and molecular interactions), D is the diffusion coefficient, and δ is the membrane thickness.

Comparison to Biological Systems. Compartment models have so far been published for the carboxysome,[34, 35] and the propanediol utilization (Pdu) microcompartment.[36] Typically, a comparison to a biological system offers credibility to a model. However, these comparisons are only justified if a full mechanistic picture of the system is available. The main missing piece in the study of bacterial microcompartments is the diffusive resistance across the shell boundary.[123] Indeed, estimates for the diffusive resistance of the alpha-carboxysome shell span three orders of magnitude, with Mangan et al.[35] suggesting a shell permeability of 10 μm/s, Hinzpeter et al.[34] using permeabilities of 90 μm/s and 18 μm/s, and Tsai et al. suggesting that diffusive resistance could reach 75% of the diffusion limited aggregation rate.[124] Instead of comparing our results to biological systems, we will therefore compare them to the results of the more complex published models which include reaction-diffusion systems and the full nonlinear regime of cascade kinetics. The goal is to test if our more basic model gives the same answers, and therefore retained the essential physics of the process while stripping out unnecessary detail.

The dynamics of the carboxysome have been modeled using reaction diffusion equations by Mangan et al.[35] In their study, the numerical solution of the reaction diffusion model for a 50-nm radius carboxysome was found to plateau and maximize product throughput for a permeability of 1.5 ± 0.7 μm/s. This translates into a diffusive conductance of $3 \pm 1 \cdot 10^7$ $M^{-1}s^{-1}$. Using the same kinetic parameters, our analysis gives an optimal diffusive conductance – limited by the saturation of the second enzyme – of $2.7 \cdot 10^7$ $M^{-1}s^{-1}$.

The dynamics of the bacterial propanediol utilization microcompartment were modeled by Jakobson et al.[36] They find that the optimal permeability for the 100 nm-radius microcompartment is 1 μm/s. This translates to a diffusive conductance of $8 \cdot 10^6$ $M^{-1}s^{-1}$. Using the same parameters

in our model, we found that the optimal diffusive conductance was limited by the saturation of the first enzyme at a value of $8.4 \cdot 10^6$ $M^{-1}s^{-1}$.

In both cases, a complex reaction diffusion model that considers a number of auxiliary interactions returns practically identical results as our simplified analysis, which only requires knowledge of the most basic reaction kinetics of the enzymes.

A microsphere surface as a compartment. An interesting parallel may be drawn between a compartment containing enzymes that participate in a cascade reaction and a microsphere whose surface is coated with enzymes that participate in the same cascade reaction. The diffusive resistance inherent to molecules approaching a large adsorbing sphere generates reaction conditions similar to a compartment, and precludes the need for a physical compartment boundary. Solving the reaction-diffusion equation for a microsphere of radius r coated with enzymes participating in a cascade reaction at densities of σ_{E1} and σ_{E2}, with catalytic efficiencies defined as in Equations 3.8 and 3.9, and absorbing boundary conditions for substrate and intermediate concentrations at infinity ($[S](r=\infty) = S_0, [I](r=\infty) = 0$), the steady state rate of product throughput on the surface can be written down as:

$$R_{opt,microsphere} = S_0 \cdot \left(\frac{\gamma_1 \sigma_{E1} \gamma_2 \sigma_{E2} \frac{D_S}{r}}{\left(\gamma_1 \sigma_{E1} + \frac{D_S}{r}\right)\left(\gamma_2 \sigma_{E2} + \frac{D_I}{r}\right)} \right) \tag{3.30}$$

Multiplying out the above expression by the microsphere surface area returns an expression equivalent to that of Equation 3.11, with $F_i = 4\pi D_i r$ as the diffusive resistance. Details on the derivation can be found in Appendix Section C.9. This result can be extended to include a competing reaction for intermediate in solution, with a rate constant k_e. In this case, the rate of product throughput on the surface of the microsphere may be written as:

$$R_{opt,microsphere} = S_0 \cdot \left(\frac{\gamma_1 \sigma_{E1} \gamma_2 \sigma_{E2} \frac{D_S}{r}}{\left(\gamma_1 \sigma_{E1} + \frac{D_S}{r}\right)\left(\gamma_2 \sigma_{E2} + \frac{D_I}{r} + \sqrt{D_I k_e}\right)} \right) \quad (3.31)$$

The competing reaction for intermediate in solution only begins to significantly affect reaction dynamics when $k_e > D_I/r^2$. The details of the calculation performed for deriving Equation 3.31 can be found in Appendix Section C.10

Conclusion

With the innovations in the experimental manipulation of compartmentalized cascades, the metabolic engineer's toolbox is continuously growing. This paves the way for the design of micro- and nanoscale bioreactors and synthetic cells[125-127] for cascade reactions with unstable intermediates. In this chapter, we consider a model for a compartmentalized cascade reaction with unstable intermediates. The model assumes a well-mixed compartment interior, a homeostatically maintained environmental substrate concentration, that steady state has been reached, and that the enzymes exhibit Michaelis-Menten kinetics. We study the case when both enzymes are functioning in the linear regime of the kinetics and the case when one enzyme is saturated. The model presented here captures in a quantitative manner the intuition that since small pores restrict substrate influx and large pores permit intermediate escape, the design challenge is to find the optimal diffusive conductances. Furthermore, we define a new strategy for the design of compartmentalized cascade reactions, and provide a simple relation for determining when a compartmentalized reaction will perform significantly better than its non-compartmentalized counterpart.

Chapter 4: An Alternative Approach to Enhancing Cascade Reaction Throughput: Microenvironment Engineering

This section discusses the electrostatic modeling of the DNA Origami surface from "*Proximity does not contribute to activity enhancement in the glucose oxidase–horseradish peroxidase cascade," by Yifei Zhang, Stanislav Tsitkov, and Henry Hess, Nature Communications 7, 13982, 2016.*

Introduction

The previous chapters have demonstrated that the spatial organization of enzyme cascades does not enhance reaction throughput when intermediate molecules are stable if a steady state exists for the reaction system. However, experimental evidence has demonstrated that the immobilization of certain enzyme cascades on DNA origami scaffolds enhances cascade reaction throughput.[47, 50, 107] In order to resolve the apparent disagreement between modeling and experimental results, it was hypothesized that the experimentally observed reaction enhancement could be a result of the highly negatively-charged DNA origami nanostructure generating a favorable microenvironment for enzyme activity,[39, 129, 130] by attracting protons from the buffer solution and locally lowering the pH. In this chapter, we test this hypothesis by modeling the electric potential near the surface of the DNA origami scaffold using the Derjaguin-Landau-Verwey-Overbeek (DLVO) theory.[131-133]

Methods

The Poisson-Boltzmann equation for charged surfaces in buffer solutions. The electrostatics of fluids near charged surfaces is described by the Poisson Boltzmann equation:[80, 134]

$$\nabla^2\Psi = -\frac{2FC_0}{\epsilon}\sinh\left(-\frac{F\Psi}{RT}\right) \tag{4.1}$$

Where F is the Faraday constant, C_0 is the bulk salt concentration, Ψ is the electric potential, R is the universal gas constant, T is the temperature, and ε is the product of the vacuum permittivity constant and dielectric constant of water. If we model the DNA origami surface as an infinite sheet of charge, we can use symmetry to reduce this equation to a one-dimensional form describing the potential along the axis perpendicular to the sheet of charge:

$$\frac{\mathrm{d}^2\Psi}{\mathrm{dx}^2} = -\frac{2FC_0}{\epsilon}\sinh\left(-\frac{F\Psi}{RT}\right) \tag{4.2}$$

Two boundary conditions are required to solve this equation. The first states that the potential at infinity is zero. The other specifies the potential at the surface. While the surface potential of a DNA origami surface has yet to be determined, we can estimate it be using the Grahame equation, which provides a relation between surface potential, surface charge density, and buffer ionic strength:

$$\sigma = \sqrt{8C_0\epsilon RT}\sinh\left(\frac{F\Psi_0}{2RT}\right) \tag{4.3}$$

Results

Solution to the linearized Poisson-Boltzmann Equation. The equation can then be solved in one using $\Psi(x = 0) = \Psi_0$ and $\Psi(x = \infty) = 0$. For low surface potentials ($\Psi_0 \ll \frac{RT}{F} \approx 25\ mV$), the Poisson Boltzmann equation can be linearized and solved in a closed form as follows:

$$\frac{\mathrm{d}^2\Psi}{\mathrm{dx}^2} = -\frac{2FC_0}{\epsilon}\sinh\left(-\frac{F\Psi}{RT}\right) = -\frac{2FC_0}{\epsilon}\cdot\frac{1}{2}\left(e^{-\frac{F\Psi}{RT}} - e^{\frac{F\Psi}{RT}}\right) = \frac{FC_0}{\epsilon}\left(\frac{2F\Psi}{RT}\right) + H.O.T. \qquad (4.4)$$

Where the higher order terms (H.O.T.) are of order $O\left(\frac{F\Psi}{RT}\right)^2$. A natural variable that appears in the above equation is:

$$\kappa = \sqrt{\frac{2F^2C_0}{\epsilon RT}} \qquad (4.5)$$

The variable κ is also known as the Debye length and describes the distance at which charged surfaces become screened by counterions in buffer solutions. Dropping out the higher order terms and substituting in the variable for the Debye length, κ, we arrive at a second order linear ordinary differential equation:

$$\frac{\mathrm{d}^2\Psi}{\mathrm{dx}^2} - \kappa^2\Psi = 0 \qquad (4.6)$$

Solving with the appropriate boundary conditions, we find that:

$$\Psi(x) = \Psi_0 e^{-\kappa x} \qquad (4.7)$$

The concentration of charged species as a function of potential can be evaluated as:[134]

$$C(x) = C_{bulk} e^{-\frac{F\Psi}{\mathrm{RT}}} \tag{4.8}$$

As a result, the concentration of protons, and also the pH, near a charged surface can be estimated as:

$$[H^+](x) = [H^+]_{bulk} e^{-\frac{F\Psi}{RT}} \tag{4.9}$$

$$\mathrm{pH}(x) = \mathrm{pH}_{bulk} + \log_{10} e \, \frac{F\Psi}{RT} = pH_{bulk} + \frac{F\Psi}{2.3RT} \tag{4.10}$$

The above expression may be used for estimating the pH profile near the charged surface of a DNA origami scaffold.

Closed form solution for the one-dimensional Poisson Boltzmann Equation. In the derivation above, we made the assumption of a low surface potential. In fact, the equation may be solved in closed form while foregoing the linearization, although it provides a less intuitive result. Solving the one-dimensional Poisson-Boltzmann equation without linearization, we arrive at the following closed form solution for the potential:

$$\Psi(x) = \frac{2RT}{F} \cdot \log\left(\frac{1 + \exp(-\kappa x)\tanh(\alpha)}{1 - \exp(-\kappa x)\tanh(\alpha)}\right) \tag{4.11}$$

$$\alpha = \frac{F\Psi_0}{4RT}, \kappa = \sqrt{\frac{2F^2 C_0}{\epsilon RT}} \tag{4.12}$$

This equation deviates from the solution to the linearized Poisson Boltzmann equation by generating a steeper potential drop off near the surface.

An issue that arises is that the Poisson Boltzmann equation tends to overestimate the concentration of counterions near highly charged surfaces.[133] The finite size of counterions results in steric restrictions on the maximum number of counterions that can accumulate near a surface. This can then extend the electric potential farther from the surface. This problem was examined in detail by Borukhov and Andelman (1997)[133], who gave expression to the concentration profile near a surface which takes into account the steric interactions which would influence the density of counterions near the surface. The presence of these steric effects implies that the counterion concentration saturates near the surface for a distance of $l^* \approx a^3\sigma/e$, where a is the radius of the counterion particle in question, σ is the surface charge density, and e is the charge of an electron.[133]

Conclusion

The main conclusion of this section is that the DNA origami scaffold can generate a microenvironment with a lowered pH extending up to 2 nm from the surface. Enzymes tethered to the charged surface then spend a non-negligible amount of time in the lower-pH environment. Since enzyme activity is known to strongly depend on pH, it is a reasonable conclusion that DNA origami scaffolds affect the activity of enzymes tether to them, and enhancement cascade reaction throughput.

Part II

Organization in Systems of Active Cytoskeletal Filaments

Chapter 5. Background on Systems of Active Cytoskeletal Filaments

This section follows *"Design of active nanosystems incorporating biomolecular motors," by Stanislav Tsitkov and Henry Hess. Out-of-equilibrium supramolecular systems and materials. Wiley. (In Press).*

Molecular motors couple the consumption of fuel, a non-equilibrium process, to the generation of mechanical work, which in turn can be used to either push a system away from or accelerate its approach to chemical equilibrium.[135, 136] In nature, dedicated proteins have evolved to serve as molecular motors. These biomolecular motors play key roles in organisms,[137] enabling them to replicate DNA with an error rate as small as 10^{-11},[138] and to move their bodies as fast as the 104 km/h top speed of a running cheetah.[139, 140] DNA replication and transcription are supported by polymerase enzymes hydrolyzing nucleotide triphosphates and adding them to the growing complementary strand while unidirectionally traversing the template strand.[141] The muscle contraction of the cheetah is powered by bundles of myosin motors of the thick filament stepping along the filamentous actin of the thin filament in the sarcomeres of muscle fibers. [142, 143] Other biomolecular motors play important roles in cellular processes as well. Protons flowing through the channels formed by the Mot protein complex generate the rotary motion required for bacterial flagellar propulsion.[144] Dynein motor proteins step along microtubules of the axoneme in motile cilia in lungs to keep the airways clear of mucus.[145] The F_1F_0 ATPase enzyme complex transports protons across membranes and catalyzes the synthesis of the cellular fuel ATP. [146, 147] Kinesin motor proteins participate in intracellular transport and in cell division.[148] In contrast to

heat engines, motor proteins directly convert chemical energy into mechanical energy, usually by the hydrolysis of adenosine 5'-triphosphate (ATP).[149] The emergent properties resulting from the integration of molecular motors into materials and structures are an active field of study; most notably, they include plasticity, adaptability, and self-healing.[150]

Over the past two decades, a growing field of study has been the incorporation of biomolecular motors into active nanosystems.[2, 41, 42, 149-163] These systems typically focus on the motors of the cellular cytoskeleton,[164] kinesin,[165, 166] dynein,[167, 168] and myosin,[169] interacting with microtubules[170-172] and actin filaments.[173] (Figures 5.1a, 5.1b) Most implementations of these systems fall into one of two categories depending on the configuration of the motors and filaments. In the "bead" or "native" configuration, motors traverse surface-immobilized filaments as they do in cells; in the "inverted" configuration, filaments glide upon surface-immobilized motors.[174](Figures 5.1c, 5.1d)

These systems are used both as a tool to study intracellular dynamics [175] and to develop ATP-powered devices outside of the cell.[176, 177] From the biomedical perspective,[178, 179] constructing these systems gives us a better understanding of the interactions between their components, which in turn helps researchers develop treatments against illnesses resulting from the dysfunction of biomolecular motors or infectious agents that hijack them.[156, 161, 180] From the technological perspective, active nanosystems incorporating biomolecular motors can be engineered to detect molecules[181] and perform computation.[182] Moreover, it is reasonable to conjecture that the trend in the shrinking size of semiconductor components defined in Moore's Law will soon be accompanied by a growing need for reliable actuation on the nanoscale.[153] Biomolecular motors are an excellent candidate for addressing this need, with the only alternative being man-made synthetic motors, which currently lag behind in functionality,

efficiency, and structural complexity despite their tremendous progress over the past two decades.[183] For example, autonomous light-activated motors[184] based on overcrowded alkenes can have rotation rates as high as 2-3 MHz,[185] and were recently used to drill holes in cell membranes.[186] Still, the force production and energetic efficiencies of these motors remain unclear.[186-188] In addition, only one autonomous chemically-fueled synthetic motor has so far been developed, and it rotates once approximately every 12 hours.[183, 189] In comparison, the motor protein kinesin takes approximately 100 steps each second and has been estimated to attain an energy efficiency of up to 80%. [190]

In this chapter, we provide an overview of the design of active nanoscale systems based on motor proteins and cytoskeletal filaments. In the first section, "Active nanosystem design," we examine the engineering objectives and provide a brief overview of the components involved; in the next section, "Biological components of active nanosystems," we describe the structure and function of the filaments and motors involved; in "Interactions between components of active nanosystems" we describe the interactions which occur between the individual components; in "Implementation of active nanosystems," we provide a brief review of applications of active nanosystems.

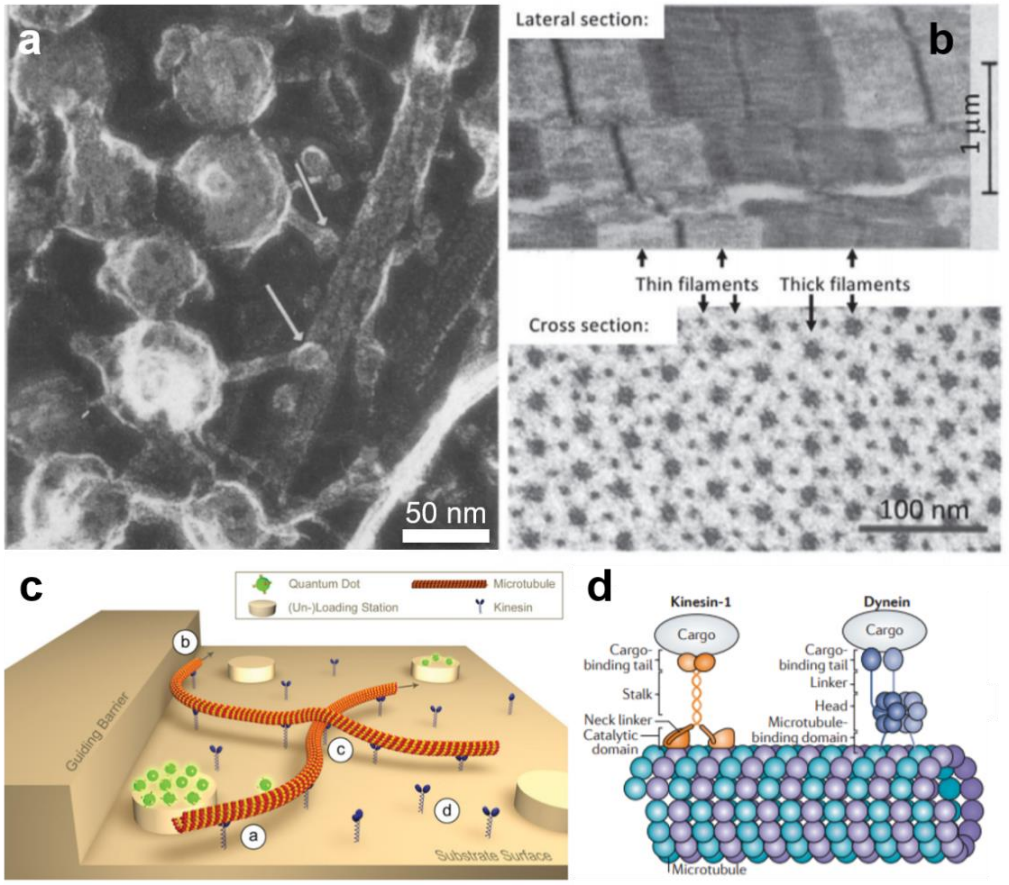

Figure 5.1: Biomolecular motors generate forces in living organisms by walking along filaments. (a) Electron microscopy images of latex microspheres crosslinked to taxol-stabilized microtubules via kinesin motors. Kinesin motor heads are indicated by white arrows. Adapted from Hirokawa et al. [191] (b) The myosin motors bundled into the thick filament step along the thin filament to generate contractile forces in the sarcomere. Top image adapted from Huxley et al.[192] Bottom image (cross section) adapted from Hawkins et al.[193] (c) Cartoon of an inverted motility assay modified for engineering purposes: microtubules gliding on a kinesin-coated surface load and unload cargo (in this case quantum dots) at specific stations. Adapted from Kerssemakers et al.[194] (d) The native configuration of kinesin and dynein-driven transport: motors bind cargo and walk along the microtubule. Adapted from Veigel and Schmidt.[195]

Active nanosystem design

Myosin and kinesin-powered active nanosystems have been used for cargo transport, [196-200] analyte concentration, [181, 201-203] force generation, [152, 204-214] detection, [160, 196, 215-221] studying biology and soft-matter physics, [222-224] and even computation.[182, 225] Depending on the application, active nanosystems typically take on one of two distinct configurations: in the native configuration, filaments are immobilized on a surface and cargo-carrying motors use them as tracks;[226] in the inverted configuration, filaments carrying cargo glide on carpets of surface-immobilized motors.[227, 228] A third configuration, where both filaments and motors are suspended in solution, has been gaining popularity as a model system for active matter and self-assembly.[214, 229] The native configuration is reminiscent of what happens in biology: motor proteins walk along filaments that are stationary, e.g. inside an axon.[179] However, the transport distance of cargo is limited by the length of single filaments, which rarely can exceed a few tens of micrometers,[230] unless cargo-carrying motors can transition between filaments. In the inverted system, filaments are propelled for large distances as long as ATP remains and filaments do not degrade or get stuck.

The dynamics of the active nanosystems can be altered by modifying the environment in which the biomolecular motors and filaments operate. The motor protein velocity is controlled by the ATP concentration and the temperature.[231] The addition of high concentrations of polymers such as methylcellulose,[213] PEG,[232] and pluronics[233] can create crowding effects and depletion forces and generate collective behavior in systems of gliding filaments. More complex approaches for environmental modifications involve engineering the surface to either reversibly[43] or controllably bind[234] motors from solution. Surfaces can be patterned using photolithography to create patches for motor binding[235] or walls for guiding gliding filaments.[236] External control

over the active nanosystems can be achieved with light[237] (modulating motor activity and fuel availability),[238] magnetic fields (acting on particles attached to gliding filaments),[239] electric fields (acting on the charged filaments),[240] mechanical forces,[241] and heat.[242]

The packaging of the active nanosystems typically consists of flow cells:[243] structures consisting of a small, 22 mm x 22 mm glass coverslip on top of a larger, 24 mm x 60 mm glass coverslip separated by a 100 μm - high spacer (such as parafilm or double-sided tape). Experiments are performed by flowing various solutions through the flow cell in order to coat surfaces and introduce ATP, motors, filaments, and the components of a molecular antifade system, which suppresses photodamage caused by fluorescent illumination by reducing the concentration of dissolved oxygen.[244, 245] The filaments and motors on the inner surfaces of the flow cell are then usually imaged with epifluorescence microscopy.[195] Alternative imaging strategies can be used as well. Nanometer-precision estimates of molecular height above reflective surfaces can be made using fluorescence interference contrast microscopy.[194, 246, 247] Recently, it was observed that surface-adhered filaments could be imaged in a fluorescence label-free manner.[248] Both optical traps[249] and total internal reflection dark field microscopy can be used to study the stepping dynamics and force-production of single motor proteins.[250]

The design process for an active nanosystem becomes an optimization problem of a function of the following variables:

- The filament used (microtubule or actin filament)
- The motor used (kinesin family, dynein family, or myosin family)
- The environment (walls and obstacles on the surface, motor patterning, etc.)

- External influences (activation/inhibition mediated by light, electric or magnetic fields, heat, and compression)

Most optimization problems are solved by determining first how a function behaves in response to changes in individual variables (i.e. by calculating the gradient), and then by changes in pairs of variables (i.e. by calculating the matrix of second derivatives, the Hessian). We will strive to take a similar approach in the remaining sections of this chapter.

Biological components of active nanosystems

This section aims to provide a brief overview of the structure and function of the cytoskeletal filaments and motor proteins frequently incorporated into active nanosystems, first describing microtubules, kinesins, and dyneins, and then actin filaments and myosins.

Microtubules. The microtubule is the most widely used filament in active nanosystems, as it is a rigid, polar rod with a high density of binding sites for motors and cargo alike. This filament takes the form of a hollow cylinder 25 nm[251] in outer diameter and 17 nm in inner diameter,[252] with a length ranging from one micrometer in a cell to tens of micrometers in active nanosystems.[230, 252] Microtubules have three levels of structure: the alpha-beta tubulin heterodimer,[253] the protofilament,[254] and the microtubule itself.[255, 256] The assembly process of a microtubule is activated by the presence of GTP. The binding of GTP to free tubulin heterodimers induces a conformational change[257] which makes dimer-dimer binding favorable. Tubulin heterodimers assemble longitudinally in a polar manner (with beta tubulin of one heterodimer binding the alpha tubulin of the next heterodimer) to form protofilaments. The alpha-beta binding orientation grants the microtubule polarity; to describe the orientation of the microtubule, the end with exposed beta-tubulin subunits is called the "plus" end of the microtubule, while the end with exposed alpha-tubulin is called the "minus" end. *In vitro*, the plus end polymerizes faster than the minus end[258], which results in an asymmetric length distribution known in polymer science as the "Schulz distribution."[259] The protofilaments assemble laterally with a 0.9 nm offset between individual protofilaments and a 4.9 nm offset at the seam (termed an A-seam, where alpha monomers laterally bind beta monomers and vice versa[260]) to form the helical structure of the microtubule.[261, 262] The number of protofilaments in

a microtubule can vary between 9 and 16.[263, 264] However, due to the lateral offset of protofilament assembly, a 13 protofilament microtubule is the only one where protofilaments are not supertwisted; microtubules consisting of different numbers of protofilaments forces the protofilaments to exhibit a helical twist around the central axis of the microtubule.[264] A recent direction of research has been analyzing the mechanical and stability properties of these 'supertwisted' microtubules.[260, 265]

An important property of microtubules is their kinetic instability. (Figure 5.2a) In the absence of stabilizing agents, microtubules exhibit a phenomenon termed, 'dynamic instability,' where they alternate between phases of growth and "catastrophe," when they rapidly disassemble.[266] This process is caused by the hydrolysis of the GTP in the heterodimer subunits into GDP, resulting in a strain on the microtubule lattice.[267-269] Considering this inherent out-of-equilibrium behavior of a polymerized microtubule,[270] it is not surprising that researchers have demonstrated that the polymerization and depolymerization of microtubules can perform work in the absence of molecular motors, making the un-stabilized microtubule a "molecular machine" even by itself.[258, 271-274]

While this kind of instability can be useful in cellular processes, where e.g. repeated cycles of microtubule assembly and disassembly facilitate the capture of chromosomes by the spindles during mitosis, it can be unfavorable in active nanosystems, where filaments must remain intact over time periods spanning several hours. As a result, microtubules are often stabilized with taxol, a molecule which reversibly binds tubulin dimers and stabilizes the microtubule against depolymerization,[275] the non-hydrolyzable GTP-analogue GMP-CPP,[268] or both.[276]

Kinesin. One of the main roles of microtubules in cells is to provide a rail for kinesin motors. Kinesin motors were first identified in 1985 as force generating proteins involved in microtubule-mediated organelle transport.[228] Typically, kinesin motors consist of motor (head) domains and a coiled-coil domain. So far, researchers have discovered 15 different families of kinesin motors, [166] which are mainly identified based on conserved sequences in their head domain.[277, 278] The families can be grouped into three groups based on the position of their motor domain; N-terminal motor domains drive kinesins toward the plus end of microtubules, C-terminal motor domains drive kinesins to the minus end of the microtubule, and motor domains located in the middle of the kinesin cause microtubule depolymerization.[166] The most commonly-used kinesin in active nanosystems is kinesin-1 (also termed KIF5 or conventional kinesin), which drives plus-end directed microtubule transport. Other kinesin superfamily proteins that have been used include kinesin-8,[279] kinesin-3,[280] and kinesin-5.[281] We will primarily focus on kinesin-1 in this chapter due to its popularity.

The kinesin-1 motor protein moves along single protofilaments of microtubules[282] towards their plus end at a maximum velocity between 0.8 μm/s and 1.8 μm/s,[283] with a stall force of 7 pN;[149, 284] these quantities are strongly dependent on the concentrations of both ATP and ADP in solution (for example, a 1:1 ratio of saturating ATP and ADP can decrease the stall force by as much as 50%). During each step, a kinesin motor moves 8 nm along the microtubule, corresponding to the length of a tubulin heterodimer.[285] An important aspect of the kinesin motor is its processivity: unlike other molecular motors, the kinesin motor stays bound to the microtubule for about 100 steps before unbinding.[174, 286]

The mechanochemistry of kinesin-1-based propulsion has been a topic of great interest ever since the motor's discovery; even now a complete consensus has not yet been reached as to

which conformational changes occur within the motor during ATP binding and hydrolysis into ADP and inorganic phosphate.[277] The key structural elements of the kinesin mechanochemical cycle are the motor head, which binds the motor to the tubulin heterodimer, and the neck linker, which provides tension-mediated coordination between the motor heads. During each step, the kinesin motor undergoes a cycle of ATP hydrolysis into ADP and inorganic phosphate.(Figure 5.2b) The motor head remains strongly bound to the tubulin heterodimer while its catalytic core is empty (apo), bound to ATP, and bound to ADP.Pi (ADP and inorganic phosphate).[287] However, once the release of a phosphate molecule from the ADP.P_i bound state leaves only an ADP molecule within the catalytic core, the motor domain undergoes a conformational change which lowers its affinity to the tubulin heterodimer, thereby allowing the motor head to detach and make a step. When the kinesin head detaches, it rotates around the coiled coil of the motor[190] and binds to the next tubulin heterodimer of the protofilament 16 nm away,[167] thereby displacing the whole motor 8 nm.

Dynein. Dynein is a motor protein that exhibits microtubule minus-end direction motion. Whereas kinesin motors transport cargo towards the periphery of the cell, dynein motor proteins transport cargo toward the interior of the cell, close to the nucleus. Understanding how this motor functions is of immense scientific interest, as it can both play a significant role in pathologies, where the motor is hijacked by an infectious agent and transports it to the nucleus of the cell,[288] and also because it has a unique structure compared to the kinesin motors.[167] There are typically two types of dynein motors in eukaryotic cells. Cytoplasmic dynein plays important roles in mitosis and retrograde cargo transport.[289] On the other hand, axonemal dynein motors are located in cilia and flagella, where they drive cellular propulsion.[290] Dynein motors

are also significantly larger than kinesin and myosin motors, weighing in at 1.5 MDa, compared to 360 kDa[174] for kinesin and 520 kDa for myosin II.[291] The step size of cytoplasmic dynein has been observed to vary between 4-32 nm.[167] Both stall force and unloaded velocity has been found to vary significantly between species, ranging from 1-2 pN and >1000 nm/s in mammalian dynein, to 5-7 pN and 100 nm/s in yeast dynein.[292]

Actin Filaments. The second cellular filament involved in motor-driven cellular dynamics is the actin filament. Actin filaments power processes ranging from cellular migration to muscular contraction, where they constitute the structure of the thin filament in the sarcomere. In cells, actin filaments (also called F-actin, for filamentous) are typically nucleated upon an Arp2/3[293] complex and grow once the critical concentration[294] of globular actin (G-actin, for globular) is high enough. Unlike microtubules which use GTP to power polymerization, actin filament polymerization is activated in the presence of ATP;[295] in fact, ATP-bound G-actin has a 20 times lower critical polymerization concentration than ADP-bound actin.[5] Similar to microtubules, actin filaments have polarity, with a front, "barbed" (+) end (where polymerization mostly occurs) and a back, "pointed" (-) end. The filament takes the shape of a two-stranded cable, with each consecutive monomer undergoing a rotation of 166^{o} and a translation of 25.5 A.[5] While actin filaments do not undergo dynamic instability as microtubules do, they still can depolymerize when the bound ATP molecule hydrolyzes into ADP. Unlike microtubules, actin filaments do not accumulate strain during polymerization and typically disassemble from their pointed end; disassembled monomers can then be reused by binding a new molecule of ATP and diffusing to the barbed end of the filament; this gives rise to the "treadmilling" phenomenon, where monomers are continuously recycled from the pointed end to be reincorporated at the

barbed end.[296] Depolymerization of actin filaments can be averted by the addition of phalloidin, a molecule that binds between F-actin subunits and inhibits the ATPase activity of the actin subunits.[297] In addition, due to its higher affinity for polymerized actin over monomer G-actin,[297] phalloidin is especially useful for targeting filamentous actin for labeling.

Myosin. Myosin motor proteins drive transport along actin filaments. In muscles, myosin motors bundle together to form the thick filament of the sarcomere, which interacts with the actin filaments of the thin filament of the sarcomere to create contractile force. Similar to kinesin, myosin is a directional motor that consumes one ATP molecule per step. Unlike kinesin however, the most widely used myosin motor in active nanosystems, myosin II, is not a processive motor: after each step, the myosin motor unbinds from the actin filament.[298] For this reason, myosin-II mediated transport must be accomplished by utilizing teams of myosin motors, so as to prevent the motors and cargo from diffusing away from the filament between rebinding events, and step sizes can vary between 5 – 15 nm.[299] This non-processive behavior allows the motor to move significantly faster along the filament; myosin II can move along actin at velocities as high as 8 μm/s, ten times faster than kinesin-1. [298] The chemomechanical cycle for myosin II is different from kinesin as well. Whereas kinesin motion is governed by neck linker docking upon ATP binding, myosin-II motion is governed by a powerstroke of its lever arm upon phosphate release.[5] Furthermore, myosin has a high F-actin affinity in the ADP-bound and Apo states, but exhibits a low affinity for actin in the ATP and ADP.Pi-bound states, [300] with undocking occurring during ATP binding and redocking occurring during the ADP.Pi state.[299]

Not all myosin motors are non-processive. For example, myosin V is a double headed motor that processively walks along the actin filament, taking at least 40 steps on average before

unbinding. This processive myosin motor achieves velocities at saturating ATP concentration of about 300 nm/s and exhibits a stall force of approximately 3 pN.[301]

The actomyosin system has also been widely used to construct active nanoscale systems due to its distinct advantages, such as 10x faster motility compared to kinesin/microtubule systems. However, binding cargo molecules to the actin filament is more difficult, due to a lower density of binding sites compared to microtubules.[291] The actomyosin system has also been employed in studies of active matter, where motor speed allows straightforward observation and analysis of dynamic topological behaviors.[302]

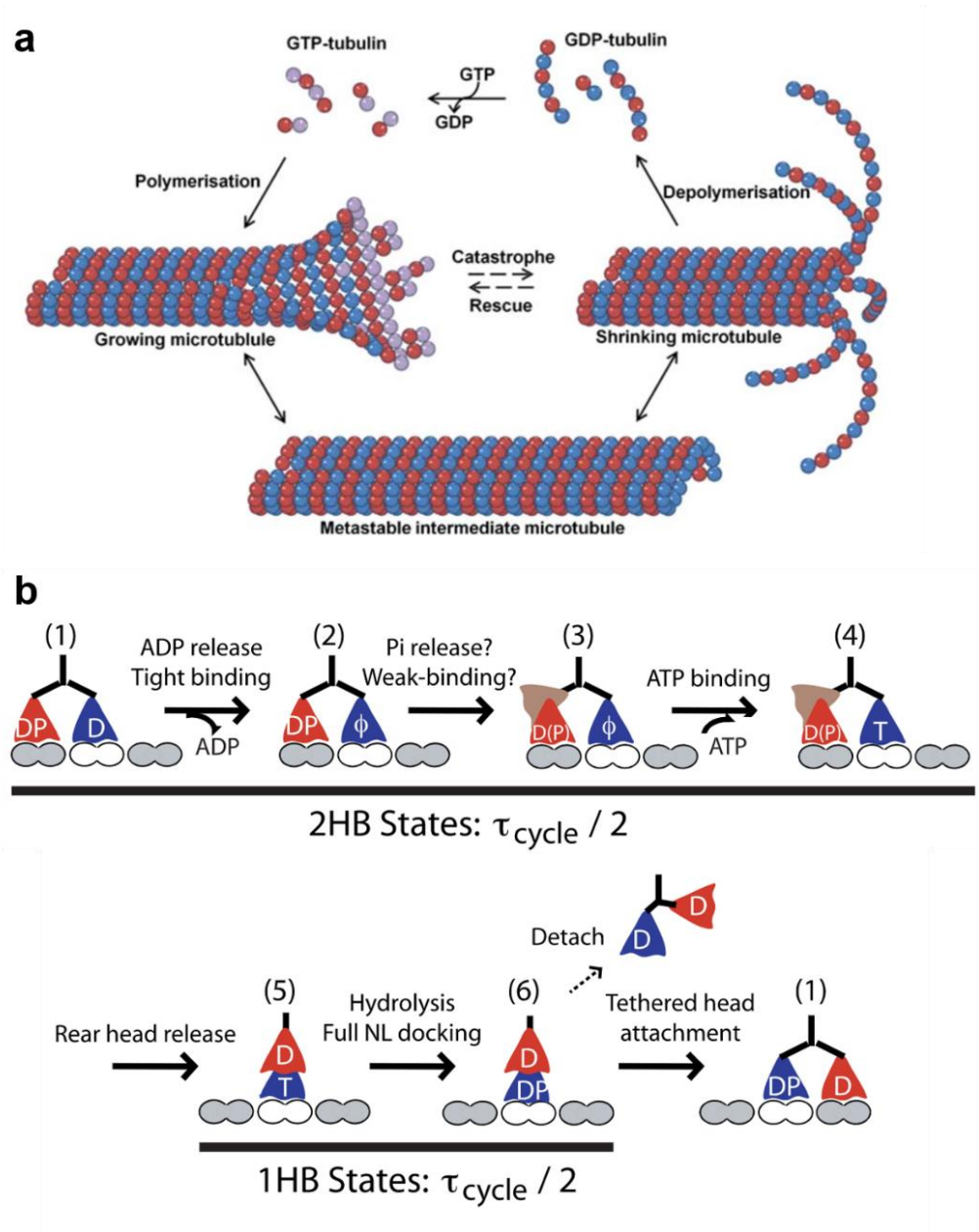

Figure 5.2: Microtubules and kinesin motors function out of equilibrium. (A) Microtubules are polar polymers consisting of a roll of laterally-bound protofilaments which consist of alpha-beta tubulin heterodimers bound end to end. Unstabilized microtubules undergo dynamic instability: a phenomenon characterized by stochastically alternating phases of polymerization and "catastrophe:" a rapid depolymerization where whole pieces of the microtubule break off due to the accumulated strain of GDP-bound tubulin heterodimers. Adapted from Calligaris et

al.[303] (B) The kinesin stepping cycle. Each kinesin head is coupled to an ATP hydrolysis cycle, with Apo (empty), ATP-bound, ADP.Pi-bound kinesin heads strongly bound to the microtubule, while the ADP-bound state is weakly bound, which allows a step to happen. Interhead coordination is mediated by tension in the neck-linker domain. Adapted from Hancock.[277]

Interactions between components of active nanosystems

In this section, we will examine the interactions between filaments and motors and their responses to external stimuli.

Filament response to external load. The mechanical properties of motor-propelled filaments determine the length scale over which they can be guided and their resistance to deformations in response to external loads. The metric that is commonly used to evaluate these quantities is the flexural rigidity of the filament, which is related to the persistence length of the filament by a factor of k_BT.[252] In the first attempt to measure the flexural rigidity of a microtubule, the distribution of end-to-end distances of microtubules stuck to a surface yielded an estimate of 74 μm for the persistence length.[304] Later, Gittes et al.[305] observed microtubules and actin filaments freely bending in solution in response to thermal fluctuations and estimated the flexural rigidity of a microtubule at 2.2×10^{-23} Nm^2 (L_P = 5.2 mm) and of an actin filament at 7.3×10^{-26} Nm^2 (L_P = 17.7 μm). While it is now accepted that the persistence length of a microtubule is on the order of 1-10 mm, a definitive number has not yet been established. Indeed, several alternative methods have been developed to calculate the persistence length, which include using hydrodynamic flows to measure bending in response to a force,[306, 307] measuring relaxation times from deformations,[308, 309] using optical tweezers to determine buckling forces,[310-313] and others.[252] Several hypotheses have been developed to explain the wide range of measurements, ranging from inaccurate drag measurements during hydrodynamic bending experiments to internal microtubule friction when measuring stiffness by analyzing the modes of thermal fluctuations.[311] Even more, there appear to be dependencies on filament length, stabilization method (unstabilized, taxol, GMP-CPP), and polymerization procedures. An additional source

of error for these measurements could be the reliance on the Euler-Bernoulli theories for beam bending, which assumes that the microtubule is a hollow cylinder of an isotropic material.[314] However, the protofilament structure of the microtubule makes it a highly anisotropic material, because the lateral bonds are much weaker than the longitudinal bonds between tubulin dimers.[311] A recent study that ventured to map out this anisotropy by measuring the strain across a microtubule while applying increasing loads conjectures that the loads that microtubules experience during passive measurements, such as when using thermal fluctuations, access a different strain regime than microtubules that are subjected to active loads, such as those by optical traps.[313]

Motor-filament interactions. The traditional role of the motor-filament interaction is propulsion.[315] However, it has also been found that motor binding can induce large scale conformational changes within the microtubule lattice,[316] which in turn can influence processes such as microtubule wear and microtubule stability, and create feedback on propulsion velocity[241, 283, 317]and even motor binding itself. [318-320]

The repetitive forces exerted by motor proteins stepping on filaments can be expected to cause mechanical wear and fatigue as in macroscopic systems. The ensuing degradation of the filament can become a rate limiting factor for system lifetime; whereas the ability to control this process could allow the introduction of regulatory pathways similar to those of the depolymerizing motors kinesin-8[279, 321, 322] and kinesin-13.[323, 324]

The question whether the cyclical motion of kinesin motors along microtubules can cause degradation has been studied by Dumont et al.[325] . It was observed that the propulsion of taxol-

stabilized microtubules on high densities of kinesin motors (300-4000 μm^{-2}) causes gradual shortening of microtubules, which exceeded the stationary Taxol-stabilized microtubule shrinking rate by over two-fold. In addition, the shrinking rate was found to increase with velocity as well as motor density as the surface-bound motors transition from a "mushroom" to a tightly packed "brush" configuration.[326]

However, Reuther et al.[327] observed that the shrinking rate of stationary microtubules decreased with increasing kinesin density at low to intermediate densities (3-30 μm^{-2}), and that the shrinking rate of gliding microtubules at intermediate densities of kinesin (30 μm^{-2}) was similar to that of stationary microtubules at low kinesin density.[327] This suggests that kinesin binding stabilizes microtubule ends against polymerization. Microtubules not stabilized with taxol have also been found to depolymerize slower in the presence of ATP and kinesin.[316]

The observations of gliding microtubules on surfaces coated with high densities of kinesin motors using high speed atomic force microscopy by Jannat Keya et al. revealed that the shrinking associated with gliding is not caused by depolymerization (which kinesin motors protect against as Reuther et al. have shown) but by forceful removal of protofilament segments from the tip of the gliding microtubules by slow or inactive kinesin motors.[328] A similar observation of microtubules splitting into protofilament bundles was observed by VanDelinder et al.[329]

Motor binding to microtubules has been shown to exhibit cooperative behavior, where the binding of one motor increases the binding rate for the next motor.[319, 320] At the same time, crowding of motors on microtubules can lower individual motor processivity; Telley et al.[330] found that mGFP-labeled kinesin motors tend to detach prematurely from microtubules upon

encountering rigor kinesin mutant roadblocks. Furthermore, experiments by Leduc et al. demonstrated that traffic jams in motor transport along microtubules were caused by two factors: motor density surpassing a critical threshold and slow dissociation of motors from microtubule ends.[279] Another mode for negative interference between microtubule-bound kinesin is only observed in systems with the inverted motility configuration. It has been found that tight mechanical coupling between motors with shortened stalks can play a significant role in decreasing the velocity of gliding microtubules.[317] If the microtubule-motor bond is especially taught, then the stepping cycle of a motor can be affected as it pushes against all other motors bound to a microtubule. These effects were observed by Bieling et al.[317] with a kinesin-1 construct consisting of the first 401 amino-terminal amino acids at densities ranging from 100 to 10000 μm^{-2}. These results were confirmed by Inoue et al.[241], who demonstrated that microtubules propelled by similarly short GFP-fused kinesin-1 motors consisting of the first 560 amino acids of human kinesin-1 achieved a maximum velocity at a motor surface density of 112 μm^{-2}.

Filament-filament interactions. Systems of active nanoscale filaments can be used to study self-assembly processes [152] and active matter.[210] The key ingredient to these studies is the incorporation of interactions between individual gliding filaments. In typical systems with the inverted motility configuration, there are no interactions; whenever gliding filaments collide, they cross over (or under) each other with no measurable change in gliding direction.[194] The introduction of inter-filament interactions usually manifests itself in higher frequencies of filament alignment during collisions. Strong interactions may be introduced in systems of gliding microtubules by incorporating biotin-streptavidin cross links,[204] or in systems of gliding

actin filaments by incorporating facsin.[208] Weaker interactions can be generated by depletion forces, induced by crowding agents such as methylcellulose or Pluronic F127.[213, 214, 233, 331, 332] Dynein motors and truncated kinesin motors can induce a strong enough filament-surface bond to prevent filament crossovers during collisions due to steric effects.[333, 334] A new approach for the self-assembly of strong microtubule-surface bonds through mutualistic interactions of microtubules and kinesins will be demonstrated in the Chapter 6.

Filament-cargo interactions. Cargo can be attached to filaments by functionalizing individual subunits of the filament.[291, 335] The simplest approach is to use sticky biotin/streptavidin bonds[335] and optimize the interaction time[336] and binding site density.[337] However, the high strength of this bond limits applications where cargo must be repeatedly dropped off or picked up. Alternative approaches include DNA functionalization,[197] antibodies,[338] and others.[339-341] A complication that can arise is that the introduction of cargo binding sites on a propelled filament may create roadblocks for motor binding.[342, 343] Somewhat surprisingly, supertwist in microtubules, which causes rotation of the microtubule, has been found to not have an effect on cargo transport reliability.[198]

Motor-surface interactions. In a traditional inverted motility assay, molecular motors are irreversibly bound to the surface. Motor immobilization on surfaces can be achieved using a variety of routes, including through the use of casein coatings which help the binding of kinesin motors in the proper orientation,[344, 345] and through the use of antibody coatings[346] that bind specific domains on the motor. In this respect, an interesting distinction between the kinesin-1

and myosin-II inverted motility assays is that kinesin motors preferentially bind hydrophilic surfaces,[347, 348] while myosin motors preferentially bind hydrophobic surfaces.[347, 349-351] Reviews on the interactions between motors and surfaces have been published by Fischer and Hess,[352] and Månsson et al.[353]

A disadvantage of systems where motors are irreversibly immobilized on a surface is that a large fraction of the motors does not participate in the propulsion of the sparsely distributed filaments. In addition, defective motors can cause microtubules to become attached, exhibit a fish-tailing behavior,[204, 354] and break. To combat these concerns, our lab recently developed a new method which reengineers the surface-motor bond by coating the surface with a nitrilotriacetic acid (NTA)-functionalized polymer which can reversibly bind hexahistidine (His_6) groups via a chelated nickel ion. The introduction of this weak His_6-Ni^{2+}-NTA bond resulted in the kinesin existing in an equilibrium between a surface-bound and free-in-solution state. Gliding microtubules were observed to have a tolerance to defective motors, with fish-tailing events never occurring.[43] Another instance of a reversible surface-kinesin bond was recently demonstrated, where motors would only bind to the surface in the presence of light,[234] allowing for the controlled landing of microtubules.

Implementations of active nanosystems

The majority of active nanosystems are based on inverted motility systems, where filaments glide upon surface-immobilized motors. In this section, we will give an overview of applications of these systems toward cargo delivery, sensing, control, and higher order structure generation. We will additionally cover how the system lifetime can be extended.

Delivering cargo in active nanosystems. Molecular motors transport cargo in cells. Similarly, a large portion of the scientific literature studying active nanosystems has focused on developing novel methods for cargo delivery. The types of cargo that have been transported include molecules,[216, 355] quantum dots,[196, 356, 357] microspheres,[237, 336] metal-organic frameworks,[358] catalysts,[359] nucleic acids,[219, 360] viruses,[361] and gold nanoparticles.[362, 363]

There have been several proof of concept demonstrations of cargo transport using molecular motors. In one of the first of such demonstrations, researchers stretched DNA molecules tethered to microtubules by biotin-streptavidin bonds.[360] In later studies, researchers focused on expanding the variety of cargo that could be delivered by engineering alternatives to the biotin-streptavidin filament-cargo tether. An "immunoassay on a filament" was implemented by functionalizing microtubules with antibodies; it was first used to detect tomato mosaic tobamoviruses,[361] and later, for multiplex sensing of the cytokines interleukin-2 and tumor necrosis factor alpha.[196]

Gold nanoparticles, fluorescent microspheres, and quantum dots can be used as model cargo to test system concepts. For example, gold nanoparticles conjugated to anti-biotin antibodies have been used as the model cargo for determining optimal conditions in a loading area of an active nanosystem,[363] where it is necessary that the cargo binds sufficiently strongly to the

"loading dock" so as to not diffuse away, but also weakly enough so that it could be pulled off by a gliding microtubule. In another study, the loading of fluorescent microspheres onto gliding filaments was observed to determine the optimal geometries for cargo loading.[336] Quantum dots loaded onto microtubules gliding on a kinesin-coated silicon surface were employed to study how the rotation of a microtubule about its central axis affects cargo retention.[246]

The next step involves both unloading and loading of cargo in the same system (Figure 5.3a).[362] In one study, quantum dots were used as model cargo in a demonstration of filament loading and unloading in solution.[197] In this system, microtubules were functionalized with a single stranded oligonucleotide, and cargo was bound to a complementary single stranded oligonucleotide. The cargo would bind to the filament by complementary base pairing as the loading phase. Then, restriction enzymes were employed to sever the microtubule-cargo bond as the unloading phase. Gold nanoparticles were used as model cargo to demonstrate spatial separation of cargo loading and unloading in an active device via the nonlinear characteristic of the force-unbinding rate curve of DNA oligonucleotides.[362] Later, pressure driven flow was combined with microtubule-drive motion to develop a device which allowed the sequential loading and unloading of molecular cargo.[364]

These concepts have been demonstrated with the actomyosin system as well.[365-367] Actin filaments gliding on myosin-coated surfaces have been observed to successfully transport liposomes,[368] microbeads,[369] quantum dots,[356] and more.[199, 370]

Sensing using active nanosystems. Filaments propelled by surface-adhered motors have been used to capture, tag, and aggregate molecular analyte for fluorescence detection, to explore the

surfaces they are moving on and report about their properties, and to exert forces to measure intermolecular interactions.

Biosensors. Motor-propelled filaments can selectively capture and move analytes and tags, and thereby replace wash steps in traditional assays.[216] For example, in the "double antibody sandwich" assay, two antibodies are chosen for a specific antigen; one antibody is conjugated to the gliding filament, and the other to a fluorescent marker. The conjugated filaments capture the antigen as they glide and then bind the second antibody and its marker. Gliding filaments with a high number of fluorescent markers indicate the presence of the analyte. This approach has been used to identify a variety of analytes, such as viruses,[361] cytokines,[196] staphylococcal enterotoxin B,[215] and even mercury ions.[220]

The dynamic properties of gliding filaments can be used as reporters for detection as well. Microtubule self-assembly has been used as a signal for the presence of leukemia microvesicles.[221] Recently, the landing rate and gliding dynamics of microtubules were suggested as parameters to evaluate the activity of isoforms of the microtubule associated protein Tau.[222] Similar studies have been employed in the actin-myosin motility assay to determine the effects of anti-F-actin antibodies, such as antigen-binding fragments of Immunoglobulin G, on smooth muscle function.[223]

Surface Characterization. Gliding filaments can sense surface obstacles and deformations. One of the first demonstrations of this used gliding microtubules to determine the positions of pillars on a surface. By observing the gliding of fluorescently-labeled microtubules on the surface and

summing the fluorescence of the images, researchers were able to create a topographic map of the surface (Figure 5.3b). [371] Gliding microtubules have also been used as probes for studying surface deformations.[241] It was found that microtubules gliding on surfaces coated with truncated kinesin motors would experience changes in velocity and direction as the surface was deformed (thus changing inter-motor distance). When depletion forces were introduced into this system, gliding microtubules were found to generate collective formations, such as streams, diamonds, and more.[372] Another study used microtubules labeled with quantum dots to map out the positions of 100 nm-wide nanoslits with 5 nm precision.[373]

Force measurements. Microtubules bend in response to external loads. By knowing the bending mechanics of a microtubule, one can extrapolate the force the filament is experiencing. This has been done to study the rupture force of the biotin-streptavidin interaction. In this experiment, the deflection of a stationary, cantilevered, biotinylated microtubule was measured in response to binding a streptavidin-coated bead which was being transported by a gliding microtubule. The measured deflection was then used to derive the force acting upon the microtubule. A particular advantage is of this approach is that, unlike traditional methods for studying molecular-scale forces, such as optical tweezers and AFM, these cantileverd microtubule allow the monitoring of several unbinding events in parallel.[374]

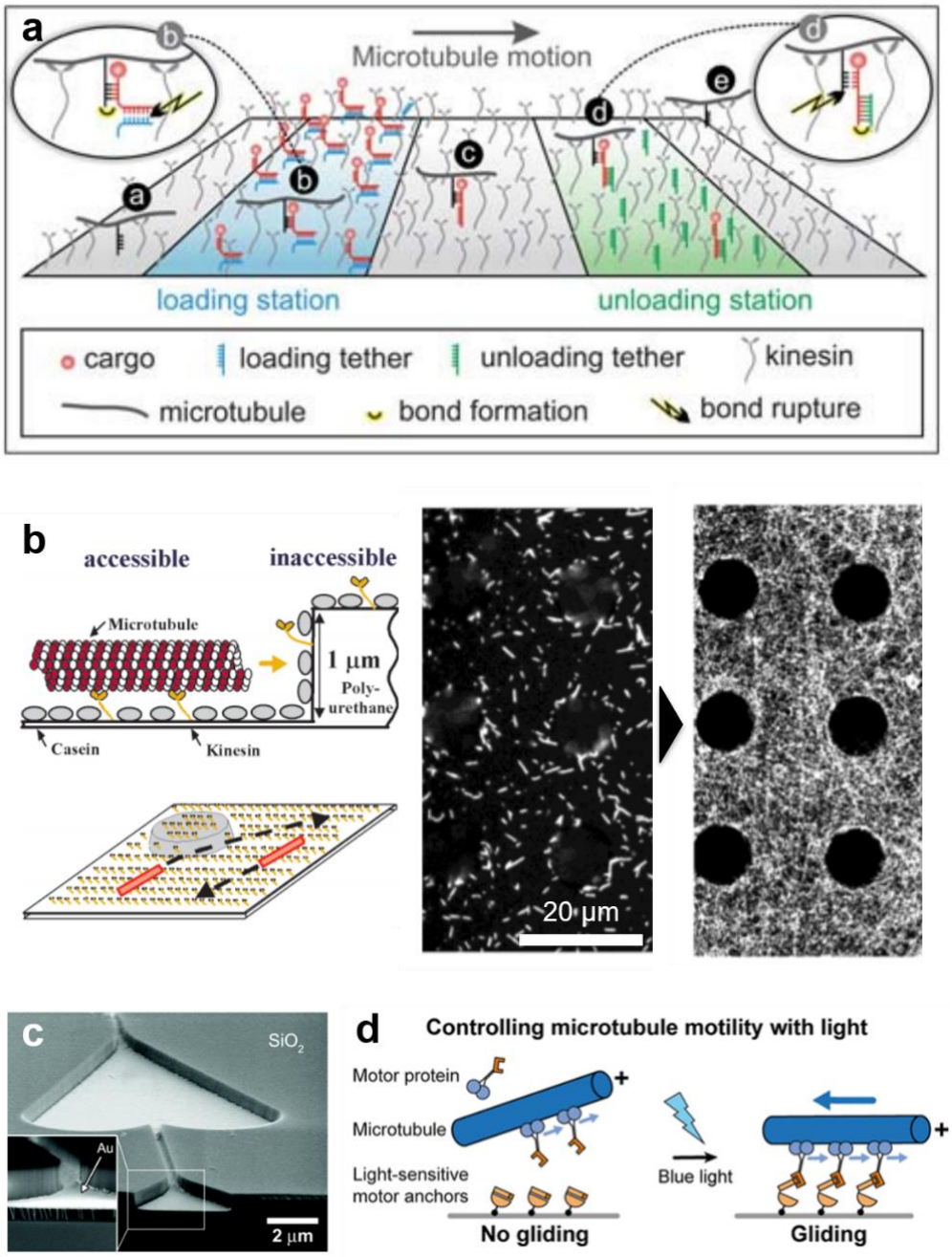

Figure 5.3: Implementations of active nanoscale systems based on cytoskeletal filaments propelled by surface-adhered motor proteins. (A) Spatial separation of microtubule loading, transportation, and unloading. Loading and unloading are achieved by using specialized oligonucleotides as tethers. The increasing bond strength from loading station over the microtubule to the unloading station enables loading and unloading. Adapted from Schmidt and

Vogel.[362] (B) The motion of fluorescently labeled microtubules on a kinesin coated surface in the presence of pillars is imaged to generate a map of the surface. Since the probability that a particular pixel has not been visited falls exponentially with time, this provides a "Monte Carlo"-type surface characterization procedure. Adapted from Hess et al.[371] (C) Microfabricated rectifiers in arrow/spade-like shapes rectify filament motion, allowing for work extraction from streams of unidirectionally gliding filaments. Filaments entering from the bottom of the arrow will funnel into the top. Filaments entering from the top of the arrow will run into the wall and be redirected. Adapted from van den Heuvel.[375] (D) Optical control of kinesin surface binding. Exposure to blue light switches the affinity of anchor molecules, so kinesin motors accumulate on the surface. This in turn causes accumulation of microtubules on the surface. Adapted from Tas et al.[234]

Controlling the behavior of active nanosystems. The function of active nanosystems may be guided by either passive or active control. Passive control introduces guidance into the system during fabrication, an example of this are guiding structures defined by lithographic techniques.[376-378] Active control, on the other hand, requires energy input during system function in the form of light,[379] electric fields,[380] magnetic fields,[239] or heat [241, 242].

Passive Control. Passive control is used to arrange filaments into work producing configurations[381] and to guide filaments for transport. This is usually done by micropatterning the surface. In the first approaches, myosin-coated elevated platforms of PTFE[382] and PMMA[383] were used to guide gliding actin filaments. However, there were two problems. First, there were no walls: filaments would gradually leave the elevated platform. Second, there was no directional control on the movement of filaments. These two problems were addressed by Hiratsuka et al.[381] by (1) replacing elevated tracks with guiding channels and (2) including rectifiers: arrow-like shapes[236] which would reorient filaments gliding in undesirable directions (Figure 5.3c). Later, modeling[384-387] and experimental studies revealed how channel width and filament persistence length relate to give optimal guidance properties to channels. Photolithographic techniques have been developed to create "overhangs" which prevent the filaments from leaving the channel.[200, 388] Alternative approaches to filament guidance include direct motor patterning in specific configurations,[389, 390] by patterning hydrophilicity,[212], PEG coatings,[391], polyNIPAM coatings,[392] UV-laser ablation,[393] and inducing photodestruction of binding sites.[235]

Active Control. Active control can be exerted over an active nanosytem through the use of light, heat, electric fields, and magnetic fields.

The first demonstration of light-mediated control of active filaments was the use of caged ATP molecules, which are photolyzed by UV light to release ATP.[237] Since then, researchers have succeeded in generating light-activated inhibitors and ATP analogs to control the function of kinesin motors.[238, 394-398] More recently, light-mediated control has been expanded beyond kinesin ATPase activity. Light-sensitive azobenzene molecules were used to control self-assembly of microtubules functionalized with DNA oligonucleotides.[211] Kinesin motors functionalized with a light-sensitive peptide were demonstrated to have controllable, light-mediated surface binding (Figure 5.3d).[234]

The controlled delivery of heat can alter the temperature of the entire device and thereby control the activity of the motor proteins[399] or it can alter the temperature of specific surface regions coated with thermoresponsive polymers which expand or collapse in response to temperature changes.[242, 400] Microtubule gliding can be gated by coating a thermo-responsive polymer onto a gold channel and transiently heating it with an electrical current to induce collapse of the polymer and permit the passage of the microtubule.[401]

The use of electric fields to control the motion of active filaments is motivated by the negative charge of microtubules, which can be as high as 48 electrons per tubulin heterodimer based on x-ray crystallography structural data[402, 403] although estimates from experiments have provided lower numbers.[380, 404] Electric fields have been used to steer and sort microtubules gliding on a kinesin coated surface,[240, 380, 405] attract microtubules to an oppositely charged surface,[406] control microtubule velocity,[407] and study the electrochemical properties of

microtubules.[404, 408] However, a drawback of using DC electric fields is that they leads to electrolysis, forming bubbles and potentially damaging both electrodes and microtubules.[408]

Magnetic fields have been used to steer gliding microtubules.[239] While the polar structure of microtubules does provide diamagnetic anisotropy to microtubules,[409] it has been observed that it takes 4-11 Tesla magnetic fields to orient microtubules.[410] Since such strong magnetic fields are not suitable for typical laboratory settings, magnetic guidance of microtubules is achieved by functionalizing microtubules with magnetic nanoparticles, such as magnetic quantum dots[411, 412] or $CoFe_2O_4$ particles.[239, 413] The advantage of magnetic fields over electric fields is that they do not create the problems associated with electrolysis and electroosmotic flow.

Higher-order structure generation. Microtubules and actin filaments are already self-assembled out-of-equilibrium structures,[42] but the addition of motors further enriches the dynamics of the system.[229] While weak and transient interactions lead to self-organization of the motor-filament system into transient structures dependent on a continuous flow of energy, strong interactions can cause "active self-assembly",[157] where emergent structures persist in the absence of motor-generated forces but dynamically assemble and disassemble when motors are activated. This is demonstrated by a system of biotinylated microtubules partially coated with streptavidin gliding on a kinesin-coated surface, where the strong biotin-streptavidin interactions between gliding microtubules lead to the formation of wires and spools (Figure 5.4a).[152] In an effort to make systems more dynamic, researchers experimented with weakening these inter-filament bonds. By the incorporation of depletion forces via addition of crowding agents such as methylcellulose[213, 331] PEG,[224] and Pluronic F127,[233] filaments were shown to form streams and bundles. The additional incorporation of mechanical forces led to the formation of diamond-like

formations (Figure 5.4b).[372] High densities of microtubules gliding on dynein motors interacted to form large scale vortex lattices.[333, 414] Recently, it was demonstrated that light activated bonds between filaments could be used to form streams and spools of filaments on demand by UV illumination.[211] Our lab recently demonstrated that kinesin motors can be self-assembled by gliding microtubules when the kinesin-surface bond is weakened (Figure 5.4c).[43, 44] In Chapter 6, we will demonstrate how mutualistic interactions between mobile kinesin motors and gliding microtubules can generate strong microtubule-surface bonds and form collective behavior.

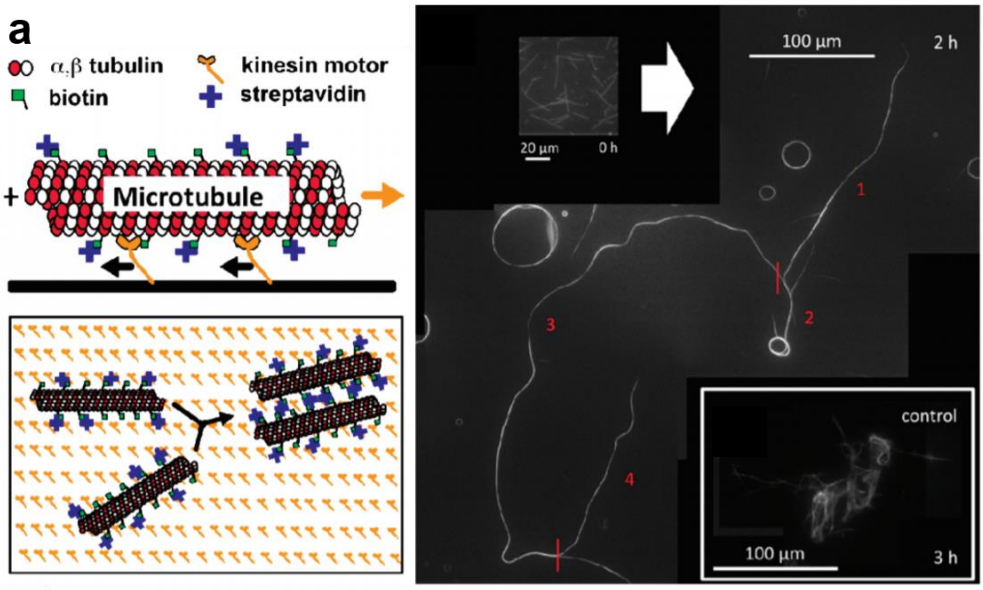
a
α,β tubulin
kinesin motor
biotin
streptavidin
Microtubule
100 µm
2 h
20 µm
0 h
1
2
3
4
control
100 µm
3 h

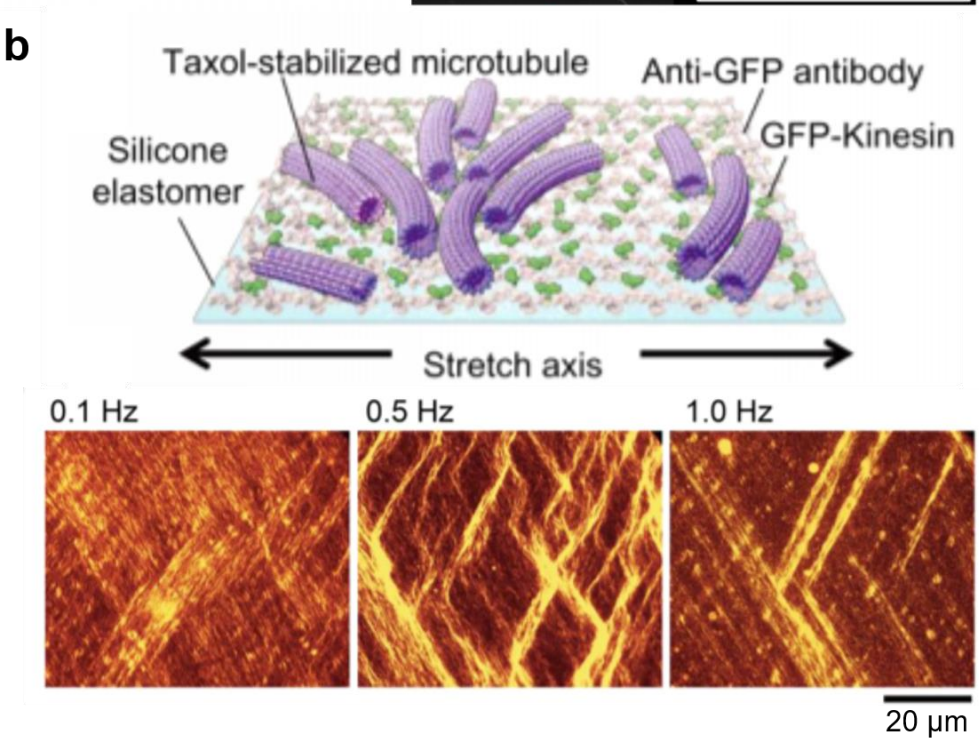
b
Taxol-stabilized microtubule
Anti-GFP antibody
GFP-Kinesin
Silicone elastomer
Stretch axis
0.1 Hz
0.5 Hz
1.0 Hz
20 µm

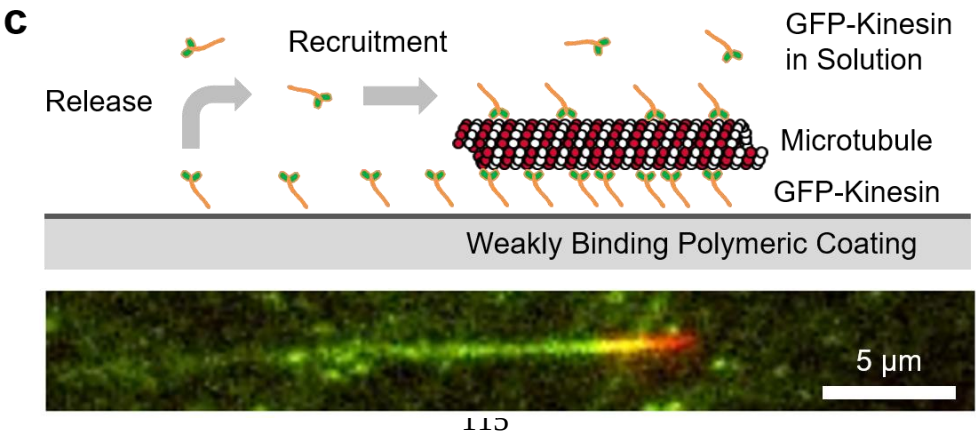
c
Recruitment
GFP-Kinesin in Solution
Release
Microtubule
GFP-Kinesin
Weakly Binding Polymeric Coating
5 µm

Figure 5.4: Self Assembly in active nanoscale systems. (A) Self-assembly in the presence of strong interactions. Biotin-functionalized microtubules gliding on a kinesin-coated surface in the presence of streptavidin stick together when they collide with one another. However, instead of forming disorganized aggregates as would be expected for purely diffusive systems, these sticky gliding microtubules form wires and spools. Adapted from Idan et al. [207] (B) Self-organization in response to dynamic boundary conditions. Microtubules gliding in the presence of methylcellulose-induced depletion forces on a kinesin coated silicone elastomer which is contracting and expanding at different rates self-assemble into dynamic diamond-like structures. Adapted from Inoue et al.[372] (C) Weakly surface-bound kinesin motors propel a microtubule. GFP-tagged kinesin motors weakly bind a polymer-coated surface via a His_6-Ni^{2+}-NTA bond. As a result, motors exist in an equilibrium between a surface-bound and in-solution state. Gliding microtubules assemble kinesin motors from solution and place them on the surface, using the motors to propel themselves forward. Motors used to propel the microtubule remain behind in a temporary wake, until they unbind back into solution. This can be observed under TIRF microscopy, where a line of kinesin motors (green) is seen left behind by the gliding microtubule (red). Adapted from Lam et al.[43]

Active nanosystems employing the native motility configuration. Studies involving the native motility configuration have been instrumental in developing the understanding of how molecular motors interact with filaments. In addition, there are several examples of how active nanosystems can be built where the molecular motor is the motile element, similar to the cell.

Biological Importance. Svoboda et al.[415-417] used the native motility configuration combined with an optical trap in order to demonstrate that kinesin-1 is a processive motor that takes discrete steps during its motion. Since then, optical trap configurations have been used to study several other processive motors, such as myosin-V[301] and dynein.[289] Recently, optical traps were used to demonstrate that kinesin motors rotate unidirectionally during stepping,[190] and to map out the two dimensional protofilament surface of a microtubule lattice by studying the 3D displacements of a kinesin motor walking along a microtubule.[265]

Active nanosystems. One of the most famous devices developed using the native motility configuration systems is the array of pixels developed by Aoyama et al.[201] In this work, microtubule seeds were anchored to the center of hexagonal chambers using photolithographic processes and a mutated T93N-kinesin. The seeds were then grown by further polymerization into aster-shaped arrays of unidirectional microtubules extending throughout the chamber. Then, dynein motors carrying pigment granules were flown into the chambers along with caged ATP, homogenously dispersing along the microtubules. Upon illumination by a light source releasing the caged ATP, the dynein motors would walk toward the minus end of the microtubules located at the center of the chamber. The increase in fluorescence at the center of the chamber enhances

the contrast against the background. Different images can be formed by selectively illuminating separate chambers. This work builds on the self-organized asters emerging from the interaction of multiheaded kinesin with microtubules in solution described by Nédélec et al., (Figure 5.5a).[229] Recent work has studied the programmability of the interplay between molecular motors, filaments, and DNA to self-assemble large scale structures for cargo loading/unloading[418] (Figure 5.5b). Multimeric kinesin motors cross-linking microtubule asters with DNA origami centers can also induce smooth muscle-like contractions in the presence of ATP.[419] Kinesin Eg5 (kinesin-5) motors mixed with microtubules were observed to create globally contractile networks under appropriate conditions.[281] These are important steps towards the construction of actuators powered by molecular motors.

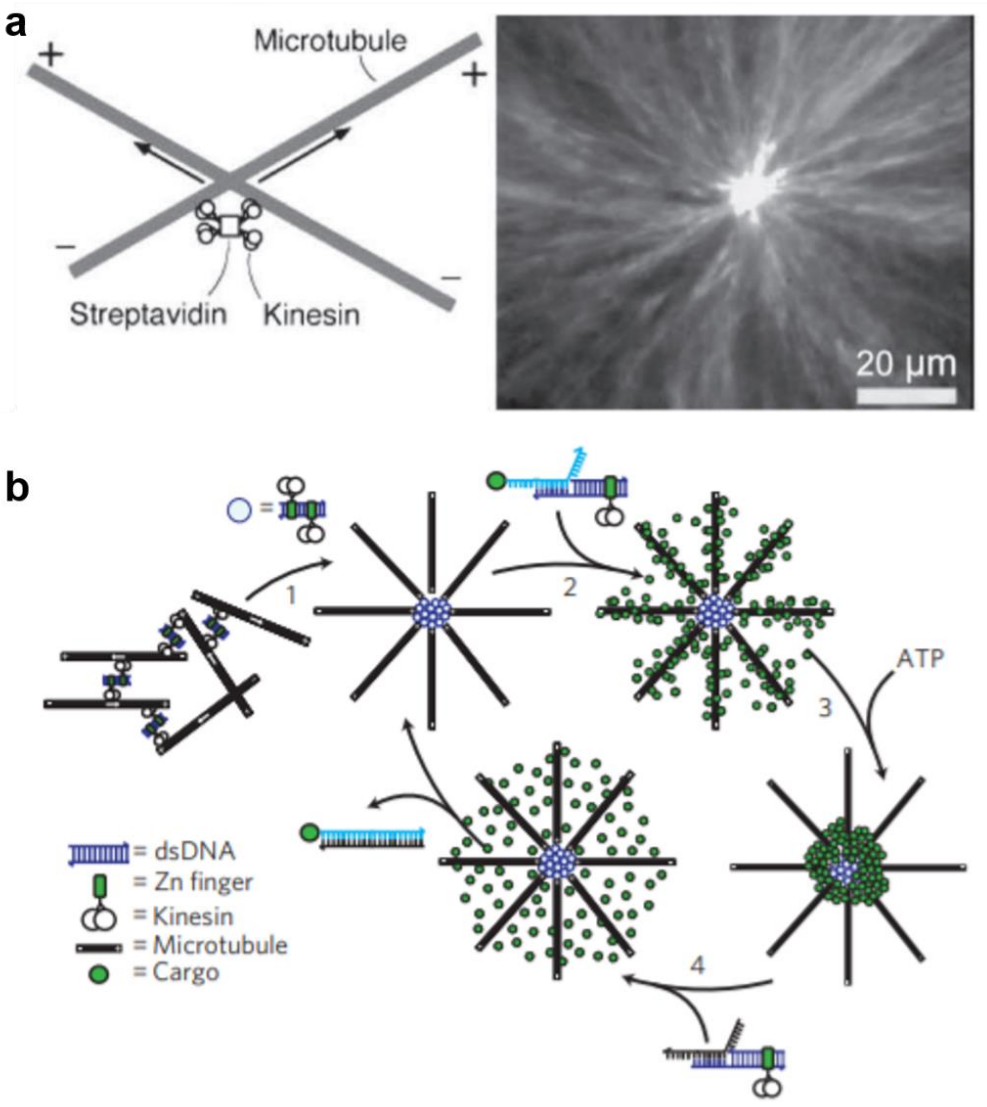

Figure 5.5: Active nanosystems in the native motor-on-filament configuration. (A) Solutions of tetrameric kinesin motors and microtubules form asters. The motion of kinesin molecules toward the plus end of microtubules combined with cross-linking of pairs of microtubules ensures that microtubules will become organized with the plus end at the center. Adapted from Nedelec et al.[229] (B) Zinc Finger and DNA bound tetrameric kinesin motors are used to assemble microtubule asters, and programmably load and unload cargo using DNA strand displacement reactions. Adapted from Wollman et al.[418]

Conclusion

The first motility assays demonstrating filament propulsion by surface-adhered motors were performed by Vale et al. in 1985[228] for the microtubule/kinesin system, and Kron and Spudich in 1986 [227] for the actomyosin system. 35 years later, scientists have developed dozens of techniques to design active nanosystems powered by motor proteins. Despite the remarkable progress, the functionality, complexity, and efficiency of these systems is still far from what they are in biological systems, such as the axons of nerve cells or sarcomeres of muscle cells.

However, the technological arc of history points towards an ever-increasing number of smaller and smaller devices, which require actuation all the way down to the molecular.[153] Hybrid nanosystems which utilize highly functional nanomachines perfected by evolution over billions of years, such as motor proteins, are promising contenders to fulfill this emerging need. At minimum, continued experimentation will clarify general challenges in molecular and nanoscale engineering of mechanically active structures. In the best case, we will demonstrate our understanding of biological design principles, by acquiring the ability to engineer man-made structures of comparable complexity, functionality, and beauty.

In this next chapter, we will build on the concepts of higher order structure generation and inter-filament interactions introduced in this chapter to demonstrate how mutualistically interacting gliding microtubules and mobile kinesin motors can generate collective behavior.

Chapter 6. Kinesin-Recruiting Microtubules Exhibit Collective Gliding Motion While Forming Motor Trails

This section follows "*Kinesin-Recruiting Microtubules Exhibit Collective Gliding Motion While Forming Motor Trails," by Stanislav Tsitkov, Yuchen Song, Juan B. Rodriguez III, Yifei Zhang, and Henry Hess. (Under Review).*

Introduction

Swarming organisms, such as flocks of birds, schools of fish, and tuxedos of penguins self-organize and respond to environmental stimuli through inter-agent interactions[420-426]. Advances in robotic technology[427-429] and synthetic biology[430-435] create a need for a fundamental understanding of how collective behaviors emerge as a function of the actions and interactions of individual agents; it would allow for better design in applications ranging from drug delivery by colonies of magneto-tactic bacteria, over directing traffic flow of fleets of self-driving cars, to aerial control of gaggles of drones[435-438]. Systems of active nanoscale filaments, such as functionalized microtubules propelled by surface-adhered kinesin motor proteins[162, 181, 237, 240, 357, 361, 363, 374, 439], are excellent testbeds for analyzing how simple interactions between agents result in dynamic self-assembly and collective behaviors.[204, 207-209, 211-214, 224, 232, 331, 334, 440, 441] One of the first systems described consisted of biotinylated microtubules gliding on a kinesin-1 motor protein-coated surface, which cross-link *via* biotin-streptavidin bonds and form spools and wires.[152, 204, 230, 442] Under optimal conditions nearly millimeter-long wires can form.[207] Microtubules gliding

on kinesin motors in the presence of weaker, depletion force-induced interactions have been shown to form nematically organized streams.[211-213, 331, 441] Microtubules gliding on truncated kinesin motors in the absence of depletion forces exhibited collective behavior dependent on kinesin surface density; these behaviors varied from long range order at low kinesin densities to clustering at high kinesin densities.[334] Actin filaments gliding on myosin motors in the presence of depletion forces have been demonstrated to form streams and density waves, and have been used to test theories of active matter.[208, 224, 440, 443] Microtubules gliding on dynein-coated surfaces have been found to nematically align upon collisions, resulting in the formation of large vortices.[209]

These nanorobotic and active matter systems are constructed in a way that prevents the utilization of a large portion of the available components: the majority of the biomolecular motors attached to the surface are idly standing by, rather than actively propelling filaments. If motors could co-localize with cytoskeletal filaments, the utilization of system components and other benefits arising from motor-filament interactions, such as enhanced filament stability,[316, 327] would be maximized. Such a mutualistic interaction[444] between motors and filaments would be reminiscent of how the spread of fruit seeds by elephants leads to the growth of fruit-bearing trees along their paths.[445-447] Our goal was to engineer such a mutualistic interaction in the microtubule-kinesin system (Figure 6.1a).

A first step towards that goal was to develop a system where motors could dynamically change their position, turning them into mobile agents. This was achieved in our previous work that described a system consisting of microtubules gliding on reversibly surface-adhered kinesins (Figure 6.1b).[43, 44] Reversibility arises from a weak interaction between kinesins and the surface *via* Ni-NTA – His-tag bonds (Figure 6.1b).[43] A microtubule gliding on the surface accumulates kinesin motors from solution, places them on the surface in a "trail" under itself, and uses them to

propel itself forward. After kinesins have reached the end of a microtubule they are left behind, and unbind from the surface within a minute. As such, kinesin motors undergo reversible transitions between four states: (1) diffusing in solution, (2) head-bound to a microtubule, (3) tail-bound to the surface, and (4) doubly-bound to both the microtubule and the surface (Figure 6.1c). The earlier experiments did not demonstrate collective behavior, due to low microtubule densities and weak interactions between microtubules. An important shortcoming of the system was that, due to the weak binding to the surface, 99% of the kinesin motors were diffusing in the solution without contributing to the generation of force.

Here, a new regime of this dynamic system is demonstrated, where the density of Ni-NTA binding sites on the surface is hundred-fold increased and the kinesin population is shifted towards the surface-bound states (states (2) and (4) in Figure 6.1c). In this regime gliding microtubules exhibit collective behavior by assembling into dense bundles (Figure 6.1d). Bundling arises from a higher microtubule density and a direct, steric interaction discouraging microtubules from crossing due to a strong, kinesin-mediated microtubule-surface interaction, similar to that observed by Tanida *et al.*[334] Kinesin motors are initially dispersed on the surface, but increasingly co-localize with the microtubule bundles. The resulting bundles provide not only a novel demonstration of mutualistic collective behavior in a system of two mobile agents, but also demonstrate the possibility of higher order self-assembly where both motors and filaments assemble hierarchically.

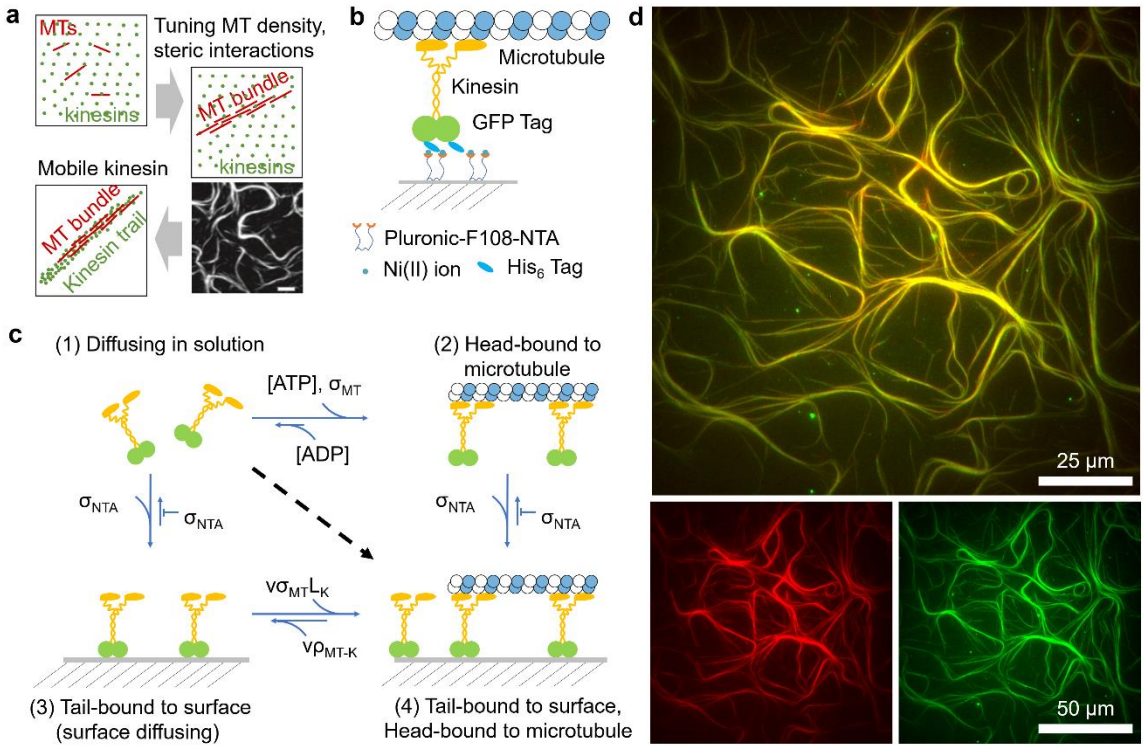

Figure 6.1. Studying collective behavior in the microtubule/kinesin system with reversible kinesin binding. (a) In the traditional microtubule-kinesin system, microtubules glide on surfaces uniformly coated with kinesin motors. By tuning the microtubule density and steric interactions, Tanida *et al.*[334] demonstrated that this system can be used to generate dense bundles (scale bar 20 μm). (Image adapted from Tanida et al. [334]). We engineer a system where kinesin motors dynamically reorganize to co-localize with microtubules. (b) Schematic of the kinesin-surface bond. In our dynamic system, kinesin motors labeled with green fluorescent protein (GFP-kinesin) and tagged with a His_6 tag reversibly bind to the Pluronic-F108-NTA coated surface *via* a weak, His_6-Ni-NTA bond. (c) Schematic of motor binding states. In our dynamic system, motors can access four states: diffusing in solution, head-bound to a microtubule, tail bound to the surface, and both head-bound to a microtubule and tail bound to the surface. The fluxes between these states strongly depend on ATP concentration ([ATP]), microtubule surface density (σ_{MT}), and kinesin surface binding site density (σ_{NTA}). The parameters L_K and $\rho_{MT\text{-}K}$ denote the reach length

of kinesin and kinesin linear density along the microtubule, respectively. (d) (Top) Composite images of HiLyte 670 microtubules (red) and GFP-kinesin motors (green) imaged using total internal reflection fluorescence (TIRF) microscopy. (Bottom) Individual channels showing the formation of bundles of HiLyte 670 microtubules (red) and trails of GFP-kinesin motors (green). Images taken 30 mins after the start of the experiment; the initial experimental conditions were 1 mM ATP, 25 nM GFP-Kinesin, and 16 μg/mL tubulin.

Results and Discussion

Dynamics of the kinesin-surface interaction in the absence of microtubules. Although stable microtubule gliding was achieved in the first demonstration of this dynamic system by Lam *et al.*[43], its analysis revealed that the interaction of GFP-kinesin motors with the surface was weaker than expected: the association constant of GFP-kinesin binding to the surface was 0.3 μm^{-2} nM^{-1}, which implied a Ni-NTA binding site surface density of 300 μm^{-2}, (based on the 1 μM dissociation constant for the NTA-His_6 bond accepted in literature[448, 449]) a value far below the maximum packing density of 62,500 μm^{-2} (considering a radius of gyration of about 2 nm for the Pluronic F108-NTA polymer). The presence of imperfections in the coating was further highlighted by high densities of non-specifically bound kinesin aggregates on the surface.

Here, the strength of the motor-surface interaction was increased by adopting a rigorous coverglass cleaning procedure, which included an acetone wash, a base etch, and a longer silanization step. Furthermore, in order to lessen the stripping of Ni(II) ions from the surface, dithiothreitol (DTT) was removed from the oxygen scavenging system, and the Ni(II) ion concentration in the 2 mg/mL Pluronic F108-NTA coating solution was increased from 50 mM $NiSO_4$ to 500 mM $NiSO_4$. The removal of DTT did not appear to have a significant effect on

photobleaching. The implementation of this cleaning procedure changed the dynamics of the interaction of GFP-kinesin with the Pluronic F108-NTA-coated surface.

The kinesin-surface interaction was characterized in experiments where kinesin motors interacted with the surfaces in the flow cell in the absence of microtubules (Figure 6.2a). Single molecule imaging of picomolar quantities of GFP-kinesins interacting with the surface were used to calibrate the fluorescence signal as a function of microscope, and camera settings and exposure time (Appendix Section D.1).

The surface density of kinesin motors changed with time, increasing from 0 μm^{-2} to 1200 μm^{-2} within the first 500 seconds of the experiment and then falling to 500 μm^{-2} within the next 1,500 seconds (Figure 2a-c). The slow rise in surface density can be attributed to the diffusion-limited landing rate of motors on the surface; the subsequent depletion of motors from the surface can be explained by the stripping of nickel ions from the surface by ethylene glycol tetraacetic acid (EGTA) molecules in the BRB80 buffer (Figure 6.2b-c). Two different models incorporating mass transport-limited surface kinetics were used to fit the data: a two-compartment model which is commonly used to analyze data from signal plasmon resonance (SPR) experiments for binding kinetics,[450, 451] and a landing rate model approximating the diffusion equation with reversible surface binding[452] (Appendix Section D.2).

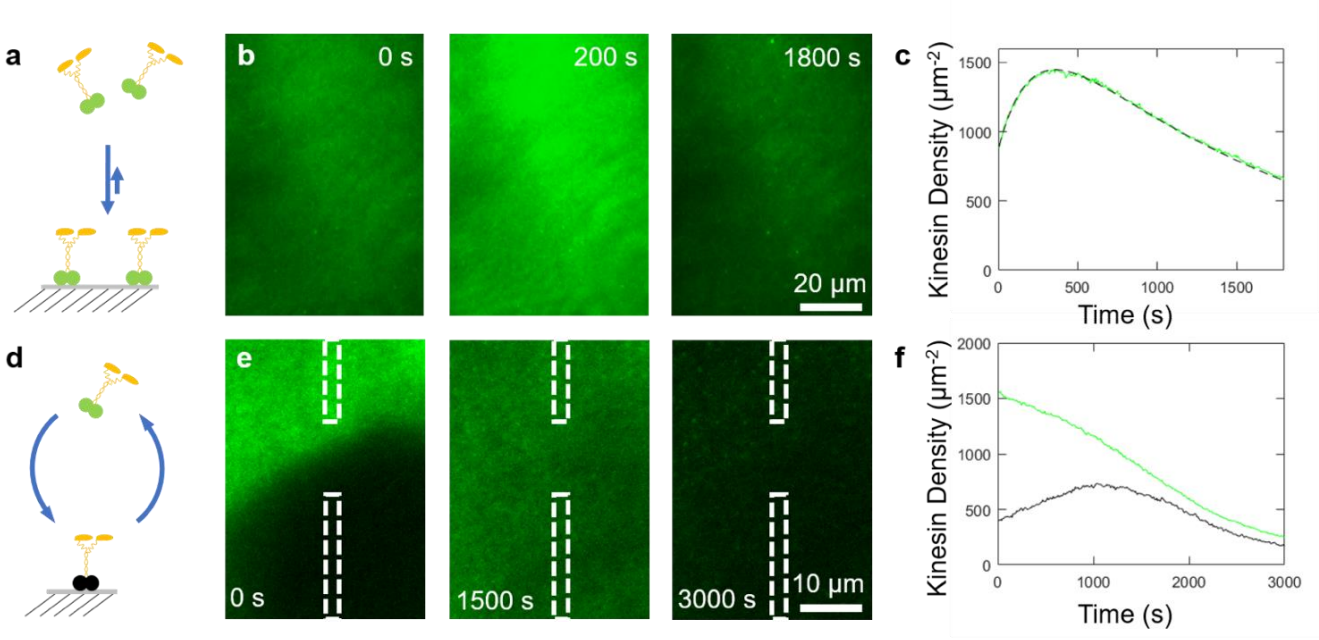

Figure 6.2. The kinesin-surface interaction via the NTA-His6 bond is dynamic even in the absence of microtubules. (a) The binding of GFP-kinesin motors to the surface is observed *via* fluorescence imaging with TIRF illumination. (b) Images of the surface at identical contrast settings taken at 0 s, 200 s, and 1800 s after the beginning of the experiment show a clear peak in fluorescence near 200 s. (c) Average kinesin density over time (green) fit with a two-compartment model (black, dashed) describing mass-transfer limited adsorption of kinesin motors to the surface. Details on the calibration can be found in Appendix Section D.1. (d) In a Fluorescence Recovery After Photobleaching (FRAP) experiment a region of the field of view is photobleached, and the recovery of fluorescence in the bleached region is observed and compared to that of a nearby unbleached region. (e) Images taken 0 s, 1500 s, and 3000 s after photobleaching, and (f) profile of fluorescence of unbleached area (green) and bleached area (black) obtained from the indicated areas as described in Appendix Section D.4.

While the models have different forms, they arrive at similar conclusions: The association constant for the motor-surface interaction is between 60-100 μm^{-2} nM^{-1}, which implies a Ni-NTA surface density of 60,000-100,00 μm^{-2} (based on the accepted K_D of 1 μM for the NTA-His_6 interaction), a value which is much closer to the packing density and compares well to SPR measurements of the Pluronic-F108 coating density on a gold surface of 58,000 μm^{-2}.[453] The rate constant for the decrease of the motor surface density at the longer time scale (>500 s) is $6 \cdot 10^{-4}$ s^{-1}, presumably due to the stripping of Ni(II) ions from the surface by the 2 mM EGTA (a chelator for divalent ions) in the BRB80 buffer. This stripping rate is comparable to the $1.7 \cdot 10^{-4}$ s^{-1} rate found by Nieba *et al.*[448] for His-tagged streptavidin leaving a Ni-NTA Bioacore surface in the presence of 300 μM EDTA and the $3 \cdot 10^{-4}$ s^{-1} stripping rate for hexahistidine peptides leaving a Ni-NTA coated surface in the experiments of Knecht *et al.*[449] Nickel ion stripping was also observed in a similar assay examining microtubule gliding on a tris-NTA coated surface by Bhagawati *et al.*[235] We ensured that the fall in fluorescence was not due to photobleaching by observing that unexposed regions of the surface 200 μm away had similar fluorescence. The surface density of motors stopped falling after 5000 s (Appendix Section D.3), at which point it reaches a steady state value of 180 ± 40 μm^{-2} (N=7, Standard Error).

To ensure that the reversible binding of the motors was still operational while the motor density was falling, a fluorescence recovery after photobleaching (FRAP) experiment (Figure 6.2d-f) was performed. The recovery of fluorescence in the bleached area was compared to that of an unbleached area 20 μm away. It was found that while the fluorescence of the unbleached portion of the surface was steadily falling, the fluorescence of the bleached area initially increased, and then fell to match the diminishing intensity of the unbleached area. The ability of the surface to

recover fluorescence after photobleaching indicates that the surface-kinesin interaction remains specific and reversible.

The unbinding rate of the kinesin from the surface was determined by single molecule imaging of individual GFP-kinesins landing and leaving the surface (Appendix Section D.5). 90% of the binding events identified by the tracking program had off-rates greater that 0.12 s^{-1}. This could correspond to the His_6-Tag-mono-NTA off rate constant of 1.8 s^{-1} found be Lata *et al.*[454]; however, the accuracy of this estimate is limited by the minimum 0.5 s exposure time necessary to image the single fluorophore and also limited by the false-positive rate of the automation of the tracking program. 10% of tracked kinesin motors unbind from the surface with an off rate of 0.024 s^{-1}, which is in excellent agreement with the experimentally determined off-rate for His_6-Tag-bis-NTA binding of 0.022 s^{-1} found by Lata *et al.*[454]

An additional interesting behavior observed in these single molecule experiments was the surface diffusion of individual motors (Appendix Section D.5). By fitting their mean square displacement (MSD) with $MSD = 4D\Delta t + c$, it was found that GFP-kinesins had a surface diffusion coefficient of $(1.70 \pm 0.02) \cdot 10^{-3}$ μm^2 s^{-1}, which is remarkable because a surface density of binding sites on the order of 60,000 μm^{-2} and an off rate as high as 1.8 s^{-1} would imply a surface diffusion coefficient of $3 \cdot 10^{-5}$ $\mu m^2/s$, suggesting that the movement of individual fluorophores is due to either displacement reactions or crawling mechanisms.[455, 456]

Dynamics of microtubule motility. In pursuit of our goal to enhance microtubule interactions as they are propelled by the kinesin on the surface, we increased the microtubule surface density five-fold relative to Lam *et al.*[43] to 14,000 mm^{-2}. The microtubules had an average length of 21 ± 1 μm and were gliding in the presence of 25 nM GFP-kinesin and an initial ATP concentration of 1

mM (initial velocity: 610 ± 10 nm/s). The microtubule density was chosen such that the rate of collisions between microtubules (proportional to the microtubule density σ, length l, and velocity v: $k_{interaction} \sim \sigma l v$) was roughly an order of magnitude larger than the rate at which a gliding microtubule loses directional information (proportional to velocity and inversely proportional to a trajectory persistence length L_P: $k_{persistence} \sim v/L_P$). This gives a critical density of $\sigma_{crit} \approx 1/L_P l = 500\, mm^{-2}$ for 20 μm-long microtubules with a trajectory persistence length of 100 μm.[385] The microtubules surface density used by us is similar to the 50,000 mm^{-2} used to form vortex lattices on dynein-coated surfaces[209] and an order of magnitude smaller than the 280,000 mm^{-2} critical density determined for microtubules gliding in the presence of methylcellulose-induced depletion forces to demonstrate ordered behavior.[213]

Under these conditions, we observe microtubule bundle assembly driven by the nematic alignment of microtubules upon collisions (Figure 1d). However, due to the rapid conversion of ATP by the 25 nM kinesin (at a rate of up to 2 μM/s), the gliding velocity begins to fall within the first 10 min of the experiment. We therefore increased the initial ATP concentration to 10 mM and imaged the dynamics over the course of 2 hours, during which the microtubule velocity had fallen from an initial 720 ± 20 nm/s down to 16 ± 1 nm/s. During this time period, gliding microtubules formed bundles and kinesin motors were redistributed from the surface to the microtubules (Figure 3a). This redistribution of kinesin can be observed in the composite images of the microtubule and kinesin channels. In these images, the color of individual microtubules changes from red at time t = 0 s to yellow at t = 7000 s. At the same time, the green background of kinesin fluorescence vanishes.

The temporal evolution of the distribution of kinesin and microtubules on the surface was quantified by recording the pixel-wise mean and variance of the flattened images of the

microtubule and kinesin channels. The means of both channels remain roughly constant over time, indicating that the numbers of microtubules and kinesins remain constant (Appendix Section D.6). However, the ratio of variance to mean (Figure 6.3b) – often employed as a measure of swarming[457] – shows a noticeable increase after 1 h. This increase is more striking in the green channel, as motors transition from being homogenously distributed across the surface to being concentrated along the microtubules. The transition is less apparent in the microtubule channel because even the initial, disordered distribution of microtubules has a high variance due to their rod-like shape. By fitting the pixel-wise green channel fluorescence as a linear function of the pixel-wise red channel fluorescence, it is possible to decompose the fluorescence of the green channel into a background and microtubule-bound component (Figure 6.3c). The rate constant for background depletion is $2 \cdot 10^{-4}$ s^{-1}, similar to the $6 \cdot 10^{-4}$ s^{-1} stripping rate constant found for kinesin leaving the surface in the microtubule-free assay described in the previous section, suggesting that as the kinesin is finding fewer binding sites on the surface, it accumulates on the microtubules.

The temporal evolution of the velocity of the microtubules is shown in Figure 6.3d, where the average velocity of 10 microtubules was recorded every 100 frames and fit with a model accounting for the Michaelis-Menten dependence of kinesin activity on ATP concentration and the resulting ATP depletion. The fit parameters were a K_M of 1.8 mM, a v_{max} of 920 nm/s, and an active kinesin concentration of 24 nM. The high K_M value originates from the accumulation of ADP and P_i in the solution as a result of ATP hydrolysis, because ADP acts as an inhibitor.[458] Microtubule velocity can also be affected by the mechanical coupling of surface-bound motors and crowding of motors along individual microtubules, which is not modeled here.[317, 459] The high concentration of active kinesin (95 % of all kinesins), demonstrates that almost all kinesins are

stepping on microtubules, because kinesin ATPase activity is dependent on microtubule binding.[460]

The drastic increase in microtubule bundling and kinesin colocalization with microtubules after one hour coincides with a significant decrease of the gliding velocity (Figure 6.3b,c). The decreasing kinesin velocity combined with a largely unchanged run length of the kinesin (Appendix Section D.7) yields a greatly reduced unbinding rate from the microtubule (as low as 0.009 s^{-1} based on a FRAP experiment). A decreasing unbinding rate from microtubules in turn stabilizes the kinesin population on the microtubules relative to the kinesin population on the surface.

The idea that longer-lasting kinesin-microtubule interactions are conducive to bundling is further supported by experiments with an additional 100 μM adenylyl-imidodiphosphate (AMP-PNP), which acts as a non-hydrolyzable analog of ATP and locks kinesin motors in the microtubule-binding ATP-bound state. This system demonstrated nematic alignment at the onset of the experiment but featured a noticeable increase in the number of spool-like bundles (Appendix Section D.8). Similar spool-like bundles have been observed by Tanida *et al.*[334] for microtubules gliding on high surface densities of kinesin, indicating that the AMP-PNP-induced spools we observe could be a consequence of a stronger microtubule-surface interaction mediated by kinesins.

The effects of varying the kinesin and microtubule concentrations are shown in Appendix Section D.9. Increasing the kinesin concentration from 25 nM to 75 nM did not have a significant effect on microtubule dynamics. However, decreasing the kinesin concentration to 3.1 nM prevented bundle formation and lowered microtubule surface-landing. Decreasing microtubule density two-fold and ten-fold resulted in less dense bundles.

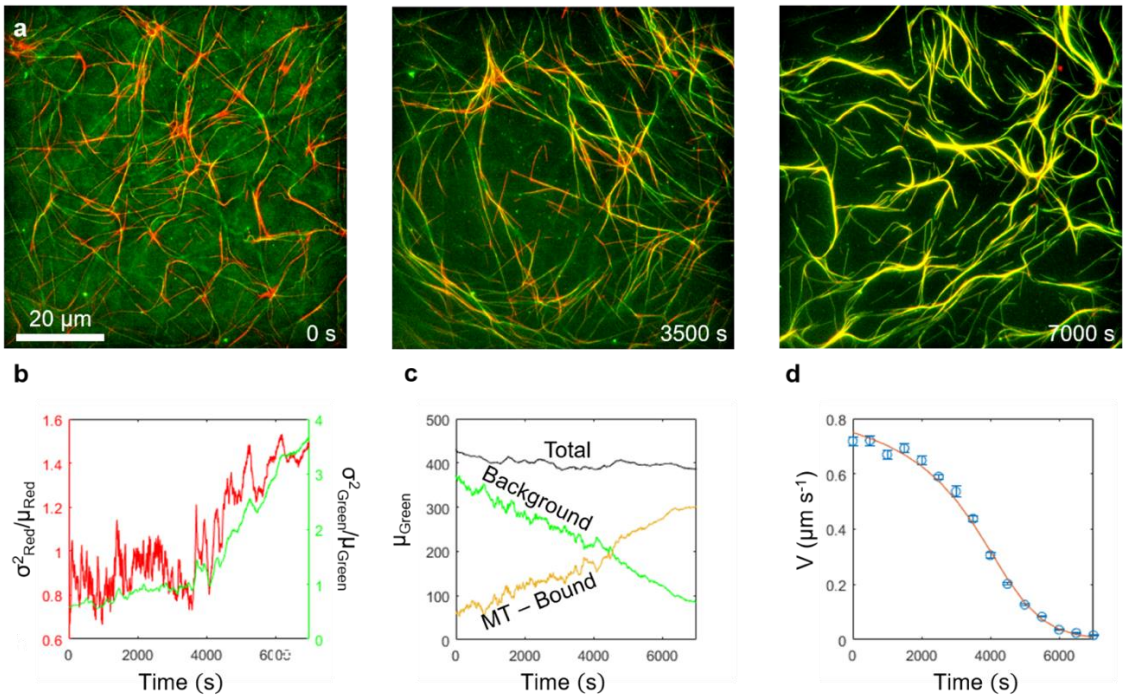

Figure 6.3. Microtubules assemble into bundles as GFP-kinesins assemble on microtubules. (a) Flattened composite images of microtubules gliding in the presence of an initial 10 mM ATP. (b-d) Analysis of flattened images in (a). (b) Ratio of pixel-wise variance to pixel-wise mean plotted against time. (c) Decomposition of mean green channel fluorescence into a background (green) and a microtubule-bound (orange) component, as determined by performing linear regression on green channel fluorescence as a function of red channel fluorescence. (d) Microtubule velocity with respect to time, fit with a function accounting for ATP-dependent velocity and velocity-dependent ATP depletion.

Collective microtubule behavior arises from nematic alignment. The emergence of collective behavior requires the presence of interactions between individual agents. In this system, the result of these interactions is the nematic alignment of microtubules upon collision (Figure 6.4a). The alignment is reversible, in that microtubules dissociate from bundles either mid bundle or at bundle turns (Figure 6.4b).

In previous studies of microtubules propelled by (permanently) surface-adhered full-length kinesins, a microtubule colliding with another microtubule usually passes either over or under it, likely as a result of height fluctuations of the advancing microtubule tip[194, 461]. In studies demonstrating collective behavior, filament alignment has been usually achieved by engineering interactions between filaments, either by the use of strong, streptavidin-biotin interactions[204], depletion forces[213] , or DNA-crosslinking[211]. A recent study examining the gliding of microtubules on SNAP-tagged kinesin motors bound to a Pluronic-F127 coated surface found that tuning kinesin surface density allowed for the control of filament alignment during collisions.[334] Alignment events were occasionally observed in the previous version of our system, but were too rare to generate collective behavior.[43]

In the current system, interactions originate primarily from steric effects and chemical guidance. High densities of GFP-kinesin motors, similar to the ones that are used in this experiment (consisting of the first N-terminal 401 amino acids of kinesin from *Drosophila melanogaster* compared to the first N-terminal 430 amino acids of rat kinesin used in these experiments), have been previously shown to mechanically influence the dynamics of microtubule gliding.[317] In this dynamic system, under the chosen conditions, microtubules generate many linkages to the surface *via* the high density of kinesin motors recruited from solution. The dense surface attachment reduces vertical fluctuations and prevents microtubules from crossing each other, forcing them to

buckle and align with the microtubule they are colliding with. This is supported by the observation that bundling increases as the density of microtubule-bound kinesin increases (Figure 3c). Additionally, the kinesin motors used here have truncated tails (430 amino acids) and are thus shorter than the full-length kinesin (963 amino acids for rat kinesin[462]), so they cannot be stretched as much to accommodate a crossover.

In further support of the concept that steric interactions are a source of nematic alignment among microtubules, we were able to observe 'ramming' events, where an incoming microtubule visibly indents another microtubule (Figure 6.4c). However, such microtubule deflections are rare; we were only able to observe a few such events in experiments initialized with 1 mM ATP. This is not surprising, since typically more kinesins hold the indented microtubules than push the ramming microtubule. However, visible deflections become more frequent if microtubules are gliding in the presence of 1 mM AMP-PNP (the non-hydrolyzable analog of ATP, adenylyl-imidodiphosphate). An example of this is shown in Figure 6.4c. AMP-PNP molecules lock kinesin motors in their strong microtubule-binding state, which increases the density of kinesin motors holding the microtubule to the surface, and most likely acts as a support to prevent microtubules from buckling early, thereby facilitating 'ramming' events.

"Snapping into alignment" contributes to bundle formation. An additional mechanism by which microtubules align is a 'snapping' event, where a microtubule that has begun to cross over another microtubule suddenly snaps to align with the microtubule it has crossed over (Figure 6.4d). This "snapping into alignment" has been observed in Brownian Dynamics simulations of gliding microtubules approaching the edge of a kinesin-track,[463] and can be considered chemical guiding by the kinesin track formed under a gliding microtubule.

A phenomenon similar to "snapping into alignment" has been observed in microtubules growing in the presence of the positively charged tetravalent starPEG-$(KA_7)_4$ cross-linker that was designed to mimic microtubule associated proteins.[464] This cross-linker, which has a dissociation constant for a microtubule of 30 nM, was found to laterally zip microtubules at cross-linker concentrations of 50 nM and 100 nM. In addition, when concentrated at the depolymerizing end of a microtubule, this cross-linker was found to produce depolymerization-coupled forces of up to 8.4 pN. Although it is likely that multi-valent kinesin motors are present in our dynamic system (discussed below), it is unlikely that the same zippering mechanism plays a significant role during snapping events, as these happen on a much faster time scale. The data shown by Drechsler *et al.*[464] suggests that zippering events happen over the course of 40-50 s, while the snapping events observed here occur in under 5 s.

Chemical guiding by the kinesin trail: The case for pheromonic interactions. Prior work on filament guiding on motor protein coated surfaces has shown that filaments follow permanent trails of motors created by chemical surface patterning if the required change in the angle of motion is small ($<15^0$ for microtubules).[390, 463, 465] This "chemical guiding" mechanism implies that the deposition of a kinesin trail by one microtubule may induce another microtubule to follow, which would be reminiscent of the trails of pheromones deposited by ants to induce other ants to follow and it would constitute another, "pheromonic" interaction mechanism between gliding microtubules.

Such pheromonic interactions were weak in our previous work using low microtubule densities,[43, 44] because it was exceedingly rare that a gliding microtubule encounters a kinesin trail under a small enough angle. In the system described here, the initially high density of kinesins on

the surface makes the kinesin trails less prominent and prevents alignment. However, steric interactions can align microtubules and the redistribution of the kinesin motors from the surface to the trails (Figure 6.3a) can increase the prominence of the kinesin trails relative to the surrounding surface, resulting in a strengthening of the pheromonic interaction. An example of a microtubule behavior potentially related to the pheromonic interaction is shown in Appendix Section D.10, where a microtubule begins to migrate away from another microtubule but soon returns to rejoin it. We initially interpreted the absence of microtubules emerging from the outside of a curved bundle as indication that the bundle must be stabilized by depletion forces (absent here, see next section), cross-linkers (weak here, see next section), or a pheromonic interaction. However, the bundle morphology observed by Tanida *et al.*[334] in the absence of the pheromonic interaction (Figure 6.1a) appears identical to the bundle morphology in our system (Figure 6.1d), demonstrating that a pheromonic interaction is not required to explain the system behavior.

Alternative mechanisms of microtubule interactions. There are two other conceivable mechanisms by which microtubules interact in our assay: (1) depletion forces induced by excess Pluronic F108-NTA remaining in solution and (2) multi-headed kinesin motors cross-linking to each other in solution and then cross-linking microtubules. However, for the reasons outlined below, we do not believe these mechanisms play a significant role.

Previous studies have reported that the generation of depletion forces in systems of active nanoscale filaments require polymer concentrations on the order of a few milligrams per milliliter. For example, the work of Inoue *et al.*[213] used a concentration of 3 mg/mL methylcellulose to induce depletion forces in a classical motility assay, and the work of Wu *et al.*[233] used 20 mg/mL of Pluronic F127. In our experiments, while we do initially flow in 20 μL of 2 mg/mL Pluronic F108-

NTA to coat the surface of the flow chamber, we then wash it out three times with 20 μL of BRB80 buffer. This suggests that the leftover Pluronic F108-NTA concentration can be expected to be as much as three orders of magnitude lower than that required for inducing depletion forces between microtubules[243]. Furthermore, the presence of depletion forces would have a constant effect on nematic alignment, which is in contrast to the velocity-dependent alignment that is observed in this dynamic system. As a result, we conclude that the Pluronic F108-NTA polymer remaining in solution is insufficient to cause significant depletion forces.

Microtubules can also interact by cross-linking *via* kinesins. This can be seen from the formation of dense microtubule clusters when microtubules and kinesin are mixed in the presence of 1 mM ATP and either 100 μM or 1 mM AMP-PNP, which locks kinesin motors in a strong microtubule-binding state. However, the forces exerted by kinesin cross-links are small compared to the forces exerted by surface-bound kinesins propelling microtubules. In Appendix Section D.11, we demonstrate that a cluster of microtubules can spread out over time. In Appendix Section D.12, we show that microtubules gliding in the presence of 1 mM AMP-PNP (while moving significantly slower overall) do not exhibit a statistically significant change in velocity even during antiparallel collisions. Since these behaviors are the opposite of what one would expect in the presence of cross-links, we find it unlikely that these kinesin cross-links can play a significant role in the dynamics of bundle formation.

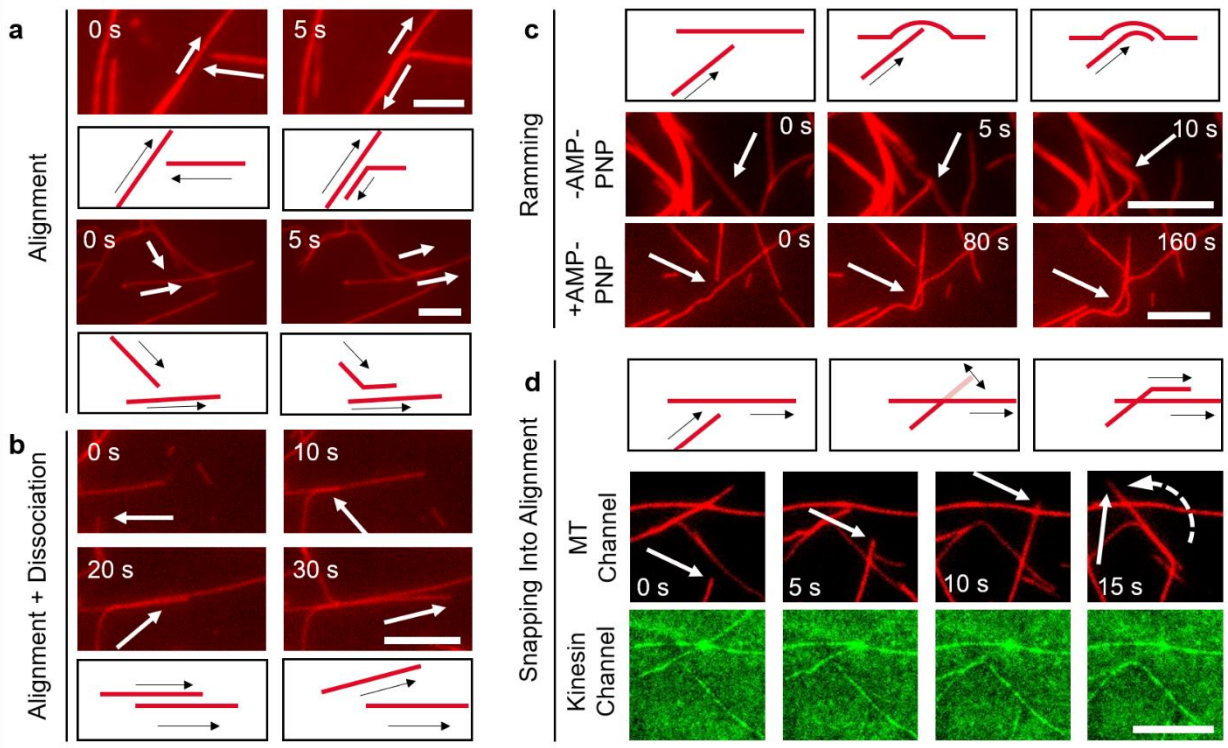

Figure 6.4. Microtubule interactions. (a) Collisions do not lead to crossing but to alignment either in antiparallel or parallel fashion depending on the angle of collision. Scale bar: 5 μm (Top), 10 μm (Bottom). (b) The alignment is reversible, as microtubules can dissociate afterwards. Scale bar: 10 μm. (c) A microtubule "ramming" another microtubule and creating an indent in the absence (top) and presence (bottom) of AMP-PNP. Scale bar: 10 μm (Top and Bottom). (d) Microtubule "snapping" to align with another microtubule that it had already crossed. Scale bar: 20 μm.

The origin of these kinesin cross-links is unclear. A likely explanation is that motors aggregate, generating multi-headed complexes that can bind multiple microtubules at once. An alternative, though unlikely, mechanism for multivalent kinesin formations is nickel ion mediated interactions of their His-tags[466]. In our experiments, it is unlikely that this mechanism plays a major role because it requires free nickel ions in solution. However, nickel ion chelating agents (NTA groups on the surface and 2 mM EGTA in the BRB80 buffer) will bind all free nickel ions and compete them away from the His-tags. In addition, such cross-linking would prevent microtubules from dissociating after aligning, which is not what we observe (Figure 6.4b).

Comparison of collective behavior to other dynamic systems. The bundles formed in our dynamic system are similar to the active foam generated in numerical simulations of Vicsek-like particles moving with memory.[414] They are also similar to the swirling, spooling, and giant flock regimes generated in simulations of gliding filaments with high rigidities and interaction energies.[467] Tanida *et al.*[334] recently investigated the effects of tunable binary collisions in a dynamic system where the strength of the microtubule-surface bond is regulated by kinesin density, and found that increasing bond strength changed the system behavior from long range order to aggregation. The bundles formed in their system at moderate kinesin surface density (example shown in Figure 6.1a) are similar to the bundles generated in our dynamic system.

Conclusions

In this study, we present a system of two agents exhibiting mutualistic collective motion where components dynamically rearrange to maximize system utility: microtubules assemble into dense bundles and kinesin motors rearrange to support the assembled bundles. These bundles have several layers of dynamic organization: first, kinesin motors are assembled by single microtubules

to allow for microtubule propulsion; next, propelled microtubules collide and align due to the strong surface bond provided by the kinesin motors (the first level of organization), forming long bundles; finally, bundles interact to form large scale networks stabilized by the migration of the kinesin from the surface to the trails. Swarming is thus achieved here through a combination of direct, steric interactions and environmental modification (the assembly of kinesins into trails on the surface).

The high degree of engagement (>95%) of the available kinesin motors in the generation of force, as indicated by the rapid consumption of ATP and the depletion of the kinesin from the surface areas between trails, is a highly desirable outcome. Dynamic turnover enables adaptation and self-repair, but ideally unproductive stores of building blocks are kept small. This has been achieved here by increasing the surface affinity for kinesin motors, which reduced the concentration of motors in the solution without impeding the kinesin trail formation.

The next steps will aim to achieve unidirectional movement of the microtubules in these bundles, for example through the utilization of asymmetric guiding structures, as well as the coupling of loads to the microtubules in the bundles to extract work from the system. Ultimately, this work pushes towards the development of artificial muscles from active nanoscale filaments.

Methods

Microtubule and Kinesin Preparation. Microtubules were polymerized by reconstituting 10 μg of HiLyte647-labeled lyophilized tubulin (Cytoskeleton Inc., Denver, CO) in 6.25 μL of polymerization buffer (BRB80 buffer and 4 mM $MgCl_2$, 1 mM GTP, 5% dimethyl sulfoxide) and incubating at 37 °C for 75 min. BRB80 buffer contains 80 mM piperazine-N,N′-bis(2ethanesulfonic acid), 1 mM $MgCl_2$, and 1 mM ethylene glycol tetraacetic acid at a pH of 6.9 (adjusted with KOH). The microtubules were then stabilized by diluting them 20-fold into BRB80

buffer with 10 μM paclitaxel (Sigma, Saint Louis, MO). A kinesin construct containing the first 430 amino acids of rat kinesin heavy chain fused to eGFP and a C-terminal His-tag at the tail domain (rkin430eGFP)[468] was expressed in Escherichia coli and purified using a Ni−NTA column (prepared by the team of G. Bachand at the Center for Integrated Nanotechnologies at Sandia National Laboratories). The concentration of the GFP-kinesin stock solution was 2.5 μM as determined by observing the absorbance at 488 nm with a Nanodrop instrument with a 1 mm path length.

Surface cleaning. Coverslips were cleaned by sonicating them for 20 minutes in acetone, rinsing with water, sonicating for 20 min in 1 M KOH, rinsing with water, and oven-drying. The dried coverslips were then UV/ozone treated on both sides for 20 min, sonicated in water for 20 min, and oven dried. The coverslips were then UV/ozone treated again, after which they were immersed in a solution of 5% dimethyldichlorosilane in toluene for 30 min. Coverslips were then rinsed two times with toluene, three times with methanol, and dried with nitrogen gas.

Experimental procedure. Cleaned coverslips were assembled into a flow cell of 1 cm width and 100 μm height using double-sided tape as spacers. A solution of 2 mg/mL Pluronic F108-NTA (gift from AllVivo Vascular) in 500 mM nickel(II) sulfate (Sigma, Saint Louis, MO) was first flowed into the flow cell. The Pluronic-F108-NTA was allowed to adsorb for 7 min. Then the solution was replaced three times with 15 μL BRB80 buffer solution. Next, a solution containing microtubules (8 μg mL^{-1}), 25 nM GFP-kinesin, 1 mM ATP in 0.5 mg/mL casein (Sigma), 10 μM paclitaxel, and an enzymatic antifade system (20 mM D-glucose, 20 μg mL^{-1} glucose oxidase, and

8 μg mL^{-1} catalase) in BRB80 buffer was flown in. The edges of the flow cell were sealed with vacuum grease to prevent evaporation.

Images were acquired with an objective-type total internal reflection fluorescence setup on an Eclipse Ti microscope (Nikon Instruments, Melville, NY) with a 100×/1.49 NA objective lens (Nikon Instruments, Melville, NY) using a 642 nm laser and a 480 nm laser (Omicron Laserage) for the imaging of microtubules and kinesin, respectively. Pairs of images were taken with a Zyla 4.2 sCMOS camera (Andor Technology) once every 5 s (exposure time of 30 ms for both channels) for as long as motility was observed. All experiments were performed at room temperature, which varied between 22-24 °C.

Conclusion

Part I: Emergent properties of colocalized enzyme cascades

In this dissertation, we have examined the kinetics of enzyme cascade reactions occurring in a tunneled multi-enzyme complex and in compartments. The primary role of spatial organization of cascading enzymes in these systems is to protect cascade intermediates that would otherwise be unstable in the environment outside of the tunnel/compartment. We showed that the stochasticity of reaction events occurring in tunneled enzyme complexes can significantly impact reaction throughput when tunnel capacities are small and catalytic rates of active sites are similar. Furthermore, it is conceivable that through evolution, control mechanisms have been selected for to decrease the effect of stochastic fluctuations in tunneled enzyme complexes; indeed, literature describing the activity of the tryptophan synthase bienzyme complex claims the presence of a gaiting mechanism between active sites which allows for matching rates between active sites. These control mechanisms in tunneled multi-enzyme complexes can be studied in further work.

In our study of compartmentalized cascade reactions, we have developed a design process for compartments containing enzymes which participate in a cascade reaction with unstable intermediates. The simple model then reveals a remarkable, yet unexpected (given the simplicity of the model) result: there exists a critical threshold at which compartmentalization becomes advantageous. Future work can focus on the characterization of this threshold for both biological and synthetic systems.

Part II: Organization in systems of active cytoskeletal filaments

In Part II of this dissertation, we examined the origins of collective behavior in a highly dynamic experimental system consisting of microtubules gliding on a surface coated with weakly-binding kinesin motors. The surface mobility of kinesin motors allowed them to be redistributed to trails surrounding microtubules, which in turn strengthened microtubule-surface bonds and resulted in alignments upon microtubule collisions. Kinesin motors and microtubules gradually assembled into long, dense bundles. Future directions of this work will can focus on controlling collective behavior in microfabricated structures to generate work.

References

1. Zhang, Y.; Hess, H., Toward Rational Design of High-Efficiency Enzyme Cascades. *ACS Catal.* **2017,** *7*, 6018-6027.

2. Hess, H.; Saper, G., Engineering with Biomolecular Motors. *Acc. Chem. Res.* **2018,** *51*, 3015-3022.

3. Woolston, B. M.; Edgar, S.; Stephanopoulos, G., Metabolic Engineering: Past and Future. *Annu. Rev. Chem. Biomol. Eng.* **2013,** *4*, 259-288.

4. Zhao, X.; Palacci, H.; Yadav, V.; Spiering, M. M.; Gilson, M. K.; Butler, P. J.; Hess, H.; Benkovic, S. J.; Sen, A., Substrate-Driven Chemotactic Assembly in an Enzyme Cascade. *Nat. Chem.* **2018,** *10*, 311-317.

5. Berg, J. M.; Stryer, L.; Tymoczko, J. L., *Biochemistry*. 7th ed.; W. H. Freeman and Company: New York, NY, 2012.

6. Quin, M. B.; Wallin, K. K.; Zhang, G.; Schmidt-Dannert, C., Spatial Organization of Multi-Enzyme Biocatalytic Cascades. *Org. Biomol. Chem.* **2017,** *15*, 4260-4271.

7. Miles, E. W.; Rhee, S.; Davies, D. R., The Molecular Basis of Substrate Channeling. *J. Biol. Chem.* **1999,** *274*, 12193-12196.

8. Roggenkamp, R., Targeting Signals for Protein Import into Peroxisomes. *Cell Biochem. Funct.* **1992,** *10*, 193-199.

9. Bayer, T. S.; Widmaier, D. M.; Temme, K.; Mirsky, E. A.; Santi, D. V.; Voigt, C. A., Synthesis of Methyl Halides from Biomass Using Engineered Microbes. *J. Am. Chem. Soc.* **2009,** *131*, 6508-6515.

10. Farhi, M.; Marhevka, E.; Masci, T.; Marcos, E.; Eyal, Y.; Ovadis, M.; Abeliovich, H.; Vainstein, A., Harnessing Yeast Subcellular Compartments for the Production of Plant Terpenoids. *Metab. Eng.* **2011,** *13*, 474-481.

11. Miles, E. W., Tryptophan Synthase: A Multienzyme Complex with an Intramolecular Tunnel. *Chem. Rec.* **2001,** *1*, 140-151.

12. Chowdhury, C.; Chun, S.; Pang, A.; Sawaya, M. R.; Sinha, S.; Yeates, T. O.; Bobik, T. A., Selective Molecular Transport through the Protein Shell of a Bacterial Microcompartment Organelle. *Proc. Natl. Acad. Sci. U. S. A.* **2015,** *112*, 2990-5.

13. Slininger Lee, M. F.; Jakobson, C. M.; Tullman-Ercek, D., Evidence for Improved Encapsulated Pathway Behavior in a Bacterial Microcompartment through Shell Protein Engineering. *ACS Synth Biol* **2017,** *6*, 1880-1891.

14. Hauer, B., Embracing Nature's Catalysts: A Viewpoint on the Future of Biocatalysis. *ACS Catal.* **2020,** *10*, 8418-8427.

15. Bailey, J. E., Toward a Science of Metabolic Engineering. *Science* **1991,** *252*, 1668-1675.

16. Zhang, F.; Rodriguez, S.; Keasling, J. D., Metabolic Engineering of Microbial Pathways for Advanced Biofuels Production. *Curr. Opin. Biotechnol.* **2011,** *22*, 775-783.

17. Nielsen, J.; Keasling, J. D., Engineering Cellular Metabolism. *Cell* **2016,** *164*, 1185-1197.

18. Hayashi, Y., Pot Economy and One-Pot Synthesis. *Chem. Sci.* **2016,** *7*, 866-880.

19. Muschiol, J.; Peters, C.; Oberleitner, N.; Mihovilovic, M. D.; Bornscheuer, U. T.; Rudroff, F., Cascade Catalysis--Strategies and Challenges En Route to Preparative Synthetic Biology. *Chem. Commun. (Camb.)* **2015,** *51*, 5798-5811.

20. Zeymer, C.; Hilvert, D., Directed Evolution of Protein Catalysts. *Annu. Rev. Biochem.* **2018,** *87*, 131-157.

21. Ebert, M. C.; Pelletier, J. N., Computational Tools for Enzyme Improvement: Why Everyone Can – and Should – Use Them. *Curr. Opin. Chem. Biol.* **2017,** *37*, 89-96.

22. Huffman, M. A.; Fryszkowska, A.; Alvizo, O.; Borra-Garske, M.; Campos, K. R.; Canada, K. A.; Devine, P. N.; Duan, D.; Forstater, J. H.; Grosser, S. T.; Halsey, H. M.; Hughes, G. J.; Jo, J.; Joyce, L. A.; Kolev, J. N.; Liang, J.; Maloney, K. M.; Mann, B. F.; Marshall, N. M.; McLaughlin, M.; Moore, J. C.; Murphy, G. S.; Nawrat, C. C.; Nazor, J.; Novick, S.; Patel, N. R.; Rodriguez-Granillo, A.; Robaire, S. A.; Sherer, E. C.; Truppo, M. D.; Whittaker, A. M.; Verma, D.; Xiao, L.; Xu, Y.; Yang, H., Design of an in Vitro Biocatalytic Cascade for the Manufacture of Islatravir. *Science* **2019,** *366*, 1255-1259.

23. Lee, J. W.; Na, D.; Park, J. M.; Lee, J.; Choi, S.; Lee, S. Y., Systems Metabolic Engineering of Microorganisms for Natural and Non-Natural Chemicals. *Nat. Chem. Biol.* **2012,** *8*, 536-546.

24. Theodosiou, E.; Frick, O.; Buhler, B.; Schmid, A., Metabolic Network Capacity of Escherichia Coli for Krebs Cycle-Dependent Proline Hydroxylation. *Microb Cell Fact* **2015,** *14*, 108.

25. Dudley, Q. M.; Karim, A. S.; Jewett, M. C., Cell-Free Metabolic Engineering: Biomanufacturing Beyond the Cell. *Biotechnol. J.* **2015,** *10*, 69-82.

26. Kim, J.; Copley, S. D., Inhibitory Cross-Talk Upon Introduction of a New Metabolic Pathway into an Existing Metabolic Network. *Proc. Natl. Acad. Sci. U. S. A.* **2012,** *109*, E2856-64.

27. Kuchler, A.; Yoshimoto, M.; Luginbuhl, S.; Mavelli, F.; Walde, P., Enzymatic Reactions in Confined Environments. *Nat. Nanotechnol.* **2016,** *11*, 409-420.

28. Avalos, J. L.; Fink, G. R.; Stephanopoulos, G., Compartmentalization of Metabolic Pathways in Yeast Mitochondria Improves the Production of Branched-Chain Alcohols. *Nat. Biotechnol.* **2013,** *31*, 335-41.

29. Qin, J.; Zhou, Y. J.; Krivoruchko, A.; Huang, M.; Liu, L.; Khoomrung, S.; Siewers, V.; Jiang, B.; Nielsen, J., Modular Pathway Rewiring of Saccharomyces Cerevisiae Enables High-Level Production of L-Ornithine. *Nat. Commun.* **2015,** *6*, 8224.

30. Zhang, Y. H., Production of Biofuels and Biochemicals by in Vitro Synthetic Biosystems: Opportunities and Challenges. *Biotechnol. Adv.* **2015,** *33*, 1467-1483.

31. Idan, O.; Hess, H., Origins of Activity Enhancement in Enzyme Cascades on Scaffolds. *ACS Nano* **2013,** *7*, 8658-8665.

32. Alam, M. T.; Olin-Sandoval, V.; Stincone, A.; Keller, M. A.; Zelezniak, A.; Luisi, B. F.; Ralser, M., The Self-Inhibitory Nature of Metabolic Networks and Its Alleviation through Compartmentalization. *Nat. Commun.* **2017,** *8*, 16018.

33. Chen, W.; Levine, H.; Rappel, W. J., A Mathematical Analysis of Second Messenger Compartmentalization. *Phys. Biol.* **2008,** *5*, 046006.

34. Hinzpeter, F.; Gerland, U.; Tostevin, F., Optimal Compartmentalization Strategies for Metabolic Microcompartments. *Biophys. J.* **2017,** *112*, 767-779.

35. Mangan, N.; Brenner, M., Systems Analysis of the Co2 Concentrating Mechanism in Cyanobacteria. *Elife* **2014,** *3*, e02043.

36. Jakobson, C. M.; Tullman-Ercek, D.; Slininger, M. F.; Mangan, N. M., A Systems-Level Model Reveals That 1,2-Propanediol Utilization Microcompartments Enhance Pathway Flux through Intermediate Sequestration. *PLoS Comput. Biol.* **2017,** *13*, e1005525.

37. Tsitkov, S.; Pesenti, T.; Palacci, H.; Blanchet, J.; Hess, H., Queueing Theory-Based Perspective of the Kinetics of "Channeled" Enzyme Cascade Reactions. *ACS Catal.* **2018,** *8*, 10721-10731.

38. Tsitkov, S.; Hess, H., Design Principles for a Compartmentalized Enzyme Cascade Reaction. *ACS Catal.* **2019,** *9*, 2432-2439.

39. Zhang, Y.; Tsitkov, S.; Hess, H., Proximity Does Not Contribute to Activity Enhancement in the Glucose Oxidase-Horseradish Peroxidase Cascade. *Nat. Commun.* **2016,** *7*, 13982.

40. Saper, G.; Hess, H., Synthetic Systems Powered by Biological Molecular Motors. *Chem. Rev.* **2020,** *120*, 288-309.

41. Agarwal, A.; Hess, H., Biomolecular Motors at the Intersection of Nanotechnology and Polymer Science. *Prog. Polym. Sci.* **2010,** *35*, 252-277.

42. Hess, H.; Ross, J. L., Non-Equilibrium Assembly of Microtubules: From Molecules to Autonomous Chemical Robots. *ChSRv* **2017**.

43. Lam, A. T.-C.; Tsitkov, S.; Zhang, Y.; Hess, H., Reversibly Bound Kinesin-1 Motor Proteins Propelling Microtubules Demonstrate Dynamic Recruitment of Active Building Blocks. *Nano Lett.* **2018,** *18*, 1530-1534.

44. Bassir Kazeruni, N. M.; Tsitkov, S.; Hess, H., Assembling Molecular Shuttles Powered by Reversibly Attached Kinesins. *J. Vis. Exp.* **2019**, e59068.

45. Idan, O.; Hess, H., Engineering Enzymatic Cascades on Nanoscale Scaffolds. *Curr. Opin. Biotechnol.* **2013,** *24*, 606-11.

46. Bashor, C. J.; Helman, N. C.; Yan, S.; Lim, W. A., Using Engineered Scaffold Interactions to Reshape Map Kinase Pathway Signaling Dynamics. *Science* **2008,** *319*, 1539-1543.

47. Wilner, O. I.; Weizmann, Y.; Gill, R.; Lioubashevski, O.; Freeman, R.; Willner, I., Enzyme Cascades Activated on Topologically Programmed DNA Scaffolds. *Nat. Nanotechnol.* **2009,** *4*, 249-54.

48. Wheeldon, I.; Minteer, S. D.; Banta, S.; Barton, S. C.; Atanassov, P.; Sigman, M., Substrate Channelling as an Approach to Cascade Reactions. *Nat. Chem.* **2016,** *8*, 299-309.

49. Lin, J.-L.; Wheeldon, I., Kinetic Enhancements in DNA–Enzyme Nanostructures Mimic the Sabatier Principle. *ACS Catal.* **2013,** *3*, 560-564.

50. Fu, J.; Liu, M.; Liu, Y.; Woodbury, N. W.; Yan, H., Interenzyme Substrate Diffusion for an Enzyme Cascade Organized on Spatially Addressable DNA Nanostructures. *J. Am. Chem. Soc.* **2012,** *134*, 5516-5519.

51. Nelson, D. L.; Lehninger, A. L.; Cox, M. M., *Principles of Biochemistry*. W.H. Freeman: New York, 2008.

52. Briggs, G. E.; Haldane, J. B. S., A Note on the Kinetics of Enzyme Action. *Biochem. J.* **1925,** *19*, 338-339.

53. Chavan, K. S.; Barton, S. C., Simulation of Intermediate Channeling by Nanoscale Confinement. *J. Phys. Chem. C* **2018,** *122*, 14474-14480.

54. Liu, Y. C.; Matanovic, I.; Hickey, D. P.; Minteer, S. D.; Atanassov, P.; Barton, S. C., Cascade Kinetics of an Artificial Metabolon by Molecular Dynamics and Kinetic Monte Carlo. *ACS Catal.* **2018,** *8*, 7719-7726.

55. Earl, E.; Calabrese Barton, S., Simulation of Intermediate Transport in Nanoscale Scaffolds for Multistep Catalytic Reactions. *Phys. Chem. Chem. Phys.* **2017,** *19*, 15463-15470.

56. Elcock, A. H.; Huber, G. A.; McCammon, J. A., Electrostatic Channeling of Substrates between Enzyme Active Sites: Comparison of Simulation and Experiment. *Biochemistry* **1997,** *36*, 16049-16058.

57. Li, G.; Zhang, C.; Xing, X. H., A Kinetic Model for Analysis of Physical Tunnels in Sequentially Acting Enzymes with Direct Proximity Channeling. *Biochem. Eng. J.* **2016,** *105*, 242-248.

58. Berg, H. C., *Random Walks in Biology*. Princeton University Press: Princeton, New Jersey, 1993.

59. Castellana, M.; Wilson, M. Z.; Xu, Y. F.; Joshi, P.; Cristea, I. M.; Rabinowitz, J. D.; Gitai, Z.; Wingreen, N. S., Enzyme Clustering Accelerates Processing of Intermediates through Metabolic Channeling. *Nat. Biotechnol.* **2014,** *32*, 1011-1018.

60. An, S.; Kumar, R.; Sheets, E. D.; Benkovic, S. J., Reversible Compartmentalization of De Novo Purine Biosynthetic Complexes in Living Cells. *Science* **2008,** *320*, 103-106.

61. Huang, X.; Holden, H. M.; Raushel, F. M., Channeling of Substrates and Intermediates in Enzyme-Catalyzed Reactions. *Annu. Rev. Biochem.* **2001,** *70*, 149-180.

62. Dunn, M. F.; Aguilar, V.; Brzovic, P.; Drewe, W. F.; Houben, K. F.; Leja, C. A.; Roy, M., The Tryptophan Synthase Bienzyme Complex Transfers Indole between The .Alpha.- And .Beta.-Sites Via a 25-30 .Ang. Long Tunnel. *Biochemistry* **1990,** *29*, 8598-8607.

63. Agapakis, C. M.; Boyle, P. M.; Silver, P. A., Natural Strategies for the Spatial Optimization of Metabolism in Synthetic Biology. *Nat. Chem. Biol.* **2012,** *8*, 527-535.

64. Good, M. C.; Zalatan, J. G.; Lim, W. A., Scaffold Proteins: Hubs for Controlling the Flow of Cellular Information. *Science* **2011,** *332*, 680-686.

65. Conrado, R. J.; Varner, J. D.; DeLisa, M. P., Engineering the Spatial Organization of Metabolic Enzymes: Mimicking Nature's Synergy. *Curr. Opin. Biotechnol.* **2008,** *19*, 492-499.

66. Simmel, F. C., DNA-Based Assembly Lines and Nanofactories. *Curr. Opin. Biotechnol.* **2012,** *23*, 516-521.

67. Xia, L.; Nguyen, K. V.; Holade, Y.; Han, H.; Dooley, K.; Atanassov, P.; Banta, S.; Minteer, S. D., Improving the Performance of Methanol Biofuel Cells Utilizing an Enzyme Cascade Bioanode with DNA-Bridged Substrate Channeling. *ACS Energy Lett.* **2017,** *2*, 1435-1438.

68. Bhattacharyya, R. P.; Remenyi, A.; Yeh, B. J.; Lim, W. A., Domains, Motifs, and Scaffolds: The Role of Modular Interactions in the Evolution and Wiring of Cell Signaling Circuits. *Annu. Rev. Biochem.* **2006,** *75*, 655-680.

69. Ovadi, J., Physiological Significance of Metabolic Channelling. *J. Theor. Biol.* **1991,** *152*, 1-22.

70. Taylor, F. W., *The Principles of Scientific Management*. Harper & Brothers: New York, 1911.

71. Helbing, D.; Deutsch, A.; Diez, S.; Peters, K.; Kalaidzidis, Y.; Padberg-Gehle, K.; Lammer, S.; Johansson, A.; Breier, G.; Schulze, F.; Zerial, M., Biologistics and the Struggle for Efficiency: Concepts and Perspectives. *Adv. Complex Syst.* **2009,** *12*, 533-548.

72. Gillespie, D. T., Stochastic Simulation of Chemical Kinetics. *Annu. Rev. Phys. Chem.* **2007,** *58*, 35-55.

73. Gnedenko, B. V.; Kovalenko, I. N., *Introduction to Queueing Theory*. Birkhäuser Boston Inc: Cambridge, 1989.

74. Hochendoner, P.; Ogle, C.; Mather, W. H., A Queueing Approach to Multi-Site Enzyme Kinetics. *Interface Focus* **2014,** *4*, 20130077.

75. Elgart, V.; Jia, T.; Kulkarni, R. V., Applications of Little's Law to Stochastic Models of Gene Expression. *Phys. Rev. B.* **2010,** *82*, 021901.

76. Peccoud, J.; Ycart, B., Markovian Modeling of Gene-Product Synthesis. *Theor. Popul. Biol.* **1995,** *48*, 222-234.

77. Kandemir-Cavas, C.; Cavas, L.; Yokes, M. B.; Hlynka, M.; Schell, R.; Yurdakoc, K., A Novel Application of Queueing Theory on the Caulerpenyne Secreted by Invasive Caulerpa Taxifolia (Vahl) C.Agardh (Ulvophyceae, Caulerpales): A Preliminary Study. *Mediterr. Mar. Sci.* **2008,** *9*, 67-75.

78. Kandemir-Cavas, C.; Cavas, L., An Application of Queueing Theory to the Relationship between Insulin Level and Number of Insulin Receptors. *Turk. J. Biochem.* **2007,** *32*, 32-38.

79. Hunt, G. C., Sequential Arrays of Waiting Lines. *Oper. Res.* **1956,** *4*, 674-683.

80. Zhao, Z.; Fu, J.; Dhakal, S.; Johnson-Buck, A.; Liu, M.; Zhang, T.; Woodbury, N. W.; Liu, Y.; Walter, N. G.; Yan, H., Nanocaged Enzymes with Enhanced Catalytic Activity and Increased Stability against Protease Digestion. *Nat. Commun.* **2016,** *7*, 10619.

81. Raushel, F. M.; Thoden, J. B.; Reinhart, G. D.; Holden, H. M., Carbamoyl Phosphate Synthetase: A Crooked Path from Substrates to Products. *Curr. Opin. Biotechnol.* **1998,** *2*, 624-632.

82. Krahn, J. M.; Kim, J. H.; Burns, M. R.; Parry, R. J.; Zalkin, H.; Smith, J. L., Coupled Formation of an Amidotransferase Interdomain Ammonia Channel and a Phosphoribosyltransferase Active Site. *Biochemistry* **1997,** *36*, 11061-11068.

83. Larsen, T. M.; Boehlein, S. K.; Schuster, S. M.; Richards, N. G.; Thoden, J. B.; Holden, H. M.; Rayment, I., Three-Dimensional Structure of Escherichia Coli Asparagine Synthetase B: A Short Journey from Substrate to Product. *Biochemistry* **1999,** *38*, 16146-16157.

84. Binda, C.; Bossi, R. T.; Wakatsuki, S.; Arzt, S.; Coda, A.; Curti, B.; Vanoni, M. A.; Mattevi, A., Cross-Talk and Ammonia Channeling between Active Centers in the Unexpected Domain Arrangement of Glutamate Synthase. *Structure* **2000,** *8*, 1299-1308.

85. Teplyakov, A.; Obmolova, G.; Badet, B.; Badet-Denisot, M. A., Channeling of Ammonia in Glucosamine-6-Phosphate Synthase. *J. Mol. Biol.* **2001,** *313*, 1093-1102.

86. Raushel, F. M.; Thoden, J. B.; Holden, H. M., Enzymes with Molecular Tunnels. *Acc. Chem. Res.* **2003,** *36*, 539-548.

87. Dunn, M. F., Allosteric Regulation of Substrate Channeling and Catalysis in the Tryptophan Synthase Bienzyme Complex. *Arch. Biochem. Biophys.* **2012,** *519*, 154-166.

88. Briggs, G. E.; Haldane, J. B. S., A Note on the Kinetics of Enzyme Action. *Biochem. J.* **1925,** *19*, 338.

89. Grima, R., Investigating the Robustness of the Classical Enzyme Kinetic Equations in Small Intracellular Compartments. *BMC Syst. Biol.* **2009,** *3*, 101.

90. Gillespie, D. T., A Rigorous Derivation of the Chemical Master Equation. *Physica A* **1992,** *188*, 404-425.

91. McQuarrie, D. A., Stochastic Approach to Chemical Kinetics. *J. Appl. Probab.* **2016,** *4*, 413-478.

92. Gillespie, D. T., Exact Stochastic Simulation of Coupled Chemical Reactions. *J. Phys. Chem.* **1977,** *81*, 2340-2361.

93. Sanft, K. R.; Gillespie, D. T.; Petzold, L. R., Legitimacy of the Stochastic Michaelis-Menten Approximation. *IET Syst. Biol.* **2011,** *5*, 58.

94. Mukai, C.; Gao, L.; Nelson, J. L.; Lata, J. P.; Cohen, R.; Wu, L.; Hinchman, M. M.; Bergkvist, M.; Sherwood, R. W.; Zhang, S.; Travis, A. J., Biomimicry Promotes the Efficiency of a 10-Step Sequential Enzymatic Reaction on Nanoparticles, Converting Glucose to Lactate. *Angew. Chem.* **2017,** *56*, 235-238.

95. Thomas, P.; Straube, A. V.; Grima, R., Stochastic Theory of Large-Scale Enzyme-Reaction Networks: Finite Copy Number Corrections to Rate Equation Models. *J. Chem. Phys.* **2010,** *133*, 195101.

96. Dallery, Y.; Gershwin, S. B., Manufacturing Flow Line Systems: A Review of Models and Analytical Results. *Queueing Syst.* **1992,** *12*, 3-94.

97. Hillier, F. S.; Boling, R. W., Finite Queues in Series with Exponential or Erlang Service Times—a Numerical Approach. *Oper. Res.* **1967,** *15*, 286-303.

98. Stefanini, M. O.; McKane, A. J.; Newman, T. J., Single Enzyme Pathways and Substrate Fluctuations. *Nonlinearity* **2005,** *18*, 1575-1595.

99. Segel, L. A.; Slemrod, M., The Quasi-Steady-State Assumption - a Case-Study in Perturbation. *SIAM Rev.* **1989,** *31*, 446-477.

100. Kou, S. C.; Cherayil, B. J.; Min, W.; English, B. P.; Xie, X. S., Single-Molecule Michaelis-Menten Equations. *J. Phys. Chem. B* **2005,** *109*, 19068-19081.

101. Grima, R.; Leier, A., Exact Product Formation Rates for Stochastic Enzyme Kinetics. *J. Phys. Chem. B* **2017,** *121*, 13-23.

102. Liu, Y. C.; Hickey, D. P.; Guo, J. Y.; Earl, E.; Abdellaoui, S.; Milton, R. D.; Sigman, M. S.; Minteer, S. D.; Barton, S. C., Substrate Channeling in an Artificial Metabolon: A Molecular Dynamics Blueprint for an Experimental Peptide Bridge. *ACS Catal.* **2017,** *7*, 2486-2493.

103. Dunn, M. F.; Niks, D.; Ngo, H.; Barends, T. R. M.; Schlichting, I., Tryptophan Synthase: The Workings of a Channeling Nanomachine. *Trends Biochem. Sci.* **2008,** *33*, 254-264.

104. Kawasaki, H.; Bauerle, R.; Zon, G.; Ahmed, S. A.; Miles, E. W., Site-Specific Mutagenesis of the Alpha Subunit of Tryptophan Synthase from Salmonella Typhimurium. Changing Arginine 179 to Leucine Alters the Reciprocal Transmission of Substrate-Induced Conformational Changes between the Alpha and Beta 2 Subunits. *J. Biol. Chem.* **1987,** *262*, 10678-10683.

105. Anderson, K. S.; Miles, E. W.; Johnson, K. A., Serine Modulates Substrate Channeling in Tryptophan Synthase. A Novel Intersubunit Triggering Mechanism. *J. Biol. Chem.* **1991,** *266*, 8020-8033.

106. Fan, Y.; Lund, L.; Shao, Q.; Gao, Y.-Q.; Raushel, F. M., A Combined Theoretical and Experimental Study of the Ammonia Tunnel in Carbamoyl Phosphate Synthetase. *J. Am. Chem. Soc.* **2009,** *131*, 10211-10219.

107. Fu, J.; Yang, Y. R.; Johnson-Buck, A.; Liu, M.; Liu, Y.; Walter, N. G.; Woodbury, N. W.; Yan, H., Multi-Enzyme Complexes on DNA Scaffolds Capable of Substrate Channelling with an Artificial Swinging Arm. *Nat. Nanotechnol.* **2014,** *9*, 531-536.

108. Farrell, H. M., Jr.; Deeney, J. T.; Hild, E. K.; Kumosinski, T. F., Stopped Flow and Steady State Kinetic Studies of the Effects of Metabolites on the Soluble Form of Nadp+:Isocitrate Dehydrogenase. *J. Biol. Chem.* **1990,** *265*, 17637-17643.

109. Tu, B. P.; Kudlicki, A.; Rowicka, M.; McKnight, S. L., Logic of the Yeast Metabolic Cycle: Temporal Compartmentalization of Cellular Processes. *Science* **2005,** *310*, 1152-1158.

110. Barabasi, A. L.; Oltvai, Z. N., Network Biology: Understanding the Cell's Functional Organization. *Nat. Rev. Genet.* **2004,** *5*, 101-13.

111. Rabe, K. S.; Muller, J.; Skoupi, M.; Niemeyer, C. M., Cascades in Compartments: En Route to Machine-Assisted Biotechnology. *Angew. Chem. Int. Ed. Engl.* **2017,** *56*, 13574-13589.

112. Chen, A. H.; Silver, P. A., Designing Biological Compartmentalization. *Trends Cell Biol.* **2012,** *22*, 662-670.

113. Zhang, G.; Quin, M. B.; Schmidt-Dannert, C., Self-Assembling Protein Scaffold System for Easy in Vitro Coimmobilization of Biocatalytic Cascade Enzymes. *ACS Catal.* **2018,** *8*, 5611-5620.

114. Garsin, D. A., Ethanolamine Utilization in Bacterial Pathogens: Roles and Regulation. *Nat. Rev. Microbiol.* **2010,** *8*, 290-5.

115. Zecchin, A.; Stapor, P. C.; Goveia, J.; Carmeliet, P., Metabolic Pathway Compartmentalization: An Underappreciated Opportunity? *Curr. Opin. Biotechnol.* **2015,** *34*, 73-81.

116. Sheldon, R. A., E Factors, Green Chemistry and Catalysis: An Odyssey. *Chem. Commun. (Camb.)* **2008**, 3352-3365.

117. Yuryev, R.; Strompen, S.; Liese, A., Coupled Chemo(Enzymatic) Reactions in Continuous Flow. *Beilstein J. Org. Chem.* **2011,** *7*, 1449-1467.

118. Li, S.; Liu, L.; Chen, J., Compartmentalizing Metabolic Pathway in Candida Glabrata for Acetoin Production. *Metab. Eng.* **2015,** *28*, 1-7.

119. Fogler, H. S., *Elements of Chemical Reaction Engineering*. Prentice-Hall PTR Inc: Upper Saddle River, New Jersey, 1999.

120. Jahnisch, K.; Hessel, V.; Lowe, H.; Baerns, M., Chemistry in Microstructured Reactors. *Angew. Chem. Int. Ed. Engl.* **2004,** *43*, 406-446.

121. Corma, A.; Iborra, S.; Velty, A., Chemical Routes for the Transformation of Biomass into Chemicals. *Chem. Rev.* **2007,** *107*, 2411-2502.

122. Skaug, M. J.; Wang, L.; Ding, Y.; Schwartz, D. K., Hindered Nanoparticle Diffusion and Void Accessibility in a Three-Dimensional Porous Medium. *ACS Nano* **2015,** *9*, 2148-2156.

123. Kerfeld, C. A.; Aussignargues, C.; Zarzycki, J.; Cai, F.; Sutter, M., Bacterial Microcompartments. *Nat. Rev. Microbiol.* **2018,** *16*, 277-290.

124. Tsai, Y.; Sawaya, M. R.; Cannon, G. C.; Cai, F.; Williams, E. B.; Heinhorst, S.; Kerfeld, C. A.; Yeates, T. O., Structural Analysis of Csos1a and the Protein Shell of the Halothiobacillus Neapolitanus Carboxysome. *PLoS Biol.* **2007,** *5*, e144.

125. Szostak, J. W.; Bartel, D. P.; Luisi, P. L., Synthesizing Life. *Nature* **2001,** *409*, 387.

126. Wilding, K. M.; Schinn, S.-M.; Long, E. A.; Bundy, B. C., The Emerging Impact of Cell-Free Chemical Biosynthesis. *Curr. Opin. Biotechnol.* **2018,** *53*, 115-121.

127. Noireaux, V.; Libchaber, A., A Vesicle Bioreactor as a Step toward an Artificial Cell Assembly. *Proc. Natl. Acad. Sci. U. S. A.* **2004,** *101*, 17669-17674.

128. Eigen, M.; Hammes, G. G., Elementary Steps in Enzyme Reactions (as Studied by Relaxation Spectrometry). In *Adv. Enzymol. Relat. Areas Mol. Biol.*, Nord, F. F., Ed. Interscience Publishers: New York, 1963; Vol. 25, pp 1-39.

129. Klitzing, R.; Moehwald, H., Proton Concentration Profile in Ultrathin Polyelectrolyte Films. *Langmuir* **1995,** *11*, 3554-3559.

130. Goldstein, L.; Levin, Y.; Katchalski, E., A Water-Insoluble Polyanionic Derivative of Trypsin. Ii. Effect of the Polyelectrolyte Carrier on the Kinetic Behavior of the Bound Trypsin*. *Biochemistry* **1964,** *3*, 1913-1919.

131. Boström, M.; Williams, D. R. M.; Ninham, B. W., Specific Ion Effects: Why Dlvo Theory Fails for Biology and Colloid Systems. *Phys. Rev. Lett.* **2001,** *87*, 168103.

132. Hermansson, M., The Dlvo Theory in Microbial Adhesion. *Colloids Surf. B. Biointerfaces* **1999,** *14*, 105-119.

133. Borukhov, I.; Andelman, D.; Orland, H., Steric Effects in Electrolytes: A Modified Poisson-Boltzmann Equation. *Phys. Rev. Lett.* **1997,** *79*, 435-438.

134. Clint, J. H., *Surfactant Aggregation*. Springer Netherlands: 1992.

135. Astumian, R. D., Microscopic Reversibility as the Organizing Principle of Molecular Machines. *Nat Nano* **2012,** *7*, 684-688.

136. Hess, H., A Landauer Limit for Robotic Manipulation. *arXiv* **2018**.

137. Schliwa, M.; Woehlke, G., Molecular Motors. *Nature* **2003,** *422*, 759-65.

138. Fijalkowska, I. J.; Schaaper, R. M.; Jonczyk, P., DNA Replication Fidelity in Escherichia Coli: A Multi-DNA Polymerase Affair. *FEMS Microbiol. Rev.* **2012,** *36*, 1105-1121.

139. Sharp, N. C. C., Timed Running Speed of a Cheetah (Acinonyx Jubatus). *J. Zool.* **1997,** *241*, 493-494.

140. Wilson, A. M.; Lowe, J. C.; Roskilly, K.; Hudson, P. E.; Golabek, K. A.; McNutt, J. W., Locomotion Dynamics of Hunting in Wild Cheetahs. *Nature* **2013,** *498*, 185-189.

141. Sengupta, S.; Spiering, M. M.; Dey, K. K.; Duan, W.; Patra, D.; Butler, P. J.; Astumian, R. D.; Benkovic, S. J.; Sen, A., DNA Polymerase as a Molecular Motor and Pump. *ACS Nano* **2014,** *8*, 2410-2418.

142. Geeves, M. A., Stretching the Lever-Arm Theory. *Nature* **2002,** *415*, 129-131.

143. Spudich, J. A.; Rock, R. S., A Crossbridge Too Far. *Nat. Cell Biol.* **2002,** *4*, E8-E10.

144. Bardy, S. L.; Ng, S. Y. M.; Jarrell, K. F., Prokaryotic Motility Structures. *Microbiology* **2003,** *149*, 295-304.

145. Shah, A. S.; Ben-Shahar, Y.; Moninger, T. O.; Kline, J. N.; Welsh, M. J., Motile Cilia of Human Airway Epithelia Are Chemosensory. *Science* **2009,** *325*, 1131-1134.

146. Sowa, Y.; Rowe, A. D.; Leake, M. C.; Yakushi, T.; Homma, M.; Ishijima, A.; Berry, R. M., Direct Observation of Steps in Rotation of the Bacterial Flagellar Motor. *Nature* **2005,** *437*, 916.

147. Jia, Y.; Li, J., Reconstitution of Fof1-Atpase-Based Biomimetic Systems. *Nature Reviews Chemistry* **2019,** *3*, 361-374.

148. Ross, J. L.; Ali, M. Y.; Warshaw, D. M., Cargo Transport: Molecular Motors Navigate a Complex Cytoskeleton. *Curr. Opin. Cell Biol.* **2008,** *20*, 41-47.

149. Hess, H., Engineering Applications of Biomolecular Motors. *Annu. Rev. Biomed. Eng.* **2011,** *13*, 429-450.

150. Hess, H.; Katira, P.; Riedel-Kruse, I. H.; Tsitkov, S., Molecular Motors in Materials Science. *MRSBu* **2019,** *44*, 113-118.

151. Saper, G.; Hess, H., Synthetic Systems Powered by Biological Molecular Motors. *Chem. Rev.* **2019**.

152. Lam, A. T.; VanDelinder, V.; Kabir, A. M. R.; Hess, H.; Bachand, G. D.; Kakugo, A., Cytoskeletal Motor-Driven Active Self-Assembly in in Vitro Systems. *Soft Matter* **2016,** *12*, 988-997.

153. Armstrong, M. J.; Hess, H., The Ecology of Technology and Nanomotors. *ACS Nano* **2014,** *8*, 4070-4073.

154. Agarwal, A.; Hess, H., Molecular Motors as Components of Future Medical Devices and Engineered Materials. *J. Nanotechnol. Eng. Med.* **2009,** *1*.

155. Vogel, V.; Hess, H., Nanoshuttles: Harnessing Motor Proteins to Transport Cargo in Synthetic Environments. In *Controlled Nanoscale Motion: Nobel Symposium 131*, Linke, H.; Månsson, A., Eds. Springer Berlin Heidelberg: Berlin, Heidelberg, 2007; pp 367-383.

156. Hess, H., Toward Devices Powered by Biomolecular Motors. *Science* **2006,** *312*, 860.

157. Hess, H., Self-Assembly Driven by Molecular Motors. *Soft Matter* **2006,** *2*, 669-677.

158. Hess, H.; Bachand, G. D., Biomolecular Motors. *Mater. Today* **2005,** *8*, 22-29.

159. Hess, H.; Bachand, G. D.; Vogel, V., Powering Nanodevices with Biomolecular Motors. *Chemistry – A European Journal* **2004,** *10*, 2110-2116.

160. Korten, T.; Månsson, A.; Diez, S., Towards the Application of Cytoskeletal Motor Proteins in Molecular Detection and Diagnostic Devices. *Curr. Opin. Biotechnol.* **2010,** *21*, 477-488.

161. Goel, A.; Vogel, V., Harnessing Biological Motors to Engineer Systems for Nanoscale Transport and Assembly. *Nat. Nanotechnol.* **2008,** *3*, 465-475.

162. Tsitkov, S.; Hess, H., Rise of the Nanorobots: Advances in Control, Molecular Detection, and Nanoscale Actuation Are Bringing Us Closer to a New Era of Technology Enhanced by Nanorobots. *IEEE Pulse* **2017,** *8*, 23-25.

163. Diez, S.; Hellenius, J. H.; Howard, J., Biomolecular Motors Operating in Engineered Environments. In *Nanobiotechnology*, Niemeyer, C. M.; Mirkin, C. A., Eds. Wiley-VCH: Weinheim, 2004.

164. Vale, R. D.; Milligan, R. A., The Way Things Move: Looking under the Hood of Molecular Motor Proteins. *Science* **2000,** *288*, 88-95.

165. Yildiz, A.; Tomishige, M.; Vale, R. D.; Selvin, P. R., Kinesin Walks Hand-over-Hand. *Science* **2004,** *303*, 676-678.

166. Hirokawa, N.; Noda, Y.; Tanaka, Y.; Niwa, S., Kinesin Superfamily Motor Proteins and Intracellular Transport. *Nature Reviews Molecular Cell Biology* **2009,** *10*, 682-696.

167. Gennerich, A.; Vale, R. D., Walking the Walk: How Kinesin and Dynein Coordinate Their Steps. *Curr. Opin. Cell Biol.* **2009,** *21*, 59-67.

168. Goldstein, L. S. B.; Yang, Z., Microtubule-Based Transport Systems in Neurons: The Roles of Kinesins and Dyneins. *Annu. Rev. Neurosci.* **2000,** *23*, 39-71.

169. Rayment, I.; Holden, H.; Whittaker, M.; Yohn, C.; Lorenz, M.; Holmes, K.; Milligan, R., Structure of the Actin-Myosin Complex and Its Implications for Muscle Contraction. *Science* **1993,** *261*, 58-65.

170. Hirokawa, N., Kinesin and Dynein Superfamily Proteins and the Mechanism of Organelle Transport. *Science* **1998,** *279*, 519-26.

171. Nayal, M.; Cera, E. D., Valence Screening of Water in Protein Crystals Reveals Potential Na^+ Binding Site. *J. Mol. Biol.* **1996,** *256*, 228-234.

172. Schliwa, M.; Woehlke, G., Switching on Kinesin. *Nature* **2001,** *411*, 424-425.

173. Svitkina, T. M.; Verkhovsky, A. B.; McQuade, K. M.; Borisy, G. G., Analysis of the Actin–Myosin Ii System in Fish Epidermal Keratocytes: Mechanism of Cell Body Translocation. *The Journal of Cell Biology* **1997,** *139*, 397-415.

174. Howard, J.; Hudspeth, A. J.; Vale, R. D., Movement of Microtubules by Single Kinesin Molecules. *Nature* **1989,** *342*, 154-158.

175. Huber, F.; Boire, A.; López, M. P.; Koenderink, G. H., Cytoskeletal Crosstalk: When Three Different Personalities Team Up. *Curr. Opin. Cell Biol.* **2015,** *32*, 39-47.

176. DelRosso, N. V.; Derr, N. D., Exploiting Molecular Motors as Nanomachines: The Mechanisms of De Novo and Re-Engineered Cytoskeletal Motors. *Curr. Opin. Biotechnol.* **2017,** *46*, 20-26.

177. Goodman, B. S.; Derr, N. D.; Reck-Peterson, S. L., Engineered, Harnessed, and Hijacked: Synthetic Uses for Cytoskeletal Systems. *Trends Cell Biol.* **2012,** *22*, 644-652.

178. Ilan, Y., Microtubules: From Understanding Their Dynamics to Using Them as Potential Therapeutic Targets. *J. Cell. Physiol.* **2019,** *234*, 7923-7937.

179. Hahn, I.; Voelzmann, A.; Liew, Y.-T.; Costa-Gomes, B.; Prokop, A., The Model of Local Axon Homeostasis - Explaining the Role and Regulation of Microtubule Bundles in Axon Maintenance and Pathology. *Neural Development* **2019,** *14*, 11.

180. Gaudin, R.; Alencar, B. C. d.; Arhel, N.; Benaroch, P., Hiv Trafficking in Host Cells: Motors Wanted! *Trends Cell Biol.* **2013,** *23*, 652-662.

181. Fischer, T.; Agarwal, A.; Hess, H., A Smart Dust Biosensor Powered by Kinesin Motors. *Nat. Nanotechnol.* **2009,** *4*, 162-166.

182. Nicolau, D. V.; Lard, M.; Korten, T.; van Delftf, F. C. M. J. M.; Persson, M.; Bengtsson, E.; Mansson, A.; Diez, S.; Linke, H.; Nicolau, D. V., Parallel Computation with Molecular-Motor-Propelled Agents in Nanofabricated Networks. *Proc. Natl. Acad. Sci. U. S. A.* **2016,** *113*, 2591-2596.

183. Baroncini, M.; Silvi, S.; Credi, A., Photo- and Redox-Driven Artificial Molecular Motors. *Chem. Rev.* **2019**.

184. Koumura, N.; Zijlstra, R. W.; van Delden, R. A.; Harada, N.; Feringa, B. L., Light-Driven Monodirectional Molecular Rotor. *Nature* **1999,** *401*, 152-5.

185. Klok, M.; Boyle, N.; Pryce, M. T.; Meetsma, A.; Browne, W. R.; Feringa, B. L., Mhz Unidirectional Rotation of Molecular Rotary Motors. *J. Am. Chem. Soc.* **2008,** *130*, 10484-10485.

186. García-López, V.; Chen, F.; Nilewski, L. G.; Duret, G.; Aliyan, A.; Kolomeisky, A. B.; Robinson, J. T.; Wang, G.; Pal, R.; Tour, J. M., Molecular Machines Open Cell Membranes. *Nature* **2017,** *548*, 567-572.

187. Roke, D.; Wezenberg, S. J.; Feringa, B. L., Molecular Rotary Motors: Unidirectional Motion around Double Bonds. *Proc. Natl. Acad. Sci. U. S. A.* **2018,** *115*, 9423-9431.

188. Cnossen, A.; Kistemaker, J. C. M.; Kojima, T.; Feringa, B. L., Structural Dynamics of Overcrowded Alkene-Based Molecular Motors During Thermal Isomerization. *The Journal of Organic Chemistry* **2014,** *79*, 927-935.

189. Wilson, M. R.; Solà, J.; Carlone, A.; Goldup, S. M.; Lebrasseur, N.; Leigh, D. A., An Autonomous Chemically Fuelled Small-Molecule Motor. *Nature* **2016,** *534*, 235-240.

190. Ramaiya, A.; Roy, B.; Bugiel, M.; Schäffer, E., Kinesin Rotates Unidirectionally and Generates Torque While Walking on Microtubules. *Proc. Natl. Acad. Sci. U. S. A.* **2017,** *114*, 10894-10899.

191. Hirokawa, N.; Pfister, K. K.; Yorifuji, H.; Wagner, M. C.; Brady, S. T.; Bloom, G. S., Submolecular Domains of Bovine Brain Kinesin Identified by Electron Microscopy and Monoclonal Antibody Decoration. *Cell* **1989,** *56*, 867-878.

192. Huxley, A. F.; Peachey, L. D., The Maximum Length for Contraction in Vertebrate Striated Muscle. *The Journal of Physiology* **1961,** *156*, 150-165.

193. Hawkins, C. J.; Bennett, P. M., Evaluation of Freeze Substitution in Rabbit Skeletal Muscle. Comparison of Electron Microscopy to X-Ray Diffraction. *J. Muscle Res. Cell Motil.* **1995,** *16*, 303-318.

194. Kerssemakers, J.; Ionov, L.; Queitsch, U.; Luna, S.; Hess, H.; Diez, S., 3d Nanometer Tracking of Motile Microtubules on Reflective Surfaces. *Small* **2009,** *5*, 1732-1737.

195. Veigel, C.; Schmidt, C. F., Moving into the Cell: Single-Molecule Studies of Molecular Motors in Complex Environments. *Nature Reviews Molecular Cell Biology* **2011,** *12*, 163-176.

196. Rios, L.; Bachand, G. D., Multiplex Transport and Detection of Cytokines Using Kinesin-Driven Molecular Shuttles. *Lab Chip* **2009,** *9*, 1005-1010.

197. Taira, S.; Du, Y.-Z.; Hiratsuka, Y.; Uyeda, T. Q. P.; Yumoto, N.; Kodaka, M., Loading and Unloading of Molecular Cargo by DNA-Conjugated Microtubule. *Biotechnol. Bioeng.* **2008,** *99*, 734-739.

198. Nitzsche, B.; Ruhnow, F.; Diez, S., Quantum-Dot-Assisted Characterization of Microtubule Rotations During Cargo Transport. *Nat Nano* **2008,** *3*, 552-556.

199. Takatsuki, H.; Rice, K. M.; Asano, S.; Day, B. S.; Hino, M.; Oiwa, K.; Ishikawa, R.; Hiratsuka, Y.; Uyeda, T. Q. P.; Kohama, K.; Blough, E. R., Utilization of Myosin and Actin Bundles for the Transport of Molecular Cargo. *Small* **2010,** *6*, 452-457.

200. Bachand, M.; Trent, A. M.; Bunker, B. C.; Bachand, G. D., Physical Factors Affecting Kinesin-Based Transport of Synthetic Nanoparticle Cargo. *Journal of Nanoscience and Nanotechnology* **2005,** *5*, 718-722.

201. Aoyama, S.; Shimoike, M.; Hiratsuka, Y., Self-Organized Optical Device Driven by Motor Proteins. *Proc. Natl. Acad. Sci. U. S. A.* **2013,** *110*, 16408-16413.

202. Lin, C. T.; Kao, M. T.; Kurabayashi, K.; Meyhofer, E., Self-Contained Biomolecular Motor-Driven Protein Sorting and Concentrating in an Ultrasensitive Microfluidic Chip. *Nano Lett.* **2008,** *8*, 1041-1046.

203. Bachand, G. D.; Hess, H.; Ratna, B.; Satir, P.; Vogel, V., "Smart Dust" Biosensors Powered by Biomolecular Motors. *Lab Chip* **2009,** *9*, 1661-1666.

204. Hess, H.; Clemmens, J.; Brunner, C.; Doot, R.; Luna, S.; Ernst, K.-H.; Vogel, V., Molecular Self-Assembly of "Nanowires" and "Nanospools" Using Active Transport. *Nano Lett.* **2005,** *5*, 629-633.

205. Luria, I.; Crenshaw, J.; Downs, M.; Agarwal, A.; Seshadri, S. B.; Gonzales, J.; Idan, O.; Kamcev, J.; Katira, P.; Pandey, S.; Nitta, T.; Phillpot, S. R.; Hess, H., Microtubule Nanospool Formation by Active Self-Assembly Is Not Initiated by Thermal Activation. *Soft Matter* **2011,** *7*, 3108-3115.

206. Lam, A. T.; Curschellas, C.; Krovvidi, D.; Hess, H., Controlling Self-Assembly of Microtubule Spools Via Kinesin Motor Density. *Soft Matter* **2014,** *10*, 8731-8736.

207. Idan, O.; Lam, A.; Kamcev, J.; Gonzales, J.; Agarwal, A.; Hess, H., Nanoscale Transport Enables Active Self-Assembly of Millimeter-Scale Wires. *Nano Lett.* **2012,** *12*, 240-245.

208. Schaller, V.; Weber, C. A.; Hammerich, B.; Frey, E.; Bausch, A. R., Frozen Steady States in Active Systems. *Proc. Natl. Acad. Sci. U. S. A.* **2011,** *108*, 19183.

209. Sumino, Y.; Nagai, K. H.; Shitaka, Y.; Tanaka, D.; Yoshikawa, K.; Chaté, H.; Oiwa, K., Large-Scale Vortex Lattice Emerging from Collectively Moving Microtubules. *Nature* **2012,** *483*, 448.

210. Needleman, D.; Dogic, Z., Active Matter at the Interface between Materials Science and Cell Biology. *Nat. Rev. Mat.* **2017,** *2*, 17048.

211. Keya, J. J.; Suzuki, R.; Kabir, A. M. R.; Inoue, D.; Asanuma, H.; Sada, K.; Hess, H.; Kuzuya, A.; Kakugo, A., DNA-Assisted Swarm Control in a Biomolecular Motor System. *Nat. Commun.* **2018,** *9*, 453.

212. Islam, M. S.; Kuribayashi-Shigetomi, K.; Kabir, A. M. R.; Inoue, D.; Sada, K.; Kakugo, A., Role of Confinement in the Active Self-Organization of Kinesin-Driven Microtubules. *Sens. Actuators B Chem.* **2017,** *247*, 53-60.

213. Inoue, D.; Mahmot, B.; Kabir, A. M. R.; Farhana, T. I.; Tokuraku, K.; Sada, K.; Konagaya, A.; Kakugo, A., Depletion Force Induced Collective Motion of Microtubules Driven by Kinesin. *Nanoscale* **2015,** *7*, 18054-18061.

214. Sanchez, T.; Chen, D. T. N.; DeCamp, S. J.; Heymann, M.; Dogic, Z., Spontaneous Motion in Hierarchically Assembled Active Matter. *Nature* **2012,** *491*, 431-434.

215. Soto, C. M.; Martin, B. D.; Sapsford, K. E.; Blum, A. S.; Ratna, B. R., Toward Single Molecule Detection of Staphylococcal Enterotoxin B: Mobile Sandwich Immunoassay on Gliding Microtabules. *AnaCh* **2008,** *80*, 5433-5440.

216. Ramachandran, S.; Ernst, K.-H.; Bachand, George D.; Vogel, V.; Hess, H., Selective Loading of Kinesin-Powered Molecular Shuttles with Protein Cargo and Its Application to Biosensing. *Small* **2006,** *2*, 330-334.

217. Katira, P.; Hess, H., Two-Stage Capture Employing Active Transport Enables Sensitive and Fast Biosensors. *Nano Lett.* **2010,** *10*, 567-572.

218. Taira, S.; Du, Y.-Z.; Hiratsuka, Y.; Konishi, K.; Kubo, T.; Uyeda, T. Q. P.; Yumoto, N.; Kodaka, M., Selective Detection and Transport of Fully Matched DNA by DNA-Loaded Microtubule and Kinesin Motor Protein. *Biotechnol. Bioeng.* **2006,** *95*, 533-538.

219. Raab, M.; Hancock, W. O., Transport and Detection of Unlabeled Nucleotide Targets by Microtubules Functionalized with Molecular Beacons. *Biotechnol. Bioeng.* **2008,** *99*, 764-773.

220. Martinez-Neira, R.; Kekic, M.; Nicolau, D.; dos Remedios, C. G., A Novel Biosensor for Mercuric Ions Based on Motor Proteins. *Biosens. Bioelectron.* **2005,** *20*, 1428-1432.

221. Chaudhuri, S.; Korten, T.; Korten, S.; Milani, G.; Lana, T.; te Kronnie, G.; Diez, S., Label-Free Detection of Microvesicles and Proteins by the Bundling of Gliding Microtubules. *Nano Lett.* **2018,** *18*, 117-123.

222. Subramaniyan Parimalam, S.; Tarhan, M. C.; Karsten, S. L.; Fujita, H.; Shintaku, H.; Kotera, H.; Yokokawa, R., Microtubule Density and Landing Rate as Parameters to Analyze Tau Protein in the Mt-Kinesin "Gliding" Assay. *Sens. Actuators B Chem.* **2017,** *238*, 954-961.

223. Mackay, I. R.; Martinez-Neira, R.; Whittingham, S.; Nicolau, D.; Toh, B.-H., Autoantigenicity of Actin. In *Actin-Binding Proteins and Disease*, dos Remedios, C. G.; Chhabra, D., Eds. Springer New York: New York, NY, 2008; pp 50-64.

224. Huber, L.; Suzuki, R.; Krüger, T.; Frey, E.; Bausch, A. R., Emergence of Coexisting Ordered States in Active Matter Systems. *Science* **2018,** *361*, 255.

225. van Delft, F. C. M. J. M.; Ipolitti, G.; Nicolau, D. V.; Perumal, A. S.; Kašpar, O.; Kheireddine, S.; Wachsmann-Hogiu, S.; Nicolau, D. V., Something Has to Give: Scaling Combinatorial Computing by Biological Agents Exploring Physical Networks Encoding Np-Complete Problems. *Interface Focus* **2018,** *8*, 20180034.

226. Block, S. M.; Goldstein, L. S. B.; Schnapp, B. J., Bead Movement by Single Kinesin Molecules Studied with Optical Tweezers. *Nature* **1990,** *348*, 348-352.

227. Kron, S. J.; Spudich, J. A., Fluorescent Actin Filaments Move on Myosin Fixed to a Glass Surface. *Proc. Natl. Acad. Sci. USA* **1986,** *83*, 6272-6.

228. Vale, R. D.; Reese, T. S.; Sheetz, M. P., Identification of a Novel Force-Generating Protein, Kinesin, Involved in Microtubule-Based Motility. *Cell* **1985,** *42*, 39-50.

229. Nedelec, F. J.; Surrey, T.; Maggs, A. C.; Leibler, S., Self-Organization of Microtubules and Motors. *Nature* **1997,** *389*, 305-8.

230. Bachand, G. D.; Bouxsein, N. F.; VanDelinder, V.; Bachand, M., Biomolecular Motors in Nanoscale Materials, Devices, and Systems. *Wires Nanomed. Nanobi.* **2014,** *6*, 163-177.

231. Böhm, K. J.; Stracke, R.; Baum, M.; Zieren, M.; Unger, E., Effect of Temperature on Kinesin-Driven Microtubule Gliding and Kinesin Atpase Activity. *FEBS Lett.* **2000,** *466*, 59-62.

232. Sanchez, T.; Welch, D.; Nicastro, D.; Dogic, Z., Cilia-Like Beating of Active Microtubule Bundles. *Science* **2011,** *333*, 456.

233. Wu, K.-T.; Hishamunda, J. B.; Chen, D. T. N.; DeCamp, S. J.; Chang, Y.-W.; Fernández-Nieves, A.; Fraden, S.; Dogic, Z., Transition from Turbulent to Coherent Flows in Confined Three-Dimensional Active Fluids. *Science* **2017,** *355*, eaal1979.

234. Tas, R. P.; Chen, C.-Y.; Katrukha, E. A.; Vleugel, M.; Kok, M.; Dogterom, M.; Akhmanova, A.; Kapitein, L. C., Guided by Light: Optical Control of Microtubule Gliding Assays. *Nano Lett.* **2018,** *18*, 7524-7528.

235. Bhagawati, M.; Ghosh, S.; Reichel, A.; Froehner, K.; Surrey, T.; Piehler, J., Organization of Motor Proteins into Functional Micropatterns Fabricated by a Photoinduced Fenton Reaction. *Angew. Chem. Int. Ed.* **2009,** *48*, 9188-9191.

236. van den Heuvel, M. G.; Butcher, C. T.; Smeets, R. M.; Diez, S.; Dekker, C., High Rectifying Efficiencies of Microtubule Motility on Kinesin-Coated Gold Nanostructures. *Nano Lett.* **2005,** *5*, 1117-22.

237. Hess, H.; Clemmens, J.; Qin, D.; Howard, J.; Vogel, V., Light-Controlled Molecular Shuttles Made from Motor Proteins Carrying Cargo on Engineered Surfaces. *Nano Lett.* **2001,** *1*, 235-239.

238. Kumar, K. R. S.; Amrutha, A. S.; Tamaoki, N., Spatiotemporal Control of Kinesin Motor Protein by Photoswitches Enabling Selective Single Microtubule Regulations. *Lab Chip* **2016,** *16*, 4702-4709.

239. Hutchins, B. M.; Platt, M.; Hancock, W. O.; Williams, M. E., Directing Transport of Cofe2o4-Functionalized Microtubules with Magnetic Fields. *Small* **2007,** *3*, 126-131.

240. Isozaki, N.; Shintaku, H.; Kotera, H.; Hawkins, T. L.; Ross, J. L.; Yokokawa, R., Control of Molecular Shuttles by Designing Electrical and Mechanical Properties of Microtubules. *Sci. Robot.* **2017,** *2*, eaan4882.

241. Inoue, D.; Nitta, T.; Kabir, A. M. R.; Sada, K.; Gong, J. P.; Konagaya, A.; Kakugo, A., Sensing Surface Mechanical Deformation Using Active Probes Driven by Motor Proteins. *Nat. Commun.* **2016,** *7*.

242. Ionov, L.; Stamm, M.; Diez, S., Reversible Switching of Microtubule Motility Using Thermoresponsive Polymer Surfaces. *Nano Lett.* **2006,** *6*, 1982-1987.

243. Howard, J.; Hunt, A. J.; Baek, S., Chapter 10 Assay of Microtubule Movement Driven by Single Kinesin Molecules. In *Methods Cell Biol.*, Scholey, J. M., Ed. Academic Press: 1993; Vol. 39, pp 137-147.

244. Harada, Y.; Sakurada, K.; Aoki, T.; Thomas, D. D.; Yanagida, T., Mechanochemical Coupling in Actomyosin Energy Transduction Studied by in Vitro Movement Assay. *J. Mol. Biol.* **1990,** *216*, 49-68.

245. VanDelinder, V.; Bachand, G. D., Photodamage and the Importance of Photoprotection in Biomolecular-Powered Device Applications. *AnaCh* **2014,** *86*, 721-728.

246. Kerssemakers, J.; Howard, J.; Hess, H.; Diez, S., The Distance That Kinesin-1 Holds Its Cargo from the Microtubule Surface Measured by Fluorescence Interference Contrast Microscopy. *Proc. Natl. Acad. Sci. U. S. A.* **2006,** *103*, 15812-15817.

247. VanDelinder, V.; Imam, Z. I.; Bachand, G., Kinesin Motor Density and Dynamics in Gliding Microtubule Motility. *Sci. Rep.* **2019,** *9*, 7206.

248. MAHAMDEH, M.; SIMMERT, S.; LUCHNIAK, A.; SCHÄFFER, E.; HOWARD, J., Label-Free High-Speed Wide-Field Imaging of Single Microtubules Using Interference Reflection Microscopy. *JMic* **2018,** *272*, 60-66.

249. Spudich, J. A.; Rice, S. E.; Rock, R. S.; Purcell, T. J.; Warrick, H. M., Optical Traps to Study Properties of Molecular Motors. *Cold Spring Harbor Protocols* **2011,** *2011*, pdb.top066662.

250. Mickolajczyk, K. J.; Cook, A. S. I.; Jevtha, J. P.; Fricks, J.; Hancock, W. O., Insights into Kinesin-1 Stepping from Simulations and Tracking of Gold Nanoparticle-Labeled Motors. *Biophys. J.* **2019,** *117*, 331-345.

251. Desai, A.; Mitchison, T. J., Microtubule Polymerization Dynamics. *Annu. Rev. Cell. Dev. Biol.* **1997,** *13*, 83-117.

252. Hawkins, T.; Mirigian, M.; Selcuk Yasar, M.; Ross, J. L., Mechanics of Microtubules. *J. Biomech.* **2010,** *43*, 23-30.

253. Nogales, E.; Wolf, S. G.; Downing, K. H., Structure of the Alpha Beta Tubulin Dimer by Electron Crystallography. *Nature* **1998,** *391*, 199-203.

254. Aher, A.; Akhmanova, A., Tipping Microtubule Dynamics, One Protofilament at a Time. *Curr. Opin. Cell Biol.* **2018,** *50*, 86-93.

255. Alushin, G. M.; Lander, G. C.; Kellogg, E. H.; Zhang, R.; Baker, D.; Nogales, E., High-Resolution Microtubule Structures Reveal the Structural Transitions in Alpha Beta-Tubulin Upon Gtp Hydrolysis. *Cell* **2014,** *157*, 1117-1129.

256. Nogales, E., An Electron Microscopy Journey in the Study of Microtubule Structure and Dynamics. *Protein Sci.* **2015,** *24*, 1912-1919.

257. van Haren, J.; Wittmann, T., Microtubule Plus End Dynamics − Do We Know How Microtubules Grow? *Bioessays* **2019,** *41*, 1800194.

258. Howard, J.; Hymann, A. A., Dynamics and Mechanics of the Microtubules Plus End. *Nature* **2003,** *422*, 753-758.

259. Jeune-Smith, Y.; Hess, H., Engineering the Length Distribution of Microtubules Polymerized in Vitro. *Soft Matter* **2010,** *6*, 1778-1784.

260. Katsuki, M.; Drummond, D. R.; Cross, R. A., Ectopic a-Lattice Seams Destabilize Microtubules. *Nat. Commun.* **2014,** *5*, 3094.

261. Cross, R. A., Microtubule Lattice Plasticity. *Curr. Opin. Cell Biol.* **2019,** *56*, 88-93.

262. Chrétien, D.; Fuller, S. D., Microtubules Switch Occasionally into Unfavorable Configurations During Elongation. *J. Mol. Biol.* **2000,** *298*, 663-676.

263. Li, H.; DeRosier, D. J.; Nicholson, W. V.; Nogales, E.; Downing, K. H., Microtubule Structure at 8 a Resolution. *Structure (Camb)* **2002,** *10*, 1317-28.

264. Chrétien, D.; Wade, R. H., New Data on the Microtubule Surface Lattice. *Biol. Cell* **1991,** *71*, 161-174.

265. Bugiel, M.; Mitra, A.; Girardo, S.; Diez, S.; Schäffer, E., Measuring Microtubule Supertwist and Defects by Three-Dimensional-Force-Clamp Tracking of Single Kinesin-1 Motors. *Nano Lett.* **2018,** *18*, 1290-1295.

266. Mitchison, T.; Kirschner, M., Dynamic Instability of Microtubule Growth. *Nature* **1984,** *312*, 237-242.

267. Zhang, R.; Alushin, G. M.; Brown, A.; Nogales, E., Mechanistic Origin of Microtubule Dynamic Instability and Its Modulation by Eb Proteins. *Cell* **2015,** *162*, 849-859.

268. Hyman, A. A.; Salser, S.; Drechsel, D. N.; Unwin, N.; Mitchison, T. J., Role of Gtp Hydrolysis in Microtubule Dynamics: Information from a Slowly Hydrolyzable Analogue, Gmpcpp. *Mol. Biol. Cell* **1992,** *3*, 1155-67.

269. Driver, J. W.; Geyer, E. A.; Bailey, M. E.; Rice, L. M.; Asbury, C. L., Direct Measurement of Conformational Strain Energy in Protofilaments Curling Outward from Disassembling Microtubule Tips. *eLife* **2017,** *6*, e28433.

270. Ragazzon, G.; Prins, L. J., Energy Consumption in Chemical Fuel-Driven Self-Assembly. *Nat. Nanotechnol.* **2018,** *13*, 882-889.

271. Mitchison, T. J., The Engine of Microtubule Dynamics Comes into Focus. *Cell* **2014,** *157*, 1008-1010.

272. Dogterom, M.; Janson, M. E.; Faivre-Moskalenko, C.; van der Horst, A.; Kerssemakers, J. W. J.; Tanase, C.; Mulder, B. M., Force Generation by Polymerizing Microtubules. *Appl. Phys. A* **2002,** *75*, 331-336.

273. Dogterom, M.; Kerssemakers, J. W. J.; Romet-Lemonne, G.; Janson, M. E., Force Generation by Dynamic Microtubules. *Curr. Opin. Cell Biol.* **2005,** *17*, 67-74.

274. Theriot, J. A., The Polymerization Motor. *Traffic* **2000,** *1*, 19-28.

275. Schiff, P. B.; Fant, J.; Horwitz, S. B., Promotion of Microtubule Assembly Invitro by Taxol. *Nature* **1979,** *277*, 665-667.

276. Hawkins, T. L.; Sept, D.; Mogessie, B.; Straube, A.; Ross, J. L., Mechanical Properties of Doubly Stabilized Microtubule Filaments. *Biophys. J.* **2013,** *104*, 1517-1528.

277. Hancock, William O., The Kinesin-1 Chemomechanical Cycle: Stepping toward a Consensus. *Biophys. J.* **2016,** *110*, 1216-1225.

278. Lawrence, C. J.; Dawe, R. K.; Christie, K. R.; Cleveland, D. W.; Dawson, S. C.; Endow, S. A.; Goldstein, L. S. B.; Goodson, H. V.; Hirokawa, N.; Howard, J.; Malmberg, R. L.; McIntosh, J. R.; Miki, H.; Mitchison, T. J.; Okada, Y.; Reddy, A. S. N.; Saxton, W. M.; Schliwa, M.; Scholey, J. M.; Vale, R. D.; Walczak, C. E.; Wordeman, L., A Standardized Kinesin Nomenclature. *J. Cell Biol.* **2004,** *167*, 19-22.

279. Leduc, C.; Padberg-Gehle, K.; Varga, V.; Helbing, D.; Diez, S.; Howard, J., Molecular Crowding Creates Traffic Jams of Kinesin Motors on Microtubules. *Proc. Natl. Acad. Sci. U. S. A.* **2012,** *109*, 6100-6105.

280. Arpağ, G.; Norris, S. R.; Mousavi, S. I.; Soppina, V.; Verhey, K. J.; Hancock, W. O.; Tüzel, E., Motor Dynamics Underlying Cargo Transport by Pairs of Kinesin-1 and Kinesin-3 Motors. *Biophys. J.* **2019,** *116*, 1115-1126.

281. Torisawa, T.; Taniguchi, D.; Ishihara, S.; Oiwa, K., Spontaneous Formation of a Globally Connected Contractile Network in a Microtubule-Motor System. *Biophys. J.* **2016,** *111*, 373-385.

282. Ray, S.; Meyhöfer, E.; Milligan, R. A.; Howard, J., Kinesin Follows the Microtubule's Protofilament Axis. *The Journal of Cell Biology* **1993,** *121*, 1083-1093.

283. Böhm, K. J.; Stracke, R.; Unger, E., Speeding up Kinesin-Driven Microtubule Gliding in Vitro by Variation of Cofactor Composition and Physicochemical Parameters. *Cell Biol. Int.* **2000,** *24*, 335-41.

284. Visscher, K.; Schnitzer, M. J.; Block, S. M., Single Kinesin Molecules Studied with a Molecular Force Clamp. *Nature* **1999,** *400*, 184-9.

285. Coy, D. L.; Wagenbach, M.; Howard, J., Kinesin Takes One 8-Nm Step for Each Atp That It Hydrolyzes. *J. Biol. Chem.* **1999,** *274*, 3667-71.

286. Hancock, W. O.; Howard, J., Processivity of the Motor Protein Kinesin Requires Two Heads. *J. Cell Biol.* **1998,** *140*, 1395-1405.

287. Cross, R. A., Review: Mechanochemistry of the Kinesin-1 Atpase. *Biopolymers* **2016,** *105*, 476-482.

288. Radtke, K.; Döhner, K.; Sodeik, B., Viral Interactions with the Cytoskeleton: A Hitchhiker's Guide to the Cell. *Cell. Microbiol.* **2006,** *8*, 387-400.

289. Mallik, R.; Carter, B. C.; Lex, S. A.; King, S. J.; Gross, S. P., Cytoplasmic Dynein Functions as a Gear in Response to Load. *Nature* **2004,** *427*, 649-652.

290. Oiwa, K.; Sakakibara, H., Recent Progress in Dynein Structure and Mechanism. *Curr. Opin. Cell Biol.* **2005,** *17*, 98-103.

291. Kumar, S.; Månsson, A., Covalent and Non-Covalent Chemical Engineering of Actin for Biotechnological Applications. *Biotechnol. Adv.* **2017,** *35*, 867-888.

292. Nicholas, M. P.; Höök, P.; Brenner, S.; Wynne, C. L.; Vallee, R. B.; Gennerich, A., Control of Cytoplasmic Dynein Force Production and Processivity by Its C-Terminal Domain. *Nat. Commun.* **2015,** *6*, 6206.

293. Robinson, R. C.; Turbedsky, K.; Kaiser, D. A.; Marchand, J.-B.; Higgs, H. N.; Choe, S.; Pollard, T. D., Crystal Structure of Arp2/3 Complex. *Science* **2001,** *294*, 1679-1684.

294. Mullins, R. D.; Heuser, J. A.; Pollard, T. D., The Interaction of Arp2/3 Complex with Actin: Nucleation, High Affinity Pointed End Capping, and Formation of Branching Networks of Filaments. *Proc. Natl. Acad. Sci. U. S. A.* **1998,** *95*, 6181-6186.

295. Kueh, H. Y.; Mitchison, T. J., Structural Plasticity in Actin and Tubulin Polymer Dynamics. *Science* **2009,** *325*, 960-963.

296. Littlefield, R.; Almenar-Queralt, A.; Fowler, V. M., Actin Dynamics at Pointed Ends Regulates Thin Filament Length in Striated Muscle. *Nat. Cell Biol.* **2001,** *3*, 544-551.

297. Cooper, J. A., Effects of Cytochalasin and Phalloidin on Actin. *The Journal of Cell Biology* **1987,** *105*, 1473-1478.

298. Howard, J., Molecular Motors: Structural Adaptations to Cellular Functions. *Nature* **1997,** *389*, 561-567.

299. Spudich, J. A., The Myosin Swinging Cross-Bridge Model. *Nature Reviews Molecular Cell Biology* **2001,** *2*, 387-392.

300. Romberg, L.; Vale, R. D., Chemomechanical Cycle of Kinesin Differs from That of Myosin. *Nature* **1993,** *361*, 168-170.

301. Mehta, A. D.; Rock, R. S.; Rief, M.; Spudich, J. A.; Mooseker, M. S.; Cheney, R. E., Myosin-V Is a Processive Actin-Based Motor. *Nature* **1999,** *400*, 590-593.

302. Seara, D. S.; Yadav, V.; Linsmeier, I.; Tabatabai, A. P.; Oakes, P. W.; Tabei, S. M. A.; Banerjee, S.; Murrell, M. P., Entropy Production Rate Is Maximized in Non-Contractile Actomyosin. *Nat. Commun.* **2018,** *9*, 4948.

303. Calligaris, D.; Verdier-Pinard, P.; Devred, F.; Villard, C.; Braguer, D.; Lafitte, D., Microtubule Targeting Agents: From Biophysics to Proteomics. *Cell. Mol. Life Sci.* **2010,** *67*, 1089-1104.

304. Mizushima-Sugano, J.; Maeda, T.; Miki-Noumura, T., Flexural Rigidity of Singlet Microtubules Estimated from Statistical Analysis of Their Contour Lengths and End-to-End Distances. *Biochimica et Biophysica Acta (BBA) - General Subjects* **1983,** *755*, 257-262.

305. Gittes, F.; Mickey, B.; Nettleton, J.; Howard, J., Flexural Rigidity of Microtubules and Actin Filaments Measured from Thermal Fluctuations in Shape. *J. Cell Biol.* **1993,** *120*, 923-934.

306. Venier, P.; Maggs, A. C.; Carlier, M. F.; Pantaloni, D., Analysis of Microtubule Rigidity Using Hydrodynamic Flow and Thermal Fluctuations. *J. Biol. Chem.* **1994,** *269*, 13353-13360.

307. Kurz, J. C.; Williams, R. C., Microtubule-Associated Proteins and the Flexibility of Microtubules. *Biochemistry* **1995,** *34*, 13374-13380.

308. Felgner, H.; Frank, R.; Schliwa, M., Flexural Rigidity of Microtubules Measured with the Use of Optical Tweezers. *J. Cell Sci.* **1996,** *109*, 509-516.

309. Felgner, H.; Frank, R.; Biernat, J.; Mandelkow, E.-M.; Mandelkow, E.; Ludin, B.; Matus, A.; Schliwa, M., Domains of Neuronal Microtubule-Associated Proteins and Flexural Rigidity of Microtubules. *The Journal of Cell Biology* **1997,** *138*, 1067-1075.

310. Kurachi, M.; Hoshi, M.; Tashiro, H., Buckling of a Single Microtubule by Optical Trapping Forces: Direct Measurement of Microtubule Rigidity. *Cell Motil.* **1995,** *30*, 221-228.

311. Kikumoto, M.; Kurachi, M.; Tosa, V.; Tashiro, H., Flexural Rigidity of Individual Microtubules Measured by a Buckling Force with Optical Traps. *Biophys. J.* **2006,** *90*, 1687-1696.

312. van Mameren, J.; Vermeulen, K. C.; Gittes, F.; Schmidt, C. F., Leveraging Single Protein Polymers to Measure Flexural Rigidity. *J. Phys. Chem. B* **2009,** *113*, 3837-3844.

313. Memet, E.; Hilitski, F.; Morris, M. A.; Schwenger, W. J.; Dogic, Z.; Mahadevan, L., Microtubules Soften Due to Cross-Sectional Flattening. *eLife* **2018,** *7*, e34695.

314. Arslan, M.; Boyce, M. C., A Micromechanically Based Anisotropic Constitutive Model for the Microtubule Wall. *Journal of Applied Mechanics* **2012,** *79*.

315. Palacci, H.; Idan, O.; Armstrong, M. J.; Agarwal, A.; Nitta, T.; Hess, H., Velocity Fluctuations in Kinesin-1 Gliding Motility Assays Originate in Motor Attachment Geometry Variations. *Langmuir* **2016,** *32*, 7943-7950.

316. Peet, D. R.; Burroughs, N. J.; Cross, R. A., Kinesin Expands and Stabilizes the Gdp-Microtubule Lattice. *Nat. Nanotechnol.* **2018,** *13*, 386-391.

317. Bieling, P.; Telley, I. A.; Piehler, J.; Surrey, T., Processive Kinesins Require Loose Mechanical Coupling for Efficient Collective Motility. *EMBO Rep.* **2008,** *9*, 1121-1127.

318. Vilfan, A.; Frey, E.; Schwabl, F.; Thormählen, M.; Song, Y.-H.; Mandelkow, E., Dynamics and Cooperativity of Microtubule Decoration by the Motor Protein Kinesin11edited by W. Baumeister. *J. Mol. Biol.* **2001,** *312*, 1011-1026.

319. Muto, E.; Sakai, H.; Kaseda, K., Long-Range Cooperative Binding of Kinesin to a Microtubule in the Presence of Atp. *The Journal of cell biology* **2005,** *168*, 691-696.

320. H Roos, W.; Campàs, O.; Montel, F.; Woehlke, G.; Spatz, J. P.; Bassereau, P.; Cappello, G., Dynamic Kinesin-1 Clustering on Microtubules Due to Mutually Attractive Interactions. *PhBio* **2008,** *5*, 046004.

321. Varga, V.; Helenius, J.; Tanaka, K.; Hyman, A. A.; Tanaka, T. U.; Howard, J., Yeast Kinesin-8 Depolymerizes Microtubules in a Length-Dependent Manner. *Nat. Cell Biol.* **2006,** *8*, 957-962.

322. Gupta, M. L.; Carvalho, P.; Roof, D. M.; Pellman, D., Plus End-Specific Depolymerase Activity of Kip3, a Kinesin-8 Protein, Explains Its Role in Positioning the Yeast Mitotic Spindle. *Nat. Cell Biol.* **2006,** *8*, 913-923.

323. Desai, A.; Verma, S.; Mitchison, T. J.; Walczak, C. E., Kin I Kinesins Are Microtubule-Destabilizing Enzymes. *Cell* **1999,** *96*, 69-78.

324. Moore, A.; Wordeman, L., The Mechanism, Function and Regulation of Depolymerizing Kinesins During Mitosis. *Trends Cell Biol.* **2004,** *14*, 537-46.

325. Dumont, E. L. P.; Do, C.; Hess, H., Molecular Wear of Microtubules Propelled by Surface-Adhered Kinesins. *Nat. Nanotechnol.* **2015,** *10*, 166-169.

326. Dumont, E. L. P.; Belmas, H.; Hess, H., Observing the Mushroom-to-Brush Transition for Kinesin Proteins. *Langmuir* **2013,** *29*, 15142-15145.

327. Reuther, C.; Diego, A. L.; Diez, S., Kinesin-1 Motors Can Increase the Lifetime of Taxol-Stabilized Microtubules. *Nat. Nanotechnol.* **2016,** *11*, 914-915.

328. Keya, J. J.; Inoue, D.; Suzuki, Y.; Kozai, T.; Ishikuro, D.; Kodera, N.; Uchihashi, T.; Kabir, A. M. R.; Endo, M.; Sada, K.; Kakugo, A., High-Resolution Imaging of a Single Gliding Protofilament of Tubulins by Hs-Afm. *Sci. Rep.* **2017,** *7*, 6166.

329. VanDelinder, V.; Adams, P. G.; Bachand, G. D., Mechanical Splitting of Microtubules into Protofilament Bundles by Surface-Bound Kinesin-1. *Sci. Rep.* **2016,** *6*, 39408.

330. Telley, I. A.; Bieling, P.; Surrey, T., Obstacles on the Microtubule Reduce the Processivity of Kinesin-1 in a Minimal in Vitro System and in Cell Extract. *Biophys. J.* **2009,** *96*, 3341-3353.

331. Saito, A.; Farhana, T. I.; Kabir, A. M. R.; Inoue, D.; Konagaya, A.; Sada, K.; Kakugo, A., Understanding the Emergence of Collective Motion of Microtubules Driven by Kinesins: Role of Concentration of Microtubules and Depletion Force. *RSC Adv.* **2017,** *7*, 13191-13197.

332. Hilitski, F.; Ward, A. R.; Cajamarca, L.; Hagan, M. F.; Grason, G. M.; Dogic, Z., Measuring Cohesion between Macromolecular Filaments One Pair at a Time: Depletion-Induced Microtubule Bundling. *Phys. Rev. Lett.* **2015,** *114*, 138102.

333. Sumino, Y.; Nagai, K. H.; Shitaka, Y.; Tanaka, D.; Yoshikawa, K.; Chate, H.; Oiwa, K., Large-Scale Vortex Lattice Emerging from Collectively Moving Microtubules. *Nature* **2012,** *483*, 448-452.

334. Tanida, S.; Furuta, K. y.; Nishikawa, K.; Hiraiwa, T.; Kojima, H.; Oiwa, K.; Sano, M., Gliding Filament System Giving Both Global Orientational Order and Clusters in Collective Motion. *Phys. Rev. B.* **2020,** *101*, 032607.

335. Malcos, J. L.; Hancock, W. O., Engineering Tubulin: Microtubule Functionalization Approaches for Nanoscale Device Applications. *Appl. Microbiol. Biotechnol.* **2011,** *90*, 1-10.

336. Agarwal, A.; Katira, P.; Hess, H., Millisecond Curing Time of a Molecular Adhesive Causes Velocity-Dependent Cargo-Loading of Molecular Shuttles. *Nano Lett.* **2009,** *9*, 1170-1175.

337. He, S. H.; Lam, A. T.; Jeune-Smith, Y.; Hess, H., Modeling Negative Cooperativity in Streptavidin Adsorption onto Biotinylated Microtubules. *Langmuir* **2012,** *28*, 10635-10639.

338. Carroll-Portillo, A.; Bachand, M.; Bachand, G. D., Directed Attachment of Antibodies to Kinesin-Powered Molecular Shuttles. *Biotechnol. Bioeng.* **2009,** *104*, 1182-1188.

339. Früh, S. M.; Steuerwald, D.; Simon, U.; Vogel, V., Covalent Cargo Loading to Molecular Shuttles Via Copper-Free "Click Chemistry". *Biomacromolecules* **2012,** *13*, 3908-3911.

340. Persson, M.; Gullberg, M.; Tolf, C.; Lindberg, A. M.; Månsson, A.; Kocer, A., Transportation of Nanoscale Cargoes by Myosin Propelled Actin Filaments. *PLoS One* **2013,** *8*, e55931.

341. Bachand, M.; Bouxsein, N. F.; Cheng, S.; von Hoyningen-Huene, S. J.; Stevens, M. J.; Bachand, G. D., Directed Self-Assembly of 1d Microtubule Nano-Arrays. *RSC Adv.* **2014,** *4*, 54641-54649.

342. Schneider, R.; Korten, T.; Walter, W. J.; Diez, S., Kinesin-1 Motors Can Circumvent Permanent Roadblocks by Side-Shifting to Neighboring Protofilaments. *Biophys. J.* **2015,** *108*, 2249-2257.

343. Schmidt, C.; Kim, B.; Grabner, H.; Ries, J.; Kulomaa, M.; Vogel, V., Tuning the "Roadblock" Effect in Kinesin-Based Transport. *Nano Lett.* **2012,** *12*, 3466-3471.

344. Ozeki, T.; Verma, V.; Uppalapati, M.; Suzuki, Y.; Nakamura, M.; Catchmark, J. M.; Hancock, W. O., Surface-Bound Casein Modulates the Adsorption and Activity of Kinesin on Sio(2) Surfaces. *Biophys. J.* **2009,** *96*, 3305-3318.

345. Verma, V.; Hancock, W. O.; Catchmark, J. M., The Role of Casein in Supporting the Operation of Surface Bound Kinesin. *J. Biol. Eng.* **2008,** *2*, 14.

346. Szkop, M.; Kliszcz, B.; Kasprzak, A. A., A Simple and Reproducible Protocol of Glass Surface Silanization for Tirf Microscopy Imaging. *Anal. Biochem.* **2018,** *549*, 119-123.

347. Albet-Torres, N.; O'Mahony, J.; Charlton, C.; Balaz, M.; Lisboa, P.; Aastrup, T.; Månsson, A.; Nicholls, I. A., Mode of Heavy Meromyosin Adsorption and Motor Function Correlated with Surface Hydrophobicity and Charge. *Langmuir* **2007,** *23*, 11147-11156.

348. Ying-Ming, H.; Uppalapati, M.; Hancock, W. O.; Jackson, T. N., Microfabricated Capped Channels for Biomolecular Motor-Based Transport. *IEEE Transactions on Advanced Packaging* **2005,** *28*, 564-570.

349. Nicolau, D. V.; Solana, G.; Kekic, M.; Fulga, F.; Mahanivong, C.; Wright, J.; dos Remedios, C. G., Surface Hydrophobicity Modulates the Operation of Actomyosin-Based Dynamic Nanodevices. *Langmuir* **2007,** *23*, 10846-10854.

350. Sundberg, M.; Rosengren, J. P.; Bunk, R.; Lindahl, J.; Nicholls, I. A.; Tågerud, S.; Omling, P.; Montelius, L.; Månsson, A., Silanized Surfaces for in Vitro Studies of Actomyosin Function and Nanotechnology Applications. *Anal. Biochem.* **2003,** *323*, 127-138.

351. Persson, M.; Albet-Torres, N.; Ionov, L.; Sundberg, M.; Höök, F.; Diez, S.; Månsson, A.; Balaz, M., Heavy Meromyosin Molecules Extending More Than 50 Nm above Adsorbing Electronegative Surfaces. *Langmuir* **2010,** *26*, 9927-9936.

352. Fischer, T.; Hess, H., Materials Chemistry Challenges in the Design of Hybrid Bionanodevices: Supporting Protein Function within Artificial Environments. *JMCh* **2007,** *17*, 943-951.

353. Månsson, A.; Balaz, M.; Albet-Torres, N.; Rosengren, K. J., In Vitro Assays of Molecular Motors--Impact of Motor-Surface Interactions. *Front. Biosci.* **2008,** *13*, 5732-54.

354. Weiss, D. G.; Langford, G. M.; Seitz-Tutter, D.; Maile, W., Analysis of the Gliding, Fishtailing and Circling Motions of Native Microtubules. *Acta Histochem. Suppl.* **1991,** *41*, 81-105.

355. Kato, K. A.; Goto, R.; Katoh, K.; Shibakami, M., Microtubule-Cyclodextrin Conjugate: Functionalization of Motile Filament with Molecular Inclusion Ability. *Biosci., Biotechnol., Biochem.* **2005,** *69*, 646-648.

356. Månsson, A.; Sundberg, M.; Balaz, M.; Bunk, R.; Nicholls, I. A.; Omling, P.; Tågerud, S.; Montelius, L., In Vitro Sliding of Actin Filaments Labelled with Single Quantum Dots. *Biochem. Biophys. Res. Commun.* **2004,** *314*, 529-534.

357. Bachand, G. D.; Rivera, S. B.; Boal, A. K.; Gaudioso, J.; Liu, J.; Bunker, B. C., Assembly and Transport of Nanocrystal Cdse Quantum Dot Nanocomposites Using Microtubules and Kinesin Motor Proteins. *Nano Lett.* **2004,** *4*, 817-821.

358. Ito, M.; Ishiwata, T.; Anan, S.; Kokado, K.; Inoue, D.; Kabir, A. M. R.; Kakugo, A.; Sada, K., Construction and Gilding of Metal-Organic Frameworks and Microtubule Conjugates. *ChemistrySelect* **2016,** *1*, 5358-5362.

359. Jia, Y.; Dong, W.; Feng, X.; Li, J.; Li, J., A Self-Powered Kinesin-Microtubule System for Smart Cargo Delivery. *Nanoscale* **2015,** *7*, 82-85.

360. Diez, S.; Reuther, C.; Dinu, C.; Seidel, R.; Mertig, M.; Pompe, W.; Howard, J., Stretching and Transporting DNA Molecules Using Motor Proteins. *Nano Lett.* **2003,** *3*, 1251-1254.

361. Bachand, G. D.; Rivera, S. B.; Carroll-Portillo, A.; Hess, H.; Bachand, M., Active Capture and Transport of Virus Particles Using a Biomolecular Motor-Driven, Nanoscale Antibody Sandwich Assay. *Small* **2006,** *2*, 381-385.

362. Schmidt, C.; Vogel, V., Molecular Shuttles Powered by Motor Proteins: Loading and Unloading Stations for Nanocargo Integrated into One Device. *Lab Chip* **2010,** *10*, 2195-2198.

363. Brunner, C.; Wahnes, C.; Vogel, V., Cargo Pick-up from Engineered Loading Stations by Kinesin Driven Molecular Shuttles. *Lab Chip* **2007,** *7*, 1263-1271.

364. Steuerwald, D.; Früh, S. M.; Griss, R.; Lovchik, R. D.; Vogel, V., Nanoshuttles Propelled by Motor Proteins Sequentially Assemble Molecular Cargo in a Microfluidic Device. *Lab Chip* **2014,** *14*, 3729-3738.

365. Månsson, A.; Sundberg, M.; Bunk, R.; Balaz, M.; Nicholls, I. A.; Omling, P.; Tegenfeldt, J. O.; Tagerud, S.; Montelius, L., Actin-Based Molecular Motors for Cargo Transportation in Nanotechnology— Potentials and Challenges. *IEEE Transactions on Advanced Packaging* **2005,** *28*, 547-555.

366. Bakewell, D. J. G.; Nicolau, D. V., Protein Linear Molecular Motor-Powered Nanodevices. *Aust. J. Chem.* **2007,** *60*, 314-332.

367. van den Heuvel, M. G. L.; Dekker, C., Motor Proteins at Work for Nanotechnology. *Science* **2007,** *317*, 333-336.

368. Iwabuchi, S.; Takahashi, T.; Hatori, K., Transport of Actin-Decorated Liposomes Along Myosin Molecules in Vitro. *Biochem. Biophys. Res. Commun.* **2012,** *422*, 164-168.

369. Suzuki, N.; Miyata, H.; Ishiwata, S.; Kinosita, K., Preparation of Bead-Tailed Actin Filaments: Estimation of the Torque Produced by the Sliding Force in an in Vitro Motility Assay. *Biophys. J.* **1996,** *70*, 401-408.

370. Patolsky, F.; Weizmann, Y.; Willner, I., Actin-Based Metallic Nanowires as Bio-Nanotransporters. *Nature Materials* **2004,** *3*, 692-695.

371. Hess, H.; Clemmens, J.; Howard, J.; Vogel, V., Surface Imaging by Self-Propelled Nanoscale Probes. *Nano Lett.* **2002,** *2*, 113-116.

372. Inoue, D.; Gutmann, G.; Nitta, T.; Kabir, A. M. R.; Konagaya, A.; Tokuraku, K.; Sada, K.; Hess, H.; Kakugo, A., Adaptation of Patterns of Motile Filaments under Dynamic Boundary Conditions. *ACS Nano* **2019,** *13*, 12452-12460.

373. Groß, H.; Heil, H. S.; Ehrig, J.; Schwarz, F. W.; Hecht, B.; Diez, S., Parallel Mapping of Optical near-Field Interactions by Molecular Motor-Driven Quantum Dots. *Nat. Nanotechnol.* **2018,** *13*, 691-695.

374. Hess, H.; Howard, J.; Vogel, V., A Piconewton Forcemeter Assembled from Microtubules and Kinesins. *Nano Lett.* **2002,** *2*, 1113-1115.

375. van den Heuvel, M. G. L.; Butcher, C. T.; Smeets, R. M. M.; Diez, S.; Dekker, C., High Rectifying Efficiencies of Microtubule Motility on Kinesin-Coated Gold Nanostructures. *Nano Lett.* **2005,** *5*, 1117-1122.

376. Doot, R. K.; Hess, H.; Vogel, V., Engineered Networks of Oriented Microtubule Filaments for Directed Cargo Transport. *Soft Matter* **2007,** *3*, 349-356.

377. Bunk, R.; Klinth, J.; Montelius, L.; Nicholls, I. A.; Omling, P.; Tagerud, S.; Mansson, A., Actomyosin Motility on Nanostructured Surfaces. *Biochemical Biophysical Research Communications* **2003,** *301*, 783-8.

378. Jaber, J. A.; Chase, P. B.; Schlenoff, J. B., Actomyosin-Driven Motility on Patterned Polyelectrolyte Mono- and Multilayers. *Nano Lett.* **2003,** *3*, 1505-1509.

379. Tucker, R.; Katira, P.; Hess, H., Herding Nanotransporters: Localized Activation Via Release and Sequestration of Control Molecules. *Nano Lett.* **2008,** *8*, 221-226.

380. van den Heuvel, M. G. L.; De Graaff, M. P.; Dekker, C., Molecular Sorting by Electrical Steering of Microtubules in Kinesin-Coated Channels. *Science* **2006,** *312*, 910-914.

381. Hiratsuka, Y.; Tada, T.; Oiwa, K.; Kanayama, T.; Uyeda, T. Q., Controlling the Direction of Kinesin-Driven Microtubule Movements Along Microlithographic Tracks. *Biophys. J.* **2001,** *81*, 1555-61.

382. Suzuki, H.; Oiwa, K.; Yamada, A.; Sakakibara, H.; Nakayama, H.; Mashiko, S., Linear Arrangement of Motor Protein on a Mechanically Deposited Fluoropolymer Thin Film. *Jap. J. Appl. Phys. Part 1* **1995,** *34*, 3937-3941.

383. Suzuki, H.; Yamada, A.; Oiwa, K.; Nakayama, H.; Mashiko, S., Control of Actin Moving Trajectory by Patterned Poly(Methylmethacrylate) Tracks. *Biophys. J.* **1997,** *72*, 1997-2001.

384. Sundberg, M.; Bunk, R.; Albet-Torres, N.; Kvennefors, A.; Persson, F.; Montelius, L.; Nicholls, I. A.; Ghatnekar-Nilsson, S.; Omling, P.; Tågerud, S.; Månsson, A., Actin Filament Guidance on a Chip: Toward High-Throughput Assays and Lab-on-a-Chip Applications. *Langmuir* **2006,** *22*, 7286-7295.

385. Nitta, T.; Hess, H., Dispersion in Active Transport by Kinesin-Powered Molecular Shuttles. *Nano Lett.* **2005,** *5*, 1337-1342.

386. Nitta, T.; Tanahashi, A.; Hirano, M.; Hess, H., Simulating Molecular Shuttle Movements: Towards Computer-Aided Design of Nanoscale Transport Systems. *Lab Chip* **2006,** *6*, 881-885.

387. Nitta, T.; Tanahashi, A.; Obara, Y.; Hirano, M.; Razumova, M.; Regnier, M.; Hess, H., Comparing Guiding Track Requirements for Myosin- and Kinesin-Powered Molecular Shuttles. *Nano Lett.* **2008,** *8*, 2305-2309.

388. Hess, H.; Matzke, C. M.; Doot, R. K.; Clemmens, J.; Bachand, G. D.; Bunker, B. C.; Vogel, V., Molecular Shuttles Operating Undercover: A New Photolithographic Approach for the Fabrication of Structured Surfaces Supporting Directed Motility. *Nano Lett.* **2003,** *3*, 1651-1655.

389. Reuther, C.; Hajdo, L.; Tucker, R.; Kasprzak, A. A.; Diez, S., Biotemplated Nanopatterning of Planar Surfaces with Molecular Motors. *Nano Lett.* **2006,** *6*, 2177-2183.

390. Nicolau, D. V.; Suzuki, H.; Mashiko, S.; Taguchi, T.; Yoshikawa, S., Actin Motion on Microlithographically Functionalized Myosin Surfaces and Tracks. *Biophys. J.* **1999,** *77*, 1126-34.

391. Ionov, L.; Stamm, M.; Diez, S., Size Sorting of Protein Assemblies Using Polymeric Gradient Surfaces. *Nano Lett.* **2005,** *5*, 1910-1914.

392. Reuther, C.; Tucker, R.; Ionov, L.; Diez, S., Programmable Patterning of Protein Bioactivity by Visible Light. *Nano Lett.* **2014,** *14*, 4050-4057.

393. Reuther, C.; Mittasch, M.; Naganathan, S. R.; Grill, S. W.; Diez, S., Highly-Efficient Guiding of Motile Microtubules on Non-Topographical Motor Patterns. *Nano Lett.* **2017,** *17*, 5699-5705.

394. Nomura, A.; Uyeda, T. Q. P.; Yumoto, N.; Tatsu, Y., Photo-Control of Kinesin-Microtubule Motility Using Caged Peptides Derived from the Kinesin C-Terminus Domain. *ChCom* **2006**, 3588-3590.

395. Perur, N.; Yahara, M.; Kamei, T.; Tamaoki, N., A Non-Nucleoside Triphosphate for Powering Kinesin-Microtubule Motility with Photo-Tunable Velocity. *ChCom* **2013,** *49*, 9935-9937.

396. Islam, M. J.; Matsuo, K.; Menezes, H. M.; Takahashi, M.; Nakagawa, H.; Kakugo, A.; Sada, K.; Tamaoki, N., Substrate Selectivity and Its Mechanistic Insight of the Photo-Responsive Non-Nucleoside Triphosphate for Myosin and Kinesin. *Org. Biomol. Chem.* **2019,** *17*, 53-65.

397. Amrutha, A. S.; Kumar, K. R. S.; Kikukawa, T.; Tamaoki, N., Targeted Activation of Molecular Transportation by Visible Light. *ACS Nano* **2017,** *11*, 12292-12301.

398. Amrutha, A. S.; Sunil Kumar, K. R.; Tamaoki, N., Azobenzene-Based Photoswitches Facilitating Reversible Regulation of Kinesin and Myosin Motor Systems for Nanotechnological Applications. *ChemPhotoChem* **2019,** *3*, 337-346.

399. Tucker, R.; Saha, A. K.; Katira, P.; Bachand, M.; Bachand, G. D.; Hess, H., Temperature Compensation for Hybrid Devices: Kinesin's K-M Is Temperature Independent. *Small* **2009,** *5*, 1279-1282.

400. Korten, T.; Birnbaum, W.; Kuckling, D.; Diez, S., Selective Control of Gliding Microtubule Populations. *Nano Lett.* **2012,** *12*, 348-353.

401. Ramsey, L.; Schroeder, V.; van Zalinge, H.; Berndt, M.; Korten, T.; Diez, S.; Nicolau, D. V., Control and Gating of Kinesin-Microtubule Motility on Electrically Heated Thermo-Chips. *Biomed. Microdevices* **2014,** *16*, 459-463.

402. Jia, L.; Moorjani, S. G.; Jackson, T. N.; Hancock, W. O., Microscale Transport and Sorting by Kinesin Molecular Motors. *Biomed. Microdevices* **2004,** *6*, 67-74.

403. Löwe, J.; Li, H.; Downing, K. H.; Nogales, E., Refined Structure of Aβ-Tubulin at 3.5 Å Resolution11edited by I. A. Wilson. *J. Mol. Biol.* **2001,** *313*, 1045-1057.

404. Stracke, R.; Bohm, K. J.; Wollweber, L.; Tuszynski, J. A.; Unger, E., Analysis of the Migration Behaviour of Single Microtubules in Electric Fields. *Biochem. Biophys. Res. Commun.* **2002,** *293*, 602-9.

405. Kim, T.; Kao, M.-T.; Hasselbrink, E. F.; Meyhöfer, E., Active Alignment of Microtubules with Electric Fields. *Nano Lett.* **2007,** *7*, 211-217.

406. van den Heuvel, M. G. L.; Butcher, C. T.; Lemay, S. G.; Diez, S.; Dekker, C., Electrical Docking of Microtubules for Kinesin-Driven Motility in Nanostructures. *Nano Lett.* **2005,** *5*, 235-241.

407. Kim, E.; Byun, K.-E.; Choi, D. S.; Lee, D. J.; Cho, D. H.; Lee, B. Y.; Yang, H.; Heo, J.; Chung, H.-J.; Seo, S.; Hong, S., Electrical Control of Kinesin–Microtubule Motility Using a Transparent Functionalized-Graphene Substrate. *Nanotechnology* **2013,** *24*, 195102.

408. Uppalapati, M.; Huang, Y.-M.; Jackson, T. N.; Hancock, W. O., Microtubule Alignment and Manipulation Using Ac Electrokinetics. *Small* **2008,** *4*, 1371-1381.

409. Glade, N.; Tabony, J., Brief Exposure to High Magnetic Fields Determines Microtubule Self-Organisation by Reaction–Diffusion Processes. *Biophys. Chem.* **2005,** *115*, 29-35.

410. Bras, W.; Diakun, G. P.; Diaz, J. F.; Maret, G.; Kramer, H.; Bordas, J.; Medrano, F. J., The Susceptibility of Pure Tubulin to High Magnetic Fields: A Magnetic Birefringence and X-Ray Fiber Diffraction Study. *Biophys. J.* **1998,** *74*, 1509-21.

411. Mahajan, K. D.; Cui, Y.; Dorcéna, C. J.; Bouxsien, N. F.; Bachand, G. D.; Chalmers, J. J.; Winter, J. O., Magnetic Quantum Dots Steer and Detach Microtubules from Kinesin-Coated Surfaces. *Biotechnol. J.* **2018,** *13*, 1700402.

412. Mahajan, K. D.; Ruan, G.; Dorcena, C. J.; Vieira, G.; Nabar, G.; Bouxsein, N. F.; Chalmers, J. J.; Bachand, G. D.; Sooryakumar, R.; Winter, J. O., Steering Microtubule Shuttle Transport with Dynamically Controlled Magnetic Fields. *Nanoscale* **2016,** *8*, 8641-8649.

413. Platt, M.; Hancock, W. O.; Muthukrishnan, G.; Williams, M. E., Millimeter Scale Alignment of Magnetic Nanoparticle Functionalized Microtubules in Magnetic Fields. *J. Am. Chem. Soc.* **2005,** *127*, 15686-15687.

414. Nagai, K. H.; Sumino, Y.; Montagne, R.; Aranson, I. S.; Chaté, H., Collective Motion of Self-Propelled Particles with Memory. *Phys. Rev. Lett.* **2015,** *114*, 168001.

415. K Svoboda, a.; Block, S. M., Biological Applications of Optical Forces. *Annu. Rev. Biophys. Biomol. Struct.* **1994,** *23*, 247-285.

416. Svoboda, K.; Block, S. M., Force and Velocity Measured for Single Kinesin Molecules. *Cell* **1994,** *77*, 773-84.

417. Svoboda, K.; Schmidt, C. F.; Schnapp, B. J.; Block, S. M., Direct Observation of Kinesin Stepping by Optical Trapping Interferometry. *Nature* **1993,** *365*, 721-727.

418. Wollman, A. J.; Sanchez-Cano, C.; Carstairs, H. M.; Cross, R. A.; Turberfield, A. J., Transport and Self-Organization across Different Length Scales Powered by Motor Proteins and Programmed by DNA. *Nat. Nanotechnol.* **2014,** *9*, 44-47.

419. Matsuda, K.; Kabir, A. M. R.; Akamatsu, N.; Saito, A.; Ishikawa, S.; Matsuyama, T.; Ditzer, O.; Islam, M. S.; Ohya, Y.; Sada, K.; Konagaya, A.; Kuzuya, A.; Kakugo, A., Artificial Smooth Muscle Model Composed of Hierarchically Ordered Microtubule Asters Mediated by DNA Origami Nanostructures. *Nano Lett.* **2019,** *19*, 3933-3938.

420. Sumpter, D. J. T., The Principles of Collective Animal Behaviour. *Philos. Trans. R. Soc. B* **2006,** *361*, 5-22.

421. Gilbert, C.; Robertson, G.; Le Maho, Y.; Naito, Y.; Ancel, A., Huddling Behavior in Emperor Penguins: Dynamics of Huddling. *Physiol. Behav.* **2006,** *88*, 479-488.

422. Fretwell, P. T.; LaRue, M. A.; Morin, P.; Kooyman, G. L.; Wienecke, B.; Ratcliffe, N.; Fox, A. J.; Fleming, A. H.; Porter, C.; Trathan, P. N., An Emperor Penguin Population Estimate: The First Global, Synoptic Survey of a Species from Space. *PLoS One* **2012,** *7*, e33751.

423. Deutsch, A.; Theraulaz, G.; Vicsek, T., Collective Motion in Biological Systems. *Interface Focus* **2012,** *2*, 689-692.

424. Vicsek, T.; Czirók, A.; Ben-Jacob, E.; Cohen, I.; Shochet, O., Novel Type of Phase Transition in a System of Self-Driven Particles. *Phys. Rev. Lett.* **1995,** *75*, 1226-1229.

425. Ballerini, M.; Cabibbo, N.; Candelier, R.; Cavagna, A.; Cisbani, E.; Giardina, I.; Lecomte, V.; Orlandi, A.; Parisi, G.; Procaccini, A.; Viale, M.; Zdravkovic, V., Interaction Ruling Animal Collective Behavior Depends on Topological Rather Than Metric Distance: Evidence from a Field Study. *Proc. Natl. Acad. Sci. U. S. A.* **2008,** *105*, 1232-1237.

426. Vicsek, T.; Zafeiris, A., Collective Motion. *Phys. Rep.* **2012,** *517*, 71-140.

427. Rubenstein, M.; Cornejo, A.; Nagpal, R., Programmable Self-Assembly in a Thousand-Robot Swarm. *Science* **2014,** *345*, 795.

428. Werfel, J.; Petersen, K.; Nagpal, R., Designing Collective Behavior in a Termite-Inspired Robot Construction Team. *Science* **2014,** *343*, 754.

429. Yang, G.-Z.; Bellingham, J.; Dupont, P. E.; Fischer, P.; Floridi, L.; Full, R.; Jacobstein, N.; Kumar, V.; McNutt, M.; Merrifield, R.; Nelson, B. J.; Scassellati, B.; Taddeo, M.; Taylor, R.; Veloso, M.; Wang, Z. L.; Wood, R., The Grand Challenges of Science Robotics. *Sci. Robot.* **2018,** *3*, eaar7650.

430. Schuerle, S.; Soleimany, A. P.; Yeh, T.; Anand, G. M.; Häberli, M.; Fleming, H. E.; Mirkhani, N.; Qiu, F.; Hauert, S.; Wang, X.; Nelson, B. J.; Bhatia, S. N., Synthetic and Living Micropropellers for Convection-Enhanced Nanoparticle Transport. *Sci. Adv.* **2019,** *5*, eaav4803.

431. Li, J.; Angsantikul, P.; Liu, W.; Esteban-Fernández de Ávila, B.; Chang, X.; Sandraz, E.; Liang, Y.; Zhu, S.; Zhang, Y.; Chen, C.; Gao, W.; Zhang, L.; Wang, J., Biomimetic Platelet-Camouflaged Nanorobots for Binding and Isolation of Biological Threats. *Adv. Mater.* **2018,** *30*, 1704800.

432. Palagi, S.; Fischer, P., Bioinspired Microrobots. *Nat. Rev. Mat.* **2018,** *3*, 113-124.

433. Karshalev, E.; Esteban-Fernández de Ávila, B.; Beltrán-Gastélum, M.; Angsantikul, P.; Tang, S.; Mundaca-Uribe, R.; Zhang, F.; Zhao, J.; Zhang, L.; Wang, J., Micromotor Pills as a Dynamic Oral Delivery Platform. *ACS Nano* **2018,** *12*, 8397-8405.

434. Alapan, Y.; Yasa, O.; Schauer, O.; Giltinan, J.; Tabak, A. F.; Sourjik, V.; Sitti, M., Soft Erythrocyte-Based Bacterial Microswimmers for Cargo Delivery. *Sci. Robot.* **2018,** *3*, eaar4423.

435. Felfoul, O.; Mohammadi, M.; Taherkhani, S.; de Lanauze, D.; Zhong Xu, Y.; Loghin, D.; Essa, S.; Jancik, S.; Houle, D.; Lafleur, M.; Gaboury, L.; Tabrizian, M.; Kaou, N.; Atkin, M.; Vuong, T.; Batist, G.; Beauchemin, N.; Radzioch, D.; Martel, S., Magneto-Aerotactic Bacteria Deliver Drug-Containing Nanoliposomes to Tumour Hypoxic Regions. *Nat. Nanotechnol.* **2016,** *11*, 941.

436. Hult, R.; Campos, G. R.; Steinmetz, E.; Hammarstrand, L.; Falcone, P.; Wymeersch, H., Coordination of Cooperative Autonomous Vehicles: Toward Safer and More Efficient Road Transportation. *IEEE Signal Process. Mag.* **2016,** *33*, 74-84.

437. Iftekhar, L.; Olfati-Saber, R. In *Autonomous Driving for Vehicular Networks with Nonlinear Dynamics*, 2012 IEEE Intelligent Vehicles Symposium, 3-7 June 2012; 2012; pp 723-729.

438. Kushleyev, A.; Mellinger, D.; Powers, C.; Kumar, V., Towards a Swarm of Agile Micro Quadrotors. *Auton. Robots* **2013,** *35*, 287-300.

439. Dennis, J. R.; Howard, J.; Vogel, V., Molecular Shuttles: Directed Motion of Microtubules Along Nanoscale Kinesin Tracks. *Nanotechnology* **1999,** *10*, 232-236.

440. Keber, F. C.; Loiseau, E.; Sanchez, T.; DeCamp, S. J.; Giomi, L.; Bowick, M. J.; Marchetti, M. C.; Dogic, Z.; Bausch, A. R., Topology and Dynamics of Active Nematic Vesicles. *Science* **2014,** *345*, 1135.

441. Keya, J. J.; Kabir, A. M. R.; Inoue, D.; Sada, K.; Hess, H.; Kuzuya, A.; Kakugo, A., Control of Swarming of Molecular Robots. *Sci. Rep.* **2018,** *8*, 11756.

442. VanDelinder, V.; Brener, S.; Bachand, G. D., Mechanisms Underlying the Active Self-Assembly of Microtubule Rings and Spools. *Biomacromolecules* **2016,** *17*, 1048-1056.

443. Schaller, V.; Weber, C.; Semmrich, C.; Frey, E.; Bausch, A. R., Polar Patterns of Driven Filaments. *Nature* **2010,** *467*, 73-77.

444. Bronstein, J. L., The Study of Mutualism. In *Mutualism*, Oxford University Press: Oxford, 2015.

445. Wing, L. D.; Buss, I. O., Elephants and Forests. *Wildlife Monographs* **1970**, 3-92.

446. Blake, S.; Inkamba-Nkulu, C., Fruit, Minerals, and Forest Elephant Trails: Do All Roads Lead to Rome? *Biotropica* **2004,** *36*, 392-401.

447. Campos-Arceiz, A.; Blake, S., Megagardeners of the Forest – the Role of Elephants in Seed Dispersal. *Acta Oecol.* **2011,** *37*, 542-553.

448. Nieba, L.; Nieba-Axmann, S. E.; Persson, A.; Hämäläinen, M.; Edebratt, F.; Hansson, A.; Lidholm, J.; Magnusson, K.; Karlsson, Å. F.; Plückthun, A., Biacore Analysis of Histidine-Tagged Proteins Using a Chelating Nta Sensor Chip. *Anal. Biochem.* **1997,** *252*, 217-228.

449. Knecht, S.; Ricklin, D.; Eberle, A. N.; Ernst, B., Oligohis-Tags: Mechanisms of Binding to Ni2+-Nta Surfaces. *J. Mol. Recognit.* **2009,** *22*, 270-279.

450. Myszka, D. G.; He, X.; Dembo, M.; Morton, T. A.; Goldstein, B., Extending the Range of Rate Constants Available from Biacore: Interpreting Mass Transport-Influenced Binding Data. *Biophys. J.* **1998,** *75*, 583-594.

451. Schuck, P.; Zhao, H., The Role of Mass Transport Limitation and Surface Heterogeneity in the Biophysical Characterization of Macromolecular Binding Processes by Spr Biosensing. In *Surface Plasmon Resonance: Methods and Protocols*, Mol, N. J.; Fischer, M. J. E., Eds. Humana Press: Totowa, NJ, 2010; pp 15-54.

452. Miura, T.; Seki, K., Diffusion Influenced Adsorption Kinetics. *J. Phys. Chem. B* **2015,** *119*, 10954-10961.

453. Chang, Y.; Chu, W.-L.; Chen, W.-Y.; Zheng, J.; Liu, L.; Ruaan, R.-C.; Higuchi, A., A Systematic Spr Study of Human Plasma Protein Adsorption Behavior on the Controlled Surface Packing of Self-Assembled Poly(Ethylene Oxide) Triblock Copolymer Surfaces. *J. Biomed. Mater. Res. A* **2010,** *93A*, 400-408.

454. Lata, S.; Reichel, A.; Brock, R.; Tampé, R.; Piehler, J., High-Affinity Adaptors for Switchable Recognition of Histidine-Tagged Proteins. *J. Am. Chem. Soc.* **2005,** *127*, 10205-10215.

455. Sitt, A.; Hess, H., Directed Transport by Surface Chemical Potential Gradients for Enhancing Analyte Collection in Nanoscale Sensors. *Nano Lett.* **2015,** *15*, 3341-3350.

456. Walder, R.; Nelson, N.; Schwartz, D. K., Single Molecule Observations of Desorption-Mediated Diffusion at the Solid-Liquid Interface. *Phys. Rev. Lett.* **2011,** *107*.

457. Narayan, V.; Ramaswamy, S.; Menon, N., Long-Lived Giant Number Fluctuations in a Swarming Granular Nematic. *Science* **2007,** *317*, 105-108.

458. Schief, W. R.; Clark, R. H.; Crevenna, A. H.; Howard, J., Inhibition of Kinesin Motility by Adp and Phosphate Supports a Hand-over-Hand Mechanism. *Proc. Natl. Acad. Sci. U. S. A.* **2004,** *101*, 1183-8.

459. Rank, M.; Frey, E., Crowding and Pausing Strongly Affect Dynamics of Kinesin-1 Motors Along Microtubules. *Biophys. J.* **2018,** *115*, 1068-1081.

460. Alonso, M. C.; Drummond, D. R.; Kain, S.; Hoeng, J.; Amos, L.; Cross, R. A., An Atp Gate Controls Tubulin Binding by the Tethered Head of Kinesin-1. *Science* **2007,** *316*, 120-123.

461. Boal, A. K.; Bachand, G. D.; Rivera, S. B.; Bunker, B. C., Interactions between Cargo-Carrying Biomolecular Shuttles. *Nanotechnology* **2005,** *17*, 349-354.

462. Consortium, T. U., Uniprot: A Worldwide Hub of Protein Knowledge. *Nucleic Acids Res.* **2018,** *47*, D506-D515.

463. Ishigure, Y.; Nitta, T., Understanding the Guiding of Kinesin/Microtubule-Based Microtransporters in Microfabricated Tracks. *Langmuir* **2014,** *30*, 12089-12096.

464. Drechsler, H.; Xu, Y.; Geyer, V. F.; Zhang, Y.; Diez, S., Multivalent Electrostatic Microtubule Interactions of Synthetic Peptides Are Sufficient to Mimic Advanced Map-Like Behavior. *Mol. Biol. Cell* **2019,** *30*, 2953-2968.

465. Clemmens, J.; Hess, H.; Lipscomb, R.; Hanein, Y.; Böhringer, K. F.; Matzke, C. M.; Bachand, G. D.; Bunker, B. C.; Vogel, V., Mechanisms of Microtubule Guiding on Microfabricated Kinesin-Coated Surfaces: Chemical and Topographic Surface Patterns. *Langmuir* **2003,** *19*, 10967-10974.

466. Surrey, T.; Nédélec, F.; Leibler, S.; Karsenti, E., Physical Properties Determining Self-Organization of Motors and Microtubules. *Science* **2001,** *292*, 1167-1171.

467. Jeffrey M. Moore, T. N. T., Matthew A. Glaser, Meredith D. Betterton, Collective Motion of Driven Semiflexible Filaments Tuned by Soft Repulsion and Stiffness. *arXiv* **2019**.

468. Rogers, K. R.; Weiss, S.; Crevel, I.; Brophy, P. J.; Geeves, M.; Cross, R., Kif1d Is a Fast Non-Processive Kinesin That Demonstrates Novel K-Loop-Dependent Mechanochemistry. *EMBO J.* **2001,** *20*, 5101-5113.

469. Parthasarathy, R., Rapid, Accurate Particle Tracking by Calculation of Radial Symmetry Centers. *Nat. Methods* **2012,** *9*, 724-726.

470. Zhang, Y.; Hess, H., Enhanced Diffusion of Catalytically Active Enzymes. *ACS Cent. Sci.* **2019,** *5*, 939-948.

471. Young, M. E.; Carroad, P. A.; Bell, R. L., Estimation of Diffusion Coefficients of Proteins. *Biotechnol. Bioeng.* **1980,** *22*, 947-955.

472. Yajima, J.; Alonso, M. C.; Cross, R. A.; Toyoshima, Y. Y., Direct Long-Term Observation of Kinesin Processivity at Low Load. *Curr. Biol.* **2002,** *12*, 301-306.

473. Milic, B.; Andreasson, J. O. L.; Hancock, W. O.; Block, S. M., Kinesin Processivity Is Gated by Phosphate Release. *Proc. Natl. Acad. Sci. U. S. A.* **2014,** *111*, 14136-14140.

474. Cross, R. A., The Kinetic Mechanism of Kinesin. *Trends Biochem. Sci.* **2004,** *29*, 301-309.

475. Mickolajczyk, K. J.; Hancock, W. O., Kinesin Processivity Is Determined by a Kinetic Race from a Vulnerable One-Head-Bound State. *Biophys. J.* **2017,** *112*, 2615-2623.

476. Isojima, H.; Iino, R.; Niitani, Y.; Noji, H.; Tomishige, M., Direct Observation of Intermediate States During the Stepping Motion of Kinesin-1. *Nat. Chem. Biol.* **2016,** *12*, 290-297.

Appendix A

A.1: Full set of ordinary differential equations describing a two-enzyme cascade

The set of ordinary differential equations describing a two-enzyme cascade are written below:

$$\frac{d[S]}{dt} = -k_{on,1}[E_1][S] + k_{off,1}[E_1S] \quad (A.1)$$

$$\frac{d[E_1S]}{dt} = k_{on,1}[E_1][S] - k_{off,1}[E_1S] - k_{cat,1}[E_1S] \quad (A.2)$$

$$\frac{d[E_1]}{dt} = -k_{on,1}[E_1][S] + k_{off,1}[E_1S] + k_{cat,1}[E_1S] \quad (A.3)$$

$$\frac{d[I]}{dt} = k_{cat,1}[E_1S] - k_{on,2}[E_2][I] + k_{off,2}[E_2I] \quad (A.4)$$

$$\frac{d[E_2I]}{dt} = k_{on,2}[E_2][I] - k_{off,2}[E_2I] - k_{cat,2}[E_2I] \quad (A.5)$$

$$\frac{d[E_2]}{dt} = -k_{on,2}[E_2][I] + k_{off,2}[E_2I] + k_{cat,2}[E_2I] \quad (A.6)$$

$$\frac{d[P]}{dt} = k_{cat,2}[E_2I] \quad (A.7)$$

In the system above, [I] is the concentration of intermediate, [E_2] is the concentration of unbound enzyme 2, [E_2I] is the concentration of enzyme 2-intermediate complex, and the rate constants are defined as previously and indexed by their respective enzyme.

A.2: Justification for a zeroth-order rate of intermediate production

The use of a zeroth-order production rate for intermediate molecules by the first enzyme in the cascade can be justified as follows. First, the time to quasi-steady state can by estimated by $\tau_{QSSA} \approx k_{on,1}\left([S] + K_{M,1}\right)^{-1} < k_{cat,1}^{-1}$ (this expression can be derived by solving the ODE in Equation 1.3 with respect to time while considering [S] as a constant). Since the processes that we will be examining take place on a time scale longer than $k_{cat,1}^{-1}$, we can employ the Michaelis-Menten Equation to describe the dynamics of the upstream enzyme. This simplifies equations A.1-A.7 to the following form:

$$\frac{d[I]}{dt} = \frac{k_{cat,1}\left[E_{1,0}\right][S]}{K_{M,1} + [S]}\left(1 - \frac{[E_2]}{\left[E_{2,0}\right]} f_{channel}\right) - k_{on}[E_2][I] + k_{off}[E_2 I] \qquad (A.8)$$

$$\frac{d[E_2 I]}{dt} = \frac{k_{cat,1}\left[E_{1,0}\right][S]}{K_{M,1} + [S]} \cdot \frac{[E_2]}{\left[E_{2,0}\right]} f_{channel} + k_{on}[E_2][I] - k_{off}[E_2 I] - k_{cat,2}[E_2 I] \qquad (A.9)$$

$$\frac{d[P]}{dt} = k_{cat}[E_2 I] \qquad (A.10)$$

Where $K_{M,1}$ is the Michaelis-Menten constant for enzyme 1. The rate constants k_{on}, k_{off}, and k_{cat} are the rate constants for enzyme 2, but their subscript was removed for brevity of notation. The concentrations $\left[E_{1,0}\right]$ and $\left[E_{2,0}\right]$ denote the total concentrations of each type of enzyme. There is a prefactor of $[E_2]/\left[E_{2,0}\right]$ before $f_{channel}$ to take into account the probability that the active site of the downstream enzyme is occupied.

As a further simplification, we assume excess initial substrate, $[S_0] \gg K_{M,1}$, so the throughput of the first reaction remains constant. Rewriting $V_S = \frac{k_{cat,1}[E_1][S]}{K_{M,1}+[S]}$, and using $[E_2] = \left[E_{2,0}\right] - [E_2 I]$, we arrive at the system of 3 ODEs shown in the main text.

A.3: Jacobian of nonlinear system of ODEs describing intermediate and intermediate-complex concentrations

The Jacobian and characteristic equation for the nonlinear system of ODEs can be written down as follows:

$$J = \begin{bmatrix} \frac{d[\dot{I}]}{d[I]} & \frac{d[\dot{I}]}{d[E_2I]} \\ \frac{d[\dot{E_2I}]}{d[I]} & \frac{d[\dot{E_2I}]}{d[E_2I]} \end{bmatrix}\Bigg|_{\substack{[I]=[I]^* \\ [E_2I]=[E_2I]^*}} =$$

$$= \begin{bmatrix} -k_{on}[E_2]^* & \frac{V_S f_{channel}}{[E_{2,0}]} + k_{on}[I]^* + k_{off} \\ k_{on}[E_2]^* & -\frac{V_S f_{channel}}{[E_{2,0}]} - k_{on}[I]^* - k_{off} - k_{cat} \end{bmatrix} \qquad (A.11)$$

$$J\vec{v} = \lambda\vec{v} \qquad (A.12)$$

$$\lambda^2 + k_{on}\left([I]^* + K_M + [E_2]^* + \frac{V_S f_{channel}}{k_{on}[E_{2,0}]}\right)\lambda + k_{cat,2}k_{on}[E_2]^* = 0 \qquad (A.13)$$

Plugging in the steady state concentrations, $[I]^*$ from equation 1.31, and $[E_2]^*$ from equation 1.29, we arrive at the characteristic equation found in the main text.

A.4: The enzyme-intermediate complex concentration rapidly reaches QSS

We can determine the characteristic time to steady state for this reaction by assuming that the arrival to QSS is much faster than the time scale of changes in [I]. Then, solving Equation 1.27 while treating [I] as a constant, we find:

$$[E_2I](t) = \frac{[E_{2,0}][\mathcal{I}]}{K_M + [\mathcal{I}]} \cdot \left(1 - e^{-\lambda_{QSSA}t}\right) \tag{A.14}$$

$$\lambda_{QSSA} = k_{on}\left(K_M + [I] + \frac{V_s}{k_{on}[E_{2,0}]} f_{channel}\right) > k_{on}K_M > k_{cat} \tag{A.15}$$

The above equation demonstrates that the time to quasi steady state, $\tau_{QSSA} = \lambda_{QSSA}^{-1}$, can bounded from above: $\tau_{QSSA} < k_{cat}^{-1}$.

The time to quasi steady state for the enzyme-intermediate complex concentration is much faster than the time to quasi steady state for the bulk intermediate concentration. This can be seen by solving Equation 1.26 while treating [E_2I] as a constant; we find the reaction time scale to be:

$$\lambda_{I,QSSA} = k_{on}\left([E_{2,0}] - [E_2I]\right) < k_{on}[E_{2,0}] \tag{A.16}$$

In contrast to the time to quasi steady state for the enzyme-intermediate complex concentration, we can only lower bound the time to quasi steady state for the intermediate concentration. Using , $\tau_{I,QSSA} = \lambda_{I,QSSA}^{-1}$, we find:

$$\tau_{I,QSSA} > \left(k_{on}\left[E_{2,0}\right]\right)^{-1} \gg (k_{on}K_M)^{-1} > \tau_{QSSA} \qquad (A.17)$$

Where we have used the fact the K_M of an enzymatic reaction, whose values usually range from the low micromolar range to high millimolar range, is usually much greater than the enzyme concentration, which usually remains in the nanomolar range.

Appendix B

B.1: Propensity functions for stochastic simulation of enzyme cascade with waiting rooms

For each waiting room i ($1 \leq i \leq N-1$), the following set of propensity functions was defined:

$$\text{Forward reaction: } \alpha_{on,i} = c_{on}\widetilde{S_i}\widetilde{E_i} \quad (B.1)$$

$$\text{Reverse reaction: } \alpha_{off,i} = c_{off}\widetilde{E_i S_i} \quad (B.2)$$

$$\text{Catalysis: } \alpha_{cat,i} = c_{cat,i}\widetilde{E_i S_i} \quad (B.3)$$

$$\text{Impatience: } \alpha_{loss,i} = c_{loss}\widetilde{S_i} \quad (B.4)$$

Where tilde symbols denote the population of the species in number of molecules.

For the first waiting room, the production of $\widetilde{S_1}$ is modelled using the following propensity function:

$$\text{Production reaction: } \alpha_{prod} = c_{cat,0} \quad (B.5)$$

We defined the total propensity function as

$$\alpha_0 = \sum_{i=1}^{N-1}\left(\alpha_{on,i} + \alpha_{off,i} + \alpha_{cat,i} + \alpha_{loss,i}\right) + \alpha_{prod} \quad (B.6)$$

The algorithm for the stochastic simulation of the enzyme cascade is detailed in Section B.2.

B.2 Algorithm for stochastic simulation of enzyme cascade with waiting rooms

In the following algorithm, propensity functions are defined as in Section B.2.

Initialization

$$For\ 1\ \leq i\ \leq N-1, \tilde{S}_i(0) = 0$$

$$\tilde{P}(0) = 0$$

System update

1. Generate two random numbers u_1 and u_2 according to a uniform law over [0,1]
2. Compute τ using the following equation

$$\tau = \frac{1}{\alpha_0(t)} \ln\left(\frac{1}{u_1}\right) \qquad (B.7)$$

   Above, $\alpha_0(t)$ is a function of time because the total propensity function depends on the number of molecules in each state at that time (i.e. number of substrate molecules in the waiting room, number of complex/free enzymes, etc.)

3. Update t: $t \rightarrow t + \tau$
4. Choose the occurring reaction using u_2 according to Gillespie et al.[92] That is, the reaction is chosen with a probability proportional to its reaction rate.
5. Update the system composition according to the occurring reaction chosen in step 4.
   a. If the reverse reaction is chosen
      i. The waiting room i is not full: $\tilde{S}_i \rightarrow \tilde{S}_i + 1$ & $\widetilde{E_\iota S_i} \rightarrow \widetilde{E_\iota S_i} - 1$
      ii. The waiting room i is full: $\tilde{S}_i \rightarrow \tilde{S}_i$ & $\widetilde{E_\iota S_i} \rightarrow \widetilde{E_\iota S_i} - 1$

b. If the production reaction performed by the upstream enzyme is chosen:

   i. The waiting room *i* is not full: $\tilde{S}_i \rightarrow \tilde{S}_i + 1$

   ii. The waiting room *i* is full: $\tilde{S}_i \rightarrow \tilde{S}_i$

c. For N-enzyme cascades ($N > 2$), if the substrate $\tilde{S}_{i+1}$production (*via* the consumption of substrate $\tilde{S}_i$) reaction processed by E_i is chosen:

   i. The following waiting room *i*+1 is not full: $\widetilde{E_i S_i} \rightarrow \widetilde{E_i S_i} - 1$ & $\tilde{S}_{i+1} \rightarrow \tilde{S}_{i+1} + 1$

   ii. The following waiting room *i*+1 is full: $\widetilde{E_i S_i} \rightarrow \widetilde{E_i S_i} - 1$ & $\tilde{S}_{i+1} \rightarrow \tilde{S}_{i+1}$

d. If another reaction is chosen:

   The state of the waiting room does not matter

6. Go back to step 1 while $t < t_{final}$

B.3: Queueing theory and Hunt's equations for 2-enzyme cascades

Our aim is to repurpose the analytical machinery of queueing theory used in operations research to gain insight into the workings of a tunneled enzyme cascade. Indeed, the conversion of molecules by sequential active sites connected by tunnels of finite capacity is analogous to the service of customers by sequential server booths connected by waiting rooms. In this section, we will compare our simulation results to those of Hunt,[79] who studied the queueing theory of two servers with different service rates. In Hunt's model, the downstream server is preceded by a finite waiting room while the first server is always busy.

Defining r as the maximum cascade output rate incoming to the upstream server, we can implement equations (24) and (25) from Hunt's paper[79] for our system as follows:

$$r = r_0 r_1 \frac{r_0^{Q-1} - r_1^{Q-1}}{r_0^{Q} - r_1^{Q}} \, , if \; r_0 \neq r_1 \qquad (B.8)$$

$$r = r_0 \frac{Q-1}{Q} \, , if \; r_0 = r_1 \qquad (B.9)$$

Where Q corresponds to the number of system states. The parameters r_0 and r_1 are the output rates of the upstream and downstream servers (or enzymes), respectively. For Hunt's system, they are equal to the server service rate μ_i. In order to take all the chemical reactions into account, we define the following rates r_0 and r_1 as:

$$r_0 = c_{cat,0} - c_{off}\langle \tilde{S} \rangle \qquad (B.10)$$

$$r_1 = c_{cat,1} \frac{\langle \tilde{S} \rangle}{\langle \tilde{S} \rangle + K_M N_A V} \qquad (B.11)$$

where $\langle \tilde{S} \rangle$ is the mean steady-state substrate population computed from our simulations.

The definition of r_0 can be interpreted as an *effective* production rate seen by the downstream enzyme. It is a balance between all the reactions which produce or consume one substrate molecule – except the reaction of the downstream enzyme itself. The definition of r_1 is chosen to coincide with the Michaelis-Menten reaction kinetics.

Figure B.1 shows that simulated data are better described by Hunt's equation than by the MM model. The best description is obtained when the number of system states, Q, is equal to the waiting room capacity plus 1.

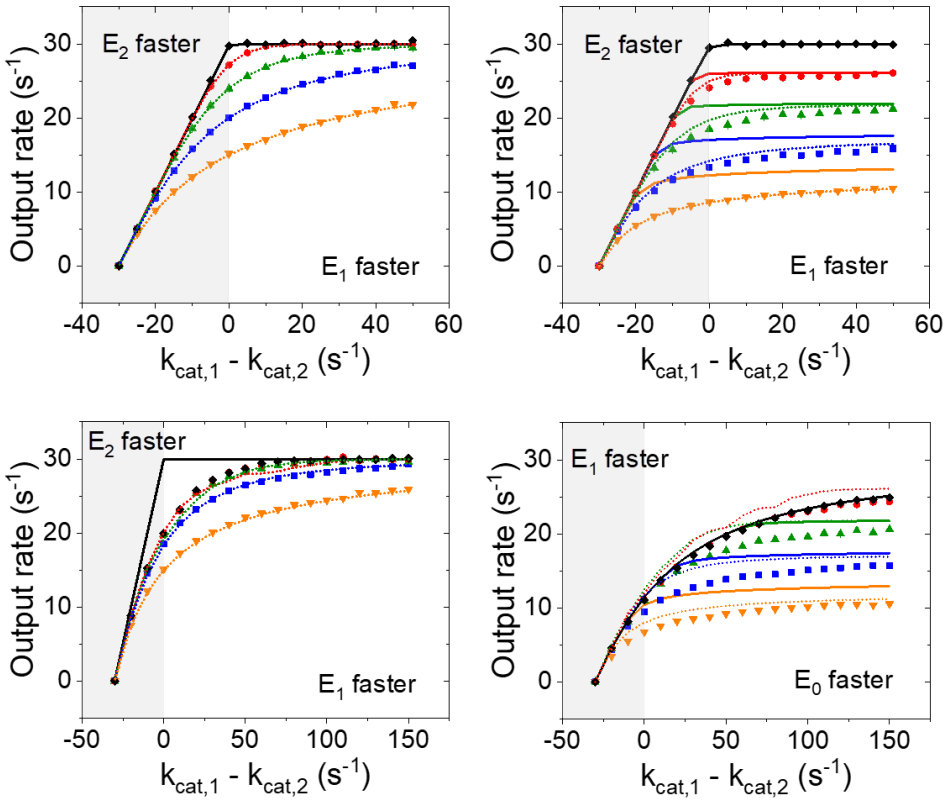

Figure B.1. Comparison of stochastic simulation results with analytical queueing theory results. Simulated data are the same as in Figure 2.3 (upper left), Figure 2.4 (upper right), Figure 2.6 (lower left) and Figure 2.7 (lower right) of the main text. The same colors and symbols are used. Dotted curves are solutions of Hunt's Equations (B.8), (B.9) with the corresponding rate definitions (B.10) and (B.11). The number of system states Q is taken equal to n_{WR} + 1. Solid curves are solutions of MM model (2.7) (main paper) with the corresponding waiting room capacity. Colors and parameters are the same as in Figure 2.3. Symbols represent the results of the stochastic simulations for a waiting room capacity of 1 (orange triangles), 2 (blue squares), 4 (green triangles), 10 (red circles) and ∞ molecules (black diamonds). Error bars for standard error are smaller than the marker.

According to Hunt, a total of n_{WR} + 3 states can be defined for a two-server system with a waiting room of size n_{WR}. These states are listed in Table B.1. The reason why we estimate the number of states by $Q = n_{WR} + 1$ for our model can be explained by analyzing the discrepancies between our model of a tunneled enzyme cascade and Hunt's model. One such discrepancy is that Hunt assumed that a customer will immediately go to the downstream server as soon as the service is completed. In our system, the molecules do not immediately enter the enzyme active site when they are full. Rather, it takes a time on the scale of c_f^{-1}. However, since $c_f >> c_{cat,2}$, the time to occupy an empty active site is not a rate-limiting factor in the cascade reaction. Therefore, we can make the same assumption.

The second discrepancy in the models is that Hunt considered that a customer served by the first server will wait in case the waiting room is full. However, we consider that the first enzyme (E1) is always processing since it produces its product either in the waiting room or in the bulk. This removes a state from Table B.1 and we update $Q = n_{WR} + 2$.

The best description of the system is attained for $Q = n_{WR} + 1$ because, as described in the Discussion and shown in Figure 8 of the main text, for K_M = 2.5 μM, the probability that the waiting room is maximally full is negligible; the state (S_0 : in service / S_1 : in service / WR : n_{WR} molecules) has a very low associated probability. This removes state number $n_{WR}+1$ from Table B.1 and we end up with:

$$Q = (n_{WR} + 3) \underbrace{-1}_{E1\ always\ processing} \overbrace{-1}^{WR\ never\ full} = n_{WR} + 1 \qquad (B.12)$$

However, while Hunt's equations do provide a good approximation for simulated data for K_M = 2.5 μM, they do not perform as well for K_M = 250 mM (Figure B.1). As explained in the Discussion

section of the main text, the waiting room occupancy fluctuates between $n_{WR} - 1$ and n_{WR} between catalysis events, spending an approximate fraction, $\frac{c_r}{c_f + c_r}$, of the time in the n_{WR} state. While this quantity is near 0 for K_M = 2.5 μM, it is greater than 0.5 for K_M = 250 mM. As a result, the probability that the waiting room is full is no longer negligible, and $Q = n_{WR} + 1$ gives only a lower bound on the total number of states.

Table B.1. States for Hunt's System (2 servers in series with a finite waiting room in front of the downstream server).

State	S_0	S_1	WR (waiting customers)
1	In service	Unoccupied	0
2	In service	In service	0
3	In service	In service	1
…	…	…	…
I	In service	In service	i-2
…	…	…	…
n_{WR} +1	In service	In service	n_{WR} -1
n_{WR} +2	In service	In service	n_{WR}
n_{WR} +3	Service completed (one customer waits in the first server)	In service	n_{WR}

Appendix C

C.1: The well mixed assumption is typically valid for compartmentalized enzyme cascades

The well-mixed assumption holds if the diffusion time scale is much less than the reaction time scale. Using the same notation as in the main text, this may be written as:

$$\frac{r^2}{D} \ll \frac{\mathrm{K_M}}{k_{cat}[E]} \qquad (C.1)$$

By keeping the number of enzymes, E_T, constant, and assuming a diffusion coefficient of $D \approx 10^{-9}$ m^2/s, and $K_M \gg 1\mu M$, we can rewrite Equation (C.1) as:

$$\frac{DK_M}{\mathrm{k_{cat}}[E]} \gg r^2 \qquad (C.2)$$

$$\frac{DK_M}{\mathrm{k_{cat}}} \gg \frac{r^2 n_E}{V} = \frac{r^2 n_E}{\frac{4}{3}\pi r^3} = \frac{3}{4}\frac{n_E}{\pi r} \qquad (C.3)$$

$$r \gg \frac{3}{4}\frac{n_E}{\pi}\frac{k_{cat}}{DK_M} \qquad (C.4)$$

According to Equation (C.4), if the compartment radius is large enough, then the well mixed assumption will hold. To find the largest value that the right hand-side of Equation (C.4) can attain, we compare it to the maximum, diffusion limited, catalytic efficiency of enzymes, which is sometimes considered to be $\frac{k_{cat}}{K_M} = 10^9 M^{-1}s^{-1}$.[128] For 100 enzymes in the compartment, this would give:

$$r \gg \frac{3}{4}\frac{100}{\pi} \cdot \frac{10^{9}\ \mathrm{M^{-1}s^{-1}}}{10^{-9}\ \mathrm{m^{2}s^{-1}}} \approx 40\ \mathrm{nm} \qquad (C.5)$$

In other words, the well mixed assumption will hold for a compartment containing 100 of the most catalytically efficient enzymes, as long as it has a radius greater than 40 nm.

C.2: Optimizing product throughput

The goal is to maximize the product outflux, given by:

$$F_P[P] = \beta_2[I] = \frac{F\beta_1\beta_2[S_0]}{(F+\beta_2)(F+\beta_1)} \qquad (C.6)$$

This may be done by taking the derivative of the right hand-side term of Equation (C.6) with respect to F, and finding where it equals zero:

$$\frac{d\beta_2[I]}{dF} = \beta_1\beta_2[S_0]\frac{(F+\beta_2)(F+\beta_1) - F\big((F+\beta_2)+(F+\beta_1)\big)}{\big((F+\beta_2)(F+\beta_1)\big)^2} =$$

$$= \beta_1\beta_2[S_0]\frac{\beta_1\beta_2 - F^2}{\big((F+\beta_2)(F+\beta_1)\big)^2} = 0 \qquad (C.7)$$

This gives the critical point:

$$F = \sqrt{\beta_1\beta_2} \qquad (C.8)$$

This critical point is a maximum because the second derivative of Equation (C.6) evaluated at this critical point is negative:

$$\frac{d^2\beta_2[I]}{dF^2} = \beta_1\beta_2[S_0]\frac{-2F\left((F+\beta_2)(F+\beta_1)\right)^2}{\left((F+\beta_2)(F+\beta_1)\right)^4} -$$

$$-\frac{(\beta_1\beta_2 - F^2)\frac{d}{dF}\left(\left((F+\beta_2)(F+\beta_1)\right)^2\right)}{\left((F+\beta_2)(F+\beta_1)\right)^4}\Bigg|_{F=\sqrt{\beta_1\beta_2}} < 0 \qquad (C.9)$$

C.3: The effect of selective permeability on optimal diffusive conductance can be interpreted as a change in the turnover rate

We model selective permeability by setting $F_I = cF_s = cF$, where c is a constant of proportionality between the diffusive conductances of intermediate and substrate. Then, we can use Equation (3.11) to rewrite the rate of product outflux as:

$$F_P[P] = \beta_2[I] = \frac{F_S\beta_1\beta_2[S_0]}{(F_I + \beta_2)(F_S + \beta_1)} = \frac{F\beta_1\beta_2[S_0]}{(cF + \beta_2)(F + \beta_1)} = \frac{F\beta_1\beta_2'[S_0]}{(F + \beta_2')(F + \beta_1)} \qquad (C.10)$$

where $\beta_2' = \beta_2/c$.

Using the same methods as in Section C.2, we find that product outflux is maximized for:

$$F = \sqrt{\beta_1\beta_2'} = \sqrt{\frac{\beta_1\beta_2}{c}} \qquad (C.11)$$

Then, the product outflux is:

$$F_P[P] = \beta_2[I] = \frac{\beta_1\beta_2'[S_0]}{\left(\sqrt{\beta_1} + \sqrt{\beta_2'}\right)^2} = \frac{\beta_1\beta_2[S_0]}{\left(\sqrt{c\beta_1} + \sqrt{\beta_2}\right)^2} \qquad (C.12)$$

Interestingly, this expression shows that if c is small enough, the reaction will be running close to maximum velocity, and lowering the value of c further only provides diminishing returns. If we assume $c\beta_1 \ll \beta_2$ and let $\epsilon = c\beta_1/\beta_2$, then we have:

$$\beta_2[I] = \frac{\beta_1[S_0]}{\left(\sqrt{\epsilon}+1\right)^2} \approx \beta_1[S_0]\left(1-2\sqrt{\epsilon}\right) \approx \beta_1[S_0] \qquad (C.13)$$

Which gives us the maximum possible throughput. So, if the ratio of the diffusive conductance rates of intermediate to substrate molecules is much less than the ratio of the turnover rates of the Enzyme 1 to Enzyme 2, the reaction will be running close to maximum velocity:

$$\frac{F_I}{F_S} \ll \frac{\beta_2}{\beta_1} \rightarrow \ \beta_2[I] \approx \beta_1[S] \qquad (C.14)$$

C.4: Choosing diffusive conductance under saturating conditions

When optimizing the diffusive conductance, it is possible that one of the enzymes in the cascade will become saturated. The case when the first enzyme is saturated is discussed in the main text. Here, we will discuss the case when the second enzyme is saturated.

We begin with Equation (3.3) from the main text:

$$\frac{k_{cat,1}[E_1][S]}{K_{m1}+[S]} - \frac{F_I[I]}{V} - \frac{k_{cat,2}[E_2][I]}{K_{m,2}+[I]} = 0 \qquad (C.15)$$

We assume that the first enzyme is not saturated, so it is in the linear regime of its kinetics and the steady state substrate concentration is given by Equation (3.10). Using the notation from the main text, and assuming that the diffusive conductances are equal, we rewrite this Equation (C.15):

$$\frac{\beta_1 F}{\mathrm{F}+\beta_1}[S_0] - \mathrm{F[I]} - \frac{\beta_2[I]}{1+\frac{[I]}{K_{m,2}}} = 0 \qquad (C.16)$$

If we set the intermediate concentration equal to the K_M of the second enzyme, we find that there are two values of diffusive conductance, *F*, that satisfy the above equation. This means that over a certain range of values of diffusive conductance, the steady state product throughput rate will

only experience a small change. For $[S_0] \gg K_{m,2}$ the range this plateau spans from $F = \frac{\mathrm{k_{cat,2}} n_2}{[S_0]}$ to $F = \beta_1 \cdot \frac{[S_0]}{K_{m,2}}$.

To find the maximum product throughput, we perform implicit differentiation on Equation (C.16). Define:

$$g([I]) = \frac{\beta_2 [I]}{1 + \frac{[I]}{K_{m,2}}} \qquad (C.17)$$

Then

$$\frac{dg([I])}{dF} = \frac{dg}{d[I]} \cdot \frac{d[I]}{dF} = \frac{\beta_1^2}{(\mathrm{F} + \beta_1)^2} [S_0] - [\mathrm{I}] - \mathrm{F} \cdot \frac{\mathrm{d[I]}}{\mathrm{dF}} = 0 \qquad (C.18)$$

Since $g([I])$ is a monotonic function in $[I]$, the same value of *F* will maximize both $g([I])$ and $[I]$. So, if $\frac{dg([I])}{dF} = 0$ then $\frac{\mathrm{d[I]}}{\mathrm{dF}} = 0$, and we find:

$$\frac{\beta_1^2}{(\mathrm{F} + \beta_1)^2} [S_0] = [\mathrm{I}] \qquad (C.19)$$

Inserting Equation (C.19) into Equation (C.16), we find an expression for *F*:

$$F^2 \left(1 + \frac{\beta_1^2}{(\mathrm{F} + \beta_1)^2} \cdot \frac{[S_0]}{K_{m,2}} \right) = \beta_1 \beta_2 \qquad (C.20)$$

If $[S_0] \ll K_{m,2}$, we arrive at the initial result that F $= \sqrt{\beta_1 \beta_2}$. However, if $[S_0] \gg K_{m,2}$, we may approximate the previous expression as:

$$F^2 \left(\frac{\beta_1^2}{(F + \beta_1)^2} \cdot \frac{[S_0]}{K_{m,2}} \right) = \beta_1 \beta_2 \qquad (C.21)$$

This expression simplifies to:

$$F = \frac{\beta_1}{\sqrt{\frac{\beta_1}{\beta_2} \cdot \frac{[S_0]}{K_{m,2}} - 1}} \approx \sqrt{\beta_1 \beta_2} \sqrt{\frac{K_{m,2}}{[S_0]}} \qquad (C.22)$$

Saturation in the second enzyme effectively lowers the optimal diffusive conductance by a factor of $\sqrt{\frac{K_{m,2}}{[S_0]}}$.

C.5: The effect of selective permeability on optimal compartment parameters can be interpreted as a change in the catalytic efficiency

As in Section C.3, we model selective permeability by setting $F_I = cF_s = cF$, where c is a constant of proportionality between the diffusive conductances of intermediate and substrate. Inserting Equations (3.10-11) into Equations (3.16-18):

$$\min_{n_{E1},n_{E2},F} \frac{F_I F_S \beta_1}{(F_S + \beta_1)(F_I + \beta_2)} = \frac{F^2 \beta_1}{(F + \beta_1)(F + \beta_2')} \tag{C.24}$$

$$\frac{F_S \beta_1 \beta_2}{(F_S + \beta_1)(F_I + \beta_2)} = \frac{F \beta_1 \beta_2'}{(F + \beta_1)(F + \beta_2')} = R \tag{C.25}$$

$$n_{E1} + n_{E2} = n_0 \tag{C.26}$$

Above, we have defined $\beta_2' = \frac{\beta_2}{c} = \left(\frac{\gamma_2}{c}\right) n_2 = \gamma_2' n_2$. The resulting optimization problem is similar to Equations (3.16-18), with the only difference being that the catalytic efficiency of Enzyme 2 is now given by $\gamma_2' = \frac{\gamma_2}{c}$.

C.6: Closed form expression for optimal diffusive conductance and enzyme numbers

To solve the optimization problem in the main text given by Equations (3.16-18), and assuming F_S=F_I, we construct the Lagrangian:

$$L(n_1, n_2, F, \lambda_1, \lambda_2) = F[I] + \lambda_1(R - \beta_2[I]) + \lambda_2(n_0 - n_1 - n_2) \qquad (C.27)$$

We insert the steady state expression for the intermediate concentration, $[I]$, from Equation (3.11), and set the gradient of the Lagrangian to zero:

$$\nabla_{n_1,n_2,F,\lambda_1,\lambda_2} L = 0 \qquad (C.28)$$

Solving the equation, we first find two expressions for critical values of F:

$$F_1 = \sqrt{\beta_1 \beta_2} \qquad (C.29)$$

$$F_2 = \frac{\beta_1 n_1}{n_2} \qquad (C.30)$$

Then, we can insert the value of F_1 and F_2 into the constraint given by Equation (3.17) to find an expression for n_1 in terms of n_2. We will use the variable $R' = \frac{R}{[S_0]}$ to maintain the brevity of expressions.

Case 1: $F_1 = \sqrt{\beta_1 \beta_2}$*:*

$$\gamma_1 \mathrm{n}_1 = \frac{\gamma_2 n_2}{\left(\sqrt{\frac{\gamma_2 n_2}{R'}} - 1\right)^2} \tag{C.31}$$

Case 2: $F_2 = \frac{\beta_1 n_1}{n_2}$*:*

$$n_1 = \sqrt{\frac{R' n_0}{\gamma_1}} \frac{\mathrm{n}_2}{\sqrt{\mathrm{n}_2^2 - \frac{R' n_0}{\gamma_2}}} \tag{C.32}$$

At this stage, if we try inserting the constraint, $n_1 + n_2 = n_0$, we will arrive at a fourth order polynomial in both cases, which does not have a nice closed form solution. However, if we plot n_1 against n_2, we see that both curves approach asymptotes given by the expressions:

Case 1: $F_1 = \sqrt{\beta_1 \beta_2}$*:*

$$\lim_{n_2 \to \infty} \gamma_1 n_1 = \frac{\gamma_2 n_2}{\frac{\gamma_2 n_2}{R'}} = R' \tag{C.33}$$

$$\lim_{n_1 \to \infty} \gamma_2 n_2 = R' \tag{C.34}$$

Case 2: $F_2 = \frac{\beta_1 n_1}{n_2}$*:*

$$\lim_{n_2 \to \infty} n_1 = \sqrt{\frac{R' n_0}{\gamma_1}} \tag{C.35}$$

$$\lim_{n_1 \to \infty} n_2 = \sqrt{\frac{R' n_0}{\gamma_2}} \qquad (C.36)$$

If n_0 is big enough, we can approximate the optimal numbers of each enzyme by inserting the above limits into the constraint, $n_1 + n_2 = n_0$. The results are the following:

Case 1: $F_1 = \sqrt{\beta_1 \beta_2}$*:*

$$(\gamma_1 n_1, \gamma_2 n_2) = \left(R', \gamma_2 \left(n_0 - \frac{R'}{\gamma_1} \right) \right) \qquad (C.37)$$

$$(\gamma_1 n_1, \gamma_2 n_2) = \left(\gamma_1 \left(n_0 - \frac{R'}{\gamma_2} \right), R' \right) \qquad (C.38)$$

Case 2: $F_2 = \frac{\beta_1 n_1}{n_2}$*:*

$$(n_1, n_2) = \left(\sqrt{\frac{R' n_0}{\gamma_1}}, n_0 - \sqrt{\frac{R' n_0}{\gamma_1}} \right) \qquad (C.39)$$

$$(n_1, n_2) = \left(n_0 - \sqrt{\frac{R' n_0}{\gamma_2}}, \sqrt{\frac{R' n_0}{\gamma_2}} \right) \qquad (C.40)$$

Equation (C.39) gives the approximate number of each enzyme which will minimize intermediate elimination under the constraints given by Equations (3.17-18).

C.7: Maximizing product outflux while constraining intermediate outflux

In this section, our goal is to take an alternative approach to the optimization problem presented in the main text. Instead of minimizing intermediate outflux while specifying a product outflux, here, we maximize product outflux while setting a constraint on intermediate outflux. The problem may be written down as (assuming F_S=F_I):

$$\max_{n_1,n_2,F} \beta_2[I] \qquad (C.41)$$

$$F[I] \leq R_I \qquad (C.42)$$

$$n_1 + n_2 = n_0 \qquad (C.43)$$

We solve this inequality constrained optimization problem by using Lagrange multipliers. The Lagrangian is:

$$L(n_1, n_2, F, \mu_1, \lambda_1) = \beta_2[I] + \mu_1(R_I - F[I]) + \lambda_1(n_0 - n_1 - n_2) \qquad (C.44)$$

First, we will set $\mu_1 = 0$, and solve the optimization problem to maximize product throughput. If the resulting intermediate elimination rate is lower than the allowed R_I, we are done. If not, then the optimal solution lies on the boundary, $\mathrm{F_I}[I] = R_I$, of the feasible set. This then becomes equivalent to the intermediate elimination minimization problem considered initially. We use the steady state concentration of intermediate given by Equation (11) in our calculations.

Case 1: $\mu_1 = 0$

$$\nabla_{n_1,n_2,F,\lambda_1} L = 0 \tag{C.45}$$

$$=> \ F = \sqrt{\beta_1 \beta_2} \tag{C.46}$$

$$=> \ n_1 = \frac{1}{1+\alpha} n_0 \tag{C.47}$$

$$=> \ n_2 = \frac{\alpha}{1+\alpha} n_0 \tag{C.48}$$

$$\alpha = \left(\frac{\gamma_1}{\gamma_2}\right)^{\frac{1}{3}} \tag{C.49}$$

Case 2: $\mu_1 \neq 0$

$$\nabla_{n_1,n_2,F,\mu_1,\lambda_1} L = 0 \tag{C.50}$$

$$F = \frac{\beta_1 n_1}{n_2} \tag{C.51}$$

$$n_2 = \frac{n_1 \gamma_1^2}{R' n_0 \gamma_2} \cdot \left(n_1^2 - \frac{R_I' n_0}{\gamma_1}\right) \tag{C.52}$$

where we have once again defined the variable $R_I' = \frac{R_I}{[S_0]}$. For the second case, we cannot get a closed form solution by inserting the constraint $n_1 + n_2 = n_0$. However, we see that at a minimum, n_1 must be greater than $\sqrt{\frac{R_I' n_0}{\gamma_1}}$ in order to satisfy the equality on intermediate outflux. This corresponds well with the result we find in previous section in Equation (C.39) for how to minimize intermediate outflux while maintaining a specified product outflux.

C.8: Compartments provide benefits only when cytosol intermediate removal rate surpasses a threshold

It is possible to generalize Equations (3.2-4) of the main text to take into account the bulk intermediate concentration. The equations become:

$$\frac{d[S]}{dt} = \frac{F_S([S_0] - [S])}{V} - \frac{k_{cat,1}[E_1][S]}{K_{m,1} + [S]} \quad (C.53)$$

$$\frac{d[I]}{dt} = \frac{k_{cat,1}[E_1][S]}{K_{m1} + [S]} - \frac{F_I([I] - [I_b])}{V} - \frac{k_{cat,2}[E_2][I]}{K_{m,2} + [I]} \quad (C.54)$$

$$\frac{d[P]}{dt} = \frac{k_{cat,2}[E_2][I]}{K_{m,2} + [I]} - \frac{F_P[P]}{V} \quad (C.55)$$

$$\frac{d[I_b]}{dt} = \frac{F_I([I] - [I_b])}{V_{cell}} - \frac{k_e}{V_{cell}}[I_b] \quad (C.56)$$

where the only new variable is $[I_b]$, which denotes the concentration of intermediate in the bulk. At steady state, in the linear regime, we find that the intermediate concentration is now dependent on the elimination rate of intermediate from the bulk:

$$[I] = \frac{1}{\frac{k_e F_I}{\mathrm{k_e} + F_I} + \beta_2} \cdot \frac{\beta_1 F_S}{F_S + \beta_1}[\mathrm{S_0}] \quad (C.57)$$

As before, the goal is to maximize the product outflux which is equal to intermediate conversion, $\beta_2[I]$. After setting the diffusive conductances equal, $F_I = F_S = F$, this equation can be maximizing by taking the derivative with respect to *F*.

The derivative of [I] with respect to *F* is zero whenever:

$$F = \begin{cases} \infty, & k_e < k_{e,crit} \\ F_{opt}, & k_e \geq k_{e,crit} \end{cases} \quad (C.58)$$

Where

$$k_{e,crit} = \beta_1 \left(\frac{1}{2} + \sqrt{\frac{1}{4} + \frac{\beta_2}{\beta_1}} \right) \quad (C.59)$$

$$F_{opt} = \frac{\frac{k_e \beta_1 \beta_2}{k_e + \beta_2} + \sqrt{\left(\frac{k_e \beta_1 \beta_2}{k_e + \beta_2} \cdot \frac{k_e^2}{k_e + \beta_2} \right)(k_e - \beta_1)}}{\frac{k_e^2}{k_e + \beta_2} - \beta_1} \quad (C.60)$$

Surprisingly, the optimal choice of *F* becomes infinite for a nonzero value of k_e. An infinite diffusive conductance corresponds to a non-compartmentalized reaction.

C.9: An enzyme-coated sphere in an infinite volume with adsorbing boundary conditions at infinity

Consider a microsphere of radius R coated with two populations of enzymes: E1 converts substrate, S, to intermediate, I, and E2 converts I to product, P. The sphere is located in an infinite environment. At infinity, $S=S_0$ and I=0. Reaction rates on the surface are taken to be first order in [S] and [I]. The system of partial differential equations in spherical coordinates describing these reactions can be written down as follows:

$$\frac{d[S]}{dt} = D_S \nabla^2 [S] = \frac{D_S}{r^2} \cdot \frac{\partial}{\partial r}\left(r^2 \frac{\partial [S]}{\partial r} \right) \qquad (C.61)$$

$$\frac{d[I]}{dt} = D_I \nabla^2 [I] = \frac{D_I}{r^2} \cdot \frac{\partial}{\partial r}\left(r^2 \frac{\partial [I]}{\partial r} \right) \qquad (C.62)$$

With boundary conditions:

$$D_S N_A \frac{d[S]}{dr}(r = R) = \frac{k_{cat,1}}{K_{M,1}} \sigma_{E1} [S](r = R) \qquad (C.63)$$

$$D_I N_A \frac{d[I]}{dr}(r = R) = -\frac{k_{cat,1}}{K_{M,1}} \sigma_{E1} [S](r = R) + \frac{k_{cat,2}}{K_{M,2}} \sigma_{E2} [I](r = R) \qquad (C.64)$$

$$[I](r = \infty) = 0 \qquad (C.65)$$

$$[S](r = \infty) = S_0 \qquad (C.66)$$

Let:

$$\gamma_1 = \frac{k_{cat,1}}{K_{M,1}} N_A^{-1} \tag{C.67}$$

$$\gamma_2 = \frac{k_{cat,2}}{K_{M,2}} N_A^{-1} \tag{C.68}$$

We can solve this system for steady state, when $\frac{d[S]}{dt} = \frac{d[I]}{dt} = 0$. The steady state solutions for the diffusion equation of the form of Equations 1 and 2 is:

$$C(r) = \frac{a}{r} + b \tag{C.69}$$

Introducing the boundary conditions, we find the concentration profiles to be:

$$S(r) = S_0 \left(1 - \frac{R}{r} \frac{\gamma_1 \sigma_E}{\gamma_1 \sigma_E + \frac{D}{R}} \right) \tag{C.70}$$

$$I(r) = S_0 \cdot \frac{R}{r} \cdot \left(\frac{\frac{\gamma_1 \sigma_{E1} D_S}{R}}{\left(\gamma_1 \sigma_{E1} + \frac{D_S}{R} \right) \left(\gamma_2 \sigma_{E2} + \frac{D_I}{R} \right)} \right) \tag{C.71}$$

The throughput is then:

$$\gamma_2 \sigma_{E2} [I](r = R) = S_0 \cdot \left(\frac{\gamma_1 \sigma_{E1} \gamma_2 \sigma_{E2} \frac{D_S}{R}}{\left(\gamma_1 \sigma_{E1} + \frac{D_S}{R} \right) \left(\gamma_2 \sigma_{E2} + \frac{D_I}{R} \right)} \right) \tag{C.72}$$

Note that this equation presents an optimization opportunity in the variable R. By picking the proper R, we can maximize the number of molecules produced per unit area. This optimal R is:

$$R_{opt} = \sqrt{\frac{D_S}{\gamma_1 \sigma_{E1}} \cdot \frac{D_I}{\gamma_2 \sigma_{E2}}} \qquad (C.73)$$

Multiplying the numerator and denominator out be the surface area, $4\pi R^2$, and replacing enzyme density with numbers of enzymes, n_{Ei}, and defining $F_i = 4\pi D_i R$ as the diffusive conductance (as derived by Berg for a sphere), and setting $\beta_i = \gamma_i n_{Ei}$ as in the compartments paper, we find that the throughput is (molecules of product produced per second):

$$\beta_2[I](r = R) = S_0 \cdot \left(\frac{\beta_1 \beta_2 F_S}{(\beta_1 + F_S)(\beta_2 + F_I)}\right) \qquad (C.74)$$

This is equivalent to Equation 3.11.

C.10: An enzyme-coated sphere in an infinite volume with adsorbing boundary conditions with a competing reaction in solution

Consider the system examined in Section C.9, albeit with a new reaction: intermediate molecules in solution are additionally eliminated with a first order rate constant, k_e. In order to model this, we need to only change Equation 2. It is replaced with:

$$\frac{d[I]}{dt} = D_I \nabla^2 [I] - k_e [I] = \frac{D_I}{r^2} \cdot \frac{\partial}{\partial r}\left(r^2 \frac{\partial [I]}{\partial r}\right) - k_e [I] \qquad (C.75)$$

At steady state, this equation takes the form:

$$I(r) = \frac{A}{r} e^{-\sqrt{\frac{k_e}{D_I}} r} + \frac{B}{r} e^{\sqrt{\frac{k_e}{D_I}} r} \qquad (C.76)$$

A and B are constants to be determined from the boundary conditions. Since we have $I(r \to \infty) \to 0$, we find that $B = 0$. Using the flux condition on the surface, we find:

$$A = V_S R e^{\alpha R} \cdot \left(\frac{D}{R}(\alpha R + 1) + \gamma_2 \sigma_{E2}\right)^{-1} \qquad (C.77)$$

$$\alpha = \sqrt{\frac{k_e}{D_I}} \qquad (C.78)$$

V_S is the throughput at the surface from the first enzyme. Note that, because the substrate conversion reaction is independent of the intermediate concentration, Equation C.70 remains valid for describing substrate concentration. As a result, the intermediate concentration profile can be written as:

$$I(r) = S_0 \cdot \frac{Re^{a(R-r)}}{r} \cdot \left(\frac{\gamma_1 \sigma_{E1} \frac{D_S}{R}}{\left(\gamma_1 \sigma_{E1} + \frac{D_S}{R}\right)\left(\gamma_2 \sigma_{E2} + \frac{D_I}{R}(\alpha R + 1)\right)} \right) \qquad (C.79)$$

The only difference between the equation above and equation C.72 is that the intermediate diffusion coefficient has been modified by a factor of $(\alpha R + 1)$ and the concentration drop off has an additional exponential factor.

The throughput for this reaction is:

$$\gamma_2 \sigma_{E2}[I](r = R) = S_0 \cdot \left(\frac{\gamma_1 \sigma_{E1} \gamma_2 \sigma_{E2} \frac{D_S}{R}}{\left(\gamma_1 \sigma_{E1} + \frac{D_S}{R}\right)\left(\gamma_2 \sigma_{E2} + \sqrt{D_I k_e} + \frac{D_I}{R}\right)} \right) \qquad (C.80)$$

Appendix D

D.1: Determination of the fluorescence of single kinesin molecules

Solutions containing 2.5 pM GFP-Kinesin and antifade but excluding microtubules were flown into UV/ozone treated flow cells and imaged using TIRF microscopy. The low concentration of GFP-Kinesin allowed for imaging of individual kinesins. Images of single kinesin molecules were taken while varying exposure time between 30 ms and 500 ms. Using open-source image analysis software,[469] we found that the Gaussian volume of individual fluorophores is a linear function of exposure time on average (Figure D.1). Linear regression on the data returned a slope of 1.62 ms^{-1} and a negligible intercept of 1.02 counts. Most experiments were carried out with an exposure time of $E_X = 30$ ms, which gives a fluorescence intensity per single kinesin of roughly 50 counts.

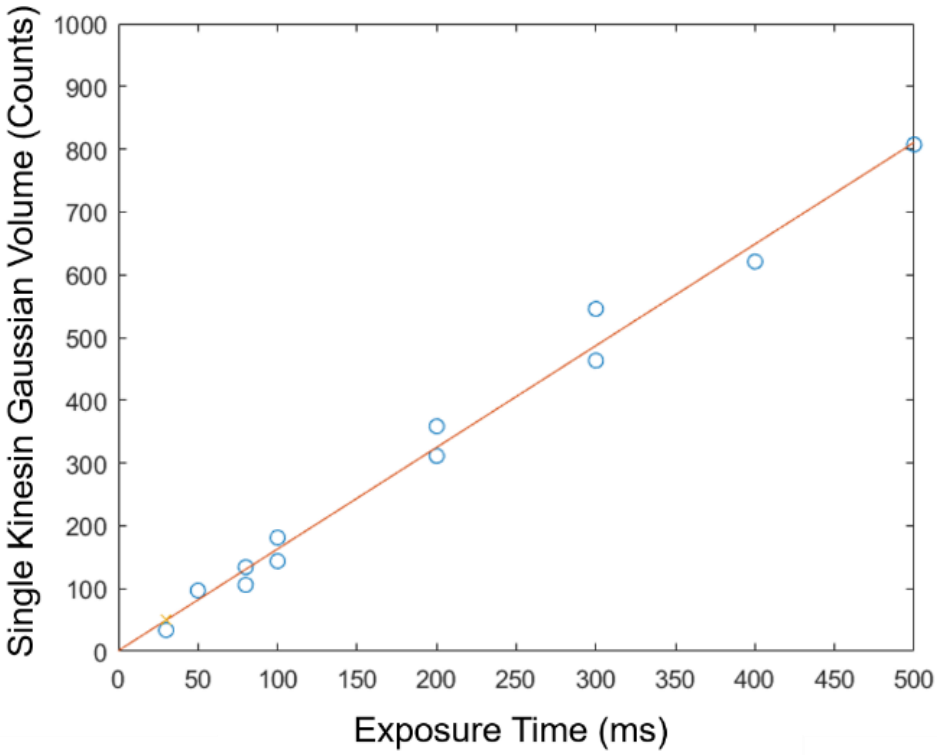

Figure D.1. Calibration curve for total light from single kinesin molecules. Average volume of Gaussian calculated for single kinesin fluorophores at various exposure times (blue dots) fit using linear regression (red line).

D.2: Models for kinesin landing on the surface

In order to describe the dynamics of kinesin motor proteins landing on the surface, we employed two approaches, modeled after studies in Signal Plasmon Resonance[450, 451] and reversible surface adsorption kinetics.[452]

Model 1: Compartmentalized kinesin concentrations

This model compartmentalizes the kinesin concentration in the flow cell into three compartments: (1) a bulk compartment concentration, $[K_{bulk}]$, which cannot react with the surface; (2) a near-surface compartment concentration, $[K_{surf}]$, which describes motors diffusing in solution yet able to bind to the surface; and (3) a surface-bound density, σ_b:

$$\frac{d[K_{bulk}]}{dt} = -k_{diff}\left([K_{bulk}] - [K_{surf}]\right) \qquad (D.1)$$

$$\frac{d[K_{surf}]}{dt} = k_{diff}\left([K_{bulk}] - [K_{surf}]\right) - \frac{1}{hN_A} \cdot \left(k_{on}(\sigma_0 - \sigma_b)[K_{surf}] - k_{off}\sigma_b\right) \qquad (D.2)$$

$$\frac{d\sigma_b}{dt} = \left(k_{on}\sigma_0[K_{surf}] - k_{off}\sigma_{bound}\right) \qquad (D.3)$$

In the above equations, k_{diff} describes the rate of transfer between the bulk and surface compartment, k_{on} is the on-rate for surface binding, k_{off} is the off-rate for surface dissociation, h is the apparent height of the near-surface compartment, and N_A is Avogadro's Number. The Quasi Steady State Approximation for this system assumes[2]:

$$\frac{d[K_{surf}]}{dt} \approx 0 \qquad (D.4)$$

This gives

$$[K_s] = \frac{k_{diff} h N_A}{k_{diff} h N_A + k_{on}\sigma_0}[K_b] + \frac{k_{off}}{k_{diff} h N_A + k_{on}\sigma_0}\sigma_b \qquad (D.5)$$

$$\frac{d\sigma_b}{dt} = k'_{on}\sigma_0[K_b] - k'_{off}\sigma_b \qquad (D.6)$$

$$k'_{on} = \frac{k'_{diff}}{k'_{diff} + k_{on}\sigma_0} k_{on} \qquad (D.7)$$

$$k'_{off} = \frac{k'_{diff}}{k'_{diff} + k_{on}\sigma_0} k_{off} \qquad (D.8)$$

$$k'_{diff} = k_{diff} h N_A \qquad (D.9)$$

$$\frac{k'_{off}}{k'_{on}} = K_D \qquad (D.10)$$

Where K_D is the dissociation constant for the kinesin-surface bond. We assume that $[K_b] \approx [K_0]$, the initial kinesin concentration that was flown in. In addition, to take into account the effect of the surface being stripped of nickel ions, and therefore kinesin binding sites, we replace σ_0 with $\sigma_0 \exp(-k_s t)$, where k_s is the stripping rate constant. That gives the following equation:

$$\frac{d\sigma_b}{dt} = k'_{on}\sigma_0 e^{-k_s t}[K_0] - k'_{off}\sigma_b \qquad (D.11)$$

The solution to this equation depends on four parameters: the initial condition, $\sigma_b(t = 0)$, and the three rate constants. They were fit using nonlinear regression on the data shown in Figure 2c of the main text. They were found to be: $k'_{off} = 4.7 \cdot 10^{-3}\ s^{-1}, k'_{on}\sigma_0[K_0] = 7.5\ \mu m^{-2} s^{-1}, k_s = 6.0 \cdot 10^{-4} s^{-1}$.

Model 2: Solving the diffusion equation with reversible binding at the solid-liquid interface.

Muira *et al.*[452] proposed approximate closed form expressions for the solution of the diffusion equation where diffusing molecules reversibly bind to the surface. According to their model, the density of binding sites on the surface can be approximated as:

$$\sigma_b(t) \approx \frac{k_{on}[K_0]\sigma_0}{k_{off}}\left(1 - e^{-k_{diff,2}t}\,\mathrm{erfc}\sqrt{k_{diff,2}t}\right) \qquad (D.12)$$

$$k_{diff,2} = \left(\frac{k_{off}}{k_{on}\sigma_0}\sqrt{D}\right)^2 \qquad (D.13)$$

Where all variables are defined as in Model 1, $k_{diff,2}$ is a new rate constant describing the time to diffuse to the surface, and D is the diffusion coefficient for the molecule of interest. As previously, we introduced a term to describe stripping of binding sites from the surface and introduced a lag time parameter to fit the data in Figure 2c of the main text. The fit equation had the following form:

$$\sigma_b(t) = \frac{k_{on}[K_0]\sigma_0}{k_{off}} \cdot e^{-k_s(t+t_{lag})}\left(1 - e^{k_{diff}(t+t_{lag})}\,\mathrm{erfc}\sqrt{k_{diff}(t+t_{lag})}\right) \qquad (D.14)$$

$$k_{diff} = \left(\frac{k_{off}}{k_{on}\sigma_0 e^{-k_s(t+t_{lag})}}\sqrt{D}\right)^2 \qquad (D.15)$$

The fit parameters for this equation were $k_{on}[K_0]\sigma_0 / k_{off} = 2.6 \cdot 10^3\ \mu m^{-2}, \left(\frac{k_{off}}{k_{on}\sigma_0}\sqrt{D}\right)^2 = 3.0 \cdot 10^{-3}\ s^{-1}, k_s = 7.5 \cdot 10^{-4}\ s^{-1}, t_{lag} = 47\ s.$

This also gives an estimate on the diffusion coefficient of kinesin molecules. Using the above values, we find:

$$D = 3.0 \cdot 10^{-3} \cdot \left(\frac{2.6 \cdot 10^{3}\ \mu m^{-2}}{0.025\ \mu M} \right)^{2} s^{-1} = 90 \frac{\mu m^{2}}{s} \qquad (D.16)$$

Considering that the GFP-Kinesin that we use has a molecular weight of about 154 kDa (a dimer, with a 48.6 kDa contribution from the first 430 N-terminal amino acids of the rat kinesin-1 heavy chain and a 28.3 kDa contribution from the GFP-tag in each monomer), this result is twice the value predicted by the Young, Carroad, and Bell model (46 $\mu m^2/s$ for a 154 kDa protein at 22° C).[470, 471]

D.3: The kinesin surface density first drops and then reaches a steady state

We measured the fluorescence from a kinesin-coated surface over a period of 6500 s, and found that the kinesin surface density stops falling after 5000 s. An example of this is shown in Figure D.2. From seven measurements, it was found that final kinesin density is 180 ± 40 μm^{-2} (N=7, Standard Error).

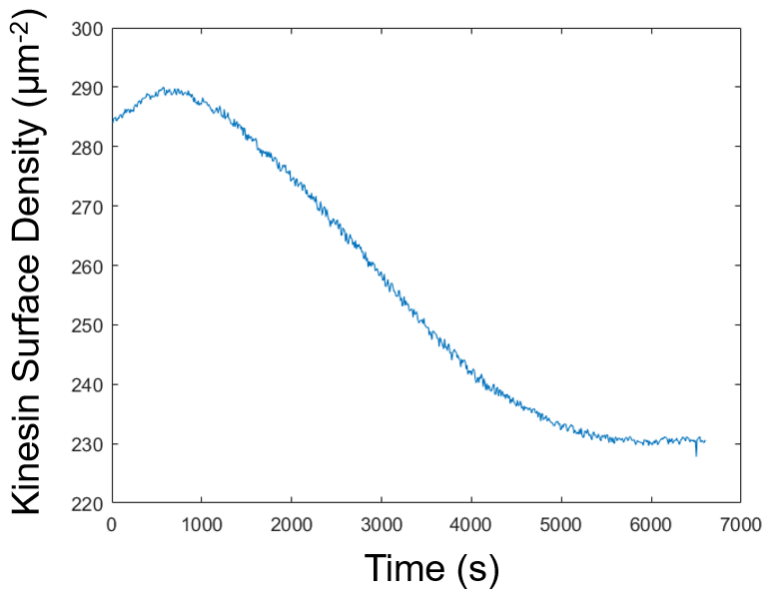

Figure D.2. Kinesin surface density over time. Plot of pixel-wise averages of image fluorescence against time. Fluorescence was converted into surface density using the calibration curve in Figure D.1.

D.4: Calculation of profiles for the FRAP experiments in Figures 2(e-f)

In order to compare the fluorescence of the bleached and unbleached region of the image in Figure 2e of the main text, the image was downsampled twice (16 pixels to 1) and the center column of pixels (outlined in dashed region), which contained portions of both the unbleached and bleached region was isolated. The mean fluorescence was separately determined for the unbleached (top dashed white box) and bleached (bottom dashed white box) region of the isolated column, converted to a kinesin density using the calibration curve described in Appendix Section 1, and plotted.

D.5: Single molecule measurements of the kinesin-surface interaction

Single kinesin off-rate measurements. Solutions containing 2.5 pM GFP-Kinesin and antifade but excluding microtubules were flown into Pluronic-F108-NTA-Ni coated flow cells and imaged using TIRF microscopy once every 1 s with 500 ms exposure time over the course of 200 s. Individual motor trajectories and residence times were recorded using open-source single molecule tracking software.[469] The data were then used to estimate the kinesin-surface off-rate constants and surface diffusion coefficients.

In the analysis of the residence time distribution of individual molecules, all molecules that were present in the first frame were excluded, and all molecules that were present in the last frame were considered right-censored. Mean residence time was estimated by calculating the integral of the empirical survival function while using the Efron correction (which counts the maximum observed residence time as observed if it is actually censored).

While analyzing the residence time distribution of individual molecules (empirical survival function plotted in Figure D.3a), we found that molecules remaining on the surface for longer periods of time displayed more robust statistics; in particular, with T denoting the random variable describing the time a molecule remains on the surface, the plot of $\mathbb{E}[T|T > t^*] - t^*$ was found to saturate at a value of roughly 40 s for $t^* > 50\ s$ (Figure D.3b), suggesting that at least part of the distribution could be described by an exponential random variable.[301] As a result, the residence time was modeled as a mixed exponential distribution with two rate parameters, with the following survival function:

$$S(t) = p_1 e^{-\lambda_1 t} + (1 - p_1) e^{-\lambda_2 t} \qquad (D.17)$$

In order to estimate the parameters, we fit the values of $\mathbb{E}[T|T > t^*] - t^*$: since,

$$\mathbb{P}(T > t|T > t^*) = \frac{\mathbb{P}(T > t, T > t^*)}{\mathbb{P}(T > t^*)} = \frac{p_1 e^{-\lambda_1 t} + (1-p_1)e^{-\lambda_2 t}}{p_1 e^{-\lambda_1 t^*} + (1-p_1)e^{-\lambda_2 t^*}}, \qquad t > t^* \qquad (D.18)$$

it follows that:

$$\mathbb{E}[T|T > t^*] - t^* = \frac{1}{\lambda_1}\frac{p_1 e^{-\lambda_1 t^*}}{p_1 e^{-\lambda_1 t^*} + (1-p_1)e^{-\lambda_2 t^*}} + \frac{1}{\lambda_2}\frac{(1-p_1)e^{-\lambda_2 t^*}}{p_1 e^{-\lambda_1 t^*} + (1-p_1)e^{-\lambda_2 t^*}}. \quad (D.19)$$

This function was fit to the data in Figure D.3b by using nonlinear regression to minimize the sum of square error. The fit parameters were: $p_1 = 0.89 \pm 0.02$, $\lambda_1 = 0.12 \pm 0.01\ s^{-1}$, and $\lambda_2 = 0.0240 \pm 0.004\ s^{-1}$. The estimate on λ_2 coincides with the off-rate for a bis-NTA bond with His_6 found by Lata *et al.*[454]. The estimate on λ_1 however is not trustworthy as it is strongly dependent on the short residence time which could be heavily influenced by false positives and discretization error originating from the long exposure time.

Single kinesin diffusion coefficient measurement. Kinesin diffusion was analyzed using the same data set as the previous section. The diffusion coefficient was calculated from molecule trajectories (sample trajectory shown in Figure D.3c) using the mean squared displacement (MSD) approach. Only particles that remained on the surface for at least 30 s were considered. A total of 77 particles were examined. The MSD was calculated for each particle up to a lag time of 25 s. The particle-wise mean MSD was determined for each lag time. Linear regression was performed on the averaged MSD data while weighting with the inverse variance of the particle-wise MSD (individual MSD plots and global fit shown in Figure D.3d). The diffusion coefficient was estimated from the fit using:

$$MSD = 4D\Delta t + c \qquad (D.20)$$

The diffusion coefficient was estimated to be $1700 \pm 20\ nm^2\ s^{-1}$.

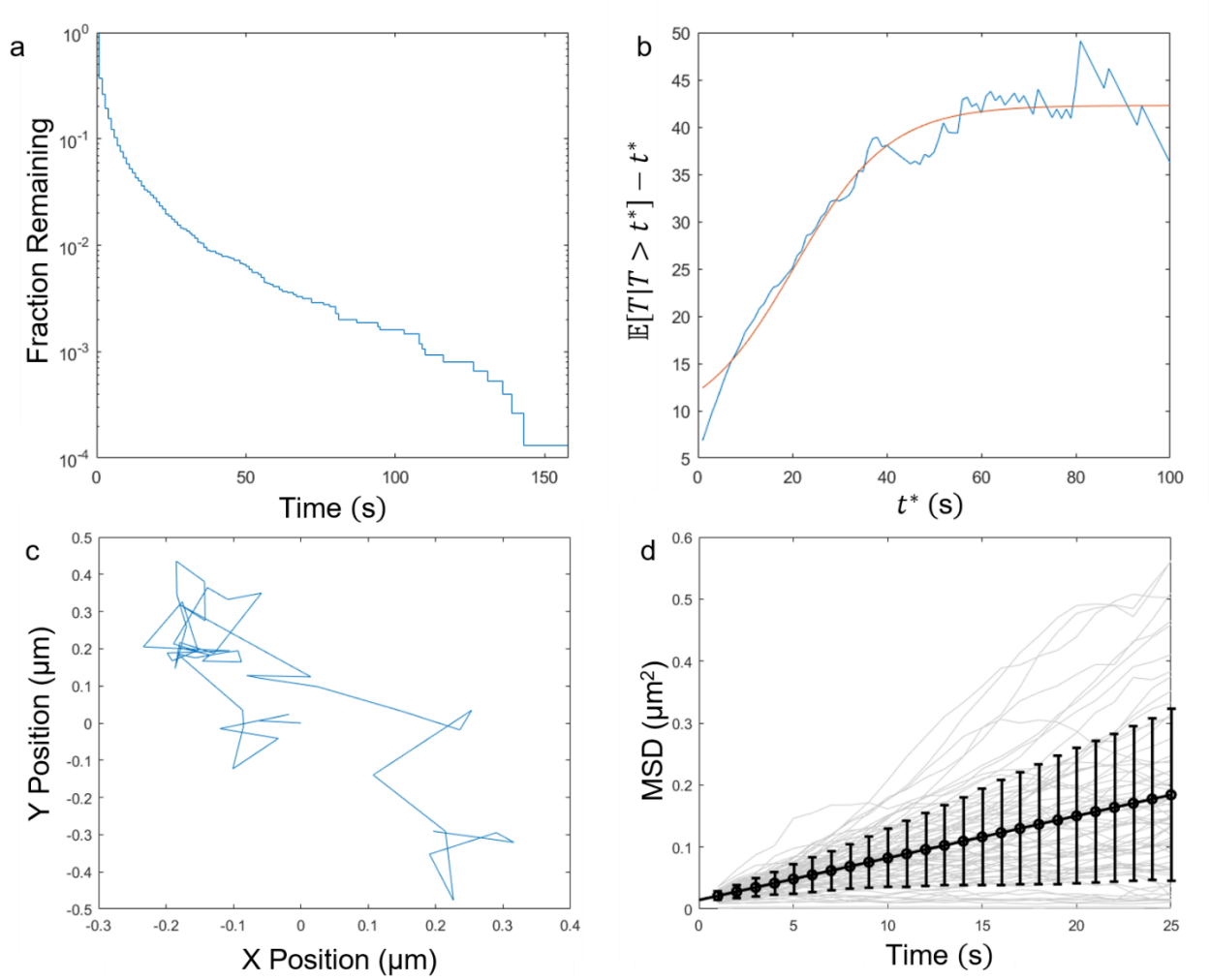

Figure D.3. Single molecule analysis of kinesin residence time and diffusion on an Ni-NTA surface in the absence of microtubules. (a) Empirical survival function of residence times with 1-frame events truncated out. (b) Plot of $\mathbb{E}[T|T > t^*] - t^*$ for the data (blue) and the fit (red). (c) Sample trajectory of a single kinesin, centered at the starting point of the trajectory. (d) Mean squared displacement of individual kinesin trajectories (gray), globally fit using linear regression (black), with weights proportional to the inverse observed particle-wise variance of the MSD at each lag time (standard deviation as black error bars).

D.6: Analysis of microtubule gliding assays

Images were flattened according to the following formula:

$$I_{Flat} = \frac{I_{orig} - O}{I_{BKGD} - O} \cdot \left(median\left(\frac{1}{I_{BKGD} - O} \right) \right)^{-1} \quad (D.21)$$

Where I_{orig} is the original 1024 x 1024 image, O is the offset (100 counts in this case), and I_{BKGD} is the image background, found by convolving a 100-pixel Gaussian blur with the original image. The median correction is implemented to return the image to original units after conversion. Only the center 512 x 512 region was used for analysis in order to avoid issues associated with image boundaries.

For each frame of the video, the pixel-wise mean and pixel-wise variance were calculated. These are shown in the figure below. The ratio of the variance to mean in each frame can be found in Figure 3c of the main text. In addition, the squared correlation coefficient between the green and red channel is found to increase with increasingly bundled behavior.

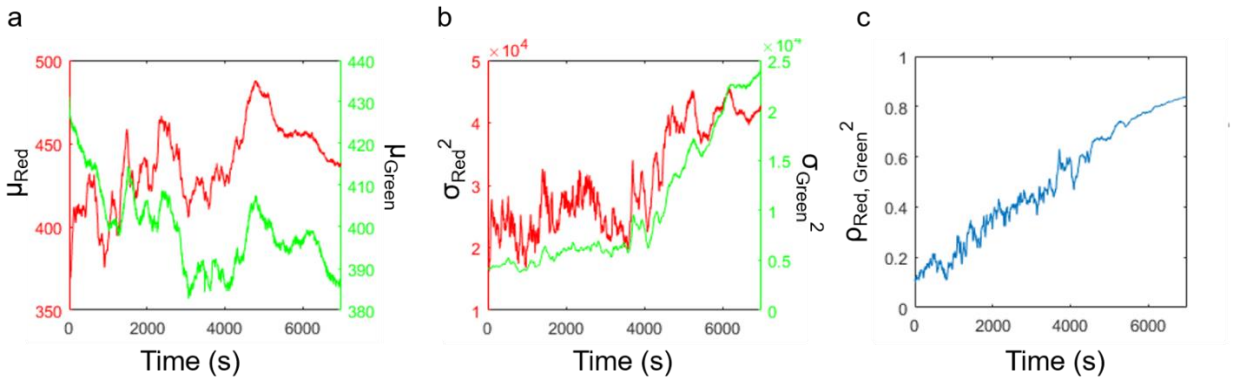

Figure D.4. Microtubules assemble into bundles as GFP-kinesins assemble on microtubules. (a) Pixel-wise mean of the red (μ_{Red}) and green (μ_{Green}) channel plotted against time. (b) Pixel-wise variance of red (σ_{Red}^2) and green (σ_{Green}^2) channel plotted against time. (c) Squared correlation ($\rho_{Red,\ Green}^2$) between the pixel-wise fluorescence counts between the kinesin and microtubule channel plotted against time.

D.7: Kinesin dwell time on microtubules increases with time

The influence of velocity on bundling behavior can be explained by considering the unbinding rate of kinesin motors from the microtubule at depleting ATP and growing ADP and P_i concentrations. In the previous analysis of this dynamic system, it was postulated that the motor unbinding rate was equal to the ratio of the velocity to motor run length.[43] During the experiment at hand, the velocity falls ten-fold. The change in run length, however, is not so clear. On the one hand, in the absence of ADP and P_i, the run length has been found to be independent of ATP concentration down to micromolar quantities.[472] On the other hand, equal concentrations of ATP and ADP were shown to decrease run length by up to 50%.[458, 472] At the same time, the addition of P_i has been observed to increase run length by up to two-fold;[473] in general, P_i has been found to have a stabilizing effect on the kinesin-microtubule bond.[277, 474] The opposing nature of the growing ADP and P_i concentrations makes it difficult to determine their cumulative effect on the kinesin density. The examination of the kinesin-1 stepping mechanism as proposed by Hancock[277] suggests that in the absence of ATP and in the presence of ADP and P_i, individual kinesin motor will be driven towards the two-head bound state, where the rear head is occupied by ADP and P_i while the leading head is bound to ADP. This state can transition backwards into the vulnerable one-head bound state. However, it was found that the reverse transition was roughly 100 times slower than the forward transition,[475] implying a saturation for dwell time with relation to ADP concentration. [475] Detachment from this vulnerable one head-bound state will then depend on phosphate release from the bound head. Since the dissociation constant for phosphate from the microtubule bound kinesin-ADP complex is in the tens of millimolar range[287, 458, 474], it is conceivable that the one head bound state will be stabilized by phosphate rebinding if the solution phosphate concentration is high enough. Using the rate

constants for the forward (3.13 +/- 2.75 s^{-1}) and reverse (329.2+/- 291.1 s^{-1} or 428 s^{-1}) [250, 475, 476] transition between the one head bound and two head bound states, and the detachment rate of a one head-bound kinesin from a microtubule (2.5 s^{-1})[277, 342], the estimate for the off-rate from the two head bound state in the presence of ADP and P_i and absence of ATP is on the order of 0.02 s^{-1}. In our experiments, microtubule bundles imaged 24 hours after the beginning of the assay were found to recover kinesin motors after photobleaching at a rate of $\lambda = 0.009\ s^{-1}$ (Figure D.5), by fitting a first order kinetics model:

$$\sigma_{K,MT}(t) = \sigma_{K,MT,0}e^{-\lambda t} + \sigma_{K,MT,max}\left(1 - e^{-\lambda t}\right) \qquad (D.22)$$

The two-fold difference between our experimentally-determined recovery rate of kinesin and our estimate from literature can be explained by the additional phosphate in solution.

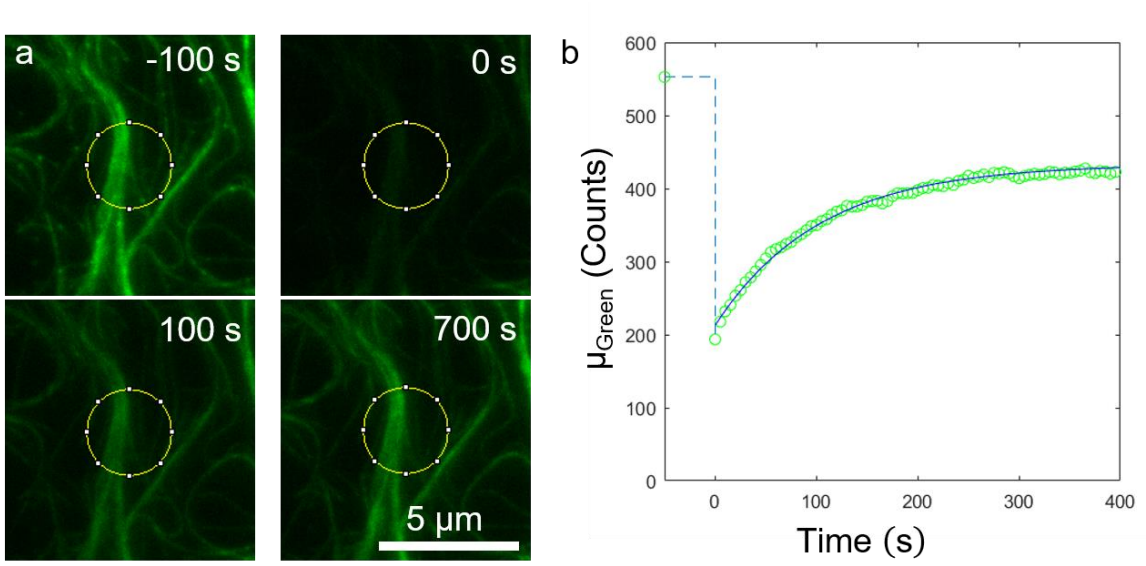

Figure D.5. Microtubule bundles fluorescence recovery after photobleaching 24 hrs after beginning of assay. (a) Microtubule bundles are photobleached 24 hrs after beginning of assay, after which they regenerate kinesin motors. Image sequence depicting the kinesin channel before photobleaching (-100 s), immediately after (0 s), 100 s and 700 s after photobleach. (b) Pixel-wise mean of kinesin fluorescence in the circle in (a) (μ_{Green}, green circles) plotted with respect to time. The data is fit with an exponential curve with saturation, revealing a recovery rate of $0.009s^{-1}$, which corresponds to the off-rate of motors from the bundle. The remaining 20% of the motors may be double-binding the microtubule to the surface.

D.8: Addition of AMP-PNP increases bundling behavior

Adenylyl-imidodiphosphate (AMP-PNP) is a non-hydrolyzable analog of ATP which locks kinesin motors in a state which strongly-binds microtubules. In order to provide further verification that the kinesin-microtubule bond strength is important to bundling dynamics, we performed experiments where an additional 100 μM AMP-PNP was added to the microtubule-kinesin-ATP-antifade solution. This experiment demonstrated nematic alignment at the onset of the experiment and featured a noticeable increase in the number of spool-like bundles (Figure D.6).

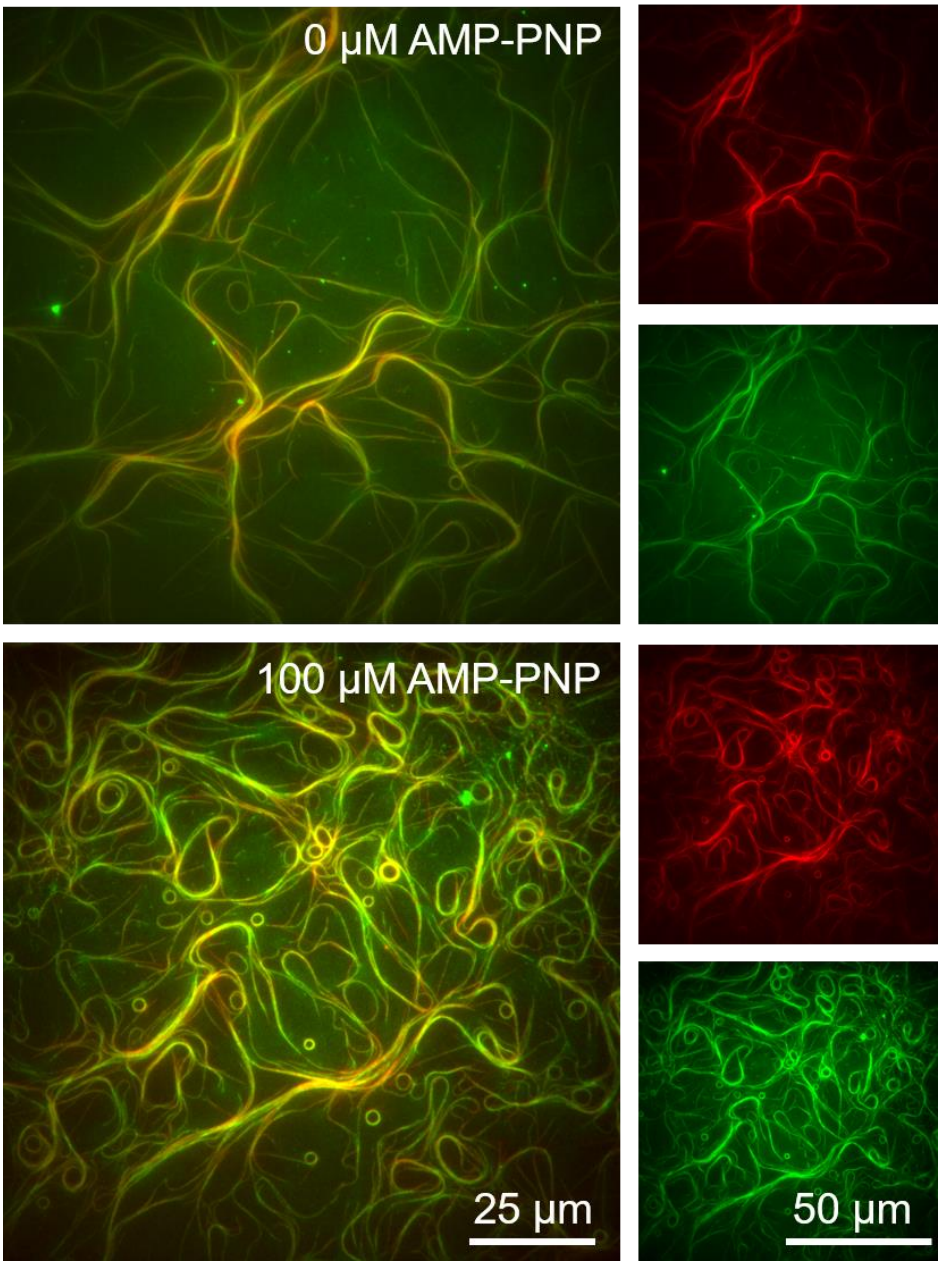

Figure D.6. Locking kinesin motors in a strong microtubule-binding state by adding AMP-PNP leads bundles to take on spool-like structures. Comparison of bundles formed 30 mins after the beginning of the experiment in the absence (top) and presence (bottom) of 100 μM AMP-PNP. Microtubules gliding in the presence of 100 μM AMP-PNP assemble more rapidly into spool-like structures.

D.9: Dependence of microtubule bundling on kinesin and microtubule concentration

Increasing the kinesin concentration 3-fold, from 25 nM to 75 nM, did not have a significant effect on bundle formation. However, decreasing the kinesin concentration 8-fold, from 25 nM to 3.1 nM, severely reduced the functionality of the dynamic system; microtubules were weakly surface bound and would not form bundles. Representative images are shown in Figure S7.

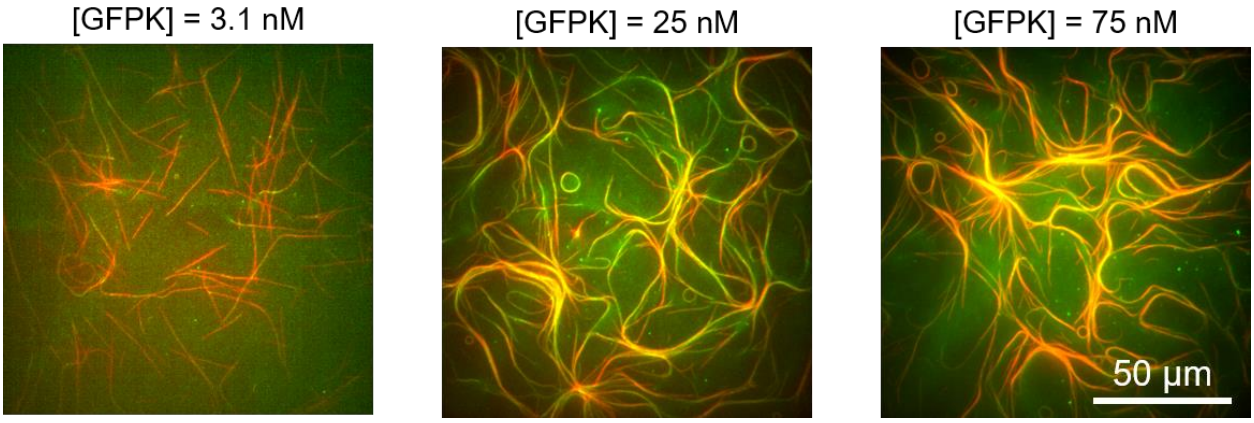

Figure D.7. Dependence of bundle formation on kinesin concentration. Bundles form at a 3-fold higher kinesin density (75 nM), yet fail to form at an 8-fold lower kinesin density (3.1 nM), as expected from our previous study. Images taken 30 mins after beginning of experiment.

Decreasing tubulin concentration from 80 nM to 40 nM and 8 nM resulted in a decrease in the density of microtubules on the surface (Figure S8). In turn, the lower densities of microtubules resulted in less bundle formation, as collision rates between microtubules fell.

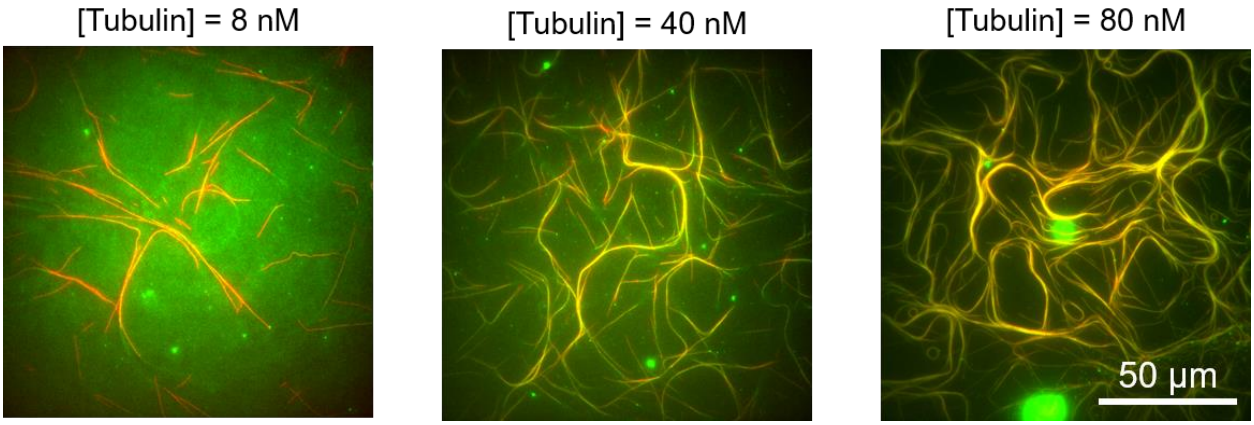

Figure D.8. Dependence of bundle formation on microtubule density. As microtubule density is lowered, microtubule bundles become more dispersed and less dense. Images taken 30 mins after beginning of experiment.

D.10: Microtubules may be attracted by the kinesin trail under neighboring microtubules

We found that the kinesin trail left behind gliding microtubules was not enough to induce following in other microtubules in a "pheromonic" manner. However, we observed events where microtubules would dissociate from and then re-associate with the same guiding microtubule shortly afterwards. An example of this is shown in Figure S9. This interaction could be due to a lateral kinesin gradient perpendicular to the axis of the guiding microtubule; however, at this stage it is not possible to differentiate it from a random event.

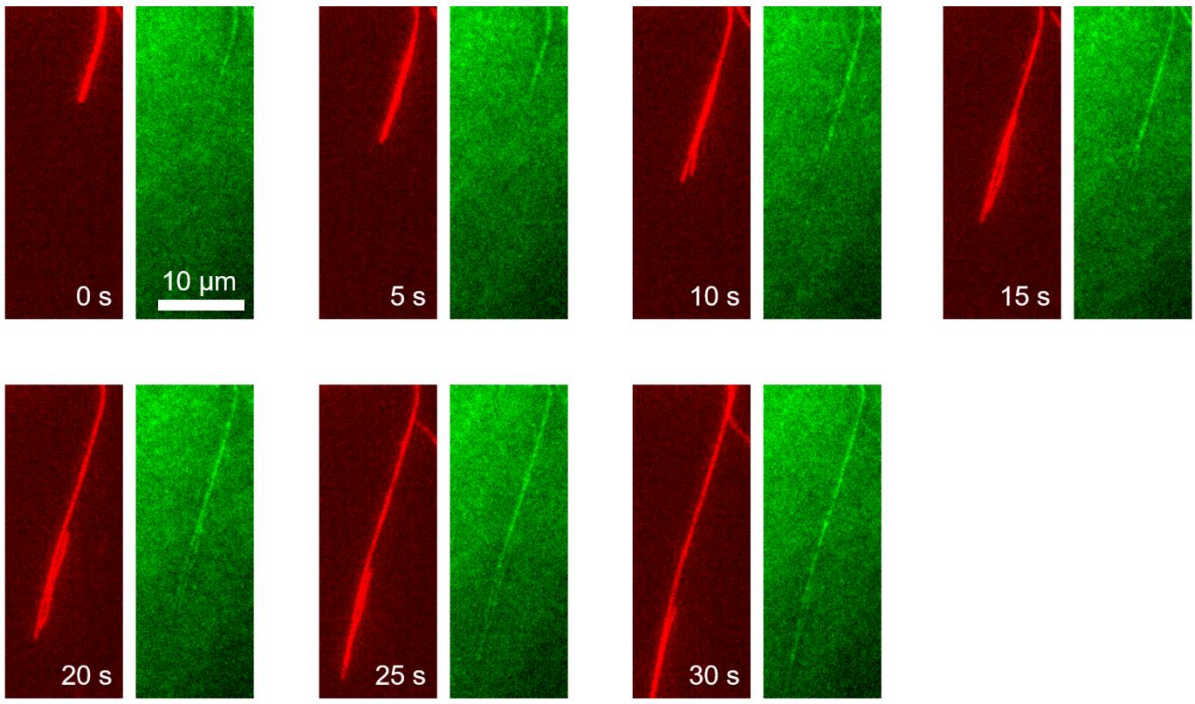

Figure D.9. Microtubule reassociation after dissociation from a guiding microtubule.

Depicted is a sequence of images where a following microtubule dissociates and then re-associates with the same microtubule. While this behavior could be due the lateral gradient of kinesin perpendicular to the axis of the guiding microtubule, it happens too rarely to distinguish it from random events.

D.11: AMP-PNP-induced microtubule bundling is weak compared to the driving force of surface-bound motors

Kinesin motors can serve as cross-links between microtubules. This can be seen by locking kinesin motors in a strong microtubule-binding state by adding 100 μM AMP-PNP into the solution containing microtubules, kinesin, ATP, and the antifade system. Initially, microtubules land in clusters (Figure D.10a). As the microtubules move in response to the 1 mM ATP in solution, the cluster spreads out radially (Figure D.10a). The spread over time was quantified by downsampling the image 128 times (Figure D.10b) and fitting the resulting image to a Gaussian of the form:

$$f(x,y) = C_0 \exp\left(-\frac{(x-\mu_x)^2}{2\sigma_x^2} - \frac{(y-\mu_y)^2}{2\sigma_y^2}\right) \quad (S6.23)$$

Where *x* and *y* are the coordinates, C_0 is the peak height, μ_x is the x-coordinate of the peak, μ_y is the y-coordinate of the peak, σ_x is the gaussian width along the x-axis, and σ_y is the gaussian width along the y-axis. C_0, μ_x, μ_y, σ_x, σ_y are the fit parameters. The total fluorescence of the field of view of the cluster does not change significantly over time (Figure D.10c). At the same time, the fit parameters reveal that the peak height, C_0, falls roughly 40% (Figure D.10d) over the span of 5000 s. In addition, the overall width of the gaussian, taken as $\sigma = \sqrt{\sigma_x \sigma_y}$, increases by 30%, or half of a downsampled pixel, amounting to about 10 μm. This indicates that microtubules are escaping from the initial cluster. The slow growth of the width can be attributed to two factors. First, the presence of the inhibitory 100 μM AMP-PNP limits microtubule velocity. Second, the spread cannot be described by simple diffusion-based kinetics, as microtubules near the center of the cluster are sterically confined from moving down the concentration gradient.

The escape of microtubules from the cluster suggests that microtubule cross-links by kinesins are not a significant factor for microtubule interactions in the absence of AMP-PNP.

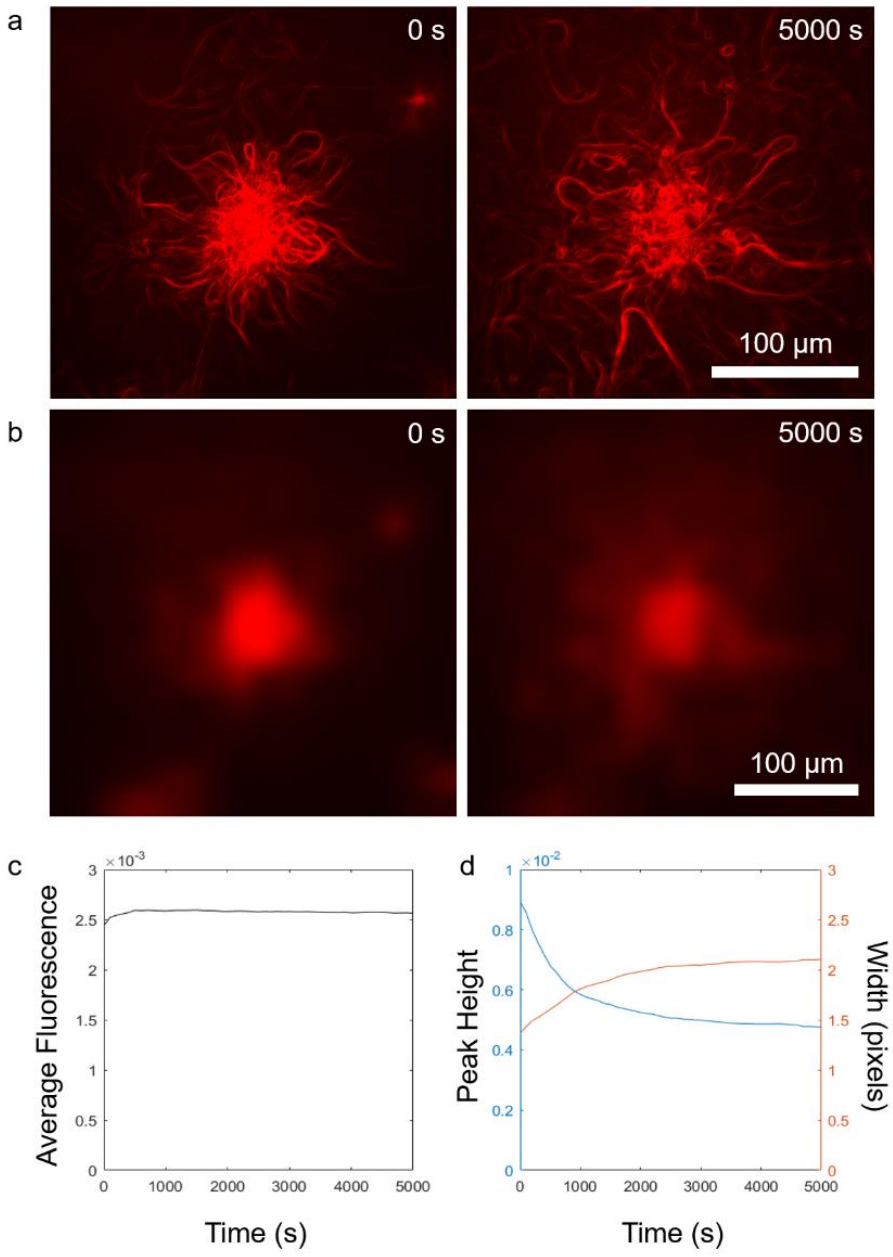

Figure D.10. Dispersion of microtubules from a cluster formed in the presence of 100 µM AMP-PNP. (a) Image of the microtubule channel of the dynamic system when 100 µM AMP-PNP is included in the motility solution at the onset of the assay (0 s) and 5000 s later taken with 40x magnification. (b) Downsampled version of images in (a), generated by downsampling by a ratio of 128^2 pixels to 1. (c) (Left) Pixel-wise average fluorescence of the downsampled image across time, and (Right) the fit gaussian peak height and fit gaussian width of the downsampled image across time.

D.12: Gliding microtubules do not experience a significant change in velocity when colliding with other microtubules in the presence of 1 mM AMP-PNP

To verify that cross-linking of microtubules by kinesin motors does not play a major role in the generation of collective behavior, we examined the velocity of microtubules gliding in the presence of 1 mM ATP and 1 mM AMP-PNP during a parallel (Fig D.11a) and anti-parallel (Fig D.11b) alignment.

The velocity was estimated by recording the distance traveled by the microtubule tip every ten frames. As expected, the velocity of microtubules decreased significantly over the course of the system lifetime due to depleting ATP. To determine whether the microtubule velocity changed significantly during a collision, the downward trend in velocity was fit using linear regression for: (1) the time period over which the colliding microtubules did not interact and (2) the time period over which the microtubules did interact (Figure D.11c-d). Using a 2-parameter Wald test, we found that the fits were not statistically different in both cases ($p=0.86$ and $p=0.67$ for the parallel and anti-parallel collisions, respectively).

Since we do not observe a statistically significant difference in the velocity under the highest AMP-PNP concentration, which should cause the highest degree of microtubule cross-linking by kinesin motors, we conclude that multi-headed kinesin motors do not play a significant role in the alignment of gliding microtubules in our dynamic system.

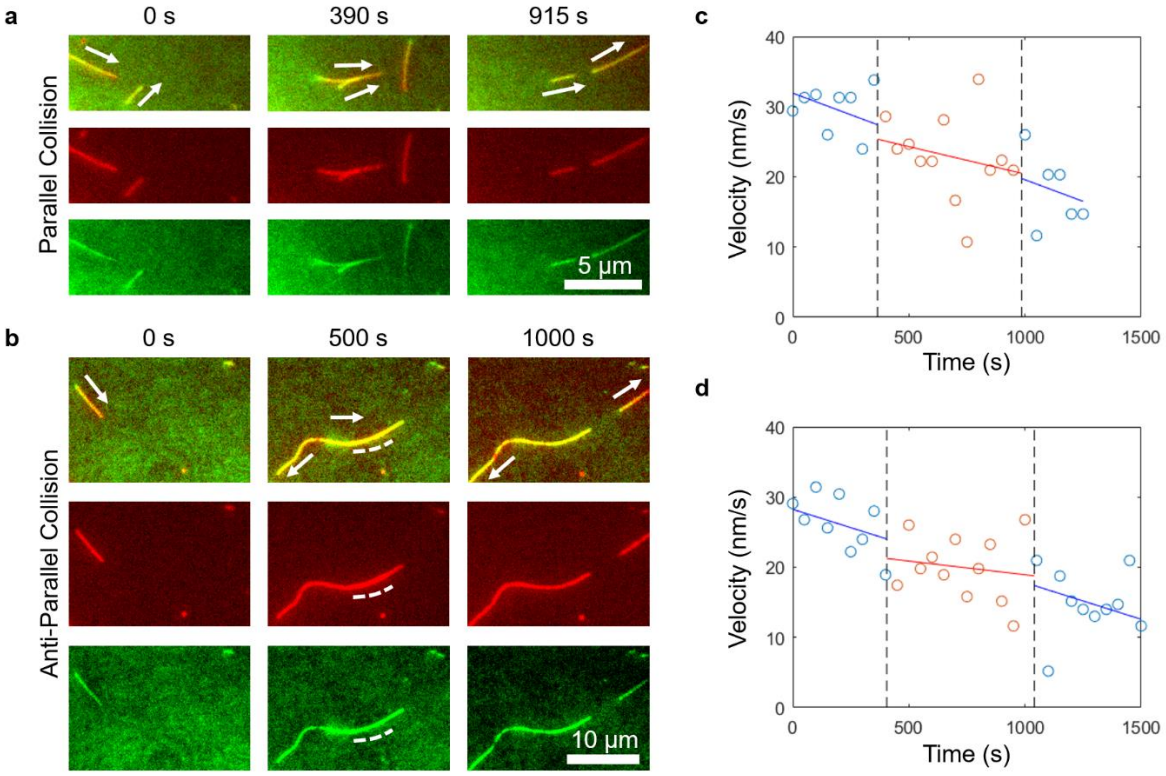

Figure D.11. Microtubule velocity does not change significantly during collisions in the presence of 1 mM AMP-PNP. (a) Image sequence of parallel collision and alignment. (b) Image sequence of anti-parallel collision and alignment. (c) Velocity of top microtubule in (a) before, during, and after the collision, fit using linear regression. (d) Velocity of top microtubule in (b) before, during, and after an anti-parallel collision fit using linear regression. Blue markers indicate time points when microtubules are not interacting; red markers indicate time points when microtubules are interacting.